Advances in Geological Science

Mitsuhiro Toriumi

Geochemical Mechanics and Deep Neural Network Modeling

Applications to Earthquake Prediction

Springer

Advances in Geological Science

Studies in the twentieth century uncovered groundbreaking facts in geophysics and produced a radically new picture of the Earth's history. However, in some respects it also created more puzzles for the research community of the twenty-first century to tackle. This book series aims to present the state of the art of contemporary geological studies and offers the opportunity to discuss major open problems in geosciences and their phenomena. The main focus is on physical geological features such as geomorphology, petrology, sedimentology, geotectonics, volcanology, seismology, glaciology, and their environmental impacts. The monographs in the series, including multi-authored volumes, will examine prominent features of past events up to their current status, and possibly forecast some aspects of the foreseeable future. The guiding principle is that understanding the fundamentals and applied methodology of overlapping fields will be key to paving the way for the next generation.

Mitsuhiro Toriumi

Geochemical Mechanics and Deep Neural Network Modeling

Applications to Earthquake Prediction

Springer

Mitsuhiro Toriumi
Kamakura, Japan

Japan Agency of Marine-Earth Science
and Technology
Yokohama, Japan

ISSN 2524-3829 ISSN 2524-3837 (electronic)
Advances in Geological Science
ISBN 978-981-19-3658-6 ISBN 978-981-19-3659-3 (eBook)
https://doi.org/10.1007/978-981-19-3659-3

Preface

Science of natural phenomena involves wide range of human recognition from what understanding is to what universe is in a few past decades. The planetary sciences extend to their research domain from the solar system to exoplanetary one by means of high-energy particle physics to astrobiology. The scientific method to investigate the nature of this complicated system endeavors the data-driven science on huge amount of various information including numerical to image data. Then, vast amounts of complicated information concerning the environments around us should be transformed availably into the simple and understandable data by means of deep machine learning or deep generative neural network modeling even within the very short time lag; although this transformation method is represented by dense connection of many nonlinear transformation units with huge amounts of parameters, and it is to say that this type of transformation from big data to simple data manifests a sequential connection of nonlinear functions involving dimension reduction with space and time.

By the way, mechanical process of the solid earth contains mechanics of various scales from crystal lattice in which various defects such as vacancies, impurities, dislocations, grain boundary, and cracks, to whole earth system containing plate motion, mantle and core convection, and seismicity. The former should be investigated by materials science and the latter by large-scale continuum mechanics based on the materials science such as rheology, fracture mechanics, thermodynamics, defect chemistry, and solution chemistry.

On the other hand, the large-scale continuum mechanics for the solid earth is very complicated because there are abundant materials parameters and various kinds of system parameters derived from inhomogeneous distribution of the different masses, fluid, and gases by which the physical parameters commonly display the discontinuous distribution.

On the other hand, in the earth science, the plate tectonics framework has been established after 1969–1970 for the global mechanics of the solid earth, and it brings us the simple feature of the solid earth mechanics by rotation motion on spherical earth of 7–10 rigid plates without accommodation problem. However, this simple model is possibly applied for the long-term average motion of superficial solid earth

in the time scale of 10^6 years. It is not applied for the short-term mechanics within several hundred to thousand years such as giant earthquake and volcanic eruption even in the subduction zone. This may be due to the reason why no mechanism relevant to the short-term plate motion and large-scale fracture process of the plate boundary cannot be understood yet. Furthermore, it seems still mysterious what is the relation among large-scale fracture or the plate boundary slip, small-scale crack process, and permeable fluid flow and its reaction with minerals in the solid earth.

It should be sure that microprocesses of earthquake are represented by small shear crack growth and successively enlarged shear crack propagation along on the large fault plane such as the plate boundary, being derived from increase of differential stress and fluid pressure. Furthermore, the earthquake source process involves rapid propagation stage and later stop of slippage of the fault in the solid earth interior. It is well known that the shear crack propagation takes place at the condition of crack tip shear stress over the fracture strength of the surrounding rock, but the mechanism of the slowdown and stop of the slip speed seems to be required for finite strain energy ranged in the mass around the present fault. This is because crack tip stress proportional to square root of crack length increases and keeps over the fracture strength with crack growth and propagation if the external stress maintains the constant value with time and space. Such inhomogeneous stress distribution of the solid earth interior may be controlled by distribution of the large faults and the fluid. The distribution of the aqueous fluid, however, should change with time according to dehydration and hydration reaction with minerals and permeable flow in the porous and faulted rocks. Therefore, it should be noteworthy that the preseismic phenomena must involve the mechanical process which is governed by growth, coagulation and propagation of shear cracks, and the fluid flow process which is controlled by the permeability, water–rock interaction, and porosity of rocks.

By the way, as noticed in the previous book, it seems that there is a possibility of probability prediction of large earthquakes by means of deep neural network modeling of global and regional correlated seismicity in the plate boundary zones, because of local seismicity and major components of correlated seismicity can be seen as a pseudo-inverse relationship in the sparse modeling. Furthermore, it may be available to understand the global seismicity behavior that the spatiotemporal variation of global and regional correlated seismicity manifests a temporal transition of mechanical network of the seismicity in the global plate boundary zone.

Furthermore, it shows that the sub-annual to tri-annual variation of the regional and global correlated seismicity and correlated partial b-value of them can be identified throughout the time series. For the near annual variations of earth rotation, gravity, and sea level change by satellite observation have been observed, it should be investigated whether the global seismicity time series is synchronous with these global satellite data series or not. Based on these detailed data analyses, it is required that the methods of probability prediction of the large earthquake along on the plate boundary region will be developed using the deep machine learning with neural network modeling applying for the huge amounts of multivariate time series data.

In this book, the author, therefore, will intend to discuss the various kinds of natural phenomena concerning the geochemical mechanics and the time scales of

their physical process relevant to the earthquake generation in the plate boundary zone in Chap. 2. The present geochemical mechanics contains the physicochemical and petrological process of the crack sealing and sub-critical crack growth, natural occurrence of the sealed shear crack with related jog and open cracks, permeable convection with metasomatic reaction in the plate boundary fractured zone as discussed in Chap. 3, and extremely rapid exhumation of the plate boundary metamorphic masses which may generate very fast slip motion of the orogenic masses occurred in the geological context (Chap. 4). On the other hand, in Chap. 5, to obtain the regularized time series (10 days step) of satellite gravity data, length of day (earth rotation), average sea level change, and the VLBI data of interplate distance time series with the global correlated seismicity, the Gaussian regression method with Bayesian modeling has been applied for clarifying the synchronous relation among them. In this study, the global and regional correlated seismicity has been extended in the period of 1990 to 2021 from 1990 to 2018. In Chap. 6, on the other hand, it will be discussed that the behavior of the global and regional seismicity network inferred from correlated seismicity is possibly analyzed by the Gaussian network modeling. In addition, the detail structure and temporal transition of the seismicity network will be discussed by the Pearson's correlation map for logarithmic seismicity time series of important localities in the plate boundary zone.

Finally, the probability prediction testing using deep neural network modeling will be tried on the base of the newly developed multilabeling and variational time-shift method for large earthquake event series in Chap. 7. In Chap. 8, it will be discussed that the DNN and GVAE modeling may be needed for enough machine learning of the correlated seismicity and multilabeling method of the large earthquake probability prediction study.

In this book, the author will intend to present several codes of CNN and VAE modeling with multilabeling and variational time-shift and timestep method (VTTM) for large earthquake prediction training and testing on KERAS with TENSORFLOW of PYTHON 3 base as listed in Appendix.

Kamakura, Japan Mitsuhiro Toriumi

Acknowledgements

Metadata and data products for this study were accessed through NOAA, IERS, GRACE, and USGS data centers for SLR, LOD, gravity data, and global seismic data. The author sincerely thanks to these organizations of the global monitoring of geophysical data for open science usage. The author intends to express sincerely thanks for Google Colaboratory to use the cloud processing by DNN modeling on KERAS with TENSORFLOW.

The author very thanks to Data Center of Earthquake Research Institute of University of Tokyo for helpful use of database of JMA-1. He also thanks much to National Institute of Earthquake Disaster for helpful use of earthquake database.

The author is also very indebted to Prof. Yoshiyuki Kaneda of University of Kagawa for many critical discussions and continuous supports for this research. He also gives me many comments of next generation of geophysical research and their social missions. He sincerely thanks Prof. Atsushi Okamoto of Tohoku University for providing the experimental data of hydrothermal flow system.

He is also indebted to Dr. Tatsu Kuwatani of Japan Agency of Marine Science and Technology for many supports on writing this book. He thanks greatly Japan Agency of Marine Science and Technology for providing the facility of the institute.

Finally, I am deeply indebted to Etsuko Toriumi for many supports and discussions, and Drs. Taeko Sato, Yosuke Nishida, Gowtham Chakravarthy and Arulmurugan Venkatasalam of Nature-Springer Publisher for many encouragements and comments.

Contents

Chapter 1
Introduction

Abstract Mechanics of the solid earth is basically very simple in the sense of the plate tectonics, but that of the solid earth interior shows us much of quite different features of complicated behavior as shown in giant earthquake and volcanic eruption. This is because the present processes contain abundant basic mechanisms with composite interactions among them and spatiotemporal heterogeneity of the constituent materials, initial and boundary conditions. Recent investigations clarify the nonlinear combination processes of rock fracture and flowing fluid–rock interaction in the solid earth interior, suggesting the necessary to study the new field of geochemical mechanics of the solid earth for developing the earthquake process.

Keywords Geochemical mechanics · Cracks · Fluid flow · DNN · Earthquake prediction testing

1.1 Introduction to Geochemical Mechanics and Deep Neural Network Prediction of Earthquake

In the present century, we experienced the giant earthquakes over magnitude 9 which damaged strongly many regions around the Indian Ocean in 2004 and Northeastern Japan region in 2011. It is regret that these giant earthquakes along on the subduction plate boundary were not predicted by any geophysical observations and investigations though the global seismic observatory networks have been founded. This is partly because we have not any scientific basis of the earthquake generation process in the solid earth though we know that the giant earthquake is the very large shear fracturing along the plate boundary and that the fracturing of rocks is due to the stress accumulation and shear crack propagation in the slip velocity softening condition. It is already known qualitatively that the deep-seated fluid is a key of geological processes controlling the frictional slip of plate boundary and the recovery of the large earthquake slip zone through geochemical reaction between fluid and minerals.

On the other hand, there are very large number of parameters governing the earthquakes in the solid earth interior because the rock mass of the plate boundary zone contains abundant cracks, faults and folds, various rock units, and water content that are formed under the long- and short-term geological processes, and these different

M. Toriumi, *Geochemical Mechanics and Deep Neural Network Modeling*,
Advances in Geological Science, https://doi.org/10.1007/978-981-19-3659-3_1

types of spatial inhomogeneity in size and materials parameters are to be finite but huge amounts of free parameters in the seismic dynamics. In addition, the large-scale sudden shear fractures take place in the nonlinear dynamical process after linear elastic deformation and nonlinear yielding of geological mass. Judging from such complexity of the earthquake dynamics in the system having large number of parameters about 10^{10} (fault bounded rock volume of 10^{-3} km^3 in geological mass of 10^6 km^3 and each rock volume has more than 10 parameters), the controlling mechanisms and their dynamics should be difficult to be modeled straightforwardly in the simple models, but in the statistical models of the geological mass as the many body system, it seems that the robust and near invariant relations of the observed parameters are to be possibly approximated as the controlling equations for the complicated seismicity dynamics as discussed in the previous book (Toriumi 2021). To obtain the near invariant relations above, it needs that huge amount of data relevant to the mechanical and seismic data are possible to be obtained as the time series like the seismicity data from global and regional seismic station networks and satellite geophysical data.

The system of the elastoplastic multibody of the geological mass that has huge number of free parameters should be also inferred to have stationary states that defined by the stable assemblage of finite number of parameters in the constraint conditions. In the previous book, the author proposed the global seismicity dynamics which is represented by the nonlinear bistable dynamics of the correlated global seismicity variables and together with the network seismic dynamics of gridded subduction zones. The specified network system of the global correlated seismicity parameters shows the temporal variation of the strongly correlated gridded localities of the subduction zones, that is inferred by the temporal change of eigenvectors having large eigenvalues of the covariant matrix of the logarithmic seismicity data matrix.

The multivariate time series of the global and down-sizing regional correlated seismicity can be investigated the instability against the time by means of the machine learning using the deep neural network regression method (e.g., Chollet 2020). In the previous book, the author tried to study the recurrent neural network (RNN), long- and short-term memory RNN (LSTM), and convolution neural network (CNN) regression to check the availability of these transformation models of one-step ahead prediction from machine learning of previous data. Then, the deep NN models having large number of parameters determined by training of early half data matrix of the correlated seismicity did not give available time series by testing of the later half data, suggesting that there is a difference in characteristic pattern of the correlated seismicity between the early and later time series (Toriumi 2021) and that the difference may be derived from the temporal change of the correlated seismicity network.

By the way, as illustrated in Fig. 1.1, the source process of earthquake is probably the shear crack propagation after subcritical slow crack growth, and large earthquake appears the large size of shear crack under nearly constant stress drop (e.g., Sibson 1977, Rice 1979, Ohnaka and Matsu'ura 2002). The shear crack propagates with the rate of K^m in the condition that the size is over the Griffith critical size, where K is the stress intensity factor and m is over 10. However, the shear slip on the crack surface should be controlled by the stress concentration with fluid entrainment at

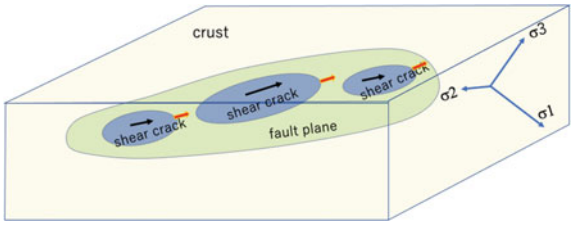

Fig. 1.1 Model of seismic source process controlled by subcritical shear crack growth and successive rapid propagation due to coagulation along on the fault plane under the stress condition. Black arrow shows the displacement, and orange one does growth of shear crack. Coagulation of growing shear cracks induces the rapid propagation of large shear crack emitting seismic wave

the tip and the resistance by jog migration and chemical relaxation due to precipitation of minerals as shown in Fig. 1.2. If the resistance of shear crack shows the negative slope against the logarithmic shear velocity, that is the shear softening, the propagation is acerated by the applied shear stress to the level of the shear velocity hardening. Therefore, the shear crack grows depending on the differential stress and the geochemical environment such as aqueous solution chemistry and existence of

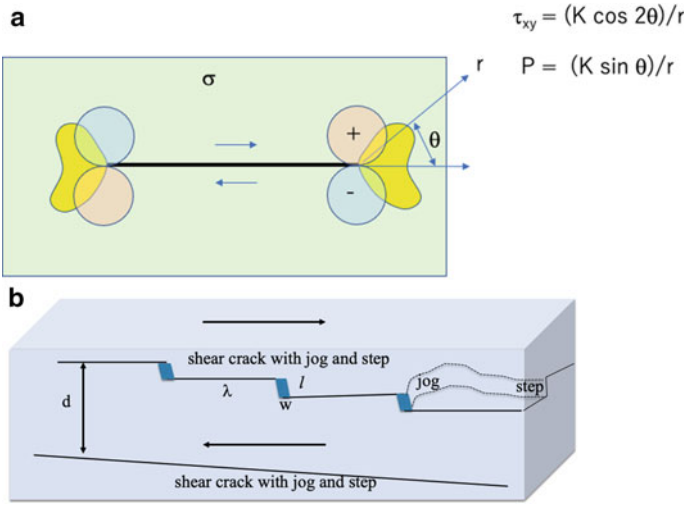

Fig. 1.2 Stress field around the shear crack tip showing the contours of compressional (+) and extensional (−) stress, and shear stress contour (yellow). K is stress intensity factor of shear crack. Around crack tip, the stress field displays the dipole. In the extensional field around the crack tip, many pores should be formed by entrainment of fluid from the compressional field. This local fluid flow makes the chemical process of dissolution—precipitation of minerals, inducing the relaxation of stress concentration at the crack tip (**a**). Shear crack commonly takes abundant and often periodic jog and step that are potentially resistant objects for shear slip and behaves as the fast path of fluid migration and as the precipitation space of minerals. The jog on shear crack is characterized by shear crack spacing ***d***, jog spacing l, jog amplitude l, and jog width w (**b**)

gaseous phase adsorbed on the shear crack surface even under the high-pressure condition (e.g., Wei 2010).

Geochemical effects on the shear crack propagation are mainly represented by decrease of the effective normal stress on shear plane and relaxation at the crack tip, by critical size of Griffith crack due to lowering of surface free energy, hydrolytic weakening by inducing the lattice defects and impurities in minerals, and chemical reactions of minerals with aqueous solution, together with pore and void formation filled with various fluids. Hydrogen embrittlement is also important in the case of open crack growth through weakened chemical bonding in minerals. Therefore, it is obvious that the above environmental processes around the large shear cracks (fault) is quite important for shear slip velocity generating elastic wave that is the seismic wave. In the natural occurrence of the geochemical environment affecting the fluid migration and mineral–solution reaction, the open cracks sealed by minerals and shear cracks having many jog sealed by elongated minerals are commonly found in the deformed rocks of the plate boundary metamorphic belt (Toriumi 1990, Toriumi and Hara 1995, Sibson 2020) as shown in Fig. 1.3. The time scales of sealing of the open cracks and jog of the shear cracks are recently investigated by Saishu et al. (2017) to be around 100–1000 years. This value of the sealing time scales is probably available for the recovery time scales for the shear faults by mineral precipitation from aqueous solution.

On the other hand, the mineral sealing of the jog on the shear cracks and of the volume of the open cracks takes place from aqueous solution at the near equilibrium conditions in the metamorphic and metasomatic rocks along the plate boundary zone. In many cases of sealed cracks, their mineral constituents are mono- and bi-mineral features and they are called as veins and mineral bands in the geological context. In additions, the mineral bands in the plate boundary rocks are characterized by the regularly repeating texture showing the alignment parallel to the shear plane in the schistose rocks. This is so-called metamorphic and metasomatic banding. On the other hand, the mineral veins commonly cut the mineral band and the shear plane of the schistose rocks, but the constituent minerals are the same as those of the mineral bands and the matrix of the rocks. Therefore, it is strongly suggested that the mineral banding and shear crack growth are mutually related in their formation process with connection of the aqueous solution entrainment into the open voids and jog of the growing cracks. It is because the sealing and filling the shear cracks are derived from precipitation of metamorphic and metasomatic minerals as well as the matrix minerals. Therefore, the geochemical processes involving the fluid migration related with fracturing of rocks in the plate boundary strongly govern the mechanical processes associated with large earthquakes (e.g., Rice 1979).

Based on the present geochemical mechanics and global and regional correlated seismicity described in the previous book, it is required that the prediction testing study of the large earthquake should be carried out by means of the deep neural network modeling (DNN) because there is a huge amount of monitoring seismic data obtained from the global and regional networks of the seismic stations. As is well-known, the deep neural network modeling of the big data is the one of the nonlinear projections to the interesting parameter space from various observables

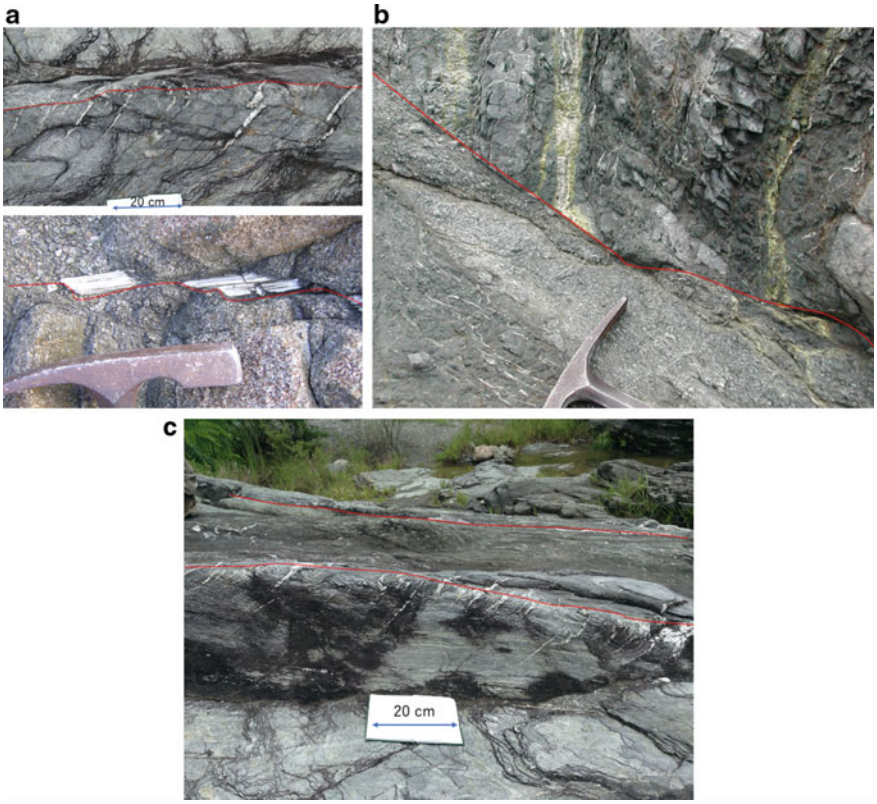

Fig. 1.3 Photographs showing the shear cracks periodically associated with coeval open cracks sealed by quartz in pelitic metamorphic rocks (**a**), jogs sealed by calcite in gabbroic rock (**b**), large sealed open crack and gouge replaced by epidote, chlorite, and calcite in basaltic rock (**c**)

space, and the projection operators are composed of many layers consisting of many nodes with mutually connection of nonlinear functions. The relation of the nodes between neighboring layers is represented by the so-called activation function such as hyperbolic–tangent type, and thus, the large number of parameters is fitted by the minimizing the square root difference of target data and calculated ones. Recently, there are many types of DNN modeling and related generative variational autoencoders (GVAEs) for the image processing and time series analysis together with anomaly detection. In this book, therefore, the author will try to investigate the prediction testing by means of various types of neural network modeling, using the big seismic data from the global and regional network of the digital seismic stations in the world.

References

Chollet F (2020) Deep learning with Python, meap version 2. Manning Publishing
Ohnaka M, Matsu'ura M (2002) The physics of earthquake generation. University of Tokyo Press, pp 378 (in Japanese)
Rice JR (1979) Theory of precursory processes in the inception of earthquake rupture, Gerlands Beitr. Geophysik Leipzig 88(2):91–127
Saishu H, Okamoto A, Otsubo M (2017) Silica precipitation potentially controls earthquake recurrence in seismogenic zones. Sci. Rep. 7:13337. https://doi.org/10.1038/s41598-017-13597-5
Sibson RH (1977) Fault rocks and fault mechanisms. J Geol Soc London 133:191–213
Sibson RH (2020) Preparation zones for large crustal earthquakes consequent on fault-valve action. Earth Planets Space 72:31. https://doi.org/10.1186/s40623-020-01153-x
Toriumi M (1990) The transition from brittle to ductile deformation in the Sambagawa metamorphic belt. J Metamorphic Geol 8(4):457–466
Toriumi M (2021) Global seismicity dynamics and data-driven science. Springer
Toriumi M, Hara E (1995) Crack geometries and deformation by the crack-seal mechanism in the Sambagawa metamorphic belt. Tectonophysics 245(3–4):249–261
Wei RP (2010) Fracture mechanics: integration of mechanics, materials science, and chemistry. Cambridge University Press

Chapter 2
Mechanics of Crack Sealing with Fluid Flow in the Plate Boundary

Abstract Fracture mechanics of the plate boundary zones is mainly governed by the dynamics of the open crack and shear cracks in rocks. The motion of these cracks has two modes related to the applied stress: one is the crack growth in the low stress conditions, and another is the crack propagation sensitive to the differential stress. The motion of open crack and shear cracks with jog is associated with formation of void space, and thus, it is obvious that the entrainment of aqueous fluid into the void and successively precipitation of minerals takes place in the void. This is called as mineral sealing and the resultant cracks are named as the sealed cracks, suggesting the possibility of analyses of stress configuration and timing by sealed cracks geometry and of geochemical interaction between cracks and aqueous solution in the fluid flow through rocks.

Keywords Crack growth and propagation · Crack sealing · Geochemical interaction of cracks · Shear crack jog

2.1 Geometry and Distribution of Naturally Sealed Cracks

Recent investigations of the multichannel seismic profiling along the subduction zone revealed that several high reflection layers exist in the accretionary wedge above the boundary between subducting slab and overriding island arc crust. These reflection layers called as DSR by Park et al. (2002) are associated with the low Vp and Vs and high Vp/Vs region under DSR, suggesting the high porosity filled with fluid water. On the other hand, along the upper boundary of the low velocity region, the bifurcated large fault can be found by Park et al. (2002) indicating the lower low velocity region with abundant fluid filled pores and open cracks.

The boundary zone between the subduction boundary and the bifurcation faults shows active seismicity and low seismic velocity narrow region even in the depth of 100 km. Tsuru et al. (2002) found the clear difference of the reflector structure in this narrow zone by the MSR images between the 2000 and 2003 experiments, suggesting the fluid accumulated layers migrated upward in the large scale after Tokachi-Oki earthquake.

M. Toriumi, *Geochemical Mechanics and Deep Neural Network Modeling*,
Advances in Geological Science, https://doi.org/10.1007/978-981-19-3659-3_2

On the other hand, Akuhara (2018) obtained the interesting results from the receiver function method that there are abundant fluid occupying lenses along boundary layers between the subduction slab and the overriding accretion prism in the Nankai Trough. It is strongly suggested that the boundary layer presented above is abundant in cracks or lens-like pores and their average orientation changes with time quickly. It seems, therefore, that the boundary layer is to be abundant in crack density and resultant high permeability. Furthermore, the permeability may change after slow slip event occurred in the layers above the present boundary layer.

In the Hikurangi subduction zone of New Zealand and in the Cascadia of Western Canada, there are similar configurations of the slow slip zone (Todd et al. 2018; Rogers and Draget 2003), and the seismic activity of nonvolcanic tremor as clarified by Schwartz and Rokosky (2006), respectively.

By the way, the structural geology of the subduction boundary rocks along the Shimanto accretionary belt of SW Japan (e.g., Taira et al. 1988) and Alaska–Aleutian belt (e.g., Byrn 1986) were investigated for long time. In these accretionary prisms, there are abundant out-of-sequence thrust and tight folds with partly sheath folds in the turbidite sequences. The large-scale thrust faults are often associated with pseudotachylite that shows melting the fault wall by shear heating, indicating the high-speed slippage emitting seismic wave (Ikesawa et al.2003). On the other hand, the sheath folds are a manifestation that soft sedimentary sequence was deformed with very large strain as a flowage style in the wet condition, and the long axial orientation is just parallel to the plate subduction direction. Furthermore, these sedimentary sequences are commonly faulted associated with shear and open sealed cracks (Toriumi 1990). It seems, therefore, that in the plate boundary rock and wet sediments, shear and open cracks showing a wide range of displacement and velocity are abundant. Next, the geometry, distribution, and mineralogy of these sealed open and shear cracks will be described in detail in the plate boundary rocks.

In this section, the sealed cracks in the slightly deep and shallow subduction zone are discussed in detail in order to clarify the role of aqueous fluid in the shear and open type cracks generated and propagated by the fluid percolation in the stressed boundary zone rocks of the subduction zone. The examples to be discussed are from the Shimanto accretionary wedge and the Sanbagawa metamorphic rocks, because of many detailed studies on physical conditions of the metamorphism in the subduction zone.

The rocks of the Shimanto accretionary wedge are suffered from low-grade metamorphism from the greenschist to prehnite–pumpellyite facies. The physical conditions of these metamorphic facies range from 150 to 300 °C in temperature and 200 to 500 MPa in pressure (Toriumi and Teruya 1988), suggesting the hanging wall crust above the subducting slab of the Philippine Sea Plate at Nankai Trough in the period from 60 to 30 Ma. On the other hand, the southern zone of the Shimanto belt comprises of shallower accretionary wedge ranging from 20 km to several km depth rather than the Northern Shimanto belt. The rocks of the southern Shimanto belt seem to be suffered from very low-grade metamorphism of about 100 to 200 °C in temperature (Ohmori et al. 1997). The tectonic situation of these rocks is approximated as shown in Fig. 2.1 (Geological Survey of Japan 2015).

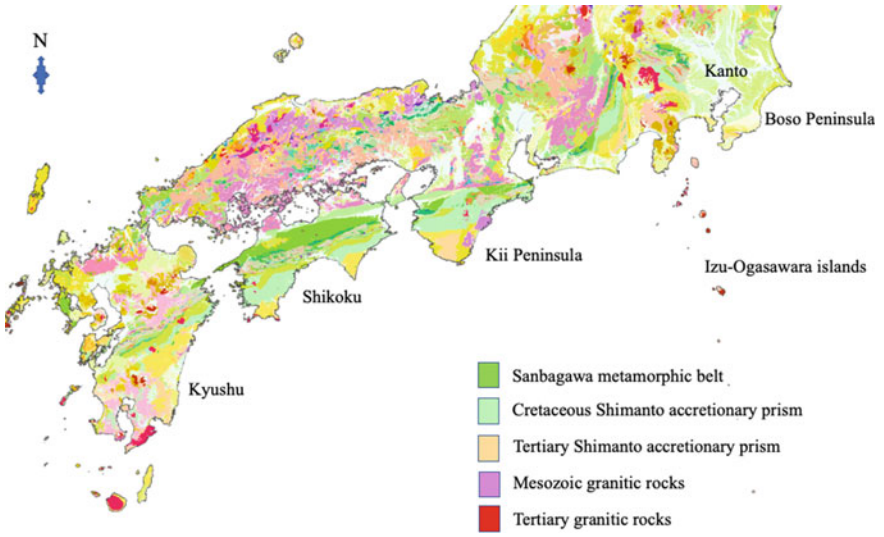

Fig. 2.1 Outline of geology of the Southwestern and Central Japan cited from database of geology in Geological Survey of Japan (https://gbank.gsj.jp/seamless/). In this book, Shimanto accretionary prism and Sanbagawa metamorphic belt of the regions of Kyushu, Shikoku, and Kii Peninsula are discussed

On the other hand, the Sanbagawa metamorphic rocks are suffered from high pressure type metamorphism ranging from 300 °C to 600 °C in temperature and in pressure from 1 to 2 GPa, and the age of the metamorphism is in the range from 60 to 90 Ma (Itaya et al. 2011). The pressure–temperature paths of the metamorphism are inferred to be likely to the adiabatic path in the rocks associated with subduction of the slab both in the prograde and retrograde metamorphism.

Plastic deformation has been clarified by Toriumi (1982), Toriumi and Noda (1984), and Toriumi and Teruya (1988), in the quartzose metamorphic rocks of the Shimanto and Sanbagawa belts by means of deformed shape of quartz-filling radiolarian fossils having originally spherical shape. They have clarified that the geometry of the strain ellipsoid of the plastic deformation in the metamorphism ranges from plane strain to flattening type in the Shimanto rocks but in the Sanbagawa rocks, it displays from prolate to plane strain type as shown in Fig. 2.2. The magnitude of plastic strain of these rocks increases with metamorphic temperature from several ten percent to several hundred percent. The differential stress which contributes to the plastic strain was inferred to be about 30–100 MPa by means of dislocation density and dynamically recrystallized grain size of quartz using TEM (Toriumi et al. 1986).

Sealed cracks are to be classified into two types: one is the folded and sometimes sheared sealed open and shear cracks, and the other is the undeformed to slightly deformed open and shear cracks sealed or partly sealed by metamorphic minerals. As noted previously, the deformed sealed cracks should be plastically deformed in the deep-seated accretionary prism, but undeformed sealed cracks were not surely

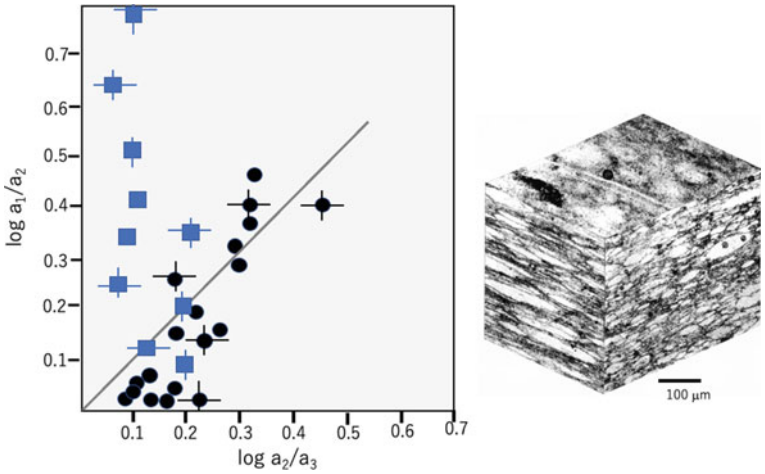

Fig. 2.2 Geometry of the strain ellipsoids determined by initially spherical radiolarian fossils in metamorphic cherts in the Shimanto (sphere) and Sanbagawa belt (square). The data points are the average of the several ten deformed radiolarian fossils in a single rock sample. The right figure shows the three-dimensional images made by photographs of three thin sections

suffered from plastic deformation during the metamorphism although surrounding metamorphic rocks were largely suffered from plastic deformation as described earlier. Thus, the sealed cracks should manifest their mechano-chemical environment in the deep plate boundary zone. In the book, the author intends to summarize the characteristic features of shear and open type cracks and their sealing through fluid flow by metamorphic minerals in the deep plate boundary zone. Furthermore, it will be described and discussed in detail that many sealed cracks show obvious plastic deformation in these metamorphic rocks.

Geometry of the sealed cracks is classified into two types: one is the sealed open cracks and another the sealed shear crack as shown in Fig. 2.3. The former is identified by the lens-like shape vein filled with metamorphic minerals that are mainly albite and chlorite in basic schists and quartz and calcite in pelitic schists of the Sanbagawa and Shimanto belts. The latter type sealed cracks are characterized by discontinuous array of small lens-like jog connected by the very thin platy dark seams (Fig. 2.4). It is obvious that the arrayed small jog is occupied by tabular to acicular grains of albite in basic schists or quartz in pelitic schists of which direction of tabular grains is apparently parallel to the schistosity plane. The schisitosity plane often cuts the preexisting sealed open cracks filled with quartz in pelitic schists, showing clearly that it is the shear cracks and associated jog filled with metamorphic minerals. The alignment of the tabular grain of minerals should be formed by the directed geometrical growth of filling mineral grains accompanied with opening the jog by shear slippage as shown in Fig. 2.3.

The relations of the shear cracks and the open cracks sealed by minerals can be obtained by measuring the orientations of sealed cracks of shear type and open type

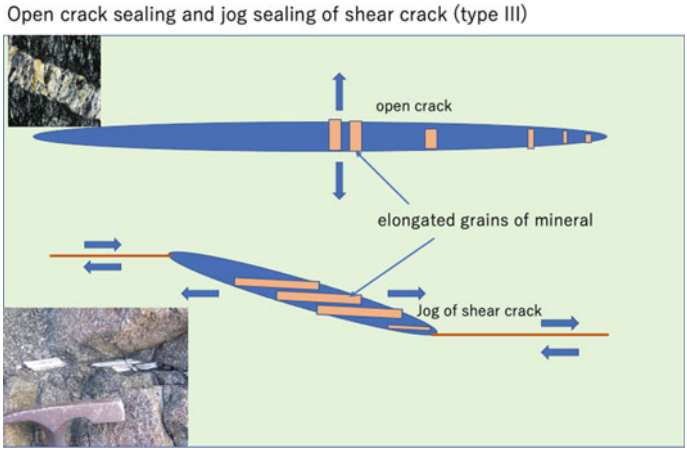

Fig. 2.3 Illustration of open crack and shear crack geometry with jog, showing elongated growth direction of sealing minerals and the examples of natural occurrence

Fig. 2.4 Photograph showing the sealed jog of shear crack containing the dark inclusion array parallel to the outline of the jog

in the field. The histograms of them are shown in Fig. 2.5, suggesting the high angle between the shear plane and open crack extension about 70–80°. Judging from the opening orientation of open crack is probably parallel to the minimum principal stress orientation and normal to the maximum orientation of the principal stress, the shear plane is slightly oblique to the maximum principal stress orientation.

The length and width (aperture) of the sealed open cracks were studied in the Sanbagawa and Shimanto belt by Toriumi and Hara (1995) and Toriumi and Yamaguchi (2000). In this study, the author measured the frequency distribution of the width of the open cracks sealed by albite and chlorite in basic schist and quartz in pelitic schists of the Sanbagawa and Shimanto belts as shown in Fig. 2.6, showing the lognormal distribution function in both basic and pelitic rocks. On the other hand, the length of the sealed open cracks is rather difficult to be measured because large flat outcrops are rare, but the length of the sealed cracks is often larger than the size

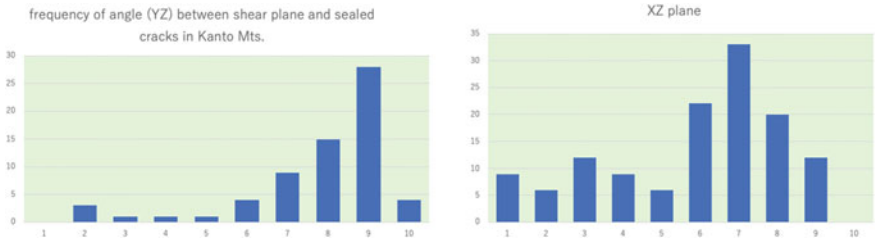

Fig. 2.5 Diagram showing the frequency distribution of angles (x10 °) between the sealed open cracks and related shear plane measured on the plane perpendicular to shear plane and parallel to shear direction (left), and normal to the shear plane and the shear direction (right)

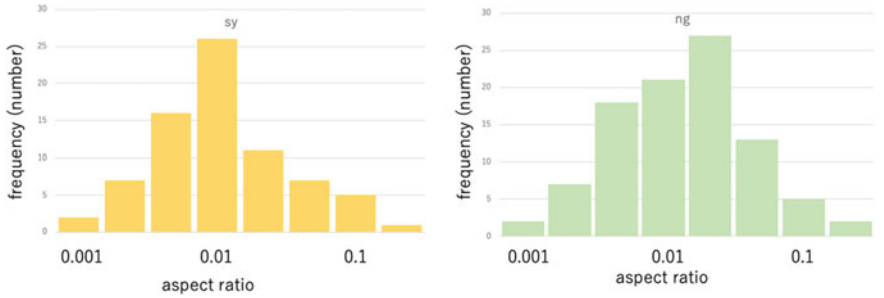

Fig. 2.6 Diagram showing frequency distribution of aspect ratio of sealed open cracks in the plate boundary metamorphic rocks of two localities in the Kanto Mountains

of flat outcrop in the field. The aspect ratio of the length and width of the sealed open cracks in Fig. 2.6 indicates the length proportional to the width of the sealed open cracks. The average ratios of the length by the width reach about 100–200, but in the case of the echelon type sealed cracks those range from 10, suggesting the different mechanics even though being associated with precipitation of minerals from flowing fluid.

Three-dimensional features against the principal stress orientation of the sealed open type cracks are probably deduced by the geometrical relations between the associated normal faults and sealed crack clusters as shown in Fig. 2.7. As the crossing axis of the conjugate normal faults should be parallel to the second principal stress axis, and the bisecting orientation against two conjugate fault plane is to minimum principal stress axis, the average length of the sealed open cracks elongated to the second principal axis and that elongated to the first principal stress axis should be measured and then the ratio of them should be estimated to be about 1.5–2.5 in the case of Shimanto and Sanbagawa rocks. Therefore, it concludes that three-dimensional shape of sealed open cracks displays about elliptical disk elongating to the second principal stress direction as illustrated in Fig. 2.8.

Next, the characteristic features near the tip of the sealed open cracks will be shown because the crack tip is the singular point of the open crack and related geochemical

Fig. 2.7 Photographs showing the coeval relations of conjugated normal faults and sealed open cracks in the Shimanto accretionary rocks in Shioku. Bar represents 30 cm in length

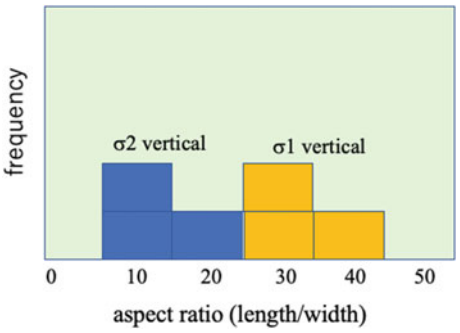

Fig. 2.8 Diagram showing the geometry of the sealed open cracks observed in a single outcrop exposed on schistosity—and lineation—normal (blue), and of schistosity normal and lineation parallel (orange) planes in the plate boundary rocks of the Kanto Mountains

and mechanical relaxation. The sealed crack tip becomes very sharp and linear, but often wavy as shown in Fig. 2.9, suggesting that the stress accumulation (stress intensity factor) makes change of principal stress orientation. It is also found that there is bifurcation of the crack tip suggesting the appearance of crack tip opening by yielding of minerals aggregates around the tip. These features at the crack tip filled with minerals are common in the rocks of Sanbagawa and Shimanto belts.

There are several types of characteristic elongation patterns showing the crack growth modes in the sealed open cracks: one is the segmented and linear pattern, and another is periodically wavy pattern as shown in Fig. 2.10, suggesting the existence of different modes of crack growth associated with precipitation of minerals in newly formed jog space which is filled primarily with fluid phase. In this context, the crack growth process is not the stage of crack propagation but of subcritical quasi-static

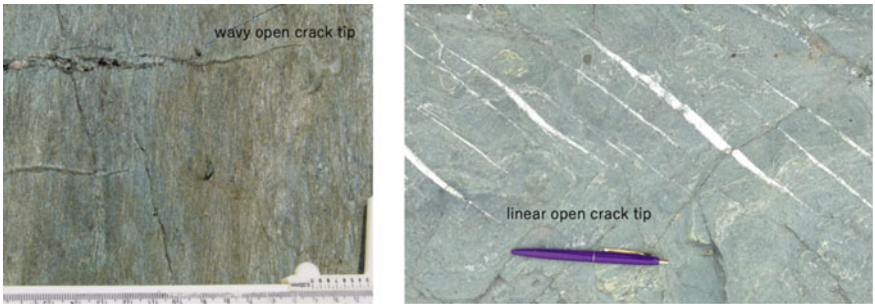

Fig. 2.9 Photographs showing the wavy shape and straight shape near the terminal parts of the open crack sealed by chlorite and albite in basic schists of the Sanbagawa metamorphic belt

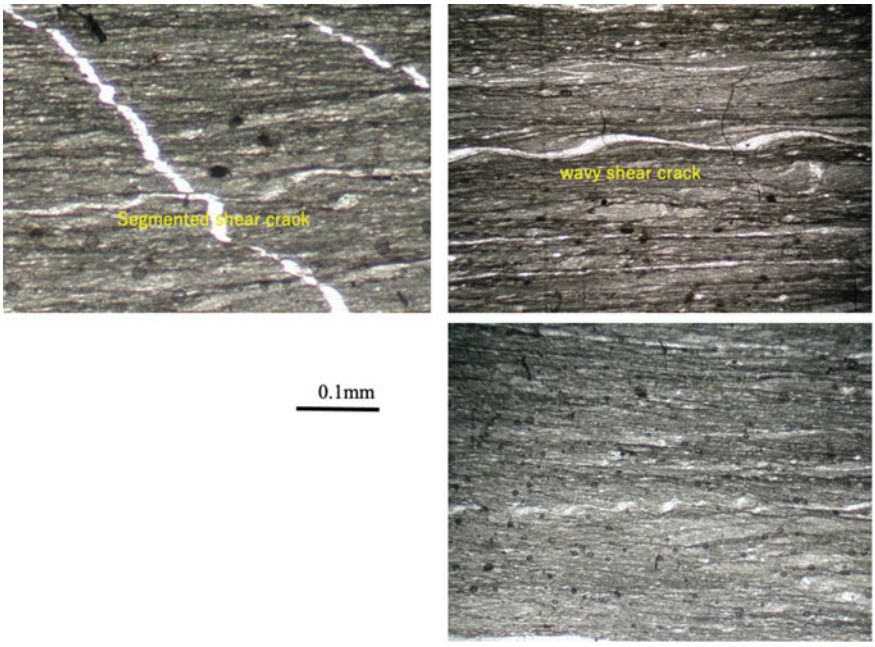

Fig. 2.10 Photographs showing the wavy slip surface of shear cracks sealed by quartz in Shimanto pelitic schists, Mimigawa, E. Kyushu. Periodic thick parts of the sealed crack are wavy jog and wavelength of them varies probably due to slip speed, judging from the sealing amounts of quartz under constant precipitation rate

slow crack growth. In this stage, crack growth rate da/dt (a; crack length) depends upon not only applied external differential stress but also environmental conditions such as mineral assemblage, grain size, fluid pressure, and solution chemistry together with pressure and temperature. Furthermore, the rate of metamorphic reaction and dissolution and precipitation with aqueous solution, and rate of plastic deformation

Fig. 2.11 Photographs showing the periodic open crack sealed by quartz in pelitic rocks of Sanbagawa metamorphic belt. The outcrop of the photo is parallel to the foliation plane and stretching lineation parallel to the arrow direction

in the dislocation and diffusion creep also contribute to the crack growth process as discussed later.

The wavy sealed open cracks are also found in the region of Shimanto belt, and those occur commonly as radial cluster, suggesting the magnitude of the minimum principal stress is identical to the second principal stress magnitude. It should be important that the wavy type sealed open cracks are also filled with quartz in fine to medium sandstone in the Shimanto belt and the width of them are approximately homogeneous. It suggests that the subcritical crack growth is likely to be slow and it is probably associated with plastic deformation around crack tip having finite crack opening distance (so-called COD or CTOD; Wei 2010). In addition, it seems that the crack growth is associated with dissolution of quartz at crack tip and precipitation of quartz at crack wall and ligament voids in front of crack tip.

Likely to the wavy open crack, echelon sealed cracks are also common both in Sanbagawa and Shimanto metamorphic rocks, and they form linear cluster with sometimes shear cracks assigned by shear displacement of the aligned—sealed open cracks as shown in Fig. 2.11. The ratio of the length and width is rather small as mentioned previously, and this type of sealed cracks sometimes display sigmoidal shape suggesting that cracks grew with shear displacement by associated type II in-plane shear crack and with precipitation of quartz or albite. These characteristic features of the wavy and echelon sealed cracks probably make us to imagine that the sharp and straight type sealed open cracks are also associated with precipitation of quartz and albite in pelitic and basic schists in both Sanbagawa and Shimanto metamorphic belts.

Distribution patterns of the sealed open type cracks in the deep plate boundary zone are very important in the geochemical–mechanical point of view because open crack density should control the fluid flux of solution dissolved many ionic and neutral components of rock-forming minerals and should decrease the yield stress and strength of surrounding rocks. There should be two types of spatial distribution of open cracks filling with fluid at once: one is the homogeneous and another is the

clustered type. These are identified by measuring the frequency distribution density of the spacing of the neighboring sealed open cracks showing the parallel alignment with each other because of the coeval situation of open crack generation in rock mass. Representative two patterns of the spatial distribution of the open sealed cracks are displayed, and the frequency distribution patterns of their spacing distance are also shown in Fig. 2.12. It is convinced that the frequency diagram of the clustered type appears likely to logarithmic Gaussian distribution, but that of the homogeneous type seems to be normal distribution (Toriumi and Yamaguchi 2000).

There are mainly two orientations of clustered sealed cracks in the rocks of Sanbagawa and Shimanto belts: one is nearly normal to the stretching lineation or the shear direction on schistosity plane and the other is subparallel to lineation and normal to the schistosity plane as shown in Fig. 2.13. These are mutually not coeval with each other, and successive order of cutting and sealing of them are often alternative,

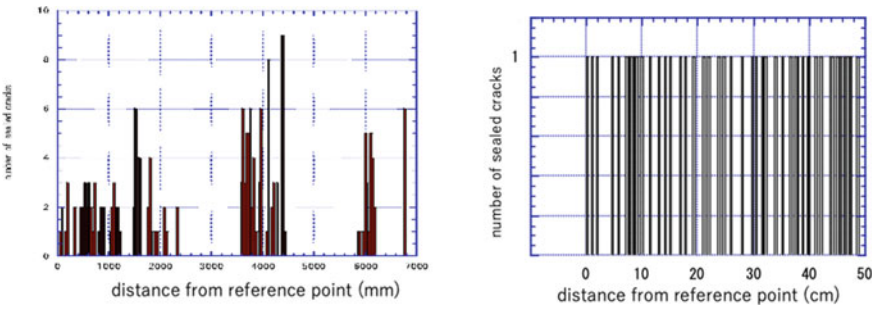

Fig. 2.12 Diagrams showing two types of distribution patterns of sealed open crack: one shows cluster pattern (left), and another is random one (right)

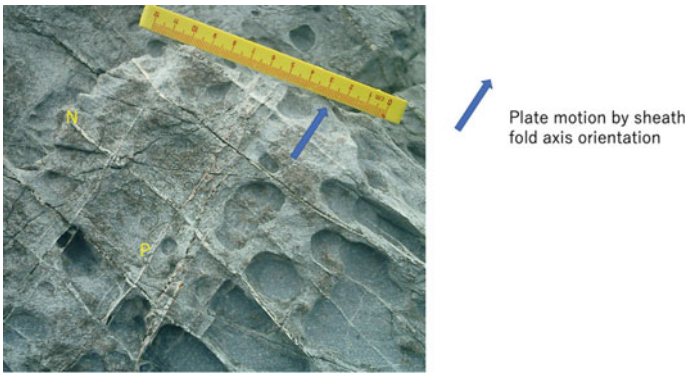

Fig. 2.13 Photograph showing two orientations of open cracks sealed by quartz appeared on bedding plane of sandstone: one is P-type (denoted by P) and another is N-type (N) and sealed cracks extend normal to the photographic plane. The arrow displays the direction of the subduction of plate defined by the sheath fold orientation of the sandstone and mudstone alternation

judging from the overprinting of precipitated minerals such as quartz and albite as noticed later. In this study, the author would like to call the lineation normal type as N-type and the lineation parallel type as P-type hereafter.

Both N- and P-types are different from the wavy sealed open cracks as described earlier. It should be noted again that the wavy sealed cracks appear radial distribution and judging from their common crossing lines are nearly parallel to the maximum shortening axis that is normal to the schistosity plane. These configuration geometry of various types of sealed open cracks manifests the instantaneous stress configuration change in the plate boundary zone from shallow to deep level, because opening orientation of the sealed open crack should indicate the minimum principal stress direction. The systematic change of the principal stress configuration will be discussed in detail in the later sections.

The timing of N- and P- types is possibly inferred by means of cutting relationship of each sealed cracks under the optical microscope. It shows that the single N-type crack is often cut by several P-type crack and it is cutting other several P-type ones even in the single thin section as shown in Fig. 2.14. Therefore, it concludes two possibilities: one is the case of coeval origin of two orientations of sealed cracks, and the other is the case of flip-flop relation of minimum and second principal stress orientations opening the N- and P-type cracks successively. If the single stress configuration would be imagined, coeval formation of very different orientation types of open cracks seems to be difficult to be interpreted by simple fracture mechanics. On the other hand, the successive change of principal stress orientations can be considered in the situation of plate convergence in the subduction zone.

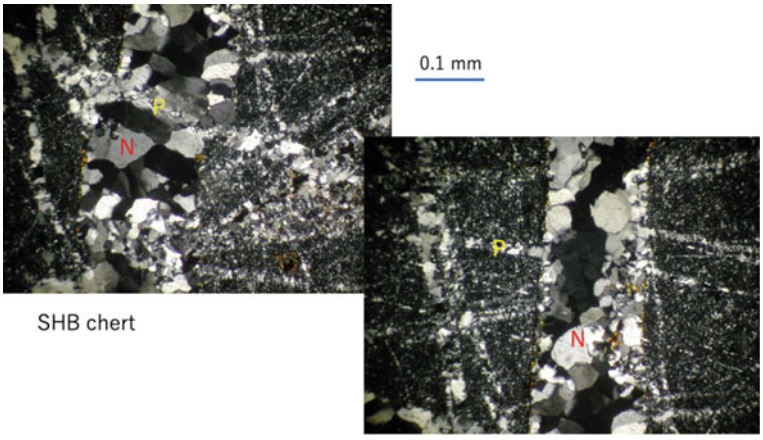

Fig. 2.14 Photographs showing interrelation of N- and P-type open cracks sealed by quartz in the sandstone of Shimanto accretionary prism under optical microscope with crossed polar. Right figure displays the N-type quartz- sealing after P-type, and left one does P after N, indicating the temporal relation displays the flip-flop type

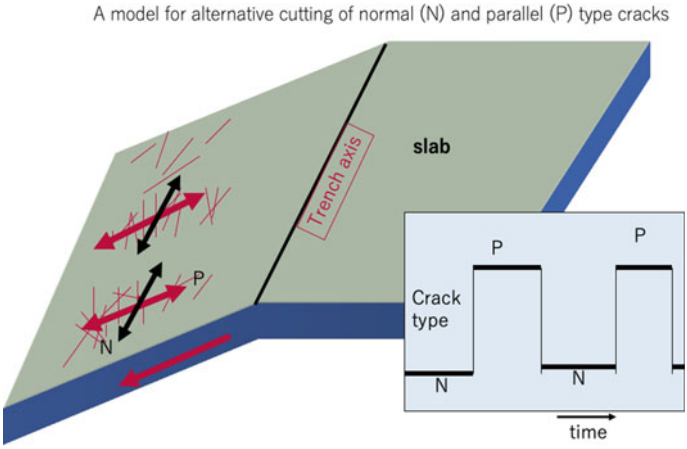

Fig. 2.15 Illustration of plate boundary crack showing the flip-flop of N- and P-type open cracks sealed by metamorphic minerals. It is noted that principal stress orientations of $\sigma 3$ are perpendicular to the sealed open crack surface

The N-type sealed crack is nearly perpendicular to the long-term maximum elongation direction and shear plane, but the P-type one appears to be nearly parallel to the long-term elongation direction and normal to the shear plane as noted in the previous sections. The timing of these two types of sealed cracks is inferred to be not the same, for there are many signatures of cutting and cut relations between these two types of sealed cracks. Thus, it is concluded that the N-type sealed cracks are sometimes postdated by P-type sometimes predated by the other P-type ones. Alternatively, the P-type sealed cracks are also predated and followed by N-type sealed cracks. It is, therefore, suggested that the P-type and N-type sealed open cracks are alternatively formed, that is the flip-flop change of sealed open crack growth in the single plate boundary zone as illustrated in Fig. 2.15.

The time scale of the flip-flop change of both crack-types is very important because it shows the time scale of the stress configuration change along the shallow and rather deep plate boundary. Maximum principal stress axis is nearly normal to the plate boundary and minimum principal stress axis is presumably nearly parallel to plate motion in the N-type but approximately normal to that in the P-type.

The model presented here for the flip-flop change of minimum and second principal stresses is such that the strength of mechanical coupling between slab and overriding accretion wedge makes the change in principal stress orientation of σ_2 and σ_3 derive from the plate subduction. If it is the case of the weak coupling between them, the situation of σ_3 normal to the plate motion is induced but the case of strong coupling between them makes σ_2 normal to the plate motion. The time scale of these stress configuration events may be deduced by both of average lifetime of crack opening and frequency of cutting events of N- and P-type sealed cracks.

Next, we must consider the mechanical state of the subduction plate boundary. The forces acting on this plate boundary zone are (1) gravitational force in the accretion

wedge, (2) bending force from the subducting slab through the plate boundary, (3) drag stress at the plate boundary plane from the slab subduction. The difference of principal stress orientations of elastic bending and drag by slab subduction is very important.

Let us consider the elastic stress derived from the bending of the slab.

For the bending geometry which is controlled by trench axis orientation, the stress tensor due to elastic strain of the slab can be expressed as.

$$\Sigma = \{\sigma ij\} \tag{2.1}$$

$\sigma_{11} = \rho gh + \sigma_{\mathrm{bn}}, \sigma_{33} = \nu\sigma_{11}/(1-\nu), \sigma_{22} = \sigma_{33} - \sigma_{\mathrm{bh}}, \sigma_{12} = \alpha\tau_p$, other components $= 0$.

In which h is the depth, τ_p is the drag stress from plate motion, σ_{bn} and σ_{bh} are the normal and tangential components of bending stress, respectively, and ρ and α are the density of rock and the coupling factor between the plate and accretion wedge, respectively.

The orientation of the principal stress α_1 is nearly vertical to the plate motion. The principal stresses α_2 and α_3 are possibly variable from nearly vertical to subparallel to the trench axis. The ratio of bending stress and drag one is surely governed by the degree of mechanical coupling between slab and overriding arc crust. It seems that the strong coupling results the large proportion of drag stress and then the σ_3 is nearly parallel to the trench axis. The misfit angle between slab velocity and σ_2 is controlled by the degree of mechanical coupling defined by α.

The stress configuration inferred from the open crack orientation changes repeatedly judging from the facts that the more than three kinds of sealed cracks can be identified. The time sequence of these sealed crack orientations can be assigned by cutting relation among them as noted earlier. It is evident that the N-type sealed cracks were formed before and after formation of the P-type ones. The reverse relation is also justified. Furthermore, the wavy sealed open cracks which occurs as radiated cluster as mentioned earlier (Fig. 2.15) should manifest the intermediate stress configuration that σ_2 is equal to σ_3, suggesting that the stress term of $\alpha\tau_p - \sigma_{\mathrm{bh}}$ to be nearly zero. Therefore, it should be clear that the stress configuration in the plate boundary rocks changed repeatedly depending upon the ratio of the mechanical coupling and bending stress of the oceanic plate.

The possible model of the flip-flop change of the N-type and P-type sealed open cracks is illustrated in Fig. 2.16, showing that the accretionary wedge subducted into shallower to deeper level is suffered from the deformation and yielding by the stress of subducting slab and fluid flow of solution from the slab. The intensity of the stress transferred from the slab through the plate boundary varies according to the frictional stress that is controlled by the subduction velocity and the mechanical coupling degree between the slab and overriding accretion wedge.

As shown in the previous text Toriumi (2021) and Schwartz and Rokosky (2006), the slow slip events occur along the plate boundary and the periodicity of them ranges from sub-annual to several annual time intervals. Considering the mechanical

Fig. 2.16 Photographs showing radiative and wavy open cracks sealed by quartz in the viewpoint on bedding plane of Shimanto sandstone, thereby suggesting the neutral stress condition of $\sigma 3$ and $\sigma 2$ at the condition of intermediate state of N- and P-type stages

coupling of the slab and the overriding wedge boundary becomes very weak during the slow slip events, it seems that the mechanical coupling degree should change periodically in the time scales of sub-annual to several annual intervals. Therefore, it is probable that the stress configuration also changes periodically from the minimum principal stress normal to the trench axis to that parallel to the trench axis, leading to the sealed open cracks corresponding to N-type to P-type as described earlier.

By the way, as clarified by Jaeger (1964) and Wei (2010), the open crack must be filled with fluid and fluid pressure is equilibrium with surrounding normal stress at the crack surface. Therefore, the open crack network should be the fast path network of fluid flow in the rocks in the plate boundary zone, suggesting that the fluid flow of solution derived from subducting slab and accretionary wedge is controlled by the network structure of the oriented N- and P-type open cracks as displayed in Fig. 2.15. Therefore, in the period of dominant N-type open crack network, the upward fluid flow may be dominant in the plate boundary zone, but in the period of P-type crack network dominant in the plate boundary zone, the along-trench fluid flow is probably dominant as shown in Fig. 2.15.

In this paper, we described the two types of crack geometry in the plate boundary. The N-type sealed cracks are perpendicular to the long-term maximum elongation direction and shear plane, but the P-type one appears to be parallel to long-term elongation direction and normal to the shear plane as noted in the previous sections. The timing of these two types of sealed cracks is not unique but there are many signatures of cutting and cut relations between two types of sealed cracks. Thus, it is concluded that the several N-type sealed cracks are followed by P-type ones and proceed the other P-type ones. Alternatively, the P-type sealed cracks are also predated and followed by N-type sealed cracks. It is, therefore, suggested that the P-type and N-type open cracks are alternatively formed in the period of the same plate boundary configuration.

The time scale of recursion of both crack types is very important because it shows the time scale of the stress configuration change along the shallow plate boundary. Maximum principal stress axis is near normal to the plate boundary and minimum principal stress axis is parallel to plate motion in the N-type but normal to that in the P-type. The stress configuration in the plate boundary strongly suggests the weak coupling between the slab and overriding accretion complex. In this configuration, the plate elastic bending and successive unbending are necessary to explain the maximum compressive stress normal to the boundary.

The model presented here is such that mechanical decoupling between slab and accretion results in the stress configuration to plate motion. If it is the case of the weak couple between them, the situation of the vertical σ_1 and σ_3 normal to plate motion is induced. On the other hand, the slightly strong coupling arises the configuration of vertical σ_1 and σ_2 parallel to the plate motion. The time scale of these stress configuration events may be inferred by both of average lifetime of crack opening and frequency of cutting events of N- and P-type sealed cracks.

Let us assume the periodicity of switching the extensional stress orientation as T, probability of crosscut of N-cracks by P-cracks to be K and the number density per unit volume of rock of N-cracks to be n_I and P-cracks to be p_I for each paired stress step as shown in Fig. 2.17. Those keep constant for the time. Further it is assumed that the time of crack sealing is t. Then, the number of crosscut of the single N-crack by P-cracks for each paired stress flip to be S_i as,

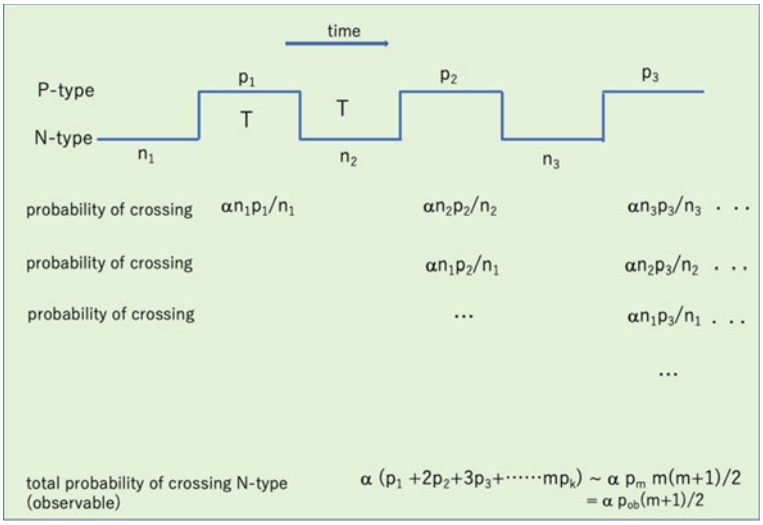

Fig. 2.17 Simple model of flip-flop temporal variation of the N- and P-type crack opening and sealing by quartz and alternative cross cutting with each other. The number of sealed cracks per unit volume of rock is n_i for N-type and p_i for P-type at i-step, and then the total number of crosscut of N-type by P-type is estimated by the bottom equation

$$\begin{aligned} S_1 &= 1\alpha p_1 \\ S_2 &= 2\alpha p_2 \\ S_3 &= 3\alpha p_3 \\ S_m &= m\alpha p_m \end{aligned} \tag{2.2}$$

Thus, we obtain the total number of crosscut as

$$\begin{aligned} S_{\text{total}} &= \Sigma S_i \\ &\sim \alpha p_m m(m+1)/2 \end{aligned} \tag{2.3}$$

Because of $n_i = n$ and $p_m = p = p_{\text{total}}/m$.

Therefore, the average number of crosscut per single N-crack holds under $m >> 1$,

$$C = S_{total} = \alpha p_{total}(m+1)/2 \tag{2.4}$$

Thus, if we can infer the relationship between the crosscut frequency and the repeating number of the stresses switching m, the frequency f can be estimated.

The average crosscut number of the N-type cracks is estimated to be about 2–5 against total P-type cracks as shown in Fig. 2.13, thereby suggesting α to be 2×10^{-2} to 5×10^{-2} for $p_{\text{total}} = 10$ and $(m+1)/2 = 10$. This crosscut frequency per single sealed crack may be proportional to the length of the sealed cracks that depends on the time scale of the single stress regime of N and P through the subcritical crack growth. If the constant growth velocity (not propagation) of the crack is the case, the average of the crack length may be proportional to the time scale above within the time scale of crack sealing. Therefore, it is expected that the crosscut frequency seems to be proportional to the time scale of the single stress regime Ts and inversely the time scale of crack seal Tc.

Thus, α becomes as.

$$\alpha = a\text{Ts}/\text{Tc}, \tag{2.5}$$

where a is a constant term.

The time scale of crack sealing may be the order of 10–10^3 years as mentioned in the previous sections, and so the duration of the single stress regime may be the range of 10^2 to 10^3 years in the case of $a = 1$, suggesting the similar time scales of the stress orientation change before and after the Tohoku-Oki 2011 giant earthquake.

Let us investigate the temporal distribution of sealed open cracks in the accretion wedge in the Shimanto belt. In this study, the isotopic age determination of mineral sealing is not the case because sealing minerals of open cracks are of quartz, albite, and chlorite but not available minerals such as zircon. In addition, the sealed open cracks in the deeply seated accretion wedge should have been deformed plastically and grain shape transformation features depending on the annealing time (Toriumi 1979) of the sealed cracks are not available for the present investigation.

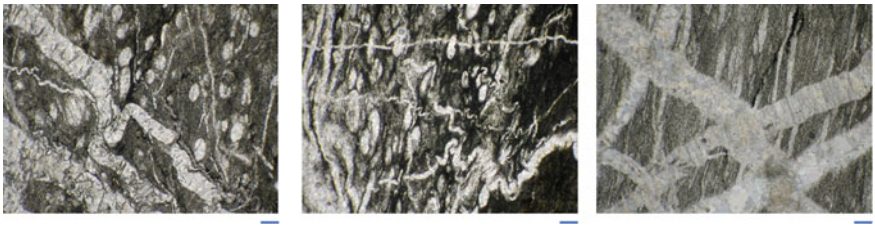

Fig. 2.18 Microphotographs of metamorphic chert thin sections showing the plastic deformation of sealed open cracks and quartz-filling radiolarian fossils in various degree of strain. See sharp cut of the quartz-filling fossils by deformed sealed open crack. Notice that the chert is almost always composed of fine-grained quartz as well as open crack and fossils. Bar represents 0.1 mm

By the way, the quartzose metamorphic rocks (metachert) contain abundant deformed radiolarian fossils filled with quartz, and many of them were primarily to be spherical shape. Toriumi and Teruya (1988) clarified that plastic deformation of the metacherts in the Shimanto metamorphic rocks in the eastern Kyushu is progressively oblate type and the magnitude of strain of these rocks increases with increasing metamorphic temperature and toward the high shear zone and long low-angle thrust with large displacement. Furthermore, in these rocks, there are abundant folded sealed open cracks filled with quartz as well as deformed radiolarian fossils as shown in Fig. 2.18. Then, the author can try to estimate the ratio of total plastic deformation of a single rock and various shortening strain magnitude of sealed open cracks in single rock specimens, which indicate the difference of time of sealing from the starting of the plastic deformation of rocks.

2.2 Successive Plastic Deformation and Temporal Distribution of Sealed Open Cracks

Shimanto accretionary metacherts contain abundant deformed radiolarians and sealed cracks. They are filled with fine-grained quartz as like as the matrix. The sealed cracks are often folded as like as a fold train, and thus, wavelength and amplitude together with thickness were possibly measured to compare the deformation of bulk rock by means of shape change of spherical radiolarians. The relations of wavelength, amplitude, and thickness of the sealed cracks are consistent with viscous multilayer folding models by Schmalhorz (2006). Accordingly, it is available that ratios of plastic deformation durations of sealed cracks and matrix of metacherts were estimated to be in the scattered range from shallow to deep accretion phases. It is, therefore, clear that crack opening and sealing took place even in the deep accretion stage together with in the shallow stage of the Shimanto accretion process.

Shimanto supergroup in SW Japan and Chugach group in Alaska and Aleutian (Byrn 1986) are typical large accretionary prism formed by continuous subduction of the Pacific Plate (Taira et al. 1988). These accretionary sediments are commonly

fractured and show many cracks sealed with quartz, albite, and calcite together with some degree of metamorphism within the rather deep subduction zone (Toriumi and Teruya 1988; Itaya et al. 2011). Sealed cracks in these rocks display the open type I crack filled with various type of above minerals, suggesting that the mechano-chemical processes operated within the deep subduction zone. Besides, these open cracks indicate the minimum stress orientations during the subduction.

The similar sealed cracks are also very common in the low-grade rocks in the Sanbagawa metamorphic belt formed at the periods from 80 to 90 Ma (Itaya et al. 2011). Toriumi (1990) clarified that the number density of the sealed cracks filled with quartz in metacherts appears a drastic increase from pumpellyite–actinolite grade to the epidote–actinolite grade and plastic strain magnitude determined by shape change of spherical radiolarians filled with quartz also increases suddenly at that boundary. The author suggested that this type of drastic change of strain mode should be due to the ductile–brittle transition occurred at the temperature about 350 °C (Toriumi 1990). In this paper, it is also indicated that the extension axes of the sealed type I cracks appear parallel to the elongation axis of plastic finite strains determined by shape change of radiolarians in metachert. Later, Toriumi and Hara (1995) studied systematics of the sealed cracks geometry and statistics in the Sanbagawa metamorphic belt in the Kanto Mountains and noted that the length toward the shortening axis of strain is shorter than that toward the intermediate axis of strain compared sealed cracks geometries having the same width.

These sealed cracks in the subduction-related metamorphic belt formed in the late stage of exhumation judging from the mineral assemblages filled with sealed cracks in basic and pelitic schists (Toriumi 1990). However, in order to know the stress geometry and its change in the deep accretion wedge, it should be studied the geometries and spatial distributions of the sealed cracks formed during the subduction of metamorphic rocks, that is, those formed during the prograde and retrograde metamorphism.

In this paper, the author proposes the new method for timing of crack sealing in the Shimanto subduction-related metamorphic belt using the plastic deformation of the matrix determined by the deformed radiolarians and deformation of sealed cracks determined by their buckling type folds in metacherts of the Shimanto belt.

The magnitude of bulk plastic deformation of metachert can be measured by means of shape change of spherical radiolarians filled with quartz as same as the matrix. The 30–50 radiolarians in the single metacherts were measured on schistosity plane and on the schistosity normal and lineation parallel plane under the microscope, and the average aspect ratios of these radiolarians are plotted in the Flinn diagram as shown in Fig. 2.2. The data of Shimanto metamorphic rocks in the eastern Kyushu are cited from Toriumi and Teruya (1988).

On the other hand, the geometries of fold of sealed cracks in the same samples are also measured like Biot (1961) and Schmalholz (2006): horizontal hinge distance (wavelength), vertical hinge distance (2 amplitude), and thickness of the sealed cracks in the plastically deformed radiolarian metacherts in order to estimate the plastic strain magnitude after formation of sealed cracks which is called as the partial plastic

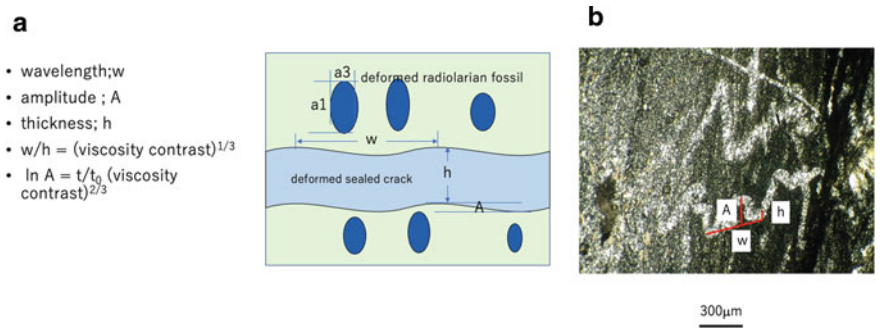

Fig. 2.19 Illustration of contrasting strain magnitudes of deformed matrix (assigned by deformation of radiolarian fossils) and sealed open crack. The matrix and radiolarian fossils are composed of quartz grains as same as the sealed open crack. The aspect ratio of fossils and wavelength, thickness and amplitude of the sealed folded crack are measured

strain (Fig. 2.18). The relations between the bulk and partial strains indicate the time lags of the formation of sealed cracks.

First, the simplified elongation strain Sc is approximated to be

$$\mathrm{Sc} = A/w \tag{2.6}$$

in which w is the wavelength (horizontal hinge distance) and A is amplitude (vertical hinge distance) of the sealed cracks as shown in Fig. 2.19.

On the other hand, the simplified elongation strain Sr (Toriumi and Teruya 1988) is defined by the ratio of the strain ellipsoid determined by average radiolarian shapes as

$$\mathrm{Sr} = a_1/a_3 \tag{2.7}$$

in which a_1 and a_3 are the lengths of long axis and short axis of the average deformed radiolarians.

On the other hand, the model for finite buckling of incompetent viscous layer requires the systematic relations of ratios between *w/h* and effective viscosities of sealed crack against matrix (Schmalholz 2006) as follows,

$$w/h = k(r)^{1/n} \tag{2.8}$$

and n is about 3 and k is constant term, and r is the viscosity ratio of matrix and sealed crack (both are filled with quartz).

Therefore, it is possible to estimate the relative time scales of plastic deformation of sealed cracks against those of bulk deformation from initiation to cessation of the accretion of the Shimanto rocks by means of comparison of Sc and Sr as following.

Elongation rates of the bulk metacherts (Sr) and sealed cracks (Sc) can be expressed by

$$\mathrm{Sc} = k\eta t_c$$
and
$$\mathrm{Sr} = \eta t_r \tag{2.9}$$

in which η is the viscosity of metachert and viscosity ratio k is a parameter between Sc and Sr. To estimate the time scale ratio after sealing cracks against bulk deformation time during the subduction, above equations yield the follows.

$$t_c/t_r = \mathrm{Sc}/k\mathrm{Sr} \tag{2.10}$$

This equation indicates the timing of the crack sealing in the subduction of the Shimanto accretionary rocks.

The metacherts samples are corrected from the Cretaceous Shimanto belt of the eastern Kyushu, SW Japan. The samples are the same as those studied in Toriumi and Teruya (1988). The geology of the eastern Kyushu Shimanto belt is composed of Cretaceous and Tertiary accretionary sediments which are separated by the horizontal thrust fault called as Nobeoka Tectonic Line (NTL). The hanging wall rocks above NTL are strongly sheared metamorphic rocks called as Shimanto metamorphic belt with thickness about 1 km. The stretching lineation defined by elongation orientation of deformed radiolarians and by acicular actinolite grains displays normal to the NTL, suggesting the displacement vectors of the northern Shimanto belt thrust up toward south-east direction. The schistosity planes defined by flattening of deformed radiolarians display nearly parallel to the NTL, thereby indicating the shear deformation of the Shimanto metamorphic rocks are accompanied with the large-scale exhumation by NTL.

Toriumi and Teruya (1988) clarified that the Shimanto metamorphic rocks over the NTL were suffered from low-grade metamorphism of prehnite–pumpellyite facies to greenschist facies, and their metamorphic minerals are characterized by prehnite, pumpellyite, epidote, chlorite, and actinolite in basic schists. Metamorphic temperatures and pressures are estimated from their chemical compositions to be ranged from 250 °C to 350 °C and 3–5 kb, respectively (Toriumi and Teruya 1988). The metamorphic temperatures increase with descending order of structural attitude to the NTL.

The strain ellipsoids determined by 3D radiolarians deformation shapes show clear plane strain to simple shortening types as seen in Flinn diagram (Fig. 2.2). Therefore, it seems that the deformation style of the Shimanto rocks over the NTL is derived from the simple shear deformation having some degree of shortening strain with plastic and brittle deformation associated with NTL motion. The deformation mechanism of Shimanto metacherts is inferred from microstructures under TEM and preferred lattice orientations of quartz to be of dislocation creep flow (Toriumi et al. 1986). The age of deformation and metamorphism may be the periods of Paleogene to Miocene (Itaya et al. 2011).

The studied samples are cut by the plane normal to schistosity and parallel to lineation, because of the sealed cracks normal to the lineation and schistosity

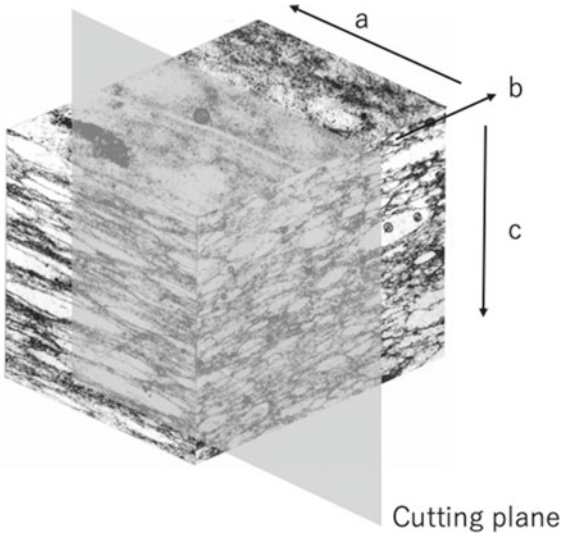

Fig. 2.20
Three-dimensional image of the deformed radiolarian metachert showing the cut plane for measurement of strain magnitudes of sealed open crack and radiolarian fossils filled by quartz

plane (Fig. 2.20). The above sections under microscope display abundant folded and straight sealed cracks filled with quartz and deformation ellipsoidal radiolarians filled also with quartz in metacherts as shown in Fig. 2.21. In these photographs, there are abundant elongated radiolarians filled with quartz, and variously folded sealed cracks filled with quartz, suggesting that the magnitudes of plastic strains of folded sealed cracks and matrix radiolarians show their wide range.

The wavelength (horizontal hinge distance named by Schmalholz (2006)), amplitude (vertical hinge distance by above paper), and thickness of sealed cracks on the thin sections (Fig. 2.21) were measured and plotted as shown in Figs. 2.22 and 2.23. In this figure, the relations between wavelength and the thickness of the folded single sealed crack are obvious, and they show an applicability of the amplitude versus wavelength relations to estimate the total strain magnitude after sealing of quartz in open cracks as shown in Fig. 2.24.

First as is shown in Fig. 2.25, it seems that the w/h ratio that means the contrast of effective viscosity between the matrix and the sealed crack with various thickness is maintained about 3 except for sealed cracks thinner than 0.1 mm. Therefore, the deformation times of bulk rock and of sealed cracks are to be compared with each other by means of previous equation of tc/tr. The ratios of A/w are plotted against the axial ratios a_1/a_3 of deformed radiolarians as shown in Fig. 2.25, suggesting that the A/w values are scattered widely from 0 to 2 with increasing the bulk stretching ratios from 1.8 to 4. It leads that the duration of the bulk plastic deformation after formation of sealed cracks changes largely, and thus, the timing of crack sealing varies from early subduction stage to late exhumation stage of the Shimanto accretionary prism. The apparent stages of this crack sealing in the Shimanto accretionary rocks are shown in the frequency diagram of the timing of crack sealing in Fig. 2.25.

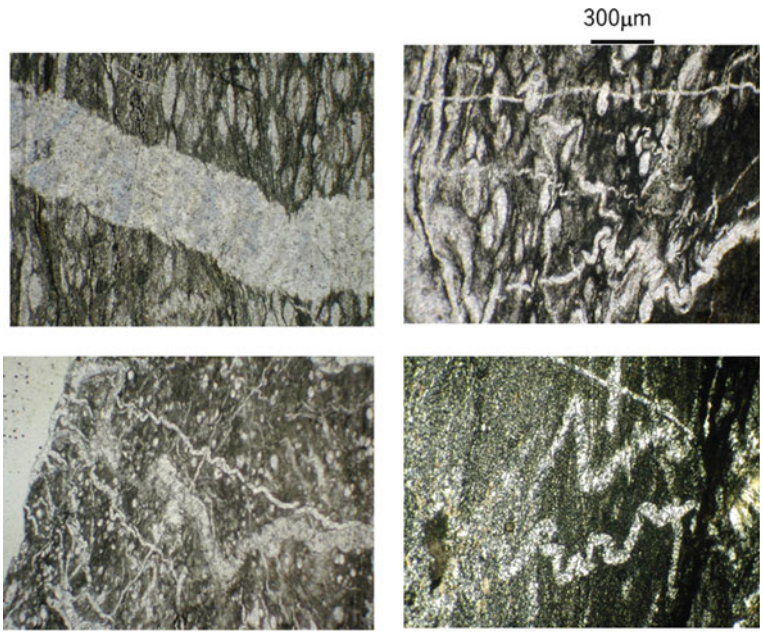

Fig. 2.21 Photographs under thin section of metacherts showing the difference of strain magnitude revealed by wavelength of fold of sealed open cracks and ellipsoidal shapes of quartz-filling spherical fossils of radiolarian of the Shimanto accretionary metacherts in E. Kyushu

In this figure, the author classifies the stage of the formation of crack sealing in the Shimanto rocks as the shallow sealed cracks, the deep sealed cracks, and the primary sealed cracks. The shallow sealed cracks are the sealed crack formation in the shallow accretionary wedge of the exhumed rocks, but the deep sealed cracks mean the sealed cracks formed in the deep-seated accretionary wedge. The primary sealed cracks are the cracks sealed in the early stage of subduction of the Shimanto sediments at the plate boundary as shown in Fig. 2.26.

It seems that the frequency of the shallow sealed cracks is dominant against deep sealed cracks and primary sealed cracks, suggesting the consolidation enough to crack propagation by the plate boundary thrust motion and relatively porous conditions of primary accretion sediments in the primary sealed cracks. Furthermore, it is important that the deep sealed cracks mean common process of the crack opening and successive sealing in the subduction and exhumation process of the accretion rocks. And the direction of crack opening is nearly parallel to the elongation direction of strain ellipsoid, and this means the instantaneous minimum stress orientation should be parallel to the plate subduction. In this situation of the stress, it seems that the maximum stress is nearly normal to the plate motion as illustrated in Fig. 2.27.

Shimanto accretionary metacherts contain abundant folded cracks sealed with quartz and deformed radiolarians filled also with quartz. The systematic studies of deformation of them in many samples from Kyushu, SW Japan, clarified that ratios

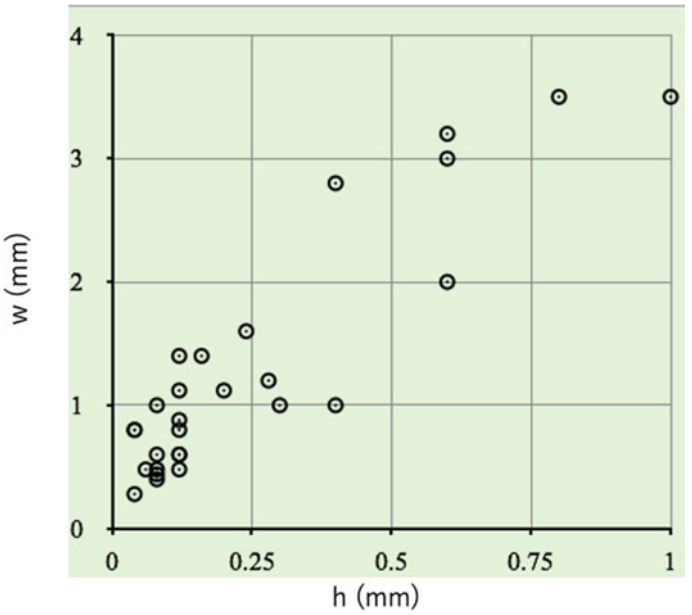

Fig. 2.22 Diagram showing the relations between wavelength and thickness of the sealed open cracks in Shimanto accretionary metacherts

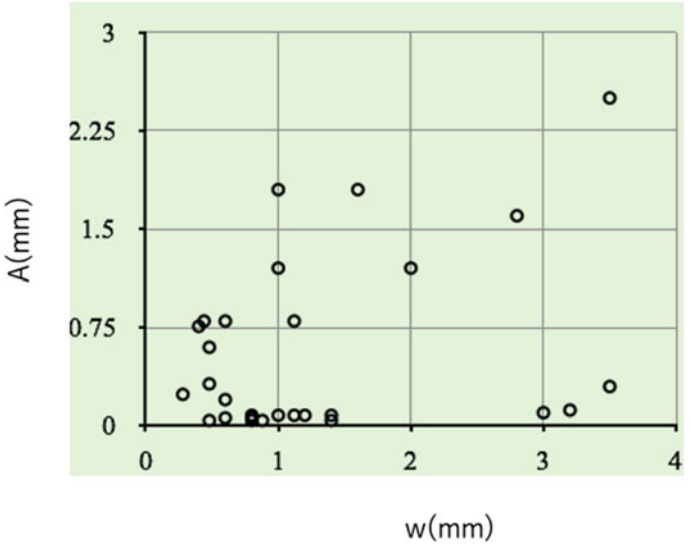

Fig. 2.23 Diagram showing the relations between the amplitude and wavelength of the sealed open cracks in Shimanto accretionary metacherts

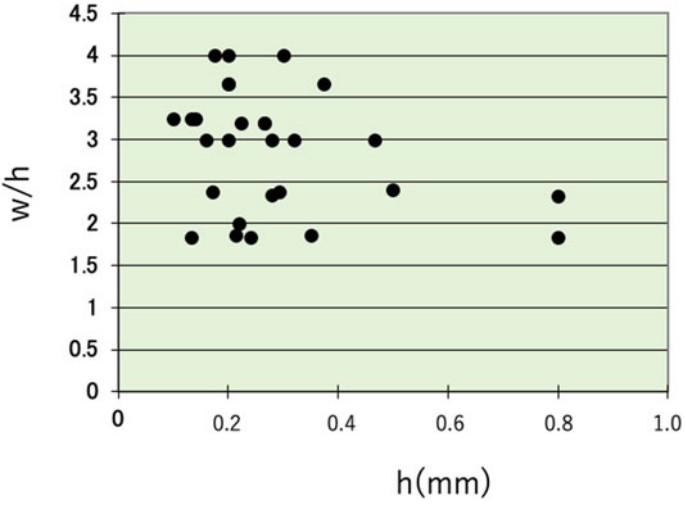

Fig. 2.24 Diagram showing the relations between the ratio of wavelength by thickness and the thickness of the sealed open cracks in Shimanto accretionary metacherts

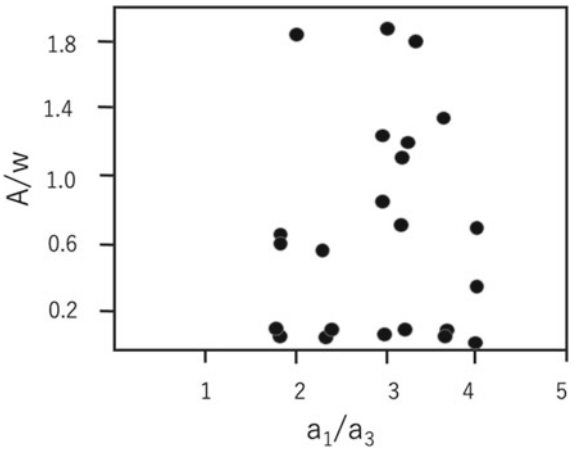

Fig. 2.25 Diagram showing the relations between the ratio of amplitude by wavelength of the sealed open cracks and the aspect ratio of deformed radiolarian fossils in Shimanto accretionary metacherts

of wavelength and thickness of the sealed cracks keep similar levels, suggesting the availability of the S models of viscous multilayer finite folding. For deformed radiolarians are abundant in the same specimens containing folded sealed cracks, the ratios of elongation strain magnitudes of them are measured under the many single specimens. The ratios range diversely between 0 and 1, suggesting that the crack sealing took place in the shallow accretionary prism together with deep one and the geometry of sealed cracks means extensional direction parallel to the plate motion and maximum stress orientation nearly normal to the plate boundary in the deep accretionary prism.

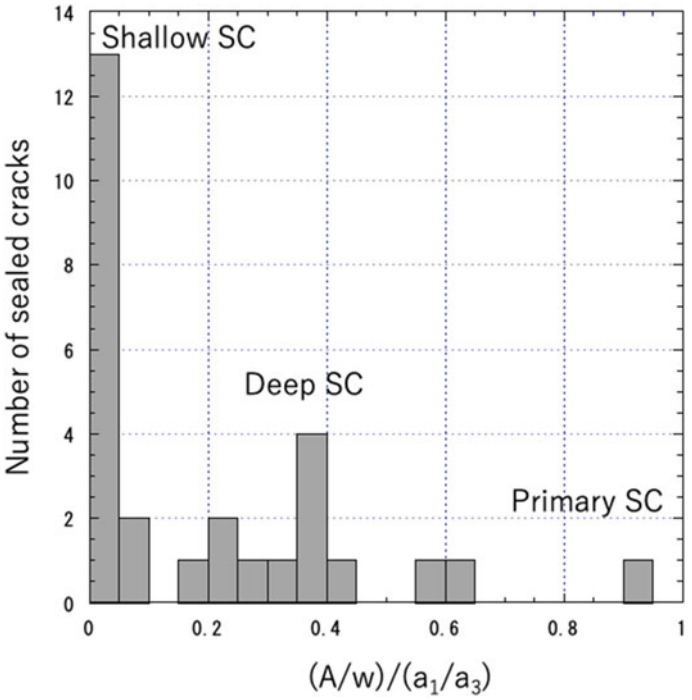

Fig. 2.26 Frequency diagram of the ratio of the strain magnitudes of the matrix (aspect ratio of the deformed radiolarian fossils) and the sealed open crack (amplitude/wavelength ratio), showing the various stage of sealed open cracks during the subduction and accretion at the plate boundary. Shallow SC is formed at accretion stage, deep SC at subduction stage and primary SC before subduction

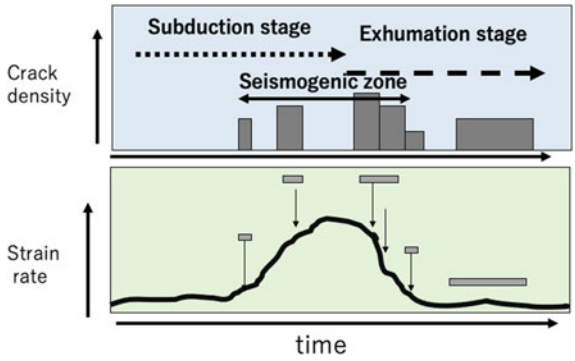

Fig. 2.27 Tectonic model showing the subduction and exhumation stages of progressive crack opening and sealing during accretionary process in the subduction plate boundary

2.3 Crack Sealing of the Subduction Boundary Rocks

Sealed open crack and sealed jog of shear crack are filled with albite and chlorite in basic schists but in pelitic and quartzose schists, they are occupied mainly by quartz and small amount of chlorite. The sealed open cracks filled with quartz can be classified into three types in terms of grain shape of quartz: one is the comb type, second is the equigranular type, and third is the grain-coarse type as shown in Fig. 2.28. The comb type displays the tabular or prismatic grains of quartz bridging both walls of the crack and grain width is nearly constant. On the other hand, the grain-coarse type appears rapid enlargement of grain size toward the center of the sealed crack. However, the equigranular type shows the granular grains occupying the cracks in the central zone.

Okamoto and Sekine (2011) also classified the sealed open cracks (mineral vein) into type I and type II in pelitic schists of the Sanbagawa metamorphic rocks, indicating that the type I is the same as the comb type and type II as the equigranular one. He suggested that the type II contains euhedral granular grains of quartz in the central zone of the crack and these grains should float in the fluid flowing in the open crack. It is important that this model enable to infer the fluid flow velocity through open crack in the plate boundary zone.

In this section, the relations of grain size of quartz in sealed open cracks classified previously are shown in Fig. 2.29. It seems that the grain width of quartz in the comb type increases very slightly toward the center from both walls, but the length of the grains sometimes reaches the width of the sealed open cracks. This type of texture of the tabular grain elongated from the walls suggests strongly the directed geometrical growth of the quartz grain (e.g., Kurz and Fisher 1986). On the other hand, the grain size of the coarse type displays the grainsize doubling pattern toward

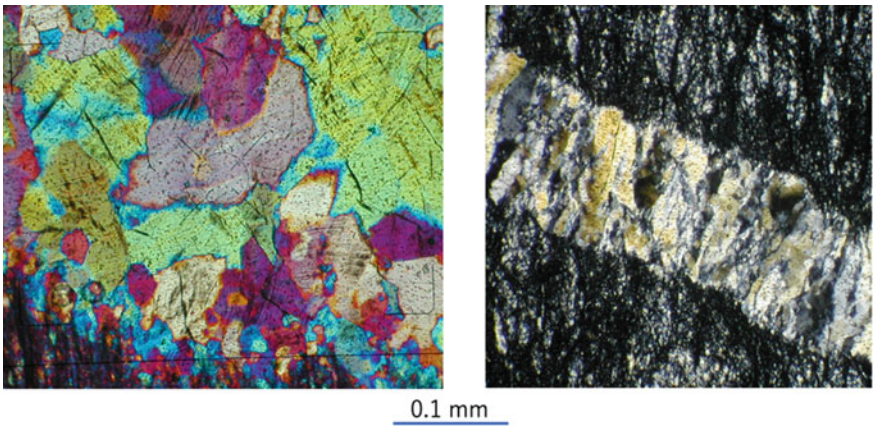

Fig. 2.28 Photographs under thin sections of equigranular (left) with sensitive plate and comb type (with crossed polars) sealed cracks of quartz filling of the metacherts in the Shimanto accretionary prism

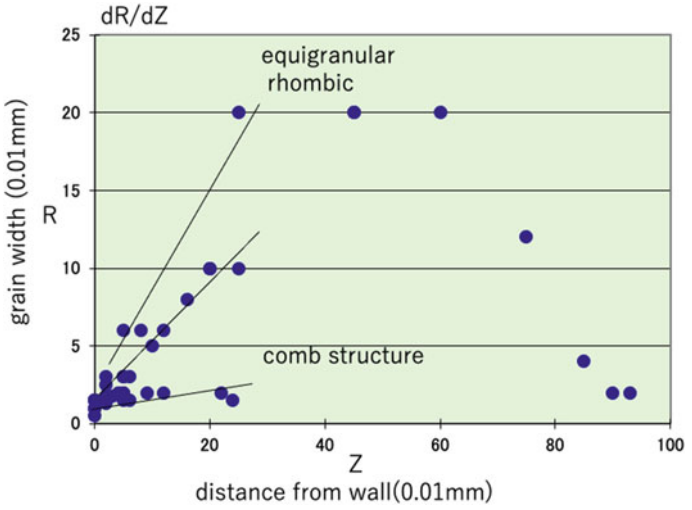

Fig. 2.29 Diagram showing the grain size coarsening trend toward the center of sealed open cracks of comb type and granular type in the Shimanto accretionary metacherts. The comb type displays nearly constant grain size, but granular type does clearly coarsen toward the center of the sealed open cracks filled with quartz

the center of the crack as illustrated in Fig. 2.30. This pattern also manifests a variety of the directed growth that the selective growth of preferential–oriented grains take place at the growth front. The grainsize doubling process at the growth front in the

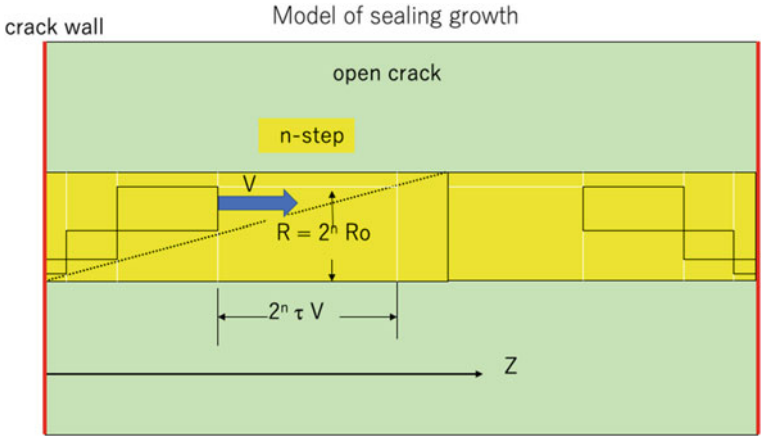

Fig. 2.30 Illustration of the coarsening model with directed and selected grain growth of quartz polycrystals in the open crack filled primarily with aqueous solution. The selection and absorption of one grain from neighboring two grains takes grain size doubling at each growth step. After n-step of grain doubling, the grain size becomes 2^{n}Ro

sealing open crack may result the systematic relation between the grain size in the central zone and the width of the sealed cracks as indicated by Toriumi and Hara (1995).

There are many jogs of the shear cracks in the basic and pelitic schists of the accretion wedge and those are sealed by mainly albite in basic schists and quartz in pelitic and quartzose schists as shown in Fig. 2.31. It is obvious that the tabular to long prismatic grains of albite is elongated parallel to the direction of the shear slippage assigned by shear displacement of crossing sealed open cracks. This type of texture in shear cracks sealed by calcite appears commonly in massive gabbroic rocks intruded in the Shimanto accretion wedge as shown in Fig. 2.32.

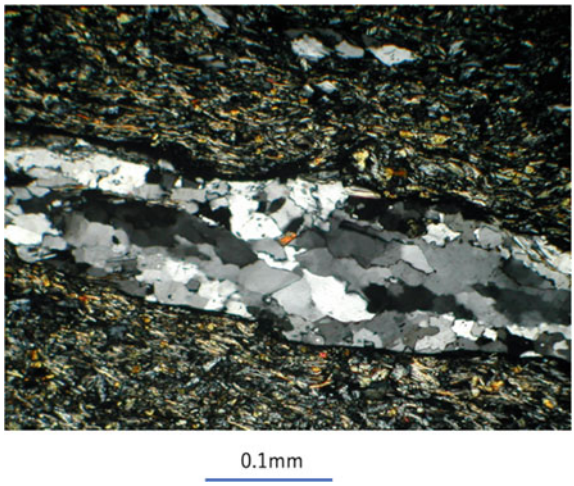

Fig. 2.31 Photograph showing the shear crack jog sealed by albite of which the grains elongate subparallel to the shear crack wall in basic schists of the Sanbagawa metamorphic belt

Fig. 2.32 Photograph showing the sealed jog array on the single shear crack filled with calcite in gabbroic rocks of the Shimanto belt

The simple mathematical model of the grainsize doubling mechanism for preferential growth of quartz is possibly proposed by the step-by-step growth with grainsize doubling as displayed in Fig. 2.30. In this figure, the timestep is defined as td by the duration that the grain of slightly rapid growth speed will overcome the nearest neighbor grain, and after n-step, the grainsize becomes R from initial size R_o and distance z of the growth front of sealing mineral from the crack wall is

$$Z = \sum \left(2^n\right) t_d V \text{ (summation is from 0 to } n) \tag{2.11}$$

in which V is the constant wall velocity of the open crack.

On the other hand, the grainsize of sealing mineral becomes

$$R = 2^n Ro \tag{2.12}$$

Then, the dR/dZ holds,

$$\begin{aligned} \mathrm{dR/dZ} &= (R_n - R_{n-1})/2^n t_d V \\ &= 2^{n-1} R_o/2^n t_d V \\ &= R_o/2 t_d V \\ &= K \end{aligned} \tag{2.13}$$

in which K is the observed relationship between grainsize of mineral and distance from the wall in the sealed open crack.

Therefore, the crack opening velocity V should be inferred as

$$V = R_o/2\, K t_d \tag{2.14}$$

In Fig. 2.29, it is possibly concluded that the opening speed of the sealed open cracks of the grain-coarse type is slower than that of the comb type ones by 5–15 times. On the other hand, term of t_d means the characteristic time for mineral growth, and it basically differs in different minerals such as albite and quartz. So, it is possible to be discussed that if the sealing by bimineralic precipitation is the case as shown in Fig. 2.33, the term t_d is probably governed by the opening speed of the open crack but not by mineral growth speed.

In order to understand the sealing process discussed above, the patterns of sealing in coarse grain type should be investigated in the crack tip, intermediate portion of crack, and central portion of crack as shown in Fig. 2.34. In these portions of the single sealed open crack, the grain size changes across the sealed crack were measured as plotted in Fig. 2.34. It is obvious that the value of dR/dZ (that is K) increases from center portion to the crack tip, suggesting that the opening velocity at the crack tip is very small, and it increases gradually to the center portion of the open crack.

Fig. 2.33 Photographs showing the bimineral open cracks filled with albite (white) and chlorite (dark green) in the basic rock of the Sanbagawa metamorphic belt

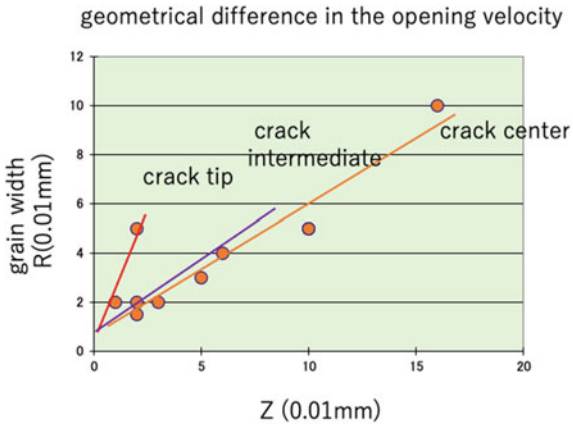

Fig. 2.34 Diagram of grain size vs distance from the wall of the single sealed open crack at the crack tip and center, showing geometrical variation of the crack opening rate (see text)

The sealed cracks of the boundary metamorphic rocks are composed mainly of quartz, albite, calcite and chlorite. The growth velocities of these minerals are controlled not only by degree of supersaturation but also by opening velocity of the crack. The parallel growth with the same size of albite and quartz with calcite straightforwardly the growth velocity controlled by kinematic opening velocity of the crack. In order to infer the time scale of crack sealing in the boundary metamorphic rocks, the model of kinetic growth of crack sealing minerals involving relationship between width of sealing and chemical compositions of minerals have been proposed.

The sealed cracks of subduction boundary metamorphic rocks are composed mainly of quartz, albite, calcite, and chlorite, but rarely of actinolite and epidote in the metachert, pelitic and basic rocks. The texture of the sealing by these minerals likes comb structure that the sizes of the tabular grains of quartz, albite, and calcite are the same with each other, suggesting that the grain growth velocity is controlled by opening of the cracks but not by growth process itself. Considering that the kinetic

growth of these minerals should be controlled by temperature, degree of supersaturation, and compositions of fluid, the above growth process suggests the existence of somewhat relationship between the apparent distribution coefficients of these minerals and growth velocities equal to the crack opening velocity.

In the single specimen, the width of the sealed cracks is widely scattered from 1 to 1 mm and then the opening velocity of them should be very different with each other as noted by Toriumi and Hara (1995). According to their paper, the width of sealed cracks is proportional to the grain size of them, suggesting that the opening velocity was large in the wide sealed cracks. Here, we suppose

$$dr/dt = aw = v \tag{2.15}$$

where w is the width of the sealed crack and a is the constant in the system.

Let us assume the concentration ratio, D of impurity component i between mineral m and fluid f in the far equilibrium growth process as follow.

$$D_i = x_{i,f}/x_{i,m}, \tag{2.16}$$

And, under the assumption of fluid common in the same crack systems of a rock specimen, we have

$$D_i = ki\, v \tag{2.17}$$

where k_i and v are constant and opening velocity of crack, respectively.

Thus, we have

$$D_{i,m}/D_{i,n} = k_{i,m}/k_{i,n} = \text{constant} \tag{2.18}$$

If we consider the ratio for the crack 1 and 2, we obtain,

$$x_{i,m,1}/x_{i,m,2} = w_1/w_2 \tag{2.19}$$

And concentrations of these two components i, and j have the following relation,

$$x_{i,m}/x_{j,m} = k_i/k_j = \text{constant} \tag{2.20}$$

These relations are to be investigated for many sealed cracks in the single locality samples.

The time scale of the crack sealing can be considered from the standard crack geometry as follows. The time scale of the crack holds,

$$\begin{aligned} t_c &= w/v \\ &= w\, k_{im}/D_{im} = w\, k_{i,m} x_{i,f}/x_{i,m} \end{aligned} \tag{2.21}$$

Further, if the shape and chemistry of the sealed crack are,

$$\begin{aligned} w(z) &= az \\ x_{i,m}(z) &= k_{i,m} w(z) x_{i,\mathrm{f}} \end{aligned} \tag{2.22}$$

Thus, the time scale of the crack sealing holds

$$\begin{aligned} t_c &= w\, k_{im}\, x_{if} / x_{im} \\ &= w\, h_m / r\, x_{im} \end{aligned} \tag{2.23}$$

where $h_m = dx_{im}/dz$ and $r = dw/dz$.

Consequently, the time scale can be determined by the observed shape parameters and transversal chemical gradient in the lens-like veins.

In the case that the chemical composition of quartz and albite in the sealed cracks varies from wall side to center, the opening velocity together with growth velocity of each mineral must change. The situation that the length of albite and quartz grains is the same and occurs side by side is very important for further discussions. If this is the case, we can infer the fluctuation patterns of the opening velocity of the cracks as,

$$v = D_i / k_i, \tag{2.24}$$

and

$$r_o = D_{io} / k_i,$$

where r_o and D_{io} are standard velocity of the crack opening and the concentration ratio, respectively.

Then, we see

$$v = r_o\, D_i / D_{i,o} \tag{2.25}$$

Assuming $x_{i,f}$ = constant, we get

$$v = r_o x_i / x_{i,o} \tag{2.26}$$

Therefore, the oscillatory zoning indicates straightforwardly the change of opening velocity during sealing cracks. As first suggested by Ramsay (1980), the multiple band structure of the sealed crack is the typical example of changing opening velocity of the crack.

The samples of sealed cracks were taken from the subduction-related metamorphic belts of Japan; those are the Sanbagawa metamorphic belt and the Shimanto metamorphic belt. The former is typical high pressure intermediate type, and the latter is low pressure type regional metamorphic belt. The Sanbagawa metamorphic

belt runs from the Kanto Mountains to the eastern Kyushu area along the Median Tectonic Line, and it consists of the glaucophane schist facies zone to eclogite facies zone. The metamorphic grade increases northward but in the central Shikoku, the grade decreases again to the north. The petrology of this metamorphic rocks has been recently carried out by Inui and Toriumi (2002), Okamoto and Toriumi (2001), and Aoya et al. (2001). According to their studies on PTt paths of metamorphic rocks, the prograde and retrograde paths are very similar to each other, and they are composed of two segments: one is low slope of dP/dT and another shows large dP/dT. The latter looks like an adiabatic process, but the former does thermally equilibrium one.

Considering the tectonic process along the subduction boundary, the nearly adiabatic mechanism needs the rapid exhumation of metamorphic rocks along the boundary. On the other hand, the small dP/dT path means the slow uplift of metamorphic rocks. Such difference of subduction modes is probably derived from the strength of mechanical coupling between the slab and the accretion mass.

The mechanical coupling strength is evaluated from the mechanical state of the accretion mass at the subduction stage. Weak coupling must result in the stress orientation scheme such that the σ_1 is vertical and σ_3 is to the plate motion and that the slow subduction and rapid exhumation of the metamorphic rocks, judging from that the subduction and exhumation of the metamorphic rocks along the slab boundary are controlled by buoyant force and the friction/drag force from subducting slab.

The weak coupling corresponding to the small dP/dT in the prograde and to the large dP/dT in the retrograde stage, therefore, is probably revealed by the coupling stress orientation suggested by sealed crack geometry. Toriumi and Yamaguchi(2000) clarified two types in crack orientations in the boundary metamorphic rocks. One is the open crack normal to the plate motion indicating that σ_3 is parallel to the plate motion and σ_1 is vertical. The other type is open crack parallel to the plate motion, which means that σ_1 is vertical and σ_3 is normal to the plate motion.

If we consider that the weak coupling is due to free water coming from metamorphic reaction, the timing of high-water production rate is to be just the weak coupling event and high dP/dT in the subduction process, but in the exhumation, it should be strong coupling and low dP/dT stage because of the case of continuous slab subduction. Toriumi and Inui (2001) and Inui and Toriumi (2004) clarified that the large water production consuming chlorite took place at 7 and 9 kb although forward modeling predicts the high production of water at the late stage of the subduction.

2.4 Shear Crack Growth and Propagation with Fluid Flow

In the plate boundary zone, there are abundant earthquakes of various magnitude with power law type frequency distribution of their magnitude. Considering the relationship between the moment magnitude of earthquake and the surface area and the shear displacement of the slip plane, the frequency of the size and displacement of shear cracks or faults satisfies the power law type in the seismic regions. Roughly speaking,

the seismic shear does not show stably constant slip velocity but has acceleration, near constant velocity and deceleration stages as being seen by regular earthquake to slow slip events. Thus, in this book, natural occurrence of various type earthquakes will be investigated from the sealed shear cracks with sealed open jog and open crack from the point of view of their population and role of the inflow of fluid and mineral precipitation in them.

Mode of shear and open cracks motion should be separated into two types: one is the subcritical growth and other is the propagation over the critical size of the crack. The critical size of the crack is obtained from the energetics of the crack generation as formulated by Griffith (e.g., Jaeger 1964).

Assuming the open crack with radius r and average strain around the crack, the total energy of the rock with a single crack is

$$W = -4\sigma^2\pi r^3/6G + 2\gamma\pi r^2 \tag{2.27}$$

in which σ is differential stress and γ is the surface energy of rock, and G is the elastic modulus of the rock.

Then, the total energy change by increase of crack size (that is crack growth) becomes

$$\begin{aligned} dW/dr &= -2\sigma^2\pi r^2/G + 4\gamma\pi r \\ &= -2\pi r(\sigma^2 r/G - 2\gamma) \end{aligned} \tag{2.28}$$

Therefore, if the crack size r is over the $r_c = 2G\gamma/\sigma^2$, the total energy change by crack size is negative and so the crack size increases naturally. On the other hand, if the size r is under r_c, then the crack should shrink and disappear. Therefore, the Griffith crack size r_c is the critical value of the crack.

On the other hand, the differential stress at the crack tip is known as the stress intensification factor and the magnitude has been estimated by Esherby (e.g., Wei 2010) as.

$$\sigma_c = \sigma_a(\pi r)^{1/2} \tag{2.29}$$

in which σ_c and σ_a are the stress at the crack tip and applied stress, respectively.

By the way, the open crack should be filled with fluid and supported mechanically by fluid pressure against the elastic stress along the crack surface. The balance condition for the stress around the crack, the following equation holds.

$$\sigma_{ij,\,j} = p_{f,j}\delta_{ij} \tag{2.30}$$

where p_f and δ are the fluid pressure and Kronecker's delta, respectively.

For simple case of one-dimensional open crack filled with fluid, the balance equation holds

$$G((2-2\upsilon)/(1-2\upsilon))d^2u/dx^2 = Bdp/dx \tag{2.31}$$

in which G and B are the rigidity and undrained rigidity of the rock, respectively, and υ is the Poisson's ratio. The u and p are the displacement of rock and fluid pressure, respectively.

On the other hand, since rocks studied here are saturated in fluid (water), open crack and jog of shear crack are filled with fluid and the surface energy is lowered by hydration of the crack surface. The change of the interfacial energy of water and mineral (or rock) is possibly estimated by the dihedral angle between them as,

$$\gamma_f = \gamma_s/2\cos(\theta/2) \tag{2.32}$$

in which γ_f and γ_s is interfacial energy of water–mineral and mineral–mineral, respectively and θ is the the dihedral angle (e.g., Holness 1993). The interfacial free energy above depends on the temperature and pressure together with pH and solution chemistry. Especially, it decreases with increasing temperature and pressure, and with increasing solubility of minerals in water filling crack (Holness 1993).

Now, considering that the decrease in interfacial energy of water filling open crack by chemical change makes the critical Griffith crack size to decrease, it should induce the instability of the crack growth to transition into explosive crack propagation under enough fluid supply to the crack. If the stationary chemical condition of large and small pH in water is the case, the critical Griffith crack size is smaller than that of the neutral condition.

On the other hand, for the case of the plastic deformation around the crack tip by stress intensity is considered, the elastic strain energy in the Griffith criterion decreases due to relaxation of the stress intensity in the finite time depending upon the deformation mechanism. In the geological context, there should be thought to be three mechanisms: one is dislocation process, second is the diffusion process, and third is the dissolution–precipitation. These processes are strongly dependent on the stress intensity around the crack tip. As shown in Fig. 2.35, at the tip of open crack and jog of shear crack, the compressive and dilation region should be formed as a dipole field of volumetric strain. Then, the elastic stress causes the mass flux from

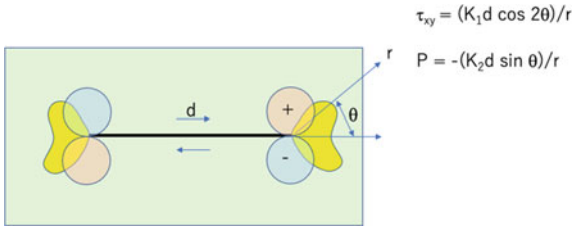

Fig. 2.35 Stress field around the shear crack tip showing the contours of compressional (+) and extensional (−) stress, and shear stress contour (yellow). $K1$ and $K2$ are material constant, and d is the displacement of shear crack. Around crack tip, the stress field shows the dipole

the compressive region to dilation region by plastic deformation mechanisms. In the case of shear crack III, the continuous shear crack growth occurs and then the stress intensity enlarges with time as,

$$K_{III}(t) = \sigma_a(r_o + Vt)^{1/2} \tag{2.33}$$

In the low temperature conditions ranging from 200 to 500 °C, the deformation mechanism of quartz and albite system is governed by the dislocation mechanism and dissolution–precipitation mechanism (e.g., Toriumi et al. 1986) or local shear band formation. These relaxation processes make clearly the dissipation of strain energy accumulated around the crack tip, and thus, it seems that the stress intensity changes at low level and the shear crack may grow. These dissipation and crack growth process may operate repeatedly so that the periodic patterns formed by plastic deformation, or the shear bands emitted from the shear crack as illustrated in Fig. 2.36. It is well known that the shear faults are commonly associated by the Riedel and penetrative subsidiary shear crack and shear bands in the geological subjects. In this context, the periodic configuration of the Riedel and penetrative shear cracks and bands may appear in the geological structure.

On the other hand, if we look at the case of dissolution–precipitation dissipation of accumulated stress at the crack tip, a mineral differentiation likely to the local metasomatism should occur in the different manner of dissolution–precipitation. In the compressional region at the crack tip, selective dissolution of minerals such as quartz and albite should take place and their component ions migrate with fluid flow to the extensional region associating compressional region and precipitate albite and quartz there. This process also dissipates strain energy of both regions at the crack tip and thus the critical Griffith crack may increase. Therefore, the shear crack

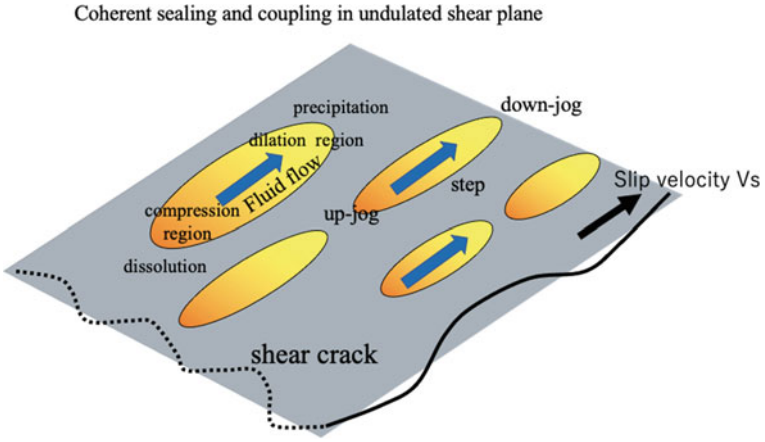

Fig. 2.36 Illustration of a model of slip velocity controlled by the permeable flux of the fluid from up-jog to down-jog on the slip plane. K is the stress intensity factor, and it controls the fluid pressure gradient

possibly grows under the condition of subcritical crack size without propagation and fracturing. In addition, it is quite important that the shear cracks under subcritical growth process continuously enlarge, being associated with residual minerals band on the one side of shear plane and on the other side with newly precipitated mineral bands as illustrated in Fig. 2.36.

Now, let us assume the periodic configuration of jog on the shear crack plane as discussed previously (Fig. 2.36), and fluid (water) flow to the jog in order to support the void space by fluid pressure. Then, the shear crack can only grow with fluid flux compensation of increase in void of jog, so that the velocity of the shear slip V_s is formulated by.

$$V_s a = k(\Delta P_f / d)$$
$$\Delta P_f = \Delta K_i = 2\sigma_a(\pi d)^{1/2} \tag{2.34}$$

in which ΔP_f and ΔK_i are the difference of fluid pressure and stress intensity at the up-jog and down-jog, k is the permeability of rock, and a and w are the amplitude of jog and distance of up-jog and down-jog, respectively, as shown in Fig. 2.37.

Therefore, the velocity of shear slip holds

$$V_s = 2k\sigma_a(\pi w)^{1/2}/ad \tag{2.35}$$

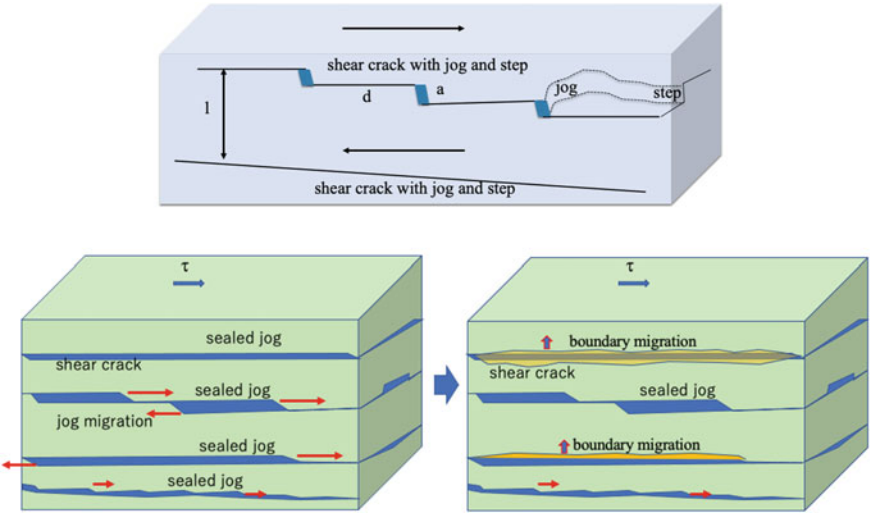

Fig. 2.37 Geometry of the jog and step on the shear crack denoted by jog spacing, jog width and shear crack distance (top). In the bottom figure, the band formation by successive mineral sealing of jog and extension of band by metasomatic reaction with aqueous solution in jog and surrounding matrix are shown

Therefore, the shear crack velocity increases with increasing the applied stress but decreases with increasing the amplitude and size of jog. It is noticed that the velocity decreases with decreasing distance between jog, that is the increase of jog density on the shear plane because of decrease of stress intensity.

By the way, the faults in the geological context commonly appear gauge zone composed of fractured and fine-grained rocks and subsidiary shear bands and the width of gauze zone seems to be correlated with fault displacement and fault length. However, the small faults do not show the clear gauze zone.

The gauze zone is often characterized by the texture of the rock fracturing and recrystallization: that is the cataclasite to mylonite and ultra-mylonite which occupy the gauze zone. The cataclasite commonly contains abundant clay minerals such as illite and montmorillonite and those are called as fault clay. These rocks are clearly formed by the fault movements with hydrothermal fluid flow in the crust. Therefore, it is not obvious that a fault system makes the elastic strain energy and surface energy by fault surface creation. On the contrary, the faults generate the large proportion of fine grains of surrounding rocks with finite width and recrystallization and reaction due to the water–rock interaction associated by large amount of mineral dissolution and precipitation of clay minerals and quartz/carbonates. This problem will be discussed in the later chapter. These energy dissipation processes contribute to the balance equation of elastic strain energy accumulation and the dissipation by particulate surface energy and metasomatic reactions, suggesting that the critical fault length-related stress accumulation will be enlarged by these factors.

So, the author will discuss the relation between the shear crack (type III) and the geological fault. The rocks along the faults and fault zone appear abundant subsidiary small faults and sealed open cracks, and often shear bands. Considering these features and signatures of recrystallization and water–rock interaction of surrounding faults, the fault slip should take place with accumulation and dissipation of elastic strain energy around faults. In addition, the long length fault does perhaps not have the huge accumulation of stress at its tip because of existence of the fracture strength of damaged rocks at the fault front.

Let us assume a single fault plane composed of many segments separated by up-jog and down-jog. The fault motion is controlled by velocity of segments on the fault plane, and thus the segments are to be the shear crack (type III) saturated by water. Therefore, the accumulated stress is partitioned at every shear crack tip on the fault plane as shown in Fig. 2.35. The size of the shear cracks of the segmented faults varies widely under the critical Griffith crack size, and the shear cracks can grow in the subcritical crack growth by water influx and relaxation by plastic deformation and dissolution and precipitation of minerals as discussed in the previous sections or the open crack formation filled with water.

Large-scale shear slippage of the fault should be derived from the cooperative shear crack propagation when the size of several shear crack segments reaches the critical Griffith crack one, because the crack propagation velocity is much faster than crack growth and it depends upon the stress intensity at the shear crack tip as

$$\mathrm{Vsc} = AK^m \tag{2.36}$$

in which K is the stress intensity of the shear crack (type III) and m is the index of this power–law (e.g., Atkinson 1984) and it is about 50. A is the constant.

The stopping of the cooperative shear crack propagation is due to the dry-up of several shear crack planes and rapid increase of frictional resistance because too fast slippage cannot be supplied of water from the surrounding rocks.

In this model, the size of separated shear crack segments may not be different in the scale of the fault size, and it should be governed by the critical Griffith crack size under applied environment stress and water pressure in the drained condition of rocks. This model probably explains the constant stress drop of the earthquakes of various magnitude ranging from M5 to M9.

Natural occurrence of jog-rich sealed shear crack can be seen frequently in the rocks of deep accretionary wedge in Shimanto belt and Sanbagawa metamorphic belt as shown in Fig. 2.10. It is very clear that the wavy shear cracks appear the periodic distribution of up-jog and down-jog on the shear. Moreover, the wavy shear cracks are surely associated with two types of small shear planes oblique to the wavy plane: one is the Riedel shear and another the penetrative shear. The down-jog is sealed by quartz and up-jog is enriched by sericite as shown in Fig. 2.10, displaying the dissolution–precipitation dissipation by stress accumulation at the jog.

The basic rocks in the Sanbagawa metamorphic belt contain abundant albite bands and lenses ranging from several micrometer to several millimeter width. It is obvious that these lenses are aligned on a plane and connected by the thin albite bands as like as they appear the shear crack having periodic jogs as seen in the Shimanto rocks previously. Considering that the sealing of the shear cracks should be performed by continuous jog extension and coeval precipitation of mineral (such as albite and quartz) accompanied with shear crack growth (not crack propagation but subcritical growth), many of albite bands and array of albite lenses connected by shear plane are formed by the successive growth of shear crack clusters and extended jogs on them and sealing, although there are many periodic banding with nearly constant thickness and distance as shown in Fig. 2.38. The latter case of regular mineral band should be treated by the metasomatic modeling in the next chapter in order to discuss the fluid flow and porosity change.

In this section, it seems to be necessary that the surficial density of the jog on the shear plane and its volume density corrected by shear crack density in the rocks of the plate boundary zone. In Fig. 2.39, the jog density on the shear plane and the aspect ratio of the jogs are shown and it is suggested that the areal density of jog on the single shear plane varies from 0.001 to 0.004 and aspect ratio of jog on the shear plane keeps about 2 against various jog density except for large one. Later, the volume density of jog per unit volume of rock (Fig. 2.40) will be discussed in order to estimate the porosity of rock.

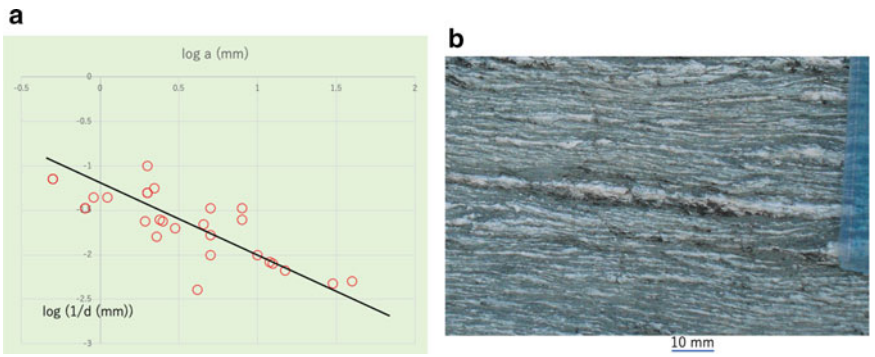

Fig. 2.38 Left logarithmic diagram of the relations between jog amplitude and jog spacing on the sealed shear cracks in the Sanbagawa metamorphic rocks. Right Photograph showing the representative albite banding derived from sealed shear cracks with many sealed jogs on normal to the schistosity and parallel to the stretching lineation of the Sanbagawa basic schist

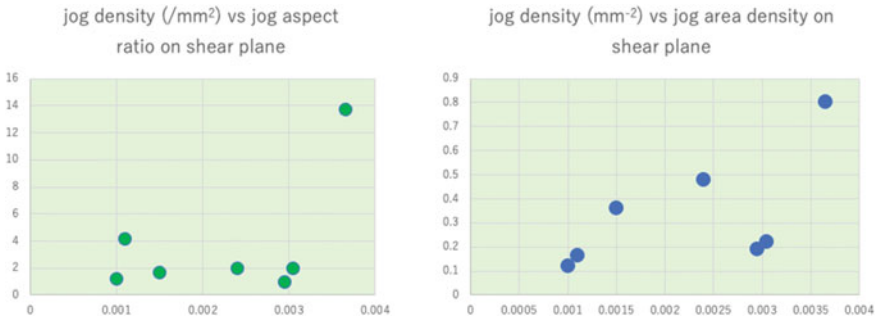

Fig. 2.39 Diagrams of the relations between jog density versus jog aspect ratio (left) and jog density versus jog area density (right) on the shear plane in the Sanbagawa basic schists

2.5 Adjoint Instability of Sealed Cracks and Velocity Change of Crack Growth in the Plate Boundary Rocks

The time scales of crack–sealing by quartz and albite are approximated to be of recovery from mechanical damage by fracturing and of lifetime of fast path of fluid flow in the plate boundary rocks. To obtain the time scales of crack sealing, it is available that Mullins–Sekerka instability (e.g., Kurz and Fisher 1986) of growing interface from solution flowing through cracks. The crack filling quartz aggregates display commonly wavy grain–grain boundary which is roughly vertical to the growing interface against solution. Considering the triple junctions of quartz–quartz–solution in sealed cracks keeping an interfacial equilibrium state during sealing, the wavy grain–grain boundary is just equivalent to the wavy interface by Mullins–Sekerka instability and is strongly dependent on growth velocity of sealing. The wavelengths of

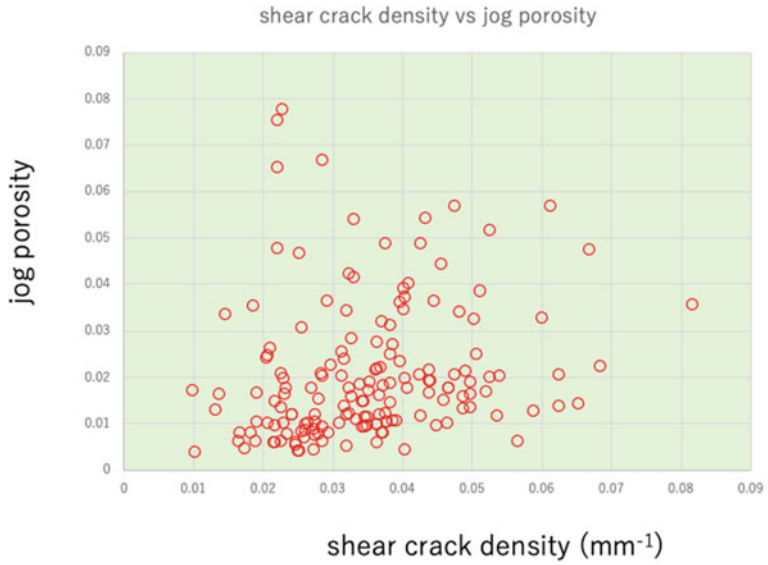

Fig. 2.40 Diagram of the relation between the calculated jog porosity and the shear crack density in the various localities of the Sanbagawa metamorphic rocks (see text for calculation)

waveform grain–grain boundary in sealed cracks of Sanbagawa and Shimanto metamorphic rocks are measured to be around 10–30 μm, suggesting that the sealing time scales range from 70 days to 20 years in the conditions of 200–350 °C.

There are abundant signatures of brittle deformation of deeply buried metamorphic rocks, being shown by the open and shear cracks sealed by metamorphic minerals. Ramsay (1980), Toriumi (1990), and Toriumi and Hara (1995) indicated that this type of microbrittle deformation may have a role of continuous deformation if opening and sealing of cracks are balanced during deformation. Recent detailed study of bimineralic quartz and chlorite sealed cracks also suggests various mode of crack opening and sealing (Becker et al., 2011). Further, Okamoto et al. (2008) clarified that there are three types of sealed cracks: one is the elongate type (comb type), and others are two equigranular types. Later Okamoto and Sekine (2011) succeeded in experimental duplication of quartz precipitations from solution flowing through precut slit of various siliceous rocks in the hydrothermal system. These various sealing textures of the veins are commonly due to the difference of sealing velocity that is the growth velocity of the sealing minerals. The time scales of sealing veins were recently estimated by means of coupled process of segregation through flowing in of surrounding solution into open crack by Saishu et al. (2017) to be about 10–100 years in the case of Shimanto accretionary rocks.

Sealing mineral grains of shear and open type cracks often show wavy grain–grain interfacial boundaries even in the case of mono-mineral sealing. This type of wavy boundary is not the case that plastic deformation of polycrystalline aggregates makes such a wavy interface due to imbalance of deformation and recovery by

applied stress. In the process of sealing the open cracks, the growing polycrystalline aggregate exists in front of the fluid phase and shows no deformation. Therefore, the wavy interface in the aggregate should be formed at the time of growth. It then straightforward that the interface between aggregate and fluid phases becomes wavy during the growth. In this situation, there should be two problems concerning the formation of wavy interface of polycrystalline aggregate in the sealed cracks; one is wavy growth interface between aggregate and fluid, and another is the adjoint (associated with growth interface) wavy grain–grain boundary within the aggregate.

The wavy interface of advancing solid and fluid phases should be derived from the instability of the growth interface as like as Mullins–Sekerka instability. In most cases, the wavy growth front of the polycrystalline aggregate is responsible for the instability derived from competition of activators and inhibitors for the interface advancing. In this case, the activators are increase of influx due to chemical gradient increase and inhibitors are the increase of interfacial free energy by curvature increase. In his case, the mean advancing velocity governs the preferential wavelength of the unstable interface.

On the other hand, the second problem what makes wavy boundary within the aggregate is still unknown. The straightforward mechanism between the growth instability and the wavy boundary within the aggregate should be powerful tool for evaluating the growth velocity of sealing by aggregate and thus opening velocity of the open and related shear cracks. Moreover, the patterns of slip velocity change of shear cracks associated with open cracks sealed with polycrystalline aggregates of minerals should be inferred by the change of the wavelength toward inward of the sealed open crack. These can compare with the seismic slip change of earthquake source processes.

In this paper, the authors intend to propose the physical and geometrical relations between the growing wavy instability and associated wavy boundary interface between grains in the sealed polycrystalline aggregates of the shear and open cracks.

Let us consider the polycrystalline aggregate grown from the crack wall facing with the fluid phase filling the open crack as illustrated in Fig. 2.41. In the figures, the triple junction of the grain–grain-fluid is required for the balancing of grain–grain interfacial tension and two grain-fluid tensions as shown in Fig. 2.41. The geometry of the triple junction must satisfy that the tangent surface of the average growing interface near triple junction T is normal to the tangent line of grain–grain boundary at triple junction because of equilibrium of interfacial energy at T. Therefore, the tracing of the grain–grain boundary must be invariantly normal to the tangent line of the growing interface at the triple junction.

If we consider the flat surface of the growing interface, the tracing of the triple junction T becomes exactly the straight line normal to the growth interface, but in the case of periodical waveform of growth interface, the tracing of the triple junction appears waveform or curvilinear grain boundary. Here, waveform grain boundary should be analyzed in order to infer the growth interface waveform which is responsible for the growth instability related to the growth velocity.

Consider the waveform of grain–grain interface as shown in Figs. 2.41 and 2.42. The grain boundary is approximated to be sinusoidal function as shown in figures.

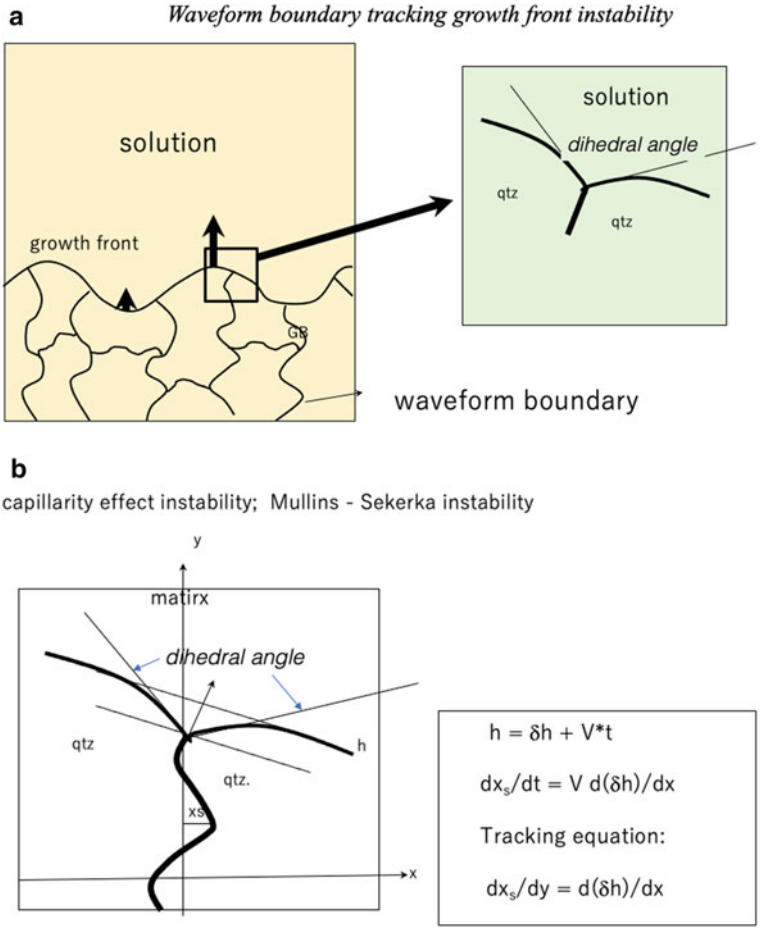

Fig. 2.41 Model of formation of waveform grain boundary in the sealing quartz aggregate growing from aqueous solution in open crack, showing the waveform growth front by Mullins–Sekerka instability and inherited wavy grain boundary in the aggregate (adjoint instability)

As the time advances, at the growth interface line intersected with above grain–grain interface curve, the tangent line of the growth interface is normal to the tangent line of the grain–grain interface because of the interfacial tension balance described above. Let us assume the following model grain–grain interface in the two dimensions,

$$l\,(x) = A \sin kx \tag{2.37}$$

in which $l(x)$ is the grain–grain interface curve, k is the wave number and A is the amplitude of the interface curve.

Along this interface curve, the growth point of the growing interface advances with time as,

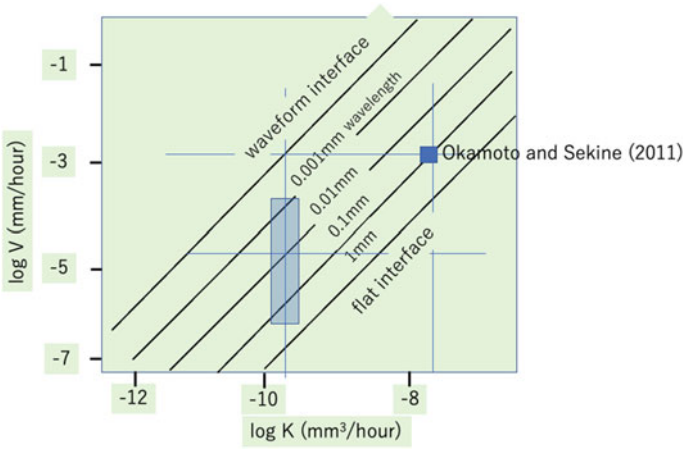

Fig. 2.42 Diagram of the relations of sealing velocity of open crack V, temperature term K, and wavelength of the wavy grain boundary in the sealing quartz aggregate in the open crack, based on the experimental data of Okamoto and Sekine (2011)

$$x\,(t) = v\,t \tag{2.38}$$

in which v is the growth velocity.

At the crossing point of both curves, the tangent lines of them are mutually orthogonal as shown in Fig. 2.41,

$$dl(x)/dx = dh(y)/dy \tag{2.39}$$

where y is vertical axis in the orthogonal coordinate system.

Applying $l(x) = A\sin kx$, we obtain

$$dh(y)/dy = Ak\cos kx \tag{2.40}$$

and

$$y = A\sin kx \tag{2.41}$$

Therefore, we obtain the following differential equation;

$$\begin{aligned} dh(y)/dy &= Ak\cos\left(\sin^{-1}(y/A)\right)/k \\ &= Ak\left(1-\sin^2(ky)\right)^{1/2} \\ &= Ak\cos ky \end{aligned} \tag{2.42}$$

Integrating this equation, we obtain

$$h(y) = A \sin ky + \text{constant} \tag{2.43}$$

The growing interface followed by adjoint grain–grain interface is, therefore, concluded to appear the sinusoidal waveform having the same wave number and amplitude of the unstably growing interface.

The waveform growing interface of polycrystalline aggregate facing with solution is very important to infer the growth velocity of sealing minerals together with time scale of sealing open cracks. Next, the author considers the instability of the growing interface by rate competing of diffusion and growth with capillary effect as Mullins–Sekerka instability. Here, we will introduce the waveform propagation of the interface as a function of growth velocity citing from Jamtveit and Anderson (1992).

They studied waveform growth interface of grandite garnet in skarn type ores by means of MS instability due to large growth velocity producing constitutional oversaturation and obtained characteristic wavelength of growth interface as,

$$\begin{aligned} l &= 1/k \\ &= 2\gamma (T_c D/mCoV)^{1/2} \\ &= K^{-1/2} V^{-1/2} \end{aligned} \tag{2.44}$$

where m is the gradient of overstepping of temperature corresponding to the oversaturation from the equilibrium saturation product, V is the growth velocity, γ is the capillary constant, D is the diffusion constant of solute ions in fluid, and Co is the equilibrium solute concentration.

In this study, the sealing mineral is quartz, and thus, D is the diffusion constant of $HS_iO_3^-$ of hydrothermal solution. The temperature of quartz sealing in the open crack is about 300–400 °C in the Sanbagawa metamorphic rocks and 200–300 °C in the Shimanto accretionary rocks (Toriumi and Teruya 1988; Toriumi 1990). Thus, the progressive change of growth velocity that is the sealing velocity can be estimated by the relation

$$V = K\lambda^{-2}, \tag{2.45}$$

and

$$dx/dt = V$$

Therefore, we obtain the logarithmic growth velocity

$$\begin{aligned} &\log V = \log K - 2 \log \lambda \\ &\text{with } K = K_o \exp(-Q/RT) \end{aligned} \tag{2.46}$$

In this equation, Q is the activation energy of ionic diffusion of $HSiO_3^{-1}$, R is the gas constant, and T is temperature.

The relations of growth velocity and parameter K with various wavelength of waveform grain–grain interface are shown in Fig. 2.42. These relations show clearly that the sealing velocity can be estimated if we obtained the activation energy of solute diffusion in water and parameter K with characteristic wavelength of waveform grain–grain interface by the precipitation experiments in hydrothermal system in high temperature conditions.

The data of sealed cracks are investigated in the samples of Sanbagawa metamorphic rocks of Shikoku and Shimanto metamorphic rocks of eastern Kyushu (Figs. 2.43 and 2.44). The sealed cracks of metacherts are composed predominantly of quartz and of minor calcite and albite. The microstructures of quartz aggregates in sealed cracks are classified into two types: one is the comb type and another the granular type as shown earlier. The diameter of the grain in both sealed cracks are shown in Fig. 2.45, indicating the gradual increase from the wall to the center of the sealed cracks of the granular type but in the comb type sealed cracks the grain size parallel to the crack wall is nearly constant or slightly increases toward the center of the sealed crack. The comb structure shows the grain shape elongated to the center of the sealed cracks. Thus, the grain diameter parallel to the crack wall was measured at the various distance from the crack wall.

On the other hand, the wavelengths of the wavy grain–grain interface which run toward the center zone of the sealed crack are measured under the optical microscope as shown in Fig. 2.46. It is concluded that the wavelength increases toward the center of the granular type of sealed crack but in the comb type ones the wavelength keeps nearly constant. The composite type of sealed cracks as shown in Fig. 2.43 is also investigated, and the wavelength of them appears its drastic increase toward the center, as like as the pattern of the grain diameter change.

Therefore, it seems that the wavelength of grain–grain interface appears uniform from the wall to the center in the case of comb type sealed cracks and that does gradual increase from the wall to the center in granular sealed cracks. The ratio of the wavelength of the center against the wall reaches about 2–5, suggesting the ratio of the sealing velocity about 0.25–0.04 judging from the velocity obtained previously.

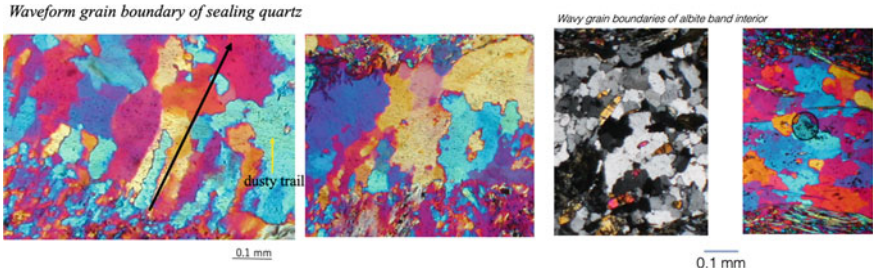

Fig. 2.43 Left photographs showing the waveform grain boundary of quartz aggregate in the sealed open cracks in Sanbagawa metapelites. Notice the wavy dust trails showing the trace of grain growth. Right figures show the wavy grain boundary of the albite bands under thin sections with crossed polar and sensitive plate (colored)

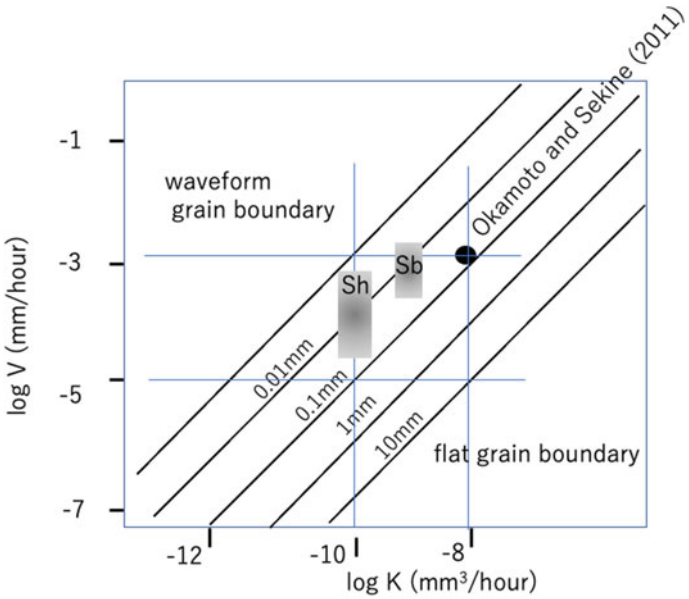

Fig. 2.44 Diagram of the relations of sealing velocity of the open crack and wavelength of the grain boundary against the temperature term K in metacherts of Sanbagawa (Sa) and of Shimanto (Sh), showing the similar opening and sealing velocity of them

The patterns of velocity change with advancing time of sealing the crack can be inferred from the wavelength change as a function of the distance from the wall to the center. Fig. 2.8 shows that the nearly uniform velocity appears in comb type open cracks and drastic change in the velocity in the composite type but in the granular type it decreases monotonously to the center as shown in Fig. 2.47.

In order to estimate the absolute velocity of the sealing the open cracks, we need experimental study about the growth of quartz in the narrow tube in the quartz rich rock in the hydrothermal system. Okamoto and Sekine (2011) investigated the hydrothermal experiments in the high temperature and high pressure flow system in the granite tube and succeeded in growth of quartz aggregates on the wall of the tube. The final interface between the aggregate and solution is not the unstable growth front at the instantaneous time, but the grain–grain interface normal to the wall displays clearly a waveform as shown in Fig. 2.8. The changing patterns of the grain–grain interface seem to be likely to the natural cases studied here. The time of this experiments took about 350 h, indicating the average velocity of the growth about 3×10^{-4} mm/h at 400 °C (Okamoto and Sekine 2011). The wavelength of this case was about 0.01 mm, thereby suggesting that the K value at growth velocity obtained previously is about 3×10^{-8} mm^3 h^{-1}.

The sealing time scales of open cracks and shear cracks are very important to discuss the fluid migration in the crust and to discuss the seismic activity associated with slow slip events. Toriumi and Hara (1995) investigated the crack geometries

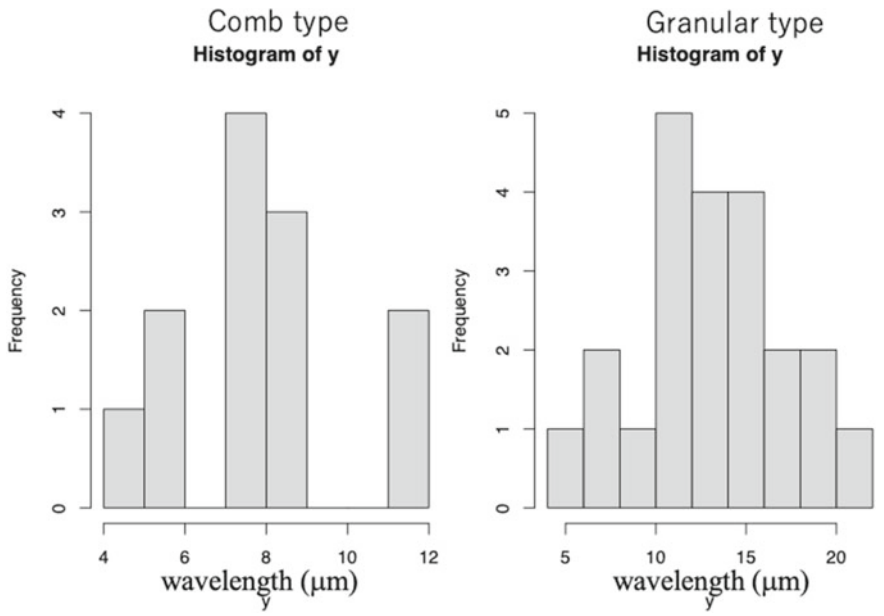

Fig. 2.45 Frequency diagrams of the wavelength of grain boundary in quartz aggregate from comb type and granular type sealed open cracks in Shimanto metacherts, showing the difference in sealing velocity of them

and their distribution patterns in the Sanbagawa metamorphic rocks. They obtained that the aspect ratios of the length against width (aperture) are ranged from 100 to 1000, and the abundant width of the quartz sealed cracks is about 1 mm. Applying the sealing velocity by quartz estimated previously, the time scale of many sealing the open cracks in the plate boundary is inferred to be in the range of 70 days in the conditions of 200 °C, assuming the activation energy about 10 kJ/mol for diffusion of ionic species of Si similar to that of Al^{3+} in solution (Li and Gregory 1974). But if the activation energy is much larger than this value and it is assumed to be 30 kJ/mol, the time scales of sealing the open cracks with width of 1 mm become around 20 years.

Saishu et al. (2017) estimated the time scales of sealing the open cracks in Shimanto accretionary rocks to be about 10–100 years, showing the good accordance with the time scales obtained here despite their different methods for estimation of time scale of sealing the crack. Considering that these methods are based on independent processes to formulate the kinetics: Saishu et al. (2017) took a time scale of flow-in of solution using the pressure difference from surrounding open crack, but the author takes a kinetics of waveform grain–grain interface derived from Mullins–Sekerka instability of growing interface. That is to say, the former is based on macroscopic process and the latter is on microprocess to be complimentary works.

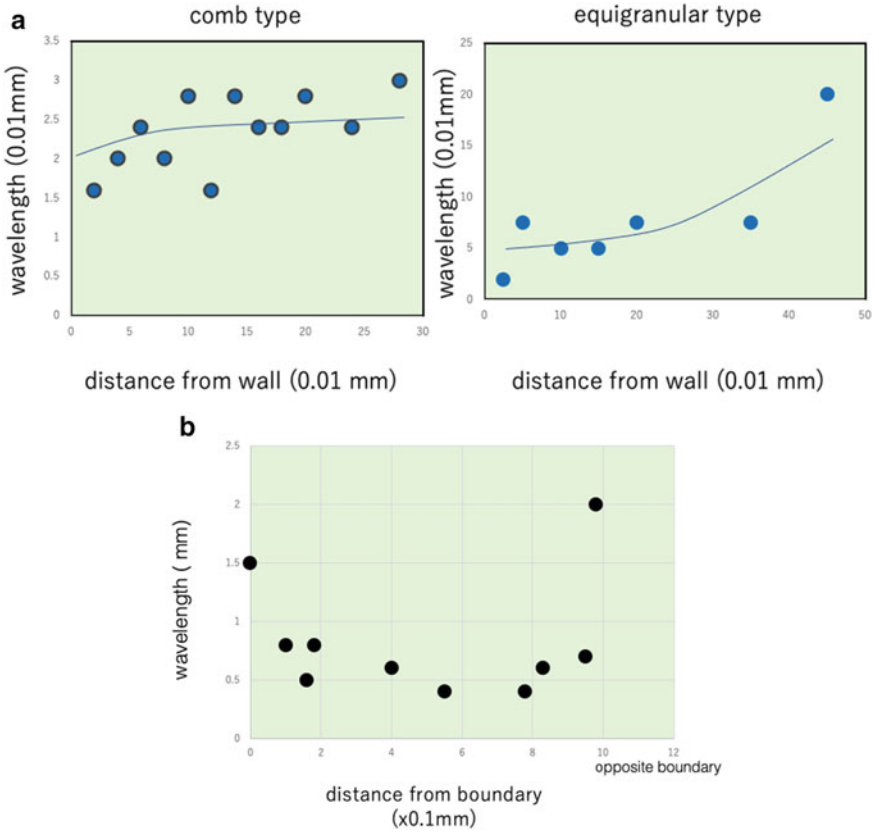

Fig. 2.46 **a** Diagrams of the wavelength against the distance from the crack wall of the comb type and granular type sealed open cracks in Shimanto metachert, showing the constant wavelength and gradual to rapid increase one, respectively. **b** Shows the wavelength against distance from the wall in the albite sealing open crack in Sanbagawa basic schist

2.6 Serpentine Sealing Open Crack in the Wedge and Slab Mantle

Recent studies in seismic profiling of the subduction plate boundary clarify the role of water giving spatial and temporal inhomogeneous distribution of the mechanical and thermochemical states of the plate boundary zone together with forearc and arc wedge mantle. The source of water, however, introduced into the upper mantle is somewhat difficult to be clearly answered because fluid migrates upward in most cases but not downward against gravity. However, seismic inversion studies by Kodaira et al. (2004) showed the sharp evidence that hydrous lithospheric mantle can be seen sporadically in the subducting oceanic plate, suggesting strong hydration just before and after subduction at the trench. Considering the 10% lowering of seismic velocity

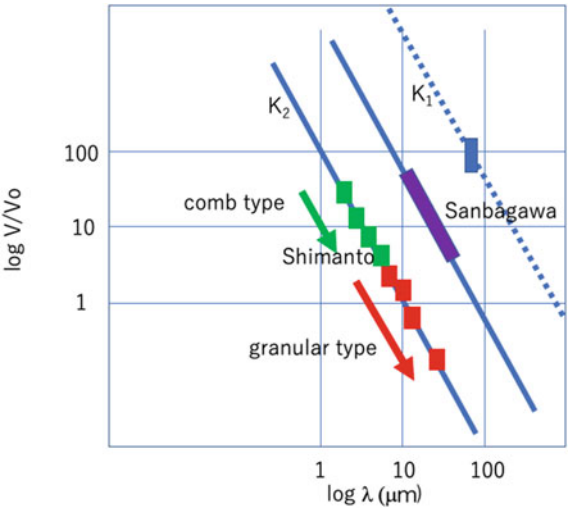

Fig. 2.47 Diagram of the relations of sealing velocity and wavelength of grain boundary in sealed open cracks (comb and granular type) in Shimanto and Sanbagawa rocks, showing the decrease in velocity from the rim to the core of the sealed cracks

in the hydrated mantle, the volume fraction of serpentine is at most 10% or less. Although the average fraction of serpentine is about 10%, the local concentration may change widely from 0 to 100% depending on the mode of occurrence of serpentine.

Peridotite contains various amounts of serpentine minerals in the alpine type, and their occurrences appear as mesh structure and sealed crack. The former represents replacement after olivine grains from grain boundary and the latter does serpentine sealing of cracks. Mesh structure shows homogeneous serpentinization (Fig. 2.48), but serpentine vein does highly inhomogeneous serpentinization and highly anisotropic structures governed by stress orientation. The open crack must develop perpendicular to the extensional stress direction, suggesting that the seismic

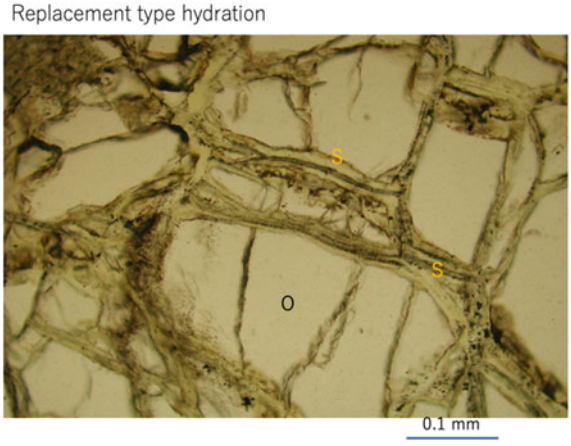

Fig. 2.48 Photographs of mesh structure of dunite showing the partly replacement of serpentine (S) after olivine (O) from the grain boundary of olivine

anisotropy derived from serpentine veins can be sharply recognized by the tectonic situation in the mantle.

The recent problems of the mantle dynamics have been focused on fluid behavior including hydration and dehydration and fluid transportation in the subducting slab.

The deep-focused earthquakes in the subducting slab are also still controversial but it seems that dehydration reaction of serpentine minerals within the slab gives an important role for mechanical instability to generate the seismic unstable displacement. Then, such dehydration instability of the shear crack dynamics needs clustered occurrence of serpentine minerals in the subducting slab likely to the crack filling serpentine aggregates. In this paper, the authors will propose a model of autonomous hydration process of the lithospheric mantle by extensional stress generation of water filling open cracks due to antigorite formation after forsterite and enstatite with water. Thermodynamic relations of forsterite, enstatite, and serpentine minerals can be considered by means of phase relations of MgO, SiO_2, and H_2O system in the pressure and temperature diagram. The phase relation of this system has been proposed experimentally by Ulmer and Trommsdorff (1995) in the high-pressure conditions. According to their results, phase relations of the MgO-SiO_2-H_2O system are shown in Fig. 2.49. In the lower temperature region, the assemblages of antigorite and brucite, antigorite and talc and forsterite, enstatite, and talc are stable. In the higher temperature region, the assemblages of enstatite–forsterite–water, forsterite–brucite–water, and enstatite–talc–water are stable. On the other hand, in the intermediate temperature conditions, the assemblages of antigorite–forsterite–water, and forsterite–talc–antigorite are stable as shown in Fig. 2.49. Therefore, it concluded that the rocks composed of forsterite and enstatite should be hydrated to form antigorite in the higher temperatures, but in the lower temperature conditions forsterite and water should react to form antigorite and brucite.

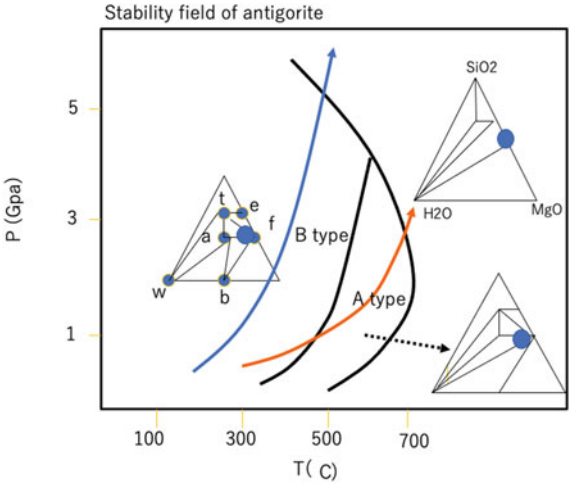

Fig. 2.49 Phase diagram of antigorite, talc, brucite, forsterite, enstatite, and H_2O in MgO-SiO_2-H_2O system after Ulmer and Trommsdorff (1995). Thermal structure of the earth interior of A-type displays the hydration trend of enstatite + forsterite to antigorite + forsterite, but that of B-type to antigorite + brucite + forsterite

These hydration reactions of forsterite and enstatite have proper volume changes, suggesting mechanical effects on cracks sealed by the serpentine minerals. If the negative volume change by hydration is the case, the crack sealing by hydration reaction should become close. However, if the case is positive volume change, the hydration sealing should make the crack to be open and then crack propagates by successive hydration reaction.

The case of hydration by antigorite and brucite from forsterite and water shows volume increase of about 1.8 cc per 1 mol water, and the other case of hydration by antigorite from forsterite and enstatite shows volume increase of about 2.5 cc/mol water. These hydration reactions thus tend to give a compressive strain around the serpentine minerals after absorption of water. In the case of open crack, the sealing by serpentine minerals can make the sealed crack to reopen and propagate.

Let us formulate the process of crack propagation derived from hydration of peridotite in the following.

First, open crack having length of 2 L and aperture of w is assumed to be filled with water as illustrated in Fig. 2.50. The hydration reactions of following types should proceed in the temperature conditions less than those of equilibrium curve of forsterite, enstatite, and antigorite with water,

1. forsterite + water = antigorite + brucite
2. forsterite + enstatite + water = antigorite.

The reaction 1 should occur in the stable regions of antigorite and brucite join. In this case of stability region of the antigorite, forsterite, and water assemblage, the

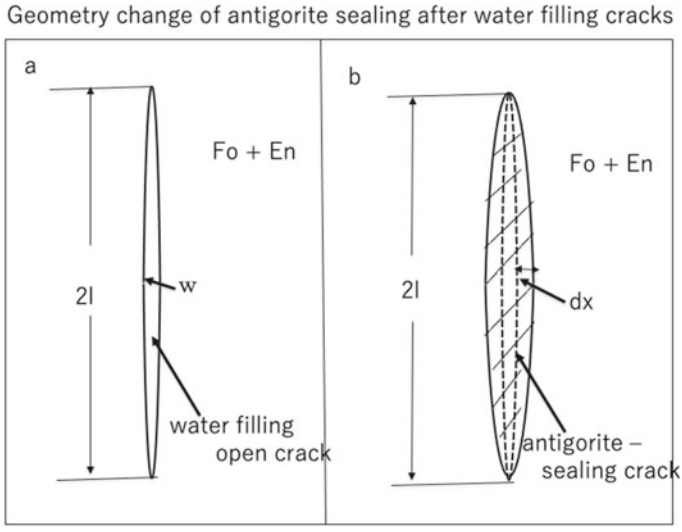

Fig. 2.50 Geometry of the serpentine crack growth model in the mantle hydration process from initial state with water filling crack with length l and width w in peridotite and b; serpentine formation from olivine and pyroxene and increase of crack width δx in which N_w is the mol of reacted water

hydration reaction becomes type 2. When degree of the hydration reaction is ξ, the change of volume by the reaction, v holds as,

$$v = \xi V \tag{2.47}$$

in which V is the volume change of the hydration reaction in the case of 1 mol of water. V is 1.8 cc for reaction 1 and 2.0 cc for reaction 2. Here, assuming V is positive, the volume increase makes elastic strain around the serpentine sealing crack. Considering the displacement dx by serpentine sealing along the crack as shown in Fig. 2.50, the balance of the mass becomes,

$$\pi L^2 dx = \pi L^2 (v/V_w) w \tag{2.48}$$

because of $\xi = 2N_w = 2\pi L^2 w/V_w$.

Therefore, we obtain,

$$\begin{aligned} dx &= (v/V_w) w \\ &= \alpha w \end{aligned} \tag{2.49}$$

The strain magnitude derived from expansion by hydration becomes

$$\begin{aligned} d\varepsilon &= dx/l \\ &= \alpha w/l \\ &= \alpha k \end{aligned} \tag{2.50}$$

in which k is the aspect ratio of the open crack before sealing.

Therefore, the elastic strain energy around the crack holds

$$\begin{aligned} \mathrm{Ue} &= 4\pi E (d\varepsilon)^2 L^3/6 \\ &= 2\pi E \alpha^2 k^2 L^3/3 \end{aligned} \tag{2.51}$$

in which E is the elastic modulus of peridotite.

On the other hand, the stored elastic strain energy is consumed by surface energy of open crack Us as follows.

$$\mathrm{Us} = 2\pi L^2 \gamma \tag{2.52}$$

in which γ is the surface energy per unit surface.

Therefore, we obtain the net energy increase by hydration and crack opening as,

$$\mathrm{Ut} = 2\pi E \alpha^2 k^2 L^3/3 - 2\pi L^2 \gamma \tag{2.53}$$

We must think about the hydration propagating crack process, and thus, we take a differential of Ut by l as follows

$$\mathrm{dUt/dL} = 2\pi L(E\alpha^2 k^2 L - 2\gamma) \tag{2.54}$$

The above function has a peak at $\mathrm{Lc} = 2\gamma/\mathrm{E}\alpha^2\mathrm{k}^2$, and if the crack length, L is larger than Lc, the crack should grow by hydration reaction along the water filling crack.

In this paper, Lc is called as the critical length of the hydration propagation crack.

On the contrary, if negative volume change is the case, the crack should shrink during hydration reaction. As stated in the previous sections, dynamics of the plate boundary zone is strongly controlled by water contents and its transportation in rocks. Tatsumi (1989) proposed the coupled process of the dehydration of subducting slab and subsequent upstream of water and magmatism of wedge mantle. Iwamori (2000) also proposed the numerical model of dynamics of fluid transportation and melting in the wedge and concluded the seismic tomography images consistent with simulation results.

On the other hand, Omori et al. (2002) and Hacker et al. (2003) proposed the model of double seismic planes derived from dehydration instability of serpentine minerals and the geometry of the DSL determining the temperature distribution in the subducting slab.

However, these models require the hydration of lithospheric mantle before subduction. Recent seismic observations by Miura et al. (2003) and Nakanishi et al. (2002) clarified that the slab has sporadically the low velocity regions under the outer rise of the Pacific Plate. Furthermore, Kodaira et al. (2004) obtained the results that there are several portions of low seismic velocity and high Vp/Vs in the subducting Philippine Sea plate.

These studies clearly indicate the sporadic hydration of lithospheric mantle, and the source of water should be the seawater because no contribution of asthenosphere under oceanic plate. In this paper, we proposed the hydration crack propagation due to expansion by hydration of dry peridotite. However, the positive change of volume by hydration takes place in the reaction from olivine and pyroxene with water to antigorite but not in the reaction to antigorite and brucite in very low pressures. It means that in the conditions just below the ocean bottom, hydration produces negative volume change. Then the cracks absorbing seawater should be formed by tectonic stresses.

Tsuru et al. (2005) showed sharply the horst and graben structure in the outer rise and subduction plate boundary near the Japan trench, suggesting clearly that the subducting slab must be bended downward producing extensional stress in the shallower zone of the Pacific Plate. It concludes that extensional vertical cracks are possibly formed in the shallower oceanic crust and mantle only near the subduction plate boundary and water penetrates downward into the uppermost mantle.

On the other hand, below 1.0–1.5 GPa the hydration reaction becomes forsterite + enstatite + water = antigorite, and the volume change should be positive, showing cracks propagation downward by hydration reaction. This type of hydration reaction

may continue to the depth of physical conditions on the univariant curve as shown in Fig. 2.51.

Judging from phase diagram, the critical depth from negative to positive volume change according to hydration of peridotite is derived from the change from antigorite and brucite formation to antigorite formation from peridotite. The critical depth of the transition is about 15 km from the univariant curve as shown in Fig. 2.52. Therefore, in the crust and mantle shallower than 15 km depth crack propagation by bending stress of the plate is dominant but the hydration propagation should dominate below 15 km to the depth of equilibrium pressure of forsterite, enstatite, antigorite, and water. The depth of this univariant curve crossing the geotherm of oceanic plate is about 70 km.

In this consequence, it is probable that hydration of the deep lithosphere is required for bending of plate and water drawback along cracks filled with serpentine minerals, indicating the localization of hydration of lithosphere. Indeed, seismic inversion studies mentioned earlier show sporadic structure of low v zone in the subducting

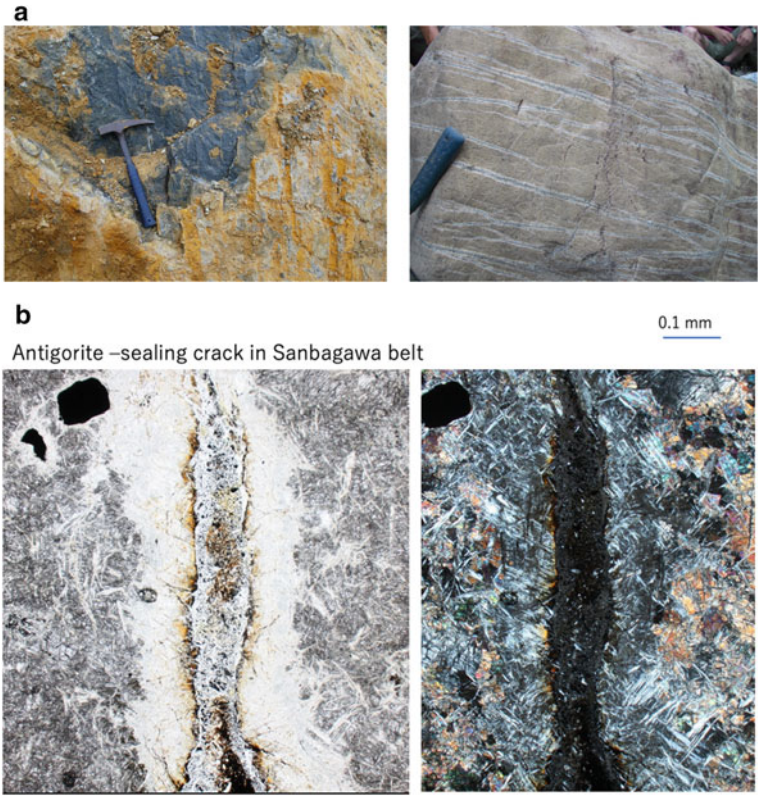

Fig. 2.51 Photographs showing the field occurrence of antigorite filling open crack array in massive peridotites (**a**) and antigorite filling open crack under thin sections with open and crossed polar (**b**) of the Sanbagawa metamorphic belt

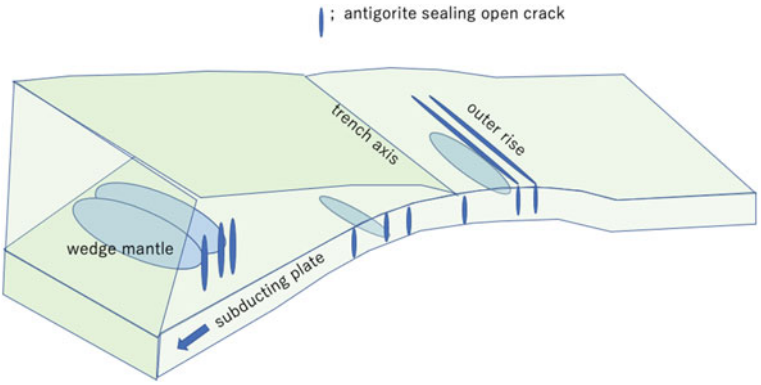

Fig. 2.52 Model of antigorite hydration of subducting plate and wedge mantle (see text)

slab. Further, it should be noted that the serpentine filling cracks must be aligned because their geometry is governed by stress orientation. Thus, the seismic anisotropy can be observed in the hydrated uppermost mantle with serpentine sealed cracks.

Serpentine sealing cracks are common in the alpine-type massive peridotite and there are two peaks of their orientations crossing at high angles near 90° as shown in Fig. 2.51. In this figure, the sealed cracks are composed of serpentine replaced after olivine. It seems that serpentine minerals were formed by hydration along cracks produced by applied stress.

On the other hand, the hydrated mantle may dehydrate in the process of subduction. This type of reaction yields heats and water, and net volume change is positive. Seno et al. (2001) and Omori et al. (2002) proposed the dehydration instability responsible for the seismic activity in the plate. Their model should be needed for cooperative dehydration within the planer zones that change to the shear crack generating elastic waves. In this study, the progressive hydration and crack propagation model near the bending field of the subducting slab can make the clusters of aligned serpentine sealing cracks on the lithospheric mantle.

The hydration cracks may have a wider range of their length and width, suggesting the wide range of the short time cooperative dehydration reaction of serpentine to produce water phase along in these sealed cracks. If this is the case, primary shear crack orientation is free from the stress orientation. And then the displacement along the dehydrating serpentine cracks is governed by the resolved shear stress component on the crack surface given by applied stress. It yields that the cracks with largest resolved shear stress are most active. In the subducting slab, the source mechanism of double seismic layers shows extensional one in the upper layer and compression one in the lower layer along the plate boundary.

Consequently, the active cracks tend to be high angles against plate boundary and the fault types of the upper layer are of normal one but those in the lower layer of reverse one. Recent studies of faults motion by means of waveform inversion suggest

above serpentine dehydration seismicity together with experimental investigations of shear instability.

2.7 Waveform Outline (Bowing) of Sealed Open Crack Tip

In many studies of the sealed cracks, the stress concentration at crack tip and its relaxation by plastic and subsidiary brittle deformation around the tip are discussed in the two dimensions, although there is almost always no investigation of the three-dimensional pattern of the crack tip line in the deep-seated rocks. This may be due to the reason that the crack edge line cannot be observed by the usual techniques in the rock mechanics (e.g., Quinn 2016).

On the other hand, the sealed open cracks of the deep-seated rocks display sharp contrast between sealed cracks and surrounding matrix because of contrasting sealing mineral under the naked eyes and optical microscope. Furthermore, the simple sealed crack reveals the sharp and straight bar having the constant width on the planar rock cut surface except for the region of crack tip, suggesting the simple form of the sealed open crack as illustrated in Fig. 2.53.

On the other hand, there are many cross-sectional patterns of the sealed cracks having the various width of the single sealed cracks. These sealed cracks commonly display periodic variation of thickness of the sealed cracks that apparently exhibits the continuous one. Considering the monotonous change of thickness of the sealed open crack from the crack edge, it shows that the thickness variation of the single sealed crack is responsible for the variation of the distance from the crack edge as illustrated in Fig. 2.54. Therefore, it is possible that the outline of the sealed open crack is drawn by the variation of the thickness of the continuous single sealed open crack.

By the way, the thickness of the sealed open cracks is often very narrow though the length of them is relatively long, and therefore, it is not easy to measure the periodic

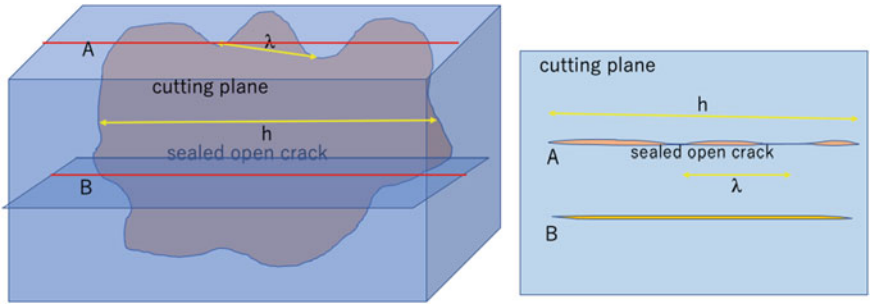

Fig. 2.53 Illustration of the bowing out sealed open crack extension in the rock and its crosscut images across the waveform tip outline (**a**) and central part (**b**). *h* is the crack size and l is the wavelength of the bowing out

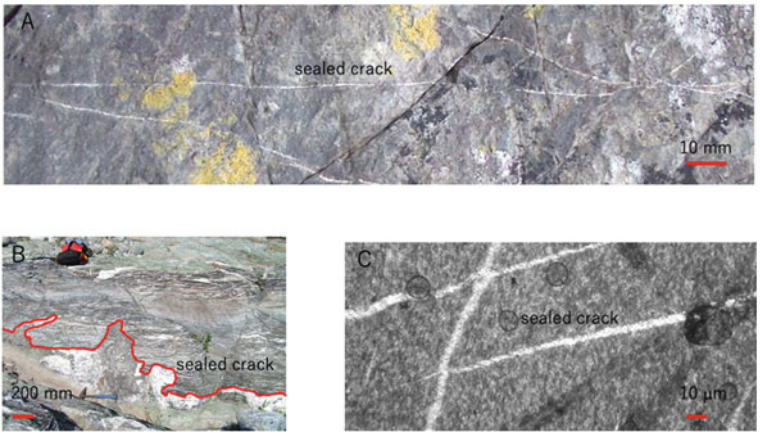

Fig. 2.54 Photographs of sealed open cracks filled with quartz (**A**, **C**) and calcite (**B**). **A** Muroto, Shimanto rock, **B** Nagatoro, Sanbagawa rock, **C** Mimigawa, Shimanto rock

thickness variation of the single sealed open crack under the usual microscope, but it is possible to measure the gray scale intensity of the constant number of the pixels under the digital images by means of the IMAGE J image analyzer. Then, the distance between the observed point and the edge (tip) of the sealed open crack can be estimated using the correlation between the average gray scale intensity of the pixels and the above distance.

The relationship for the correction coefficient of the distance from the edge from the square of the gray scale intensity of pixels is obtained from the simple monotonous sealed open crack by measurement of the width and pixel gray intensity along the whole crack length as shown in Fig. 2.55, showing the linear relation between them. Furthermore, the shortest distance from the crack can be estimated from the width of the sealed open crack using the geometry of the simple monotonous sealed crack (Fig. 2.56).

The characteristic wavelength of the periodic outline of the sealed crack edge has not been discussed in the previous papers of the rock mechanics. In this book, the author intends to formulate the instability of the crack edge outline filled with aqueous fluid.

Let us consider that the flat open crack edge outline appears in the initial condition, and after the enough short time, it changes to the wavy outline of the edge changes small perturbation with wavelength λ as shown in Fig. 2.57.

As shown in Fig. 2.57, it is obvious that there is a sharp relationship between the size of the sealed open crack and the bowing wavelength with the following type,

$$\log \lambda(\mathrm{mm}) = \log h(\mathrm{mm}) + \text{constant} \tag{2.55}$$

In this equation, it should be available that the constant term may contain the differential stress term because the crack growth velocity is related to the stress

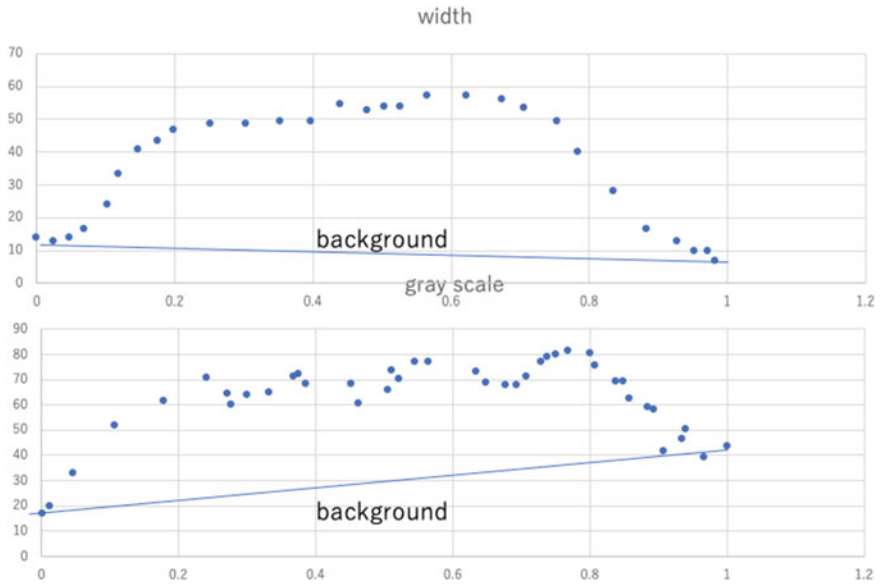

Fig. 2.55 Width and gray scale change measured by microscope and image analyzer (Image) in single sealed open crack in Shimanto rock

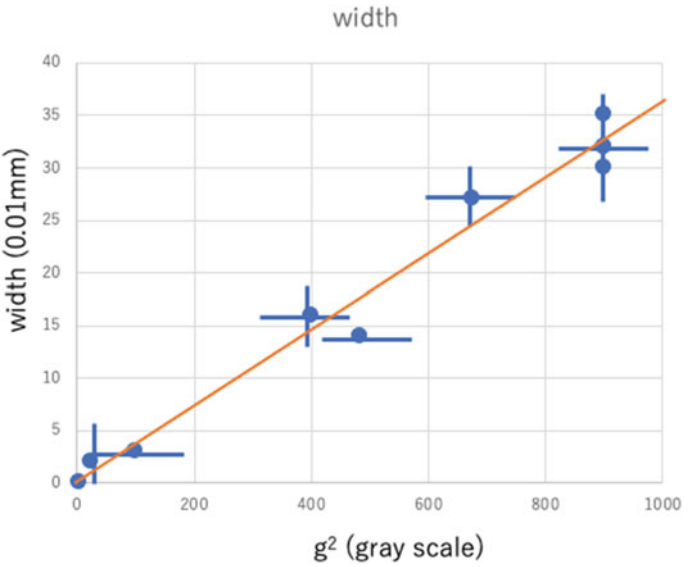

Fig. 2.56 Relation of width and gray scale in the quartz-sealing open crack

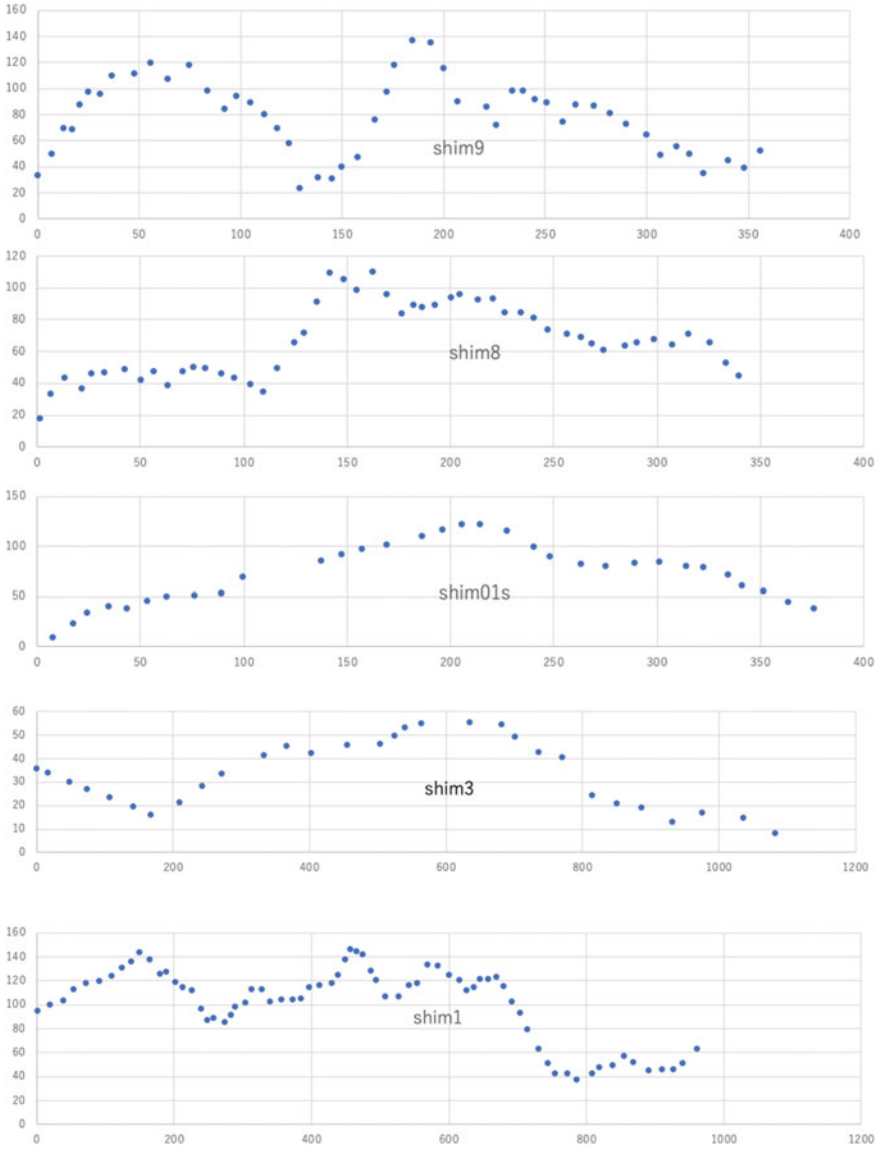

Fig. 2.57 Gray scale change along the sealed open cracks filled with quartz showing the wavy outline of the crack tip

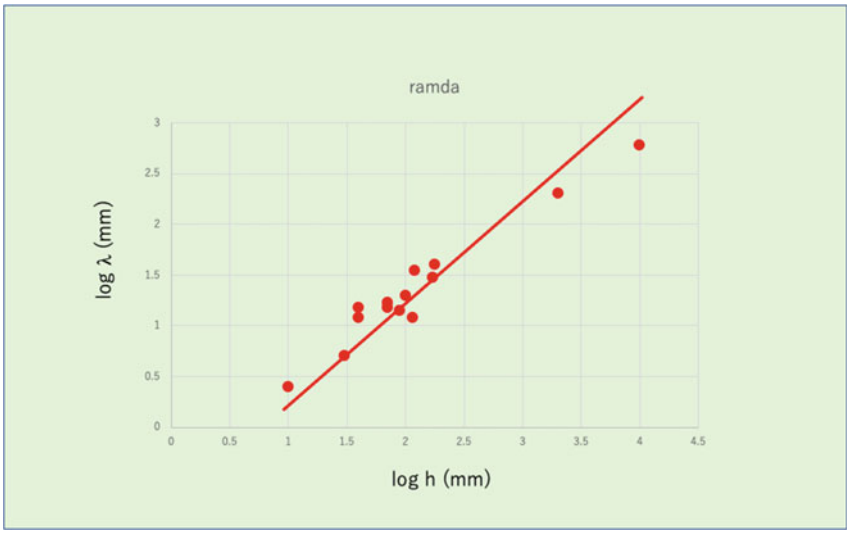

Fig. 2.58 Diagram of the wavelength of bowing structure and the length of the sealed open cracks in the Shimanto and Sanbagawa rocks showing the wavelength proportional to the length of the sealed crack

intensity factor (e.g., Wei, 2010). In this diagram (Fig. 2.57), the differential stress acting during the formation of sealed open cracks of the studied rocks may be approximated to be of the similar order, and thus, the above relation seems to be universal (Fig. 2.58).

The bowing out the crack tip outline seems to be derived from the pining force by high fracture strength islands at the front of the growing crack. The characteristic length of the high strength islands spacing along the crack front is determined by the force balance between the crack tip stress with pinned point and the critical strength of the high strength island (obstacle) as shown in Fig. 2.59.

Then, it holds,

$$aK/\lambda^{1/2} = F_p \tag{2.56}$$

in which K is stress intensity factor from curved crack tip and λ is the obstacle spacing, F_p is the critical strength of the obstacle, and a is the constant.

And thus, we obtain in the case of crack size h,

$$\begin{aligned} \lambda &= (aK/F_p)^2 \\ &= a^2\pi h\sigma^2/F_p^2 \end{aligned} \tag{2.57}$$

Then, it holds,

$$\log\lambda = \log h + 2\log\sigma + \text{constant} \tag{2.58}$$

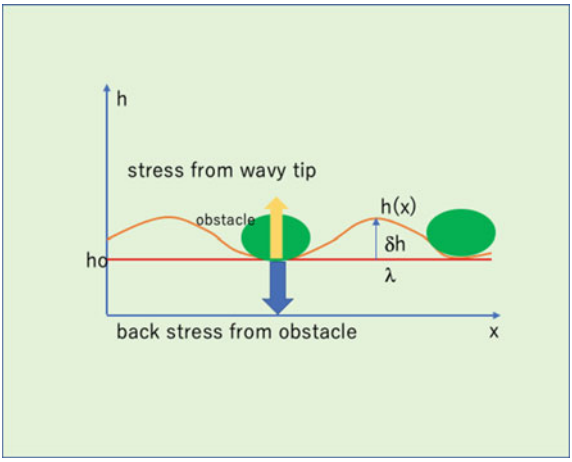

Fig. 2.59 Obstacle model of the bowing out crack tip in the process of the open crack growth showing the force balance of the back stress by obstacle along the crack tip and the stress from the bowing out tip

Therefore, it is obvious that the bow-out structure of the crack tip under the size of λ diminishes with growing crack. Therefore, the log h and log λ diagram (Fig. 2.57) is in good accordance with the present obstacle model of the crack front.

References

Akuhara T (2018) Fluid distribution along the Nankai-Trough megathrust fault off Kii Peninsula, Springer Nature

Aoya M (2001) P-T-d path of eclogite from the Sambagawa belt deduced from combination of petrological and microstructural analyses. J Petrol 42:1225–1248

Atkinson BK (1984) Subcritical crack growth in geological materials. J Geophys Res 89:4077–4114

Becker S, Hilgers C, Kukla EE, Urai JL (2011) Crack–seal microstructure evolution in bi-mineralic quartz-chlorite veins in shales and siltstones from the RWTH-1 well, Aachen, Germany. J Struct Geol 33:676–689

Biot MA (1961) Theory of folding of stratified viscoelastic media and its implications in tectonics and orogenesis. Geol Soc Am Bull 72:1595–1620

Byrn T (1986) Eocene underplating along the Kodiak shelf, Alaska: implications and regional correlations. Tectonics 5:403–421

Geological Survey of Japan AIST (ed) (2015) Seamless digital geological map of Japan 1: 200,000. May 29, 2015 version. Geological Survey of Japan, National Institute of Advanced Industrial Science and Technology

Hacker BR, Peacock SM, Abers GA, Holloway SD (2003) Subduction factory-2. Are intermediate—depth earthquakes in subducting slabs linked to metamorphic dehydration reactions? J Geophys Res 108(B1). https://doi.org/10.1029/2001JB00129

Holness MB (1993) Temperature and pressure dependence of quartz-aqueous fluid dihedral angles: the control of absorbed H_2O on the permeability of quartzites. Earth Planet Sci Lett 117:363–377

Ikesawa E, Sakaguchi A, Kimura G (2003) Pseudotachylyte from an ancient accretionary complex: Evidence for melt generation during seismic slip along a master décollement? Geology 31:637

Inui M, Toriumi M (2002) Prograde pressure–temperature paths in the pelitic schists of the Sanbagawa metamorphic belt, SW Japan. J Metamorphic Geol 20:563–580

Inui M, Toriumi M (2004) A theoretical study on the formation of growth zoning in garnet consuming chlorite. J Petrol 45:1369–1392
Itaya T, Tsujimori T, Liou JG (2011) Evolution of the Sanbagawa and Shimanto high-pressure belts in SW Japan: insights from K-Ar (Ar-Ar) geochronology. J Asian Earth Sci 42:1075–1090
Iwamori H (2000) Deep subduction of H2O and deflection of volcanic chain toward backarc near triple junction due to lower temperature. Earth Planet Sci Lett 181:41–46
Jaeger JC (1964) Elasticity, fracture and flow with engineering and geological applications. Methuen
Jamtveit B, Anderson TB (1992) Morphological instabilities during rapid growth of metamorphic garnets. Phys Chem Minerals 19:176–184
Kodaira S, Hidaka T, Kato A, Park J-D, Iwasaki T, Kaneda Y (2004) High pore fluid pressure may cause silent slip in the Nankai trough. Science 28:1295–1298
Kurz W, Fisher DJ (1986) Fundamentals of Solidification, Trans Tech Publication, Netherlands
Li Y-H, Gregory S (1974) Diffusion in ions in sea water and in deep-sea sediments. Geochim Cosmochim Acta 38:703–714
Miura S, Kodaira S, Nakanishi A, Tsuru T, Takahashi N, Hirata N, Kaneda Y (2003) Structural characteristics controlling the seismicity of southern Japan Trench fore-arc region, revealed by ocean bottom seismographic data. Tectonophysics 363:79–102
Nakanishi A, Kodaira S, Park J-P, Kandea Y (2002) Deformable backstop as seaward end of coseismic slip in the Nankai Trough seismogenic zone. Earth Planet Sci Lett 203:255–263
Ohmori K, Taira A, Tokuyama H, Sakaguch A, Okamura M, Aihara A (1997) Paleothermal structure of the Shimanto accretionary prism, Shikoku, Japan: Role of an out-of-sequence thrust, Geology 25:327
Okamoto A, Kikushi T, Tsuchiya N (2008) Mineral distribution within polyminerali veins in the Sanbagawa belt, Japan: implications for mass transfer during vein formation. Contrib Mineral Petrol 156:323–336
Okamoto A, Sekine K (2011) Textures of syntaxial quartz veins synthesized by hydrothermal experiments. J Struct Geol 33:1764–1775
Okamoto A, Toriumi M (2001) Application of differential thermodynamics (Gibbs' method) to amphibole zonings in the metabasic system, Contri Mineral Petrol 141:268–286
Omori S, Kamiya S, Maruyama S, Dapeng Z (2002) Morphology of the intraslab seismic zone and devolatilization phase equilibria of the subducting slab peridotite. Bull Earthq Res Inst Univ Tokyo 76:455–478
Park J, Tsuru T, Takahashi N, Hori T, Kodaira S, Nakanishi A, Miura S, Kaneda Y (2002) A deep strong reflector in the Nankai accretionary wedge from multichannel seismic data: implications for underplating and interseismic shear stress release. J Geophys Res 107(B4):2061. https://doi.org/10.1029/2001JB000262
Quinn GD (2016) Fractography of ceramics and glasses. NIST Special Publication 960-16e2
Ramsay JG (1980) The crack-seal mechanism of rock deformation. Nature 284:135–139. https://doi.org/10.1038/284135a0
Rogers G, Draget H (2003) Episodic tremor and slip on the Cascadia subduction zone: the chatter of silent slip. Science 300:1942–1943
Saishu H, Okamoto A, Otsubo M (2017) Silica precipitation potentially controls earthquake recurrence in seismogenic zones. Sci Rep 7:13337. https://doi.org/10.1038/s41598-017-13597-5
Schmalhorz SM (2006) Scaled amplification equation: a key to the folding history of buckled viscous sinlge-layers. Tectonophysics 419:41–53
Schwartz S, Rokosky JM (2006) Slow slip events and seismic tremor at circum-Pacific subduction zones. Rev Geophys **45**:RG3004. https://doi.org/10.1029/2006rg000208
Seno T, Zhao D, Kobayashi Y, Nakamura M (2001) Dehydration of serpentinized slab mantle: seismic evidence from southwest Japan. Earth Planets Space 53:861–871
Taira A, Katto J, Tashiro M, Okamura M, Kodama K (1988) The Shimanto belt in Shikoku—evolution of Cretaceous to Miocene accretionary prism. Mod Geol 12:5–48
Tatsumi Y (1989) Migration of fluid phases and genesis of basaltic magmas in subduction zones. J Geophys Res 94:4697–4707

Todd EK, Schwartz SY, Mochizuki K, Wallace LM, Sheehan AF, Webb SC, Williams CA, Naka J, Yarce J, Fry B, Henry S, Ito Y (2018) Earthquakes and tremor linked to seamount subduction during shallow slow slip at the Hikurangi margin, New Zealand

Toriumi M (1979) A mechanism of shape-transformation of quartz inclusions in albite of regional metamorphic rocks, Lithos 12:325–333

Toriumi M (1982) Strain, stress and uplift. Tectonics 1:57–76

Toriumi M (1990) The transition from brittle to ductile deformation in the Sambagawa metamorphic belt, Japan. J Metamorphic Geol 8:457–466

Toriumi M (2021) Global Seismicity Dynamics and Data-Driven Science, Springer

Toriumi M, Hara E (1995) Crack geometries and deformation by the crack-seal mechanism in the Sambagawa metamorphic belt. Tectonophysics 245:249–261

Toriumi M, Inui M (2001) Pressure–temperature–water production rate paths in the subduction metamorphism. Bull Earthq Res Inst Univ Tokyo 76:367–376

Toriumi M, Noda H (1984) The origin of strain patterns resulting from contemporaneous deformation and metamorphism in the Sambagawa metamorphic belt, J Metamorphic Geol 4:409–420

Toriumi M, Teruya J (1988) Tectono-metamorphism of the Shimanto belt. Mod Geol 12:303–324

Toriumi M, Teruya J, Masui M, Kuwahara J (1986) Microstructures and flow mechanisms in regional metamorphic rocks in Japan. Contrib Mineral Petrol 94:54–62

Toriumi M, Yamaguchi H (2000) Dehydration and the mechanics of metamorphic belts, J Geography 109:600–613

Tsuru T, Park J-P, Miura S, Kodaira S, Kido Y, Hayashi T (2002) Along-arc structural variation of the plate boundary at the Japan Trench margin: implication of interpolate coupling. J Geophys Res 107:B12

Tsuru T, Park J-O, Kido Y, Ito A, Kaneda Y, Yamada T, Shinohara M, Kanazawa T (2005) Did expanded porous patches guide rupture propagation in 2003 Tokachi-oki earthquake. Geophys Res Lett 32:L20310. https://doi.org/10.1029/2005GL023753

Ulmer P, Trommsdorff V (1995) Serpentine stability to mantle depths and subduction related magmatism. Science 268:858–861

Wei RP (2010) Fracture mechanics: integration of mechanics, materials science, and chemistry. Cambridge University Press

Chapter 3
Large-Scale Permeable Convection in the Plate Boundary Zone

Abstract The plate boundary zone is the most active region of the solid earth interior in long-term and short-term processes of deformation, metamorphism, volcanism, deep fluid circulation, and seismicity. Then, the rocks of the plate boundary zone are highly fractured and reacted with abundant aqueous fluid, and they form a permeable zone in which the fluid should circulate in the mode of permeable convection.

Keywords Plate boundary · Damage zone · High permeability · Permeable convection of fluid

3.1 Damage Zone and Sealed Crack Along the Plate Boundary

The active seismicity regions are seen in the plate boundary zones and especially in the subduction zone. The seismic activity in the subduction zone is characterized by the inland activity of the shallow earthquakes within the crust over 10–20 km depth and of the plate boundary zone and the inner subduction plate, and by the outer arc region. Giant earthquakes, for example, the Sumatra earthquake 2004 and the Tohoku-Oki earthquake 2011 are the plate boundary earthquake, and these are accompanied with huge amounts of post seismic activity. On the other hand, the seismic activity of the inner subducting slab is characterized by the double seismic zones in the shallower region above 200–250 km depth and by the deep seismic region of the 400–700 km. The source mechanism of the large earthquakes of the plate boundary is characterized by thrust type and overriding crust moves upward. Many plate boundary earthquakes occur in the range from 10 to 50 km depth although Tohoku-Oki giant earthquake slip reached to the ocean bottom along the trench line.

On the other hand, the outer rise earthquakes occurred in 2015 about M7 were the normal fault type reaching about 50 km depth in the uppermost mantle nearly parallel to the Japan trench axis, showing clearly the elastic bending of the Pacific Plate in front of the subduction under the Japanese arc. On the other hand, inner slab earthquakes of the Pacific Plate in the shallow part show the down-dip compression but in the deeper part do the down-dip extension type.

M. Toriumi, *Geochemical Mechanics and Deep Neural Network Modeling*,
Advances in Geological Science, https://doi.org/10.1007/978-981-19-3659-3_3

The plate boundary zone over the subducting plate boundary displays little activity of earthquakes with several km thickness but in the shallow depth characteristic nonvolcanic tremor earthquakes are clustered within this boundary zone. This zone, however, manifests the low velocity of P- and S-waves compared with surrounding region of the plate boundary zone. The boundary between this low Vp and Vs narrow region and surrounding normal Vp and Vs region displays often the strong reflection by the multichannel survey as being found by Park et al. (2002) along Nankai Trough and by along the Japan Trench. In addition, it is important that the detailed investigation by seismic tomography clarified the high Vp/Vs ratio suggesting the large porosity filled with aqueous fluid (Takei 2002) both in the boundary zone over the subducting slab along the Nankai Trough and the Japan Trench.

It is noteworthy that the slow slip event and very low frequency earthquake occur along the shallow plate boundary ranging from 30 to 50 km depth under the giant plate boundary earthquake zone as schematically shown by Fig. 3.1. The slow slip events in the subduction zones of the world are summarized by Schwartz and Rokosky (2006) and occur periodically in the time intervals between several hundred days to several years.

By the way, the pores and voids of the plate boundary rocks are certainly filled with aqueous fluid, and these are mainly derived from the open crack (type I crack) and the jog of shear cracks (type II and type III cracks) as mentioned in the previous chapter. The aspect ratios of open cracks which now sealed by minerals such as albite in basic schists and quartz in quartzose schists probably range from 0.01 to 0.001 as proposed previously but in the jogs sealed by above minerals their shape appears like lens with aspect ratio around 0.1–0.01. The schematic illustrations of the assemblages of sealed shear cracks and sealed jog, and sealed open cracks are

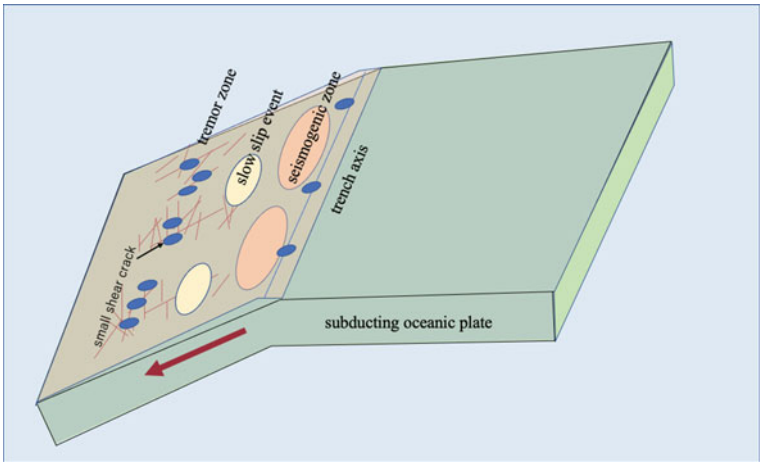

Fig. 3.1 Illustration of mechanical model a of the subduction plate boundary showing the heterogeneous distribution of representative seismic zones; seismogenic zone, tremor zone, slow slip zone, and overlapping small shear cracks zone

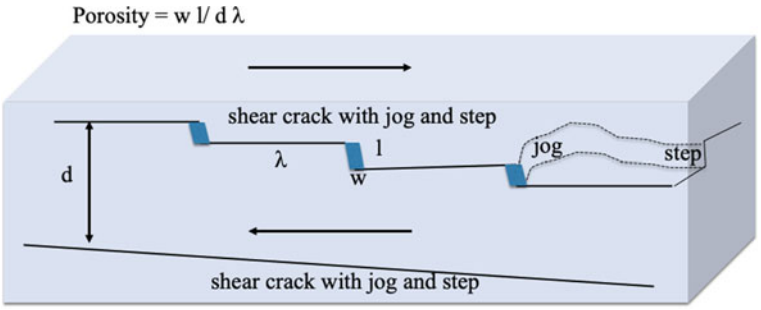

Fig. 3.2 Illustration of shear crack, jog, and step, and denoted geometrical parameters determining porosity of rocks

shown in Fig. 3.2, suggesting that the density of jog and open crack is possibly estimated from the observable sealed shear crack density that appears as the mineral band described earlier in order to infer the void density of the plate boundary rocks.

Furthermore, it is reasonable that the possible open crack and jog density of the plate boundary rocks may be inferred from the natural rocks in the outcrops of the paleoplate boundary zone, that is the accretionary wedge from shallow (Shimanto belt) to deep levels (Sanbagawa belt). As commonly seen in gauge rocks in the fault zone, there are abundant fault breccia composed of cataclastic rocks, various sized breccia, and cementing rocks and minerals in the case of normal fault, transcurrent fault and even thrust fault. For examples, the fault zone rocks along the large seismogenic thrust fault containing the pseudo-tachylite (shear molten rocks) in the Shimanto accretionary rocks have abundant sealed shear and open cracks filled with carbonates, but fault zone basaltic rocks are suffered from metasomatism to change the chlorite and albite rocks (Kitamura et al. 2005).

Therefore, the author tried to estimate the permeability of the rocks in the plate boundary zone over the subduction slab from the open crack density and jog density accompanied with sealed shear cracks as described in the previous chapter.

Here, the porosity is defined by the volume ratio of voids and pores filled with fluid against rock volume as like as

$$\begin{aligned}\phi &= V_{\text{void}}/V_{\text{rock}} \\ &= \left(V_{\text{oc}} + V_{\text{ig}}\right)/V_{\text{rock}} \\ &= n_c n_s w + n_s n_{\text{jg}} v_{\text{jg}} \\ &= w\left(n_c l_c^2/L^3\right) + l_{\text{jg}}^2 \text{dn}_{\text{jg}}/D_{sc}L^2 \\ &= \text{aw}/D_{\text{oc}} + \left(n_{\text{jg}} l_{\text{jg}^2}/L^2\right)\left(d_{\text{jg}}/D_{\text{sc}}\right)\end{aligned} \tag{3.1}$$

In which a is the constant, D_{oc} and D_{sc} are average distance of open crack and shear crack, respectively. In this equation, w and d is the average width of open crack and average thickness of jog on shear crack, respectively. Besides, n_c and n_{jg}, and l_c

and l_{jg} are number density of open crack, jog on shear plane, length of open crack, and length of jog on shear plane, respectively.

In Fig. 3.3, the open crack density and jog density accompanied with shear crack and the density of clustered open cracks are shown from the Sanbagawa and Shimanto plate boundary rocks. The actual porosity estimated by these data is shown from the natural occurrence of sealed open crack and jog in the deep plate boundary rocks. The estimated porosity values are about 0.02–0.04, suggesting that these values are in consistent with those inferred from the Poisson's ratio (or Vp/Vs ratio) of the plate boundary zone as indicated in Fig. 3.4.

On the other hand, the anisotropic nature of the shear and open cracks should be considered for the seismic nature of the plate boundary zone because recent investigation of the seismic velocity anisotropy manifested the fast orientation of Vs parallel to the trench axis in the plate boundary zone in the subduction zone of the world (Schwartz and Rokosky 2006). Inasmuch as the velocity reduction of primary and secondary seismic waves is due to the crack and jog filled with aqueous fluid and these voids are statistically aligned by the applied stress configuration, the anisotropy

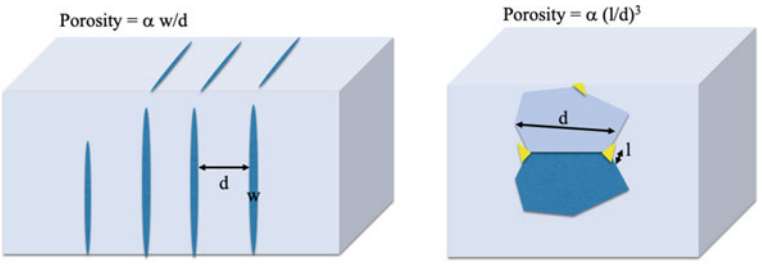

Fig. 3.3 Simple model of open crack and corner of grain boundary determining the porosity of rock

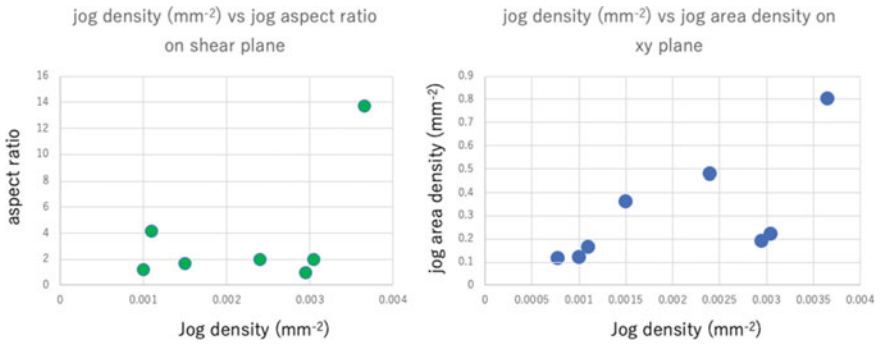

Fig. 3.4 Relations of the aspect ratio of shear crack jog and jog density (left) and jog areal density on shear crack and jog density (right) measured in the Sanbagawa plate boundary rocks. The shear crack and jog are sealed with albite in basic schists and quartz in pelitic schists

of the seismic velocity should be checked by the orientation anisotropy of the crack and jog disks in the boundary zone.

In the previous chapter, the author presented the anisotropy of the sealed open cracks in the shallow and deep accretionary wedge in the subduction zone such that the two types of crack disk orientation are found. The one of sealed open cracks is parallel to the trench axis, and the other formed at different time is perpendicular to the axis. Therefore, it is suggested that the anisotropy of the Vs must show the splitting of two stage: One is the fast direction parallel to trench axis and another perpendicular to the trench axis. The conclusion of the previous chapter about geometry of the sealed cracks is such that when the mechanical coupling between the subducting slab and overriding plate is strong, the trench parallel fast is satisfied, but weak coupling of them brings the perpendicular fast configuration as shown in Fig. 3.5.

By the way, does above configuration of the open cracks and jogs extend to the wedge mantle over the subducting slab? In many subduction zones, the angle of the slab subduction changes from about several to several 10 °s. For example, in the case of Nankai Trough, the angle changes from about 5–30 °, but in the case of Japan trench it changes from 2 to 4 ° to 45 °under the 40 km depth. Thus, it seems that the angle of the subducting slab reaching the wedge mantle becomes over 30 °. Furthermore, the boundary between slab and wedge mantle appears the lack of giant boundary earthquake below the depth of the wedge mantle, suggesting the weak mechanical coupling between slab and wedge mantle. This is probably due to the weak frictional coefficient of boundary slippage derived from serpentinite and/or fluid accumulation along on the boundary plane. It is noteworthy that there are abundant nonvolcanic

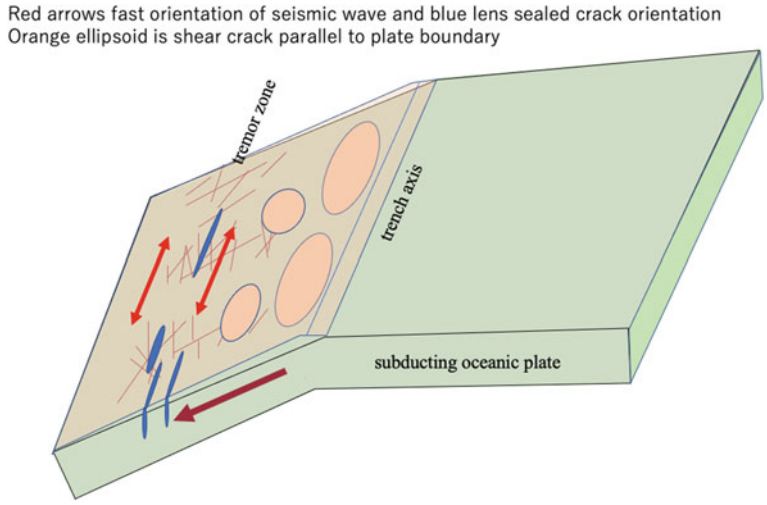

Fig. 3.5 Illustration of mechanical state in the plate boundary zone showing orientations of the sealed open crack (blue) and of fast seismic velocity (red). The orange ellipsoids represent the shear slip plane of the plate boundary large earthquakes

tremor signals along on the above boundary zone near the Nankai Trough (Obara 2002).

In this region of the wedge mantle, it seems that the observed anisotropy of Vs is derived from preferred lattice orientation of serpentine in the wedge mantle and/or the parallel alignment of many sealed open and shear cracks filled with serpentine (antigorite) and fluid dehydrated from subducting slab. If the sealed open crack is the case, the orientation of the crack lenses should be parallel to the trench axis, because the observed seismic anisotropy described above shows the fast direction parallel to the trench axis. Therefore, it is probable that the extensional stress orientation is perpendicular to the trench axis, suggesting the weak mechanical coupling again between the slab and the wedge mantle.

3.2 Porosity and Permeability of the Plate Boundary Derived from Open Crack and Shear Crack Jog Density

In the previous section, the author discussed the porosity represented by the density of open crack and shear crack jog in the deep-seated rocks in the plate boundary zone. These pores and voids are formed by the fracturing of rocks by differential stress condition in the solid earth interior, and these are filled with migrating fluid composed mainly by H_2O at the time of formation. However, these are often healed by the change of stress configuration and dewater the fluid into surrounding rocks and newly open crack favorable to the new stress configuration. For example, considering the fluid filling open crack parallel to the trench axis, the maximum principal axis changes to the direction perpendicular to the trench axis and then the parallel open crack should close and spray out the fluid into the surrounding rocks. Furthermore, the sprayed fluid may be absorbed by the newly formed open crack perpendicular to the old open crack at the new configuration of the applied stress.

Above change of the open crack orientation by environmental stress change brings also the synchronous inflow of the fluid into the jogged shear cracks around the open crack. It follows that some of subcritical-growing shear cracks exceed the critical Griffith crack due to decrease of surface energy of the wet shear crack surface and so those shear cracks suddenly propagate and should emit the seismic wave. In this process, the seismic bursting of small earthquakes (shear crack propagation) may happen at the time of the change in regional stress configuration.

Rapid stress configuration change should be taken place by the change of mechanical coupling between the slab and overriding plate derived not only the very slow slip but also large earthquake generating rapid slip at the plate boundary. In Cascadia and Nankai Trough region, the clusters of the nonvolcanic tremor appear just after the slow slip event at the plate boundary of them, suggesting that the recharge of fluid into shear crack and jog should occur by the stress change just after the slow slip event. This model for the progressive process from SSE to tremor cluster may be consistent with the east-westward migration (Obara 2002) of the tremor cluster in

SW Japan that means the open crack orientation change and permeability anisotropy change discussed previously.

Well, the permeability of the rock rich in the small open crack is expressed by the porosity as,

$$k = c\phi^2 \tag{3.2}$$

in which k and ϕ are the permeability and porosity, respectively and c is the geometrical constant (Landau and Lifshiz 1964). On the other hand, ϕ becomes,

$$\phi = n_c w \tag{3.3}$$

In which n_c is the crack density (mm^{-1}) and is measured as the ratio of total area of crack against unit volume of rock, and w is the width of the open crack (mm). As seen in Fig. 3.6, the porosity in the studied plate boundary rocks ranges commonly from 0.02 to 0.04 in the case of sealed open cracks but in the case of sealed shear crack jog does from 0.01 to 0.04 in the deep-seated accretionary rocks, showing the nearly like porosity between them.

On the other hand, the porosity of the open crack in a single rock is clearly large in the region of the crack cluster, but in the region between clusters it must be very low porosity. In the mixed case of the clusters in the single rock, the actual porosity ratio and permeability (k_a) of the rock may be inferred by the simple connection of the blocks having permeability of k_1 with thickness of l_1 and k_2 with l_2 as illustrated

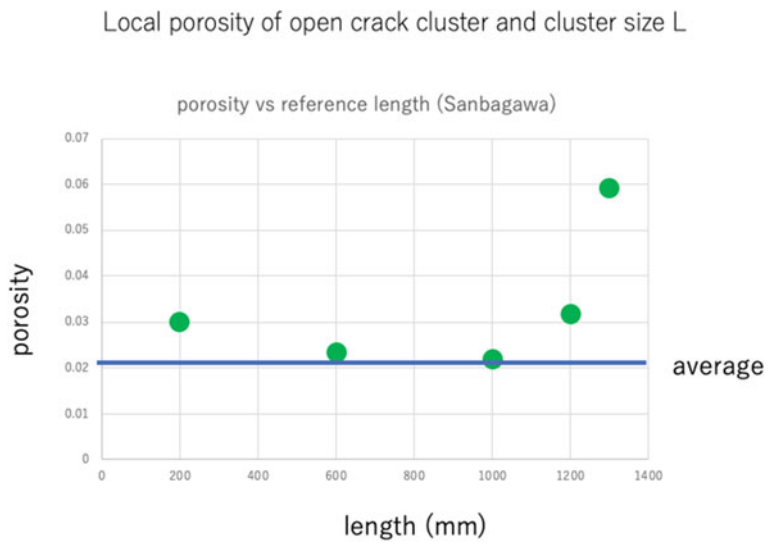

Fig. 3.6 Diagram of calculated porosity from the density of sealed open cracks associated with large shear cracks against the reference length of shear cracks

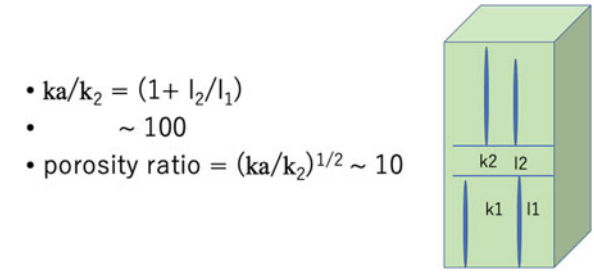

Fig. 3.7 Illustration of a model of porosity ratio and average permeability k_a by open crack clusters with permeability k_1 and length of open cracks l_1, and crack poor domain with crack size of l_2 and permeability k_2

in Fig. 3.7. Assuming the outflow at the end of k_1 block equal to that of the inflow of connected k_2 block by mass balance of fluid at the boundary between them, the Darcy flow is satisfied the following equations,

$$\begin{aligned} k_a &= (l_1 + l_2)/(l_1/k_1 + l_2/k_2) \\ &= k_1 k_2 (1 + \rho)/(k_2 + \rho k_1) \\ &= k_2 (1 + \rho)/(k_2/k_1 + \rho) \end{aligned} \tag{3.4}$$

and,

$$\begin{aligned} k_a/k_2 &= (1 + \rho)/(\beta + \rho) \\ &= (1 + \rho)/\rho \\ &= \rho^{-1} \sim 100 \end{aligned} \tag{3.5}$$

here, the relations of $k_2/k_1 = \beta$, $l_2/l_1 = \rho$, and $\beta < \rho$ are satisfied. In this case, the porosity ratio is approximated as $(k_a/k_2)^{1/2} \sim 10$.

By the way, considering the microvoids filled with fluid in a crystalline rock, the interface between fluid and mineral should be equilibrated by surface tension at their boundary, especially corner and edge. In the conditions of dihedral angle between them larger than 60° and small porosity, the microvoids should be distributed in the corner and edge of the mineral grains, but in the case of smaller dihedral angle than 60° those are localized in the corner. The microvoids may be isolated in the corner in the latter, but in the former, these partly connected each other, suggesting the higher permeability in the former case than that in the latter one. Further, it is important that this type of permeability increases with increasing the grain size of the rock, and thus the mylonite to ultra-mylonite rocks formed by large fault movement in the deep crust appears the low permeability rather than the surrounding cataclastic coarse-grained rocks.

Well, the crack healing derived from change in stress configuration may produce the array of microvoids trapping fluid along the grain boundary and in the grain interior, which are called as secondary fluid inclusion. These microvoids compose the porosity of the rocks and contribute the permeable fluid flow. The porosity of the

microvoids derived from crack healing can be estimated as

$$\phi = 4\pi n_v r_v^3/3 \tag{3.6}$$

in which n_v and r are the number density and average radius of microvoids, respectively.

Considering that r is about 0.1 m and n_v is about 100–1000/1mm^3, the porosity above estimated to be about $10^{-12} \times 10^3 = 10^{-9}$, showing the very small compared with the porosity by open crack and shear crack jog presented in the earlier. Therefore, the porosity of the subduction plate boundary zone should be represented by that of open crack and shear crack jog density as described in the previous section.

On the other hand, how thick is the high porosity zone in the subduction zone over the plate boundary? For solve this problem, the shear stress intensity is necessary to be estimated around the fault or shear crack. As same as the stress field of a dislocation in a crystal, the compressional stress intensity is in a function of distance d from the edge of the shear crack as

$$\sigma = \mathrm{Gu}\cos\theta/d \tag{3.7}$$

where u is the displacement of the shear crack. The compressional stress at the distance from shear fault is also expressed by above equation (Jaeger 1964). Then, if this stress intensity is over the critical stress of the Griffith crack, the compatible shear cracks should be activated to propagate and generate the jog and accompanied open crack cluster. Therefore, the width of the shear crack active zone neighboring the fault is determined by

$$(2G\gamma/r_c)^{1/2} = \mathrm{Gu}\cos\theta/d \tag{3.8}$$

and then, it holds at the direction of $\cos\theta = 1$,

$$d_c = u(Gr_c/2\gamma)^{1/2} \tag{3.9}$$

in which d_c and r_c are the width of cracked zone beside the fault and critical size of Griffith crack, respectively, and u and γ are the displacement of fault and surface energy of the rock, respectively. G is the elastic constant of the rock. This equation shows that the width of fractured zone (gouge zone) is proportional to the displacement of the fault. It is noticed that the displacement of shear crack u corresponds to the instantaneous displacement before fault movement at the maximum slip resistance force. Therefore, the displacement appears just before the sudden displacement, that is at the earthquake, and it is at most 1 cm for the fault length about 1 km. At this case, the dc reaches about 10 m.

3.3 2D Convection of Porous Filling Fluid of the Plate Boundary Zone

As seen in previous chapter and sections, the plate boundary zone is characterized by the fractured zone by plate subduction and various intermittent boundary fault earthquakes. Furthermore, it is obvious that the dewatering and dehydration of subducting plate and trench sediments take place with continuous subduction (e.g., Kasahara et al. 2003). Dehydration reaction of the pelitic rocks during the subduction process is simply simulated by the garnet forming reaction as

$$\text{Chlorite} + \text{quartz} = \text{garnet} + H_2O$$

Theoretical investigation of water emission from this equation in the process of prograde metamorphism, that is the subduction process, was carried out by Inui and Toriumi (2004), showing that the peak amount of emission rate of water occurs at the physical condition of 350 °C and 1 GPa for the common pelitic compositions. On the other hand, the basic rocks of oceanic crust should be suffered from decomposition kinetics of unstable relict pyroxene with chlorite and epidote to form actinolite and/or sodic amphibole (glaucophane and crossite) in the similar physical condition mentioned above. During prograde metamorphism of basic rocks, dehydration reaction of actinolite + epidote + chlorite to subcalcic hornblende or baroisite + H_2O occurs in the condition over 1 GPa and 400 °C (Okamoto and Toriumi 2001).

On the other hand, the subducting slab is also potential source of H_2O by dehydration reaction of serpentine (especially antigorite) in the lithospheric mantle and chlorite in basaltic rocks (e.g., Omori et al. 2002), below the depth about 50–150 km. Water released from the subducting slab migrates upward and flows into the wedge mantle and accretionary wedge adjacent to the subduction boundary. In addition, sea water also seems to bring into the deep accretionary wedge by subduction of porous sediments and then it liberates by dewatering with compaction and cementation of the sediments (e.g., Moore and Vrolijk 1992).

It is imagined possibly that the above water saturated and fractured zone adjacent the plate boundary should be suffered from the hydrodynamical motion within the porous fault, especially the permeable convection of porous flow. Vertical to slightly inclined fractured zone along the fault has been theoretically discussed by Murphy (1979), and he obtained the neutral stability conditions for permeable convection that the Rayleigh number is proportional to the permeability, thermal gradient, and square of length of the fractured zone, but it is inversely proportional to the thermal conductivity as

$$R = \rho\, g\, \alpha\, k\, h^2 G / \mu \kappa_m \tag{3.10}$$

The permeable convection takes place at the Rayleigh number over the critical number about 10. As discussed by Murphy, the onset condition of permeable convection is largely controlled by the permeability and the thermal gradient together with

thermal exchange between the surrounding rocks and the fractured zone because of thin fractured zone in the case of fault zone of the hydrothermal area. However, the fractured zone shows the wide thickness with about 2–5 km as clarified by Tsuru et al. (2002), and thus, it is probable the thermal exchange between surroundings and plate boundary fractured zone is very small as noted later. However, it remains that the gravitational force in the inclined plate boundary zone driving the convection becomes smaller than that of the vertical fault zone. The plate boundary of the Nankai Trough and the NE Japan Trench appears the angle of the shallow level about 5 ° and at rather deeper level it changes about 10 ° and then it does 30–45 ° in the wedge mantle (Nakanishi et al. 2002). Therefore, in the range from trench axis to the depth of uppermost wedge mantle, the inclined fractured zone over the plate boundary has gravitation acceleration of g sin θ (~0.17g) where θ is the subduction angle in the shallow zone, and the length of the present fracture zone is about 100 km with 2 km of thickness.

The thermal structure of the plate boundary zone is also important for discussion about the hydrodynamical behavior of fluid in the porous fracture zone along the plate boundary zone. Toriumi and Teruya (1988) studied the physical conditions of metamorphism in the Shimanto accretionary wedge by means of thermodynamic analyses of element partition between constituent minerals and of geothermometry of carbonaceous matters reflectance in the metamorphic sediments. It is inferred that the temperature of the chemical composition relations among prehnite, pumpellyite, and epidote with actinolite and chlorite assemblage ranges from 250 to 300 °C and pressure about 0.2–0.3 GPa (Toriumi and Teruya 1988). On the other hand, the thermal structure of the accretionary wedge is possibly inferred by the heat flow data at the bottom of ocean in the subduction zone (Hyndman et al. 1997; Hacker et al. 2003). Their results of the thermal structure of the accretionary wedge are consistent with those deduced by plate boundary metamorphic rocks mentioned above. Therefore, the thermal structure of the present plate boundary fracture zone is such that the temperature of the 10 km depth is about 200 °C and that of trench depth about 0 °C, as being indicated in Fig. 3.8.

Next, let us discuss the mode of permeable flow in this fracture zone over the plate boundary following the formulation by Murphy (1979).

Assuming the permeability k, thermal diffusivity κ, thermal capacity c, thermal conductivity λ, and fluid density ρ in the materials of the present system. Here, thermal diffusivity $\kappa = \lambda/\rho c$ is satisfied.

The system considered is possibly approximated to be two-dimensional one because the system is 100 km × 500 km × 2 km size and fluid flow within this inclined fracture zone is represented by laminar porous flow having flat velocity and boundary layer beside the boundary wall as like as Murphy (1979) and Zhao et al. (2004). Therefore, it will be possible that the velocity u and v are averaged velocity of the flat laminar flow as shown in Fig. 3.9.

Then, the controlling equations in the system of Fig. 3.10 become as,

$$\partial u/\partial x + \partial v/\partial y = 0 \tag{3.11}$$

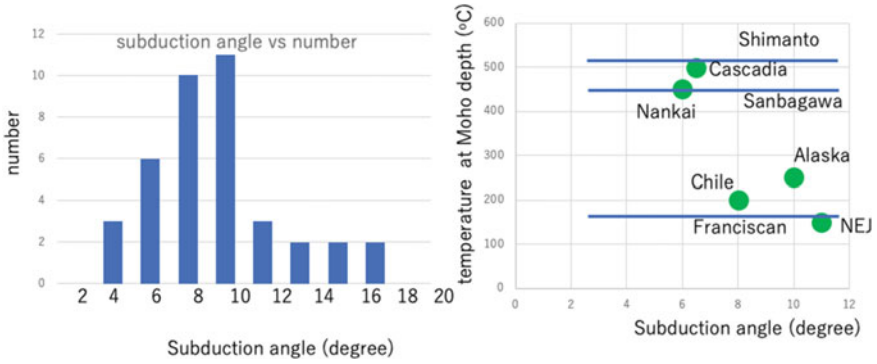

Fig. 3.8 Diagrams of frequency subduction angles (left) and their temperature at the Moho depth (right) of the various plate boundaries

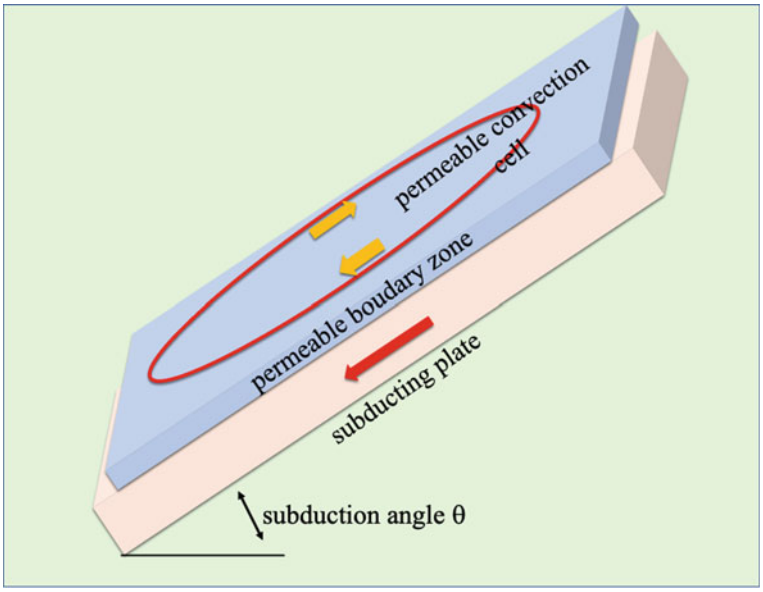

Fig. 3.9 Illustration of geometry of the permeable convection in the damage zone of the plate boundary

$$u = -(k/\mu)\partial P/\partial x$$
$$v = -(k/\mu)(\partial P/\partial y - \rho g \alpha T) \tag{3.12}$$

$$\rho_m c_m \partial T/\partial t - \rho_f c_f v(\partial T/\partial y) = \rho_f c_f \kappa_m \Delta T - 2e/w$$
$$\partial T/\partial y = G \tag{3.13}$$

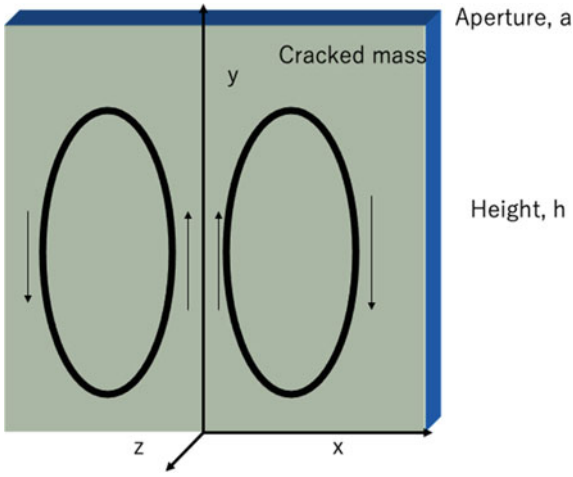

Fig. 3.10 Illustration of permeable thermal convection cell in the cracked plate boundary zones with a subduction angle

Combining above equations and operating Laplacian, the following thermal equation can be obtained,

$$(\mu kG)\left(\partial/\partial t + \left(2\kappa_r b_r \phi/w^2\right) - \kappa_m \Delta\right)\Delta T = \rho g \alpha \partial^2 T/\partial x^2 \tag{3.14}$$

where $e = \lambda_r\, \phi\, T/w$ is approximated using the term ϕ named as heat transfer function by Murphy.

Appling the linear neutral instability for this equation, the factor of amplifying the small perturbation wave following above equation as,

$$T(x, y, t) = A \exp(\omega t) \sin(\pi\, m\, y/h) \sin(\pi\, l\, x/h) \tag{3.15}$$

in which ω is the amplification term, m and l is the wave number of temperature perturbation on y axis and x axis, respectively. If ω is positive, the present perturbation should growth but if negative the perturbation will diminish. Thus, the neutral stability condition is expressed as $\omega = 0$ as indicated in Fig. 3.11. Inserting this type of linear solution into above energy equation about temperature, the following equation can be obtained,

$$\omega h^2/\kappa_m = \left(m^2 + l^2\right)R/l^2 - 2(\lambda_r/\lambda_m)(h/w)^2\phi - \pi^2\left(m^2 + l^2\right) \tag{3.16}$$

and

$$R = \rho g \alpha k h^2 G/\mu\kappa_m$$

and,

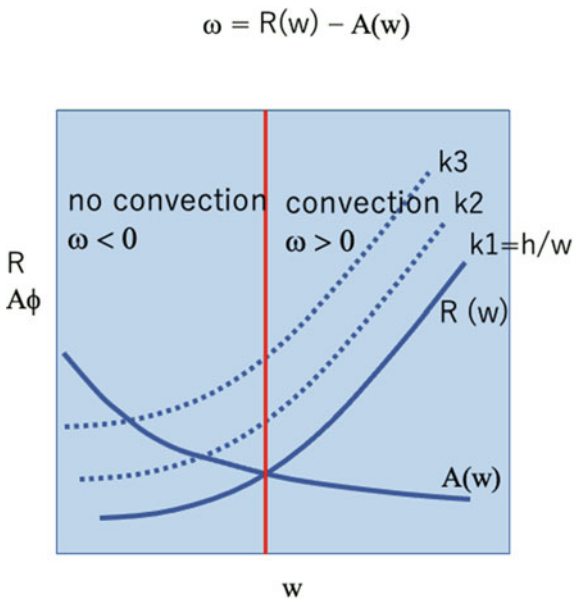

Fig. 3.11 Diagram of the theoretical relationship between Rayleigh number and thermal loss term A for the permeable convection condition ($w > 0$) with time for various thickness w of cracked plate boundary zone

$$\omega = \kappa_m\left(m^2 + l^2\right)R/h^2l^2 - 2(\lambda_r/\lambda_m)_m\kappa_m\phi/w^2 - \kappa_m\pi^2\left(m^2 + l^2\right)/h^2 \tag{3.17}$$

in which R is the Rayleigh number of the present system.

Therefore, we obtain the neutral stability condition from $\omega = 0$ for $m = 1$ as,

$$R = \left(\left(1 + l^2\right)\left(2(\lambda_r/\lambda_m)(h/w)^2\phi + \pi^2\left(1 + l^2\right)\right)\right)/l^2 \tag{3.18}$$

Now, the minimum R can be obtained by taking the minimum condition of above R against l, and it is called as critical Rayleigh number for neutral stability condition. As is well known, if the Rayleigh number R is over the critical Rayleigh number Rc, the permeable perturbation growth at the wave number of l which means the length scale of the convection grown from small perturbation. This is the two-dimensional convection in the subduction zone over the plate boundary as shown in Fig. 3.9. The Rc is inferred from the minimum condition determined by dR/dl = 0, and thus the Rc is obtained as,

$$Rc = 2(\lambda_r/\lambda_m)(h/w)^2\phi \tag{3.19}$$

In this equation, Rc involves h^2 term as well as Rayleigh number R, thus the condition of $R = \mathrm{Rc}$ becomes,

$$\rho g\alpha k w^2 G/\mu\kappa_m = 2(\lambda_r/\lambda_m)\phi \tag{3.20}$$

where λ_r/λ_m is the ratio of thermal conductivity between surrounding rock and porous rock, and it seems to be nearly 1 because of small porosity. Then, the critical Rayleigh number holds,

$$Rc = 2(h/w)^2\phi \tag{3.21}$$

It is obvious that the heat transfer function ϕ is important factor for onset of the convection in the fracture zone over the plate boundary from this equation. In the case of fracture zone along the fault as discussed in Murphy (1979), the thermal energy of porous flow should effectively dissipate into surrounding rocks through the wall because of narrow zone. On the other hand, the plate boundary fracture zone has the thickness over 2–3 km, showing the several thousand times thick compared with that of fault zone. Therefore, the dissipation thermal energy from the fracture zone is much smaller than that in the case of fault zone.

It is probable that the permeable flow pattern in the wide fracture zone should display the constant velocity in the wide central part and thin boundary layer at the boundary zone with the surrounding rocks. The ratio in thickness of this boundary layer by the main central flat velocity zone is possibly given by $s = \mathrm{Re}^{-1/2}$ by Landau and Lifshitz (1987), where Re is the Reynolds number. Then, it seems that the effective thermal transfer function may become s ϕ. Thus the Rc holds,

$$Rc = 2(h/w)^2 s\phi \tag{3.22}$$

If the boundary layer is very thin and s is about 0.01 (this corresponds to the thickness of boundary layer about 20 m), as the maximum transfer function ϕ is about 1 from Murphy (1979), the Rc is approximately $5000 \times 0.01\text{x}1 = 50$ in the case of $h = 100$ km and $w = 2$ km as mentioned previously. Then, the wave number of the convection should be about 2–3 from the relation of the growing perturbation of the velocity, suggesting that the width of the permeable convection is about 30–50 km.

Therefore, it concludes that the plate boundary zone is possibly characterized by three types of domains related to the permeable flow of aqueous fluid; one is the up-flow zone, the second is the down-flow zone, and third is the stagnant zone as shown in Fig. 3.12. The aqueous fluid in the lower bound of the fracture zone is supplied partly from the dehydration of the subducting slab, but in the upper bound it is also supplied partly from the fluid-rich trench sediment and the ocean. Considering the supply of aqueous fluid, the up-flow zone of the convection cell should flow out the aqueous fluid from the deep level and the down-flow zone should absorb the oceanic water.

As discussed in the next section, the aqueous solution of the down-flow zone is mixed with oceanic water in some content, and it is undersaturated in the solubility of quartz and albite and chlorite which are abundant in the porous rocks in the down-flow zone. Therefore, it seems that grains of these common minerals should be dissolved into permeable aqueous fluid and the rocks may increase their porosity by dissolution of grains.

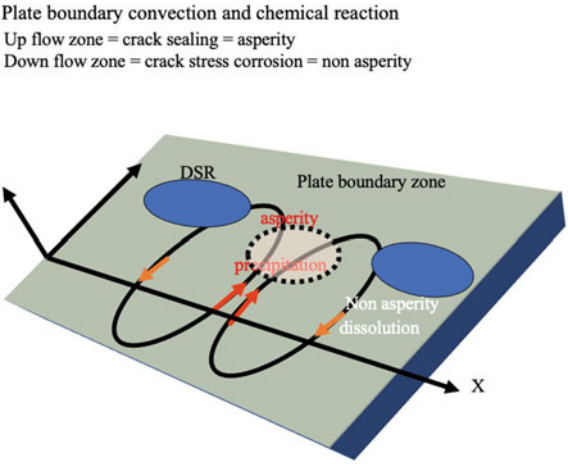

Fig. 3.12 Illustration of the up-flow and down-flow of the permeable convection and possible asperity zone with strong mechanical coupling and the deep seismic reflector with weak mechanical coupling with subduction slab due to large fluid-filled pores

On the other hand, the up-flow zone in the convective zone is comprised with relative warm aqueous fluid with chemical compositions saturated by albite, quartz, chlorite, calcite, and others, and thus for the pressure and temperature of the aqueous solution decrease with uprising, the solution should change the condition of oversaturation on above minerals. It is sure that the precipitation of minerals above makes the porosity decrease along the zone of the up-flow.

Above dissolution in the down-flow region and precipitation in the up-flow region are both effective to the convection in the boundary zone, because these mechanisms bring the permeability change locally. It seems that the convection cell may migrate by means of the migration of the up-flow position toward the down-flow bottom region where the permeability increases by dissolution. However, this process is possible only in the case that the time scales of precipitation of minerals at pores and voids of open crack and shear jog are enough smaller than that of the onset and development of permeable convection of the present system.

By the way, the periodic structure of the porosity distribution in the fracture zone over the plate boundary is favorable for the deep seismic reflector (DSR) discovered by Park et al. (2002). It is possible that the down-flow region of the fracture zone should be observed as the region of high Poisson's ratio because of the large volume fraction of fluid in rocks against the surrounding rocks and thus as the DSR of high seismic reflectance of their boundary as illustrated in Fig. 3.12. On the other hand, the up-flow region corresponds probably to the zone poor in fluid volume, and then it should be low Poisson's ratio that appears also low Vp/Vs ratio. Therefore, it is available that the plate boundary fracture zone may manifest the paired zone of the high and low Vp and Vp/Vs regions in the seismic observation. Recent studies of the Nankai Trough by Hasegawa and Nakajima (2017) clarified that the periodic Vp structure over the plate boundary along the Nankai Trough, suggesting the above mentioned paired seismic structure of the fractured boundary zone, though they suggested that in the high Vp region of the boundary zone it appears active in low

frequency earthquakes (nonvolcanic tremor) and low activity in LFE activity in the low Vp region, suggesting that the undrained condition is satisfied in the active LFE region. On the contrary, it seems natural that the high Vp region should comprise the drained rocks and it is poor in pore fluid, but the low Vp region should contain abundant pore fluid. However, Nakajima and Hasegawa pointed out that the active LFE region is located under the observed high Vp region and then it is occupied by the undrained pore fluid rocks. Anyway, it is important that there are contrasting high and low Vp region in the plate boundary zone over the subducting slab along the Nankai Trough, and the average distance between their regions is estimated to be about 200 km. It is also noted that the LFE activity shows the periodic structure along the Nankai Trough having the peak-to-peak distance of about 50 km (Obara 2002).

3.4 Geochemical Periodicity of Inflow and Outflow of Fluid Along the Subduction Zone

In the previous sections, the author presents the appearance of permeable convection of aqueous fluid in the fractured zone over the plate subduction boundary, and it should be proved by the observation of paired high and low Vp and Vp/Vs regions in the zone. The permeable convection of aqueous solution controls surely the temperature, chemical composition, and pH and Eh conditions. In addition, the case of convection-driven electrokinetic potential in the large convection cell is possible to be appeared in the boundary fractured zone (Ishido and Mizutani 1981). In this case, the zeta potential is derived from the absorption of some kinds of ionic species on pore wall during the up-flow and down-flow of the convection and it generates the electric potential and resultant current in the fracture zone. According to Ishido and Mizutani (1981), the electric potential may reach about 100 mV per unit pressure gradient and then the charge difference will be induced between upstream and downstream regions.

On the other hand, it should be necessary to be investigated that water–rock interaction in the up-flow and down-flow zone occurs in the different physical conditions and their paths, and it changes mineral compositions of open cracks and shear crack jogs by mineral dissolution and precipitation from aqueous solution. The mode of mineral precipitation from aqueous solution is controlled by thermodynamical process related to the solution chemistry of pores and voids. In the following, the geochemical process in the down-flow and up-flow region of the permeable convective system will be discussed.

At first, the equilibrium condition of minerals and aqueous solution will be formulated. Let us assume the system composed of aqueous solution having chemical composition $\{Xi\}$ and small amounts of end component minerals $\{Mi\}$ which have stoichiometry formula of $\{ai\}$, and the list of minerals concerned is shown in Fig. 3.13.

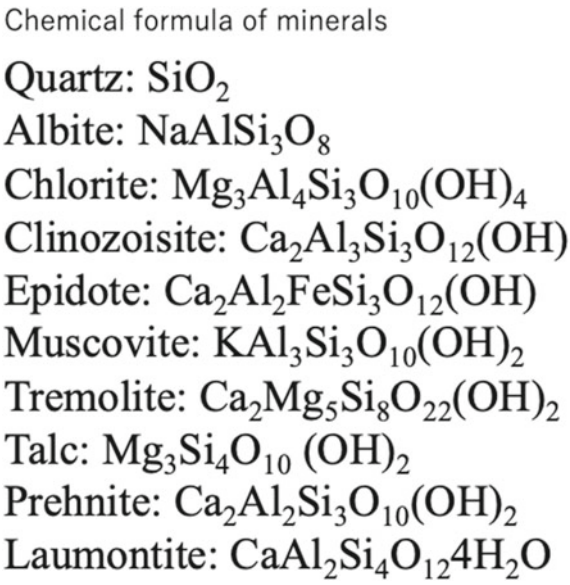

Fig. 3.13 Chemical formula of minerals related to dissolution and precipitation of the plate boundary zone

The thermodynamical equilibria of the minerals are expressed for several minerals as,

Quartz: $SiO_{2\,s} = SiO_{2aq}$
Albite: $NaAlSi_3O_8 + 4H^+ = Na^+ + Al^{3+} + 3SiO_{2\,aq} + 2H_2O$
Chlorite: $Mg_3Al_4Si_3O_{10}(OH)_4 + 18H^+ = 3Mg^{2+} + 4Al^{3+} + 3SiO_{2\,aq} + 7H_2O$
Clinozoisite: $Ca_2Al_3Si_3O_{12}(OH) + 13H^+ = 2Ca^{2+} + 3Al^{3+} + 3SiO_{2\,aq} + 7H_2O$
Muscovite: $KAl_3Si_3O_{10}(OH)_2 + 10H^+ = K^+ + 3Al^{3+} + 3SiO_{2\,aq} + 4H_2O$
Tremolite: $Ca_2Mg_5Si_8O_{22}(OH)_2 + 14H^+ = 2Ca^{2+} + 5Mg^{2+} + 8SiO_{2\,aq} + 6H_2O$
Talc: $Mg_3Si_4O_{10}(OH)_2 + 6H^+ = 3Mg^{2+} + 4SiO_{2\,aq} + 2H_2O$
Prehnite: $Ca_2Al_2Si_3O_{10}(OH)_2 + 10H^+ = 2Ca^{2+} + 2Al^{3+} + 3SiO_{2\,aq} + 4H_2O$
Laumontite: $CaAl_2Si_4O_{12}4H_2O + 8\,H^+ = Ca^{2+} + 2Al^{3+} + 4SiO_{2\,aq} + 8H_2O$.

Considering above chemical equations of dissociation of minerals, it is obvious that the equilibrium conditions of them are governed by temperature, pressure, and pH in terms of saturation product of ionic and neutral species of solute components in aqueous solution. The concentration products of soluble components in aqueous solution are defined as

$$\mathrm{Kab} = \left(X_{\mathrm{sio_2aq}}\right)^3 \left(X_{\mathrm{Na^+}}\right)\left(X_{\mathrm{Al^{3+}}}\right)$$
$$\mathrm{Kqz} = \left(X_{\mathrm{sio_2aq}}\right)$$
$$\mathrm{Kch} = \left(X_{\mathrm{sio_2aq}}\right)^3 \left(X^{2+}_{\mathrm{Mg}}\right)^3 \left(X_{\mathrm{Al^{3+}}}\right)^4$$
$$\mathrm{Kcz} = \left(X_{\mathrm{sio_2,aq}}\right)^3 \left(X_{\mathrm{Ca^{2+}}}\right)^2 \left(X_{\mathrm{Al^{3+}}}\right)^3$$

$$\begin{aligned}
\mathrm{Kms} &= \left(X(\mathrm{sio}_{2aa})^3\left(X_K^+\right)\left(X_{Al}^{3+}\right)^3\right. \\
\mathrm{Kpr} &= \left(X_{\mathrm{sio_2aq}}\right)^3\left(X_{\mathrm{Ca^{2+}}}\right)^2\left(X_{\mathrm{Al^{3+}}}\right)^2 \\
\mathrm{Ktr} &= \left(X_{\mathrm{sio_2aq}}\right)^8\left(X_{\mathrm{Ca^{2+}}}\right)^2\left(X_{\mathrm{Mg}}^{2+}\right)^5 \\
\mathrm{Ktc} &= \left(X_{\mathrm{sio_2aq}}\right)^4\left(X_{\mathrm{Mg}}^{2+}\right)^3 \\
\mathrm{Klm} &= \left(X_{\mathrm{sio_2aq}}\right)^4\left(X_{\mathrm{Ca^{2+}}}\right)\left(X_{\mathrm{Al}}^{3+}\right)^2
\end{aligned} \tag{3.23}$$

in which X_i is the mol fraction (m/l) of i-species component in aqueous solution.

On the other hand, corresponding to above chemical equations (mass balance equations), the following equilibrium relations are satisfied,

$$\begin{aligned}
a\Delta\mathrm{Gab}(T, P)/\mathrm{RT} &= \log \mathrm{Kab} + 4\mathrm{pH} \\
a\Delta\mathrm{Ggz}(T, P)/\mathrm{RT} &= \log \mathrm{Kqz} \\
a\Delta\mathrm{Gch}(T, P)/\mathrm{RT} &= \log \mathrm{Kch} + 18\mathrm{pH} \\
a\Delta\mathrm{Gcz}(T, P)/\mathrm{RT} &= \log \mathrm{Kcz} + 13\mathrm{pH} \\
a\Delta\mathrm{Gms}(T, P)/\mathrm{RT} &= \log \mathrm{Kms} + 10\mathrm{pH} \\
a\Delta\mathrm{Gtr}(T, P)/\mathrm{RT} &= \log \mathrm{Ktr} + 14\mathrm{pH} \\
a\Delta\mathrm{Gtc}(T, P)/\mathrm{RT} &= \log \mathrm{Ktc} + 6\mathrm{pH} \\
a\Delta\mathrm{Glm}(T, P)/\mathrm{RT} &= \log \mathrm{Klm} + 8\mathrm{pH}
\end{aligned} \tag{3.24}$$

where X_{H2O} is approximated to be 1, and a is 0.43.

If albite is in equilibrium with quartz and aqueous solution, the following equation holds

$$a(\Delta\mathrm{Gab}(T, P) - 3\Delta\mathrm{Gqz}(T, P))/\mathrm{RT} = \log X_{\mathrm{Na^+}} + \log X_{\mathrm{Al3^+}} + 4\mathrm{pH} \tag{3.25}$$

For chlorite and quartz equilibrium condition, it holds,

$$a(\Delta\mathrm{Gch}(T, P) - 3\Delta\mathrm{Gqz}(T, P))/\mathrm{RT} = 3\log X_{\mathrm{Mg^{2+}}} + 4\log X_{\mathrm{Al3^+}} + 18\mathrm{pH} \tag{3.26}$$

For epidote and quartz is in equilibrium, it becomes,

$$a(\Delta\mathrm{Gcz}(T, P) - 3\Delta\mathrm{Gqz}(T, P))/\mathrm{RT} = 2\log X_{\mathrm{Ca^{2+}}} + 3\log X_{\mathrm{Al3^+}} + 13\mathrm{pH} \tag{3.27}$$

Therefore, in the system of aqueous solution composed of mainly Na^+, Ca^{2+}, and Mg^{2+} with SiO_{2aq}, the single-phase stability condition is di-variant, and two-phase one is univariant system as shown in the composition diagram at constant X_{Al3+} and X_{SiO2aq} (Fig. 3.14).

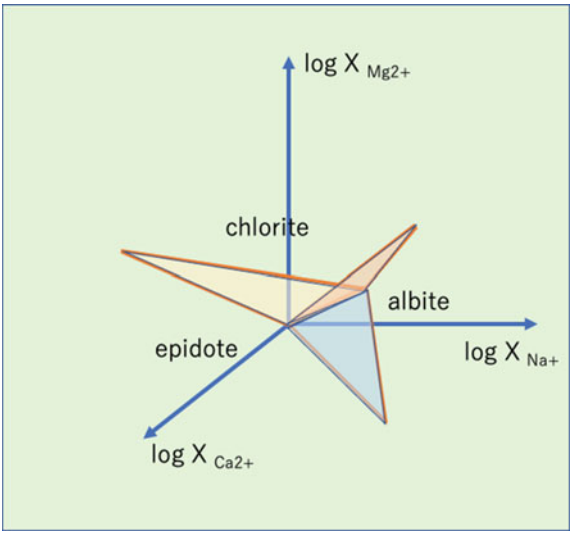

Fig. 3.14 Stability field of chlorite, albite, and epidote in the chemical concentration diagram

On the other hand, the equilibrium conditions of chlorite and albite with quartz appear the following equation,

$$\begin{aligned} &a(4\Delta\mathrm{Gab}(T,P) - 9\Delta\mathrm{Gqz}(T,P) - \Delta\mathrm{Gch}(T,P))/\mathrm{RT} \\ &= 4\log X_{\mathrm{Na^+}} + 4\log X_{\mathrm{Al3+}} + 16\mathrm{pH} - \left(3\log X_{\mathrm{Mg^{2+}}} + 4\log X_{\mathrm{Al3+}} + 18\mathrm{pH}\right) \\ &= 4\log X_{\mathrm{Na^+}} - 3\log X_{\mathrm{Mg^{2+}}} - 2\mathrm{pH} \end{aligned} \tag{3.28}$$

Therefore, at the constant temperature and pressure, coexistence of chlorite and albite needs the linear relation between ln $X_{\mathrm{Na+}}$ and ln $X_{\mathrm{Mg2+}}$ as shown in Fig. 3.15.

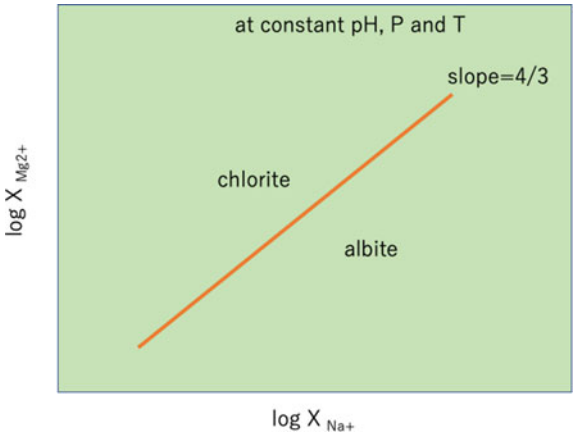

Fig. 3.15 Stability relation of albite and chlorite assemblage at the constant temperature and pressure condition in the chemical concentration diagram

In this section, the author intends to estimate the precipitating minerals filling the open crack and shear jog both in the up-flow and down-flow regions of the permeable convection system proposed in the earlier sections. In the case, the initial chemical composition of the down-flow aqueous solution is approximated to be that of the sea water because the down-flow region contacts directly with ocean sea bottom or the very porous and soft sediment at the trench axis. Thus, the aqueous solution of sea water composition should change its chemistry by water–rock interaction between pore fluid and surrounding various minerals. In the case that the rocks of the down-flow region are composed mainly of sandstone and mudstone, aqueous fluid should react with quartz, plagioclase, micas, and lithic fragments. For the aqueous fluid may be undersaturated in these detritus minerals in sedimentary rocks, the porous flow into the downward should dissolve slowly these minerals surrounding the pores and voids. The solubility of quartz in the down-flow aqueous solution increases with increasing pressure along on the down-flow convection and, thus, the sinking aqueous solution should keep the near undersaturated chemistry until the deep zone of the convection cell. On the other hand, the down-flow solution may increase gradually chemical composition of Al^{3+}, K^{+}, and Mg^{2+} due to dissolution of detritus micas. It seems that this enrichment of Al^{3+} and Mg^{2+} causes the saturation of chlorite and albite because the sea water contains abundant Na^{+} and Mg^{2+} ions. Therefore, it may be concluded that in the deep part of the down-flow region albite and chlorite should precipitate in the pores and voids.

On the other hand, in the up-flow region of the convection cell the initial chemistry appears the high $X_{SiO2\ aq}$ and K^{+} together with high content of Ca^{2+}, for the initial solution at the bottom of the convection cell should inherit the chemistry of the down-flow aqueous solution at the bottom. By the way, the solubility becomes small with decreasing pressure and temperature, and so the aqueous solution of the up-flow regime should oversaturate about quartz, K-micas and/or K-feldspars (microcline) and clinozoisite or laumontite.

Let us compare the difference in concentration products concerning the solubility of minerals mentioned above between sea water and aqueous solution after water–rock interaction enough by high temperature and pressure experiments (Shikazono, 2003). The saturation concentration of solvable SiO_2 for quartz, K-feldspar (microcline), albite, chlorite, and muscovite in aqueous solutions is shown in Fig. 3.16, suggesting large difference of them. The sea water at physical conditions near earth surface and sea bottom is probably saturated in several kinds of minerals, but the aqueous solution obtained from hydrothermal experiments of water-basalt and water-sandstone system may be saturated partly in quartz, chlorite, albite, and others (e.g., Shikazono 2003).

On the other hand, the equilibrium solubility products of quartz, albite, chlorite, and other minerals are possibly estimated by using thermodynamic parameters listed in Holland and Powell (1998). In the system of the permeable convection studied here, it is available that dissolution and precipitation of abundant quartz grains in porous sandstone and mudstone and basaltic glass rich in silica (50 wt%) are important control factor in degree of undersaturation and oversaturation of albite, chlorite, muscovite, and other minerals in the column of the up-flow and down-flow regime

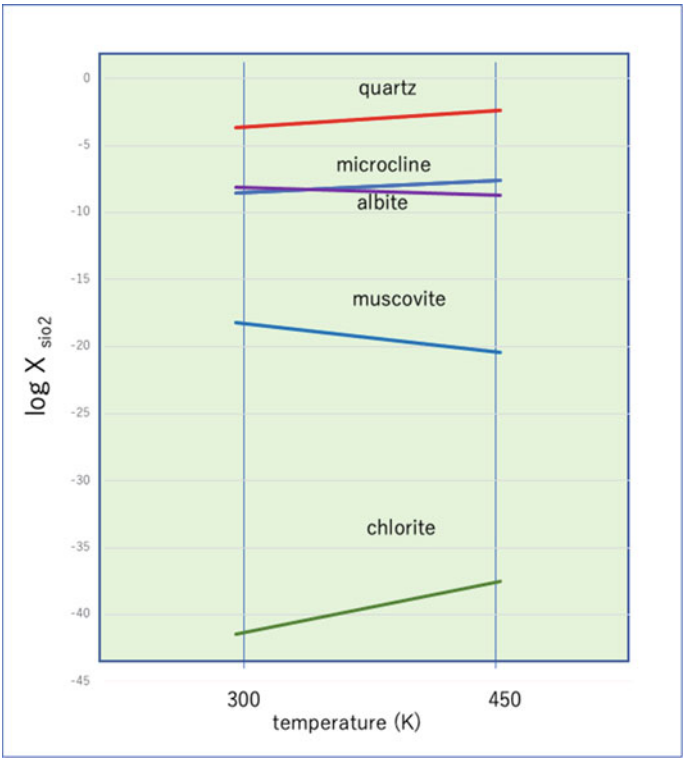

Fig. 3.16 Equilibrium diagram of minerals with permeable aqueous solution in the diagram of log X_{SiO2aq} (m/l) and temperature at available concentrations (seawater) of other ionic species

in the convection system of the plate boundary zone, judging from the concentration products of them. Therefore, it is necessary to know the concentration pattern of $SiO_{2\,aq}$ in the up-flow and down-flow column of the simple stationary permeable flow system as discussed in the follows.

Let us assume near constant temperature conditions along the up-flow and down-flow column in the permeable convection system as shown in Fig. 3.17. The concentration change of $SiO_{2\,aq}$ is surely governed by the following mass balance equation along the y-axis defined earlier,

$$d\phi X_{SiO_2aq}/dt + V d\phi X_{SiO_2aq}/dy = k\phi\left(X^{o}_{SiO_2aq} - X_{SiO_2aq}\right) \tag{3.29}$$

in which f and V are the porosity and velocity of aqueous solution, respectively. Xi is the concentration of SiO_{2aq} in solution, and X_{SiO2aq} is the equilibrium concentration of SiO_{2aq} with quartz. It is available that the V is very small and constant and dX_{SiO2aq}/dt is zero in the case of the steady state. Then, we obtain

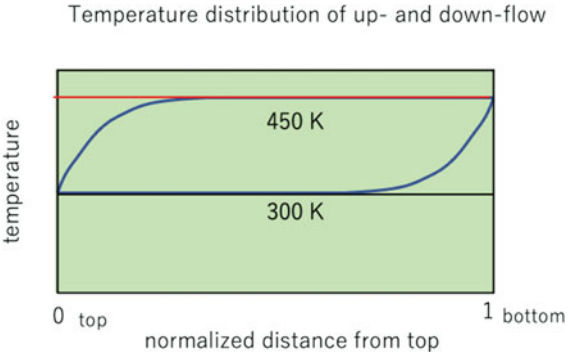

Fig. 3.17 Simplified temperature condition of up-flow and down-flow region of the permeable convection cell in the plate boundary zone

$$\mathrm{dX_{SiO_2aq}}/\mathrm{dy} = k\left(X^{\circ}_{\mathrm{SiO_2aq}} - X_{\mathrm{SiO_2aq}}\right)(\mathrm{down-flow})$$

and

$$\mathrm{dX_{SiO_2aq}dy} = k\left(X_{\mathrm{SiO_2aq}} - X^{\circ}_{\mathrm{SiO_2aq}}\right)(\mathrm{up-flow}) \tag{3.30}$$

where that $X_{\mathrm{SiO2aq}}{}^{\mathrm{o}}$ is proportional to the depth is derived from the equilibrium solubility is dependent on exp $(-\Delta G^{\mathrm{o}}\ (T, P)/\mathrm{RT})$ from thermodynamic equations and $\Delta \mathrm{G^o}$ is the Gibbs free energy change of dissolution or precipitation reaction mentioned above.

Thus, the simple equation corresponding to above equation holds under the approximation of constant $\mathrm{X_{SiO2aq}}{}^{\mathrm{o}}$,

$$d\left(X_{\mathrm{SiO_2aq}} - X_{\mathrm{SiO_2aq}^{\circ}}\right)/\left(X_{\mathrm{SiO_2aq}} - X_{\mathrm{SiO_2aq}^{\circ}}\right)\mathrm{dy} = -k \tag{3.31}$$

Thus, for the down-flow, we obtain,

$$\begin{aligned} X_{\mathrm{SiO_2aq}} &= X^{\circ}_{\mathrm{SiO_2aq}} + A\exp(-\mathrm{ky}) \\ A &= X^{1}_{\mathrm{SiO_2aq}} - X^{1}_{\mathrm{SiO_2aq}}(\mathrm{at}\ y = 0) \\ X^{2}_{\mathrm{SiO_2aq}} &= X^{\circ}_{\mathrm{SiO_2aq}} + \left(X^{l}_{\mathrm{SiO_2aq}} - X^{l}_{\mathrm{SiO_2aq}^{\circ}}\right)\exp(-k) \sim X^{\circ}_{\mathrm{SiO_2aq}}\,(\mathrm{at}\ y = 1) \end{aligned} \tag{3.32}$$

And for up-flow, it is,

$$d\left(X_{\mathrm{SiO_2aq}} - X^{2}_{\mathrm{SiO_2aq}}{}^{\circ}\right)/\left(X_{\mathrm{SiO_2aq}} - X^{2}_{\mathrm{SiO_2aq}}{}^{\circ}\right)d(1-y) = -k$$

and

$$\begin{aligned} X_{\mathrm{SiO_2aq}} &= X^{2}_{\mathrm{SiO_2aq}^{\circ}} + A\exp(-k(1-y)) \\ A &= X^{2}_{\mathrm{SiO_2aq}} - X_{\mathrm{SiO_2aq}^{\circ}} \quad (\mathrm{at}\ y = 1) \end{aligned}$$

and,

$$X_{SiO_2aq^3} \sim X^2_{SiO_2aq^\circ} \quad (\text{at } y = 0) \tag{3.33}$$

It is shown that in the case of undersaturation the concentration of present ionic species increases but in the oversaturation case it must decrease. The simulation experiments under simple parameters can be easily carried out as shown in Fig. 3.18, suggesting the general pattern of the concentration change of important ionic species (here SiO_{2aq}) displays the gradual increase with increasing depth of the down-flow region and decrease with decreasing depth of the up-flow region. Therefore, in the down-flow region the dissolution of quartz is dominant and thus the rocks of the down-flow region become rich in pores and voids filling aqueous solution. On the other hand, rocks of the up-flow regions decrease in porosity and thus change poor in fluid for precipitation of quartz in pores and voids of open cracks and shear crack jogs.

By the way, the critical solubility of SiO_{2aq} can be considered as the important parameter of porosity and mineralogy of the up- and down-flow region for it controls the precipitation and dissolution of other silicates such as albite, chlorite, epidote, and muscovite. The following equations are possibly available for these mineral precipitation in the pores and voids related to the cracks.

$$3 \log X^{\circ ab}_{SiO_2aq} = \log \mathrm{Kab} - \log\left(X_{Na^+} X_{Al^{3+}}\right)$$

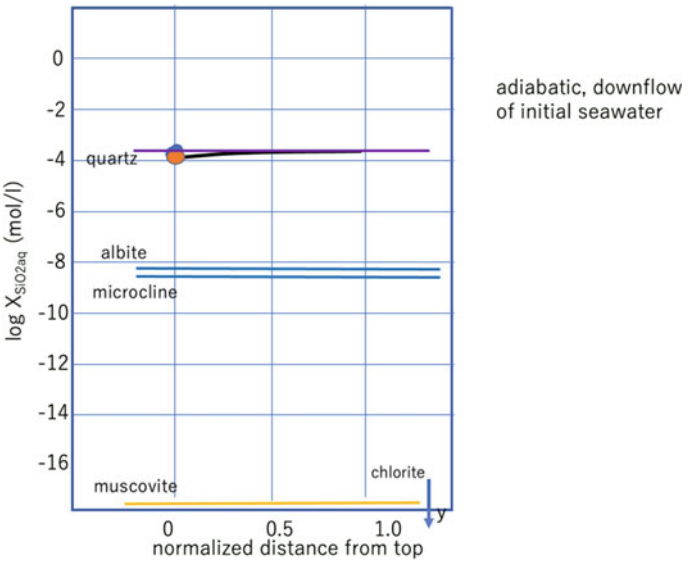

Fig. 3.18 Equilibrium diagram of temperature and concentration of $SiO_{2aq.}$ in the aqueous solution of down-flow in the convection cell and precipitation conditions of from permeable solution

$$
\begin{aligned}
3\log X^{\circ ch}_{SiO_2aq} &= \log \mathrm{Kch} - \log\left(X^3_{Mg^{2+}} X^4_{Al^{3+}}\right) \\
3\log X^{\circ cz}_{SiO_2aq} &= \log \mathrm{Kcz} - \log\left(X^2_{Ca2t}\, X^3_{Al^{3+}}\right) \\
3\log X^{\circ ms}_{SiO_2aq} &= \log \mathrm{Kms} - \log\left(X_{K^+} X_{Al^{3+}}\right)
\end{aligned} \tag{3.34}
$$

These relations give the conditions of $X_{SiO2aq}{}^{o}$ at precipitation of quartz, albite, chlorite, muscovite, and clinozoisite in the up-flow and down-flow regions of the permeable convection zone in the plate boundary. As shown in the previous section, the chemistry of sea water appears that the concentrations of Na^+, K^+, and Ca^{2+} are lower than those in aqueous solution obtained in the experimental water–rock interaction of basalt and sandstone (Shikazono 2003). Furthermore, it seems that concentration of Mg^{2+} is obviously higher than that in the aqueous solution of experimental products.

Considering precipitation and dissolution path along the up-flow and down-flow, the temperature and pressure dependence of solubility product K in equations above. Thermodynamical equations for ln K at the equilibrium condition of aqueous solution and minerals hold as,

$$
\begin{aligned}
\log \mathrm{Kqz} &= 0.43\Delta \mathrm{Gqz}(T, P)/\mathrm{RT} \\
\log \mathrm{Kab} &= 0.43\Delta \mathrm{Gab}(T, P)/\mathrm{RT} \\
\log \mathrm{Kch} &= 0.43\Delta \mathrm{Gch}(T, P)/\mathrm{RT}
\end{aligned} \tag{3.35}
$$

and then,

$$
\begin{aligned}
d\log \mathrm{Kqz}/\mathrm{dT} &= 0.43\left(\Delta H^{\circ}_{qz} - \Delta v_{qz}(P-1)\right)/T^2 \\
d\log \mathrm{Kab}/\mathrm{dT} &= 0.43\left(\Delta H^{\circ}_{ab} - \Delta v_{ab}(P-1)\right)/T^2 \\
d\log \mathrm{Kch}/\mathrm{dT} &= 0.43\left(\Delta H^{\circ}_{ch} - \Delta v_{ch}(P-1)\right)/T^2
\end{aligned} \tag{3.36}
$$

in which ΔH and Δv are the enthalpy and volume change in the chemical equation above, respectively. For volume change is very small, the solubility product at equilibrium conditions of aqueous solution and each mineral depends mainly on the temperature and the term of enthalpy change. Following Holland and Powell (1998), the enthalpy change of quartz and chlorite is positive and thus the term of ln K increases with increasing temperature, though that of albite is negative and ln K decreases with increasing temperature.

By the way, considering the convection system of the fractured zone studied here, along the down-flow region temperature should be near the adiabatic profile at low temperature but along the up-flow region is at high temperature condition. Therefore, it seems possible that the equilibrium saturation concentration of quartz of the down-flow regime is lower than that of the up-flow regime. Furthermore, if the concentration of SiO_{2aq} is likely to that of sea water at the initial down-flow input, it should be much

lower than that of equilibrium concentration even at the temperature of the down-flow. If this is the case of the down-flow chemistry, it should be available that the concentration path of the down-flow displays the simple dissolution trend as obtained previously. As a result, concentration of SiO_{2aq} even at the bottom of the down-flow region must be lower than that of equilibrium one as shown in Fig. 3.19. On the other hand, along the up-flow regime, the concentration path should be asymptotic to the new equilibrium concentration higher than that of down-flow regime as shown in Fig. 3.20.

Next, let us think about the precipitation and dissolution of albite and chlorite and chrysotile serpentine in the up-flow and down-flow region. The phase relation of these minerals in the log X_{SiO2aq} and temperature diagram is displayed in Fig. 3.16, showing that the solubility curve of albite and serpentine is running near that of quartz but the solubility concentration curve of chlorite in equilibrium with ionic species OH^- is different against them, and it has large gradient in temperature-log X_{SiO2aq} diagram. Therefore, the chlorite (amesite) is oversaturated in the low temperature conditions, and it changes undersaturated condition in the higher temperature. These phase relations of solubility concerning the X_{SiO2aq} are satisfied in the compositional conditions of aqueous solution given in this text.

Therefore, the aqueous solution chemistry in the initial condition at the top of the convection cell must be thought here. When the sea water buffered in the ocean bottom

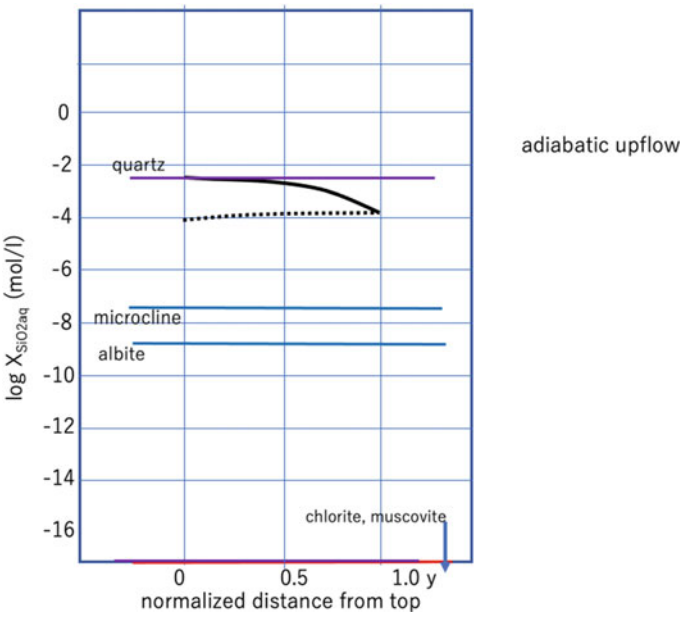

Fig. 3.19 Equilibrium diagram of temperature and concentration of $SiO_{2aq.}$ in the aqueous solution of up-flow in the convection cell and precipitation conditions of from permeable solution. Dotted line shows the down-flow

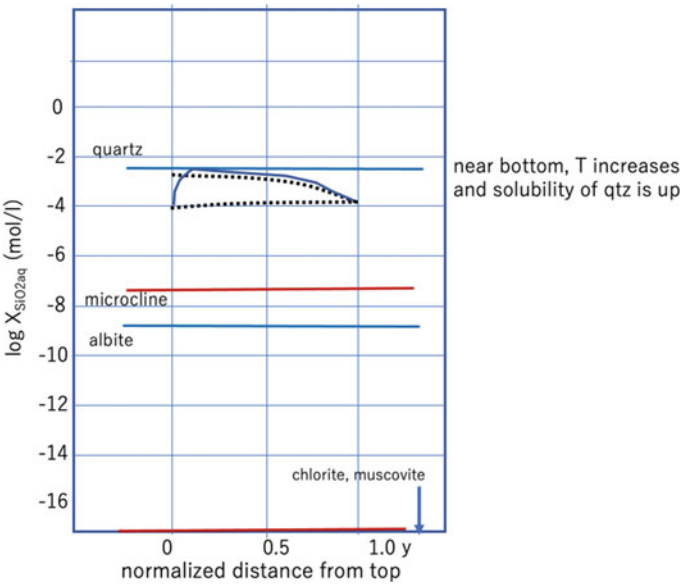

Fig. 3.20 Equilibrium diagram of temperature and concentration of SiO_{2aq} showing the possible concentration (full line) of the up-flow aqueous solution

near the subduction zone entrains into the permeable convection of down-flow region, the Mg^{2+} content surely decreases with increasing the depth because of precipitation of chlorite. On the other hand, quartz in the sandstone and SiO_2 component in basaltic glass should continuously dissolve, for the sea water chemistry keeps undersaturated in the down-flow still in the deeper part because of positive curve of solubility product against temperature of quartz as shown in Fig. 3.21.

In addition, the diagram of the distance and the SiO_{2aq} content in permeable flow of aqueous solution potentially displays the dissolution and/or precipitation of minerals present parenthesis according to the down-flow and up-flow regime. It is seen that dissolution of quartz and precipitation of chlorite should be satisfied in the down-flow but in the up-flow precipitation of albite, quartz, and serpentine may occur together with muscovite because of high log X_{SiO2aq} through the upwelling of the permeable solution in Fig. 3.21.

Furthermore, as discussed previously, it is shown that the up-flow region should appear the high Vp and low Vp/Vs because of low volume ratio of aqueous solution, but in the down-flow region the low Vp and high Vp/Vs ratio judging from the contrasting volume ratio of aqueous solution in down-flow regions. The characteristic features of these Vp and Vs and Vp/Vs ratio in the plate boundary zone will be discussed in the later section.

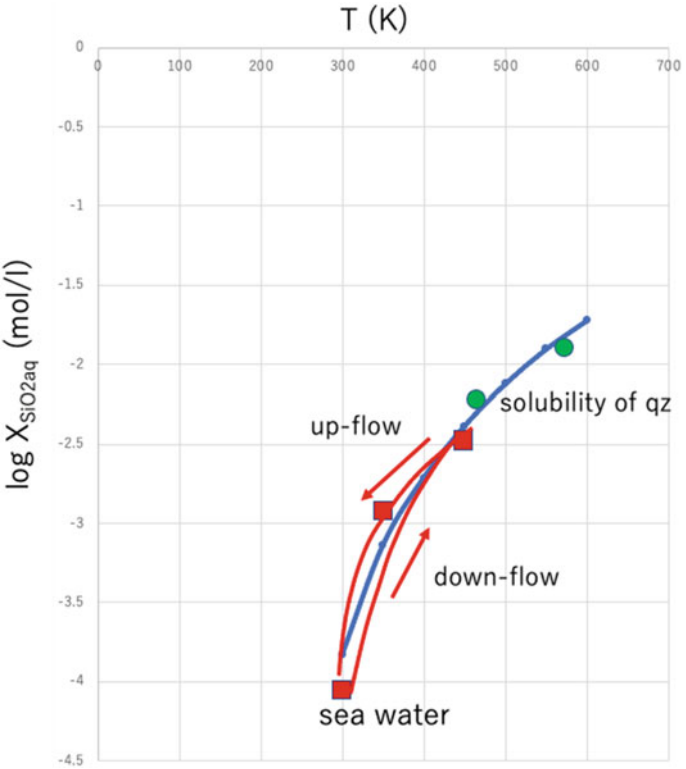

Fig. 3.21 Possible trends of the SiO_{2aq} concentration in up- and down-flow aqueous solution showing the data (green dots) of hydrothermal experiments (Shikazono 2003) in the diagram of temperature and X_{SiO2aq}

3.5 Periodicity of Fluid Composition and Mechanical Coupling of the Subduction Zone

In the previous sections, it is shown that there should be developed the permeable convection in the narrow zone of the accretionary wedge just over the subduction boundary because that zone consists of fractured and aqueous fluid rich rocks. This type of permeable convection in high permeability zone is characterized by the up-flow and down-flow regime of aqueous solution with water–rock interaction dynamics, and thus chemical composition of the pore and void of the open crack and shear crack jog changes during their permeable flow. The solution chemistry of the permeable convection seems to be buffered nearly by sea water of the ocean bottom in the top of the convection cell at the subduction axis, and at the bottom of the convection cell, it is modified by the aqueous fluid dehydrated from subducted oceanic crust and mantle materials.

Therefore, it is natural to be inferred that the water–rock interaction in the zone of the accretionary wedge may be classified into two types: One is the dissolution and precipitation in region of the up-flow, and another is of the down-flow. The rocks of the up-flow region must be suffered from water–rock reaction in the decreasing temperature and pressure condition, although those in the down-flow region done in the increasing condition of them. For equilibrium saturation product of common rock forming minerals in low temperature metamorphic rocks such as quartz, albite, chlorite, and muscovite depends on temperature and pressure and ionic species in aqueous solution, the progressive dissolution and/or precipitation of such minerals should pass the different way between these regions. Furthermore, it is quite important that such different mode of reaction progress of the rocks and aqueous solution brings the periodic change in the porosity of open crack and shear crack jog filled with fluid, and that the mechanical and elastic properties of these rocks become contrasting between the up-flow and down-flow regions.

As shown in Fig. 3.17, considering that the temperature of the up-flow and the down-flow itself changes rapidly near the top and bottom regions, respectively, the more realistic pattern of progressive change of the log X_{SiO2aq} should appear likely to those in this figure. Moreover, it seems possible that X_{SiO2aq} becomes over the equilibrium saturation of quartz in the upper portion of the up-flow region, but it keeps undersaturation on quartz. Therefore, it concludes that the porosity of the down-flow area and lower part of the up-flow area should be high because of dissolution of quartz but that of the up-flow area be low because of its precipitation in the upper parts.

As seen in the previous chapter, the fracture strength and the frictional strength of shear fault (shear crack) decrease with increasing volume content of aqueous fluid which occupies the shear crack jog and open crack. Therefore, the strength of the mechanical coupling between the subducting slab and overriding accretionary wedge should become weakened in the area of the down-flow, but on the contrary, the mechanical coupling strengthens in the area of the up-flow in the fractured zone above the subduction plate boundary.

Well, it should be very important that the repeating strong mechanical coupling and weak coupling regions appear periodically along the subduction zone according to the size of convection cell mentioned in the previous section. The size of the convection cell is inferred to be about 50 km in the case of its length with 100 km, and so the strong coupling area should be arranged by the distance of 50 km along the accretion wedge. It is probably considered that the strong coupling zone corresponds to the so-called asperity which is primarily defined as the large seismic moment release zone of the large earthquake by Aki and Richards (1980). Later, sporadic occurrence of the large asperity zones has been found along the northeastern Japan Trench by Yamanaka and Kikuchi (2004). The average distance between the asperity zones reaches about 30–50 km and between them the weak coupling zone can be found. Recently, the weak coupling region is characterized by the high b-value that is defined as the slope in Gutenberg–Richter law, suggesting that there are abundant active small shear cracks emitting the small earthquakes rather than in the strong coupling zone.

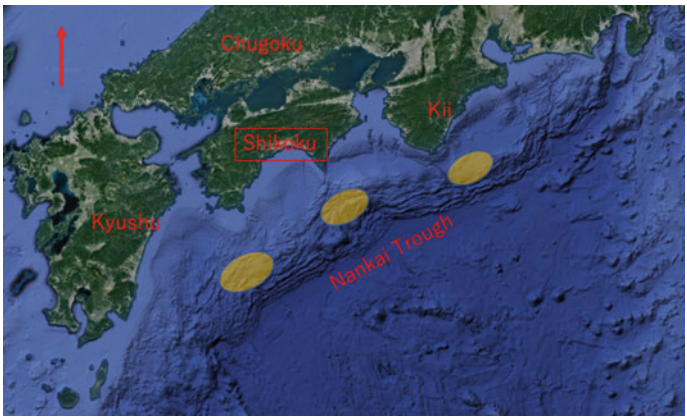

Fig. 3.22 Distribution of the deep seismic reflectors (DSR) along the Nankai Trough by Park et al. (2002)

On the other hand, along the Nankai Trough, the high seismic reflection zones called as the deep seismic reflector (DSR) are found by means of multichannel seismic survey and those occur periodically with distance of about 50–100 km along the trench axis (Park et al. 2002). These DSRs of the off-Shikoku and Kii Peninsula of SW Japan are separated from the asperity area of the Nankai and Tonankai plate boundary earthquakes as shown in Fig. 3.22, showing that the strong mechanical coupling area between subducting slab and overriding island arc crust is also separated from the DSR area. Moreover, recent detailed investigation by the network GPS clarified the slow slip event (SSE, called as quiet earthquake) near the DSR between Shikoku and Kyushu in SW Japan.

On the other hand, Obara (2002) has found the dense zone of nonvolcanic tremors in the north of the DSR and SSE of the Shikoku to Kii and Hamamatsu of the SW Japan which occur at the depth of about 30–40 km near the front of wedge mantle under SW Japan. Considering that these tremors appear the continuous excitation of small shear cracks on many slip planes incorporated by aqueous fluid flow, it seems that the weak mechanical coupling of the plate boundary zone is partly responsible for the fluid flow from these zones together with fluid flow from the bottom of the ocean.

It is also found that in the Cascadia of Canada and North Island of New Zealand, there are sporadic DSR and SSE areas along the subduction zone and these are associated with NVT activity within the areas. In addition, the Cascadia subduction boundary zone shows the sharp relationship between the long-term geodetic displacement and the NVT active period such that the sudden change of geodetic displacement is coeval with the short-term high frequency of NVT, thereby suggesting that the geodetic displacement which occurs periodically of every year is derived from dewatering of plate boundary zone and it enhances rapidly the activity of NVT. The author of this book also suggested that the interseismic activity of small to microearthquakes

between the slow slip events (SSEs) even along the Nankai Trough, but its periodicity varies from sub-annual to tri-annual one (Toriumi 2021).

In the previous book, the author proposed a geochemical mechanics model of seismic process in the plate boundary zone that the periodic slow slip event along the plate boundary itself is derived from the accumulation of aqueous fluid along the very plate boundary by the collapse of open crack and shear crack jog in the zone above the boundary. Therefore, the continuous increase of the mechanical coupling at the plate boundary such as that the maximum stress orientation operates the closure of open cracks. By this accumulation of fluid along on the plate boundary, the weakened boundary coupling may cause the transition from mechanical coupling state to uncoupling one and becomes unstable sliding to liberate the stress in the surrounding rocks.

After the slow slip event, the mechanical coupling changes to weaken and emission of aqueous fluid toward the fractured zone above the plate boundary again. Furthermore, there come abundant open crack and shear crack jog filled with aqueous fluid. It seems that the time scale of the above intermittent slow slip at the plate boundary is controlled by the recovery rate which depends on the precipitation rate of minerals at the boundary.

By the way, it is known that the time scale of the repeating slow slip event and the seismicity rate of small earthquakes appears about 0.5–3 years and at most 7 years as summarized by Schwartz and Rokosky (2006). On the other hand, the precipitation of quartz and albite in the open cracks of the Shimanto accretionary rocks was inferred to be about 1–100 years in the same situation of environmental conditions as shown in later chapters, thereby suggesting the consistency with the repeating time of the SSE and seismic activity.

The slow slip event is obviously an important basic process for weakening the mechanical coupling between the accretionary wedge and subducting slab, and also the large to giant plate boundary earthquakes make that boundary to weaken and emit the aqueous fluid. Besides, the recovery process of the softened plate boundary should be strongly controlled by crack sealing due to mineral precipitation as like as the case of slow slip event. What is the difference in time scale between the giant plate boundary earthquake and slow slip event? It is natural to be considered that the slow slip event occurs in the mechanical weak coupled zone having high porosity, but large and giant earthquake does in the mechanically strong coupled zone of low porosity. Therefore, it may be inferred that the precipitation time scale in the low porosity zone is longer than that in the high porosity zone, for the supply rate of source aqueous species of sealing minerals in the fluid flux depends on permeability of the rocks around the plate boundary.

Next, let us compare the mineral assemblages of precipitation and dissolution between the up-flow and down-flow regions in the fractured zone above the plate boundary. The equilibrium saturation diagram of temperature ranging from 300 to 450 °C and concentration of SiO_2 species in aqueous solution is already displayed in the previous section. This temperature range chosen parenthesis is from the model convection system of fractured zone along the subducting plate ranges from the bottom of the ocean to the 30 km depth under the accretionary wedge as discussed

earlier. In this section, modified phase diagram of solution equilibria with some kinds of minerals is required because of inference of the stable mineral assemblage concerning precipitation and dissolution. Before preceding discussion about possible mineral assemblages, let us summary the mineral assemblages in the plate boundary rocks exhumed from the rather deep accretionary wedge along on the subducting slab, such as rocks of the Shimanto and Sanbagawa metamorphic belts.

When recrystallization by metamorphism in the deep accretionary wedge will be investigated on basaltic rocks, it is quite important but not concerned at all until now that there are abundant rocks containing less kinds of mineral species manifesting the large number of thermodynamic freedom because these rocks have been suffered from metasomatic reaction with aqueous fluid. In the viewpoint of the petrological investigation, the mineral assemblages manifesting the smaller number of thermodynamic degree of freedom are much required for estimation of the physical equilibration conditions and pressure–temperature paths of rocks. It is because the chemical compositions of solid solution minerals in the less variant mineral assemblages can be applied well to the relationship between temperature and pressure change from various chemical zonings of these minerals as the geothermo-barometer.

However, the less kind of mineral species rocks must be a potential indicator for the water–rock interaction (metasomatic reaction) and change in aqueous solution chemistry derived from dissolution and precipitation of minerals in not only open crack and shear crack jog but also preexisting mineral grains. The author once noticed the replacement microstructure and chemical change of relic augite grains in slightly metamorphosed basaltic rocks in the Sanbagawa metamorphic belt in Kanto Mountains. Moreover, he also gave an attention to the number of mineral species and discussed the reason why the mineral assemblages of chlorite and calcite, chlorite and epidote, and chlorite and albite are dominant in low-grade metamorphosed basalts. At that time, it was suggested that the basaltic rocks change their chemical composition together with water content by precipitation of chlorite, albite, calcite, and epidote after dissolution of basaltic glass, plagioclase, pyroxenes, and olivine through penetrating aqueous fluid. At the same time, augite grains were randomly replaced by minute grains of albite, chlorite, epidote, and aegirine (Toriumi 1975).

Furthermore, it was pointed out that such metasomatic rocks appear sporadic in the same metamorphic grade and in the axial parts of the recumbent fold, albite and chlorite, and chlorite and calcite rocks are dominant but in the wing zones the actinolite–albite–chlorite rocks can be seen. In addition, it was noted that rather large grains (porphyroblastic grains) of albite (so-called albite spot) can be seen in the core region of the recumbent folds, suggesting that the local permeable flow of aqueous fluid might appear associated with plastic deformation of metamorphic rocks.

Similarly, it is noteworthy that the basic schists of the Ille de Groix, Armorican, in western France, contain large amount of albite porphyroblastic grains in the core of sheath fold and intrafolial fold although the common greenschists after eclogitic rocks are dominant in the wing parts of such folds. It seems that the local fluid flow may control the mineral assemblages of the rocks during late-stage metamorphism.

By the way, it should be worth to be described that like basaltic rocks should be changed into different rock type classified by their mineral assemblages in the sense

of metamorphic petrography as mentioned above in the various metamorphic belts formed in the deep to rather deep accretionary wedge of the plate boundary zone. In Shimanto metamorphic belt, which is extended along the Ryukyu trench and the Nankai Trough from Okinawa to Kanto Mountains in SW to central Japan.

There are two rock-type regions in the Shimanto metamorphic belt: One is the chlorite–albite and chlorite–calcite rock type (type A), and another is the pumpellyite–prehnite–epidote–chlorite–albite type (type B), which contains small amounts of actinolite and quartz. As shown in mineral facies diagram Na_2O-Al_20_3-MgO + FeO-CaO of Fig. 3.23, type A locates on the hyper plane of calcite–albite–chlorite, and type B does within the volumes of albite–chlorite–prehnite–pumpellyite and albite–chlorite–epidote–actinolite. Judging from the average composition of common basalts plotted central in the volume of albite–chlorite–epidote–actinolite, the chemical compositions of the former type A are far from the average compositions of common basalts, thereby suggesting the large modification of their bulk chemistry in common basalts by migration of aqueous species of Mg^{2+}, Ca^{2+}, Na^{+}, Al^{3+}, and SiO_{2aq} in the percolating aqueous fluid. In addition, let us look at the average chemical compositions of basaltic rocks in the various localities of Shimanto belt from Kyushu, Shikoku, Kii, and Akaishi Mountains (Suzuki 1988) as shown in Fig. 3.24. It is obvious that there are two groups of chemical composition concerning the contents of $CaCO_3$ and Fe_2O_3: One is that rich in them, and another poor in them. The former occurs in the Shikoku and Akaishi mountains, but the latter does in the Kyushu and Kii. On the other hand, as FeO and MgO contents in the average rocks of them are not different between two groups above, suggesting that the abnormal concentration of $CaCO_3$ and Fe_2O_3 is not responsible for the decomposition of clinopyroxene and anorthite-rich plagioclase into calcite but for their addition by calcite and hematite, and Fe^{3+} containing epidote precipitation. This fact seems surely consistent with the sporadic occurrence of chlorite–albite–calcite assemblage having rather large freedom of mineral facies mentioned previously.

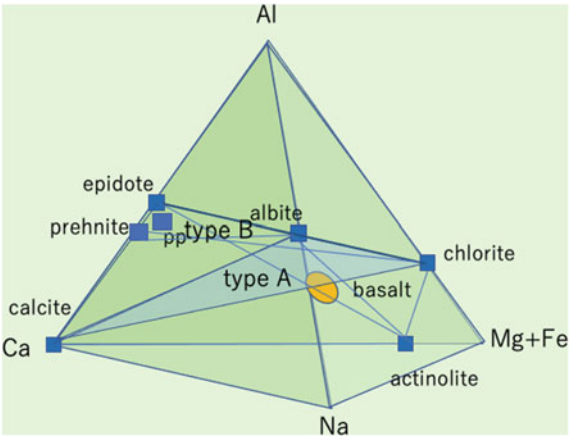

Fig. 3.23 Tetrahedral diagram showing the mineral assemblages in the up-flow and down-flow metasomatic rocks from common basaltic rocks. Type A consists of chlorite, albite, actinolite, and calcite, and type B does of epidote (or prehnite), chlorite, albite, and calcite

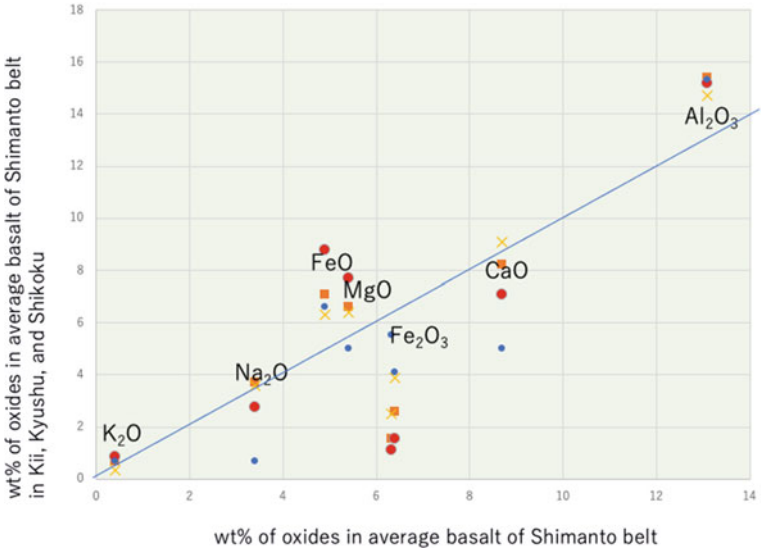

Fig. 3.24 Diagram of chemical compositions in metasomatic basalts from Kyushu, Sikoku, and Kii of the Shimanto accretionary rocks showing the change from average basalt of the Shimanto basaltic rocks

It is also found in the rather small-scale metamorphic area of Tanzawa Mountains that the low-grade metamorphic area can be classified into the zeolite facies and prehnite–pumpellyite facies zones below the greenschist and amphibolite facies zones, and the mineral assemblages of chlorite and albite with epidote in the western part of the prehnite–pumpellyite zone are dominant with about 60% of metabasaltic rocks though those percentage is at most 30–40% of metabasaltic rocks in the eastern part. Those rocks manifest large thermodynamic freedom from small number of mineral species and appear the allowance of various chemical compositions of aqueous solution producing that mineral assemblage (Toriumi and Arai 1989).

Here, the thermodynamic freedom of the relevant mineral assemblages in the metamorphic and metasomatic rocks including sealed open crack and shear crack jog is to be required for interpretation. Based on chemical thermodynamics, phase rule of the thermodynamic system consisting of c components and p phases in which phases means mineral species and fluid or gas phase in the rocks in equilibrium at given temperature and pressure holds.

$$f = c - p + 2 \tag{3.37}$$

in which f is the number of freedoms of the system. If $p = c + 2$, then f becomes zero, that is called as invariant system, and if $p = c + 1$, then f becomes unity and called as univariant system. At these cases, it is important that if the system

is invariant, but the fluid phase and mineral phases contain genuine nature of variable compositions such as aqueous solution dissolved various species of ionic and neutral components and solid solution such as (Na, K) $AlSi_3O_8$ of alkali feldspar, the chemical compositions of them must be uniquely constant together with given temperature and pressure. Furthermore, if the system is univariant, the chemical composition of aqueous fluid is strongly dependent on the temperature at constant pressure and chemical compositions of minerals.

On the other hand, if p is less than c at the given temperature and pressure (isothermal and isobaric condition), the system is called as multivariant system and aqueous solution is possible to have various chemical compositions in equilibrium with small number of mineral assemblages such as chlorite–albite–calcite. In the composition, mineral assemblage diagram as shown in Fig. 3.23, the relationship between the chemical composition and the equilibrium mineral assemblages is displayed clearly at the given pressure and temperature condition. The tetrahedral diagram of Na-Al-(Mg + Fe)-Ca appears the critical assemblage of calcite–albite–chlorite with quartz separating the Al-rich from the Mg-rich domain and the common basaltic compositions exhibit in the latter domain, suggesting distinctively the calcite and albite excess precipitation derived from water–rock interaction. Accordingly, the sporadic appearance of dominant calcite and albite rocks in the metamorphic–metasomatic region of the deep subduction boundary manifests the inhomogeneous aqueous fluid flow in the region such as permeable convection and fracture-associated flow.

As being predicted above, the calcite–albite and calcite–chlorite rocks occur commonly in the fractured rocks as sealed open crack and shear crack with jog. Those are likely to metamorphic bands parallel and subparallel to the foliation plane of the deformed schists, but there is common appearance of brecciated rocks with abundant open cracks sealed by calcite, albite, and chlorite in the Shimanto and Sanbagawa metamorphic belts as shown in Fig. 3.25 (photos of calcite sealing breccia). Yamaguchi et al. (2011) reported that ankerite $(Ca,Fe)CO_3$ grains precipitate along on the large fault plane with partly pseudo-tachylite and associated open cracks are sealed by calcite in the Shimanto belt, thereby suggesting the active aqueous fluid along the fractured zone accompanied with large high-speed faults.

Considering the phase diagram of $\log X_{Ca2+}$ vs temperature as seen in Fig. 3.26, the calcite saturation curve appears negative slope against the temperature. Therefore, it is obvious that the calcite mineral is stable in the high temperature region at the same content of Ca^{2+} in aqueous solution. In the permeable convection of the aqueous fluid in the fractured plate boundary zone, the down-flow region seems to be the zone of dissolution of calcite but the up-flow one to be of precipitation zone of calcite.

Next, it will be discussed in detail what the dominant rock type appears in the up-flow and down-flow regions of the permeable convection system in the fractured zone of the plate boundary based on the phase diagram of ln X_{SiO2} and temperature as shown in Fig. 3.16. In this diagram, the solubility curves of all minerals are well approximated as linear relation because of small range of temperature from 300 to 450 K. The temperature profiles of the down-flow and up-flow are likely to be composed of nearly isothermal path and rapid change near the top and bottom of the convection cell as shown in Fig. 3.17. On the one hand, it is probably assumed that the

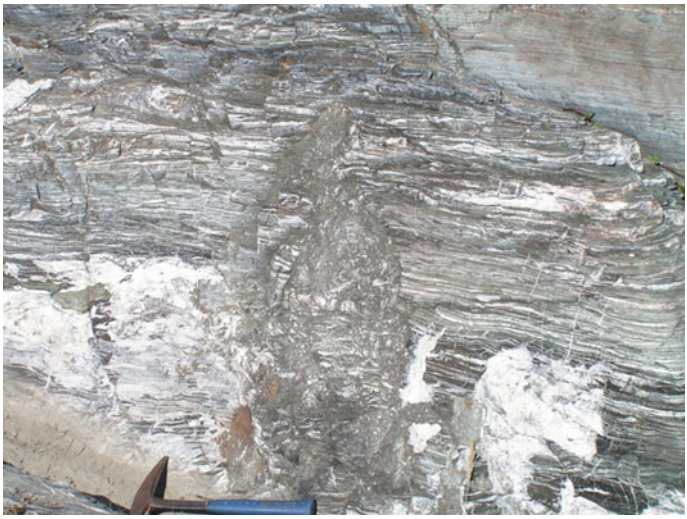

Fig. 3.25 Photographs showing the highly brecciated metamorphic rocks and matrix calcite of the pelitic schists of the Kanto Mountains in the Sanbagawa metamorphic belt

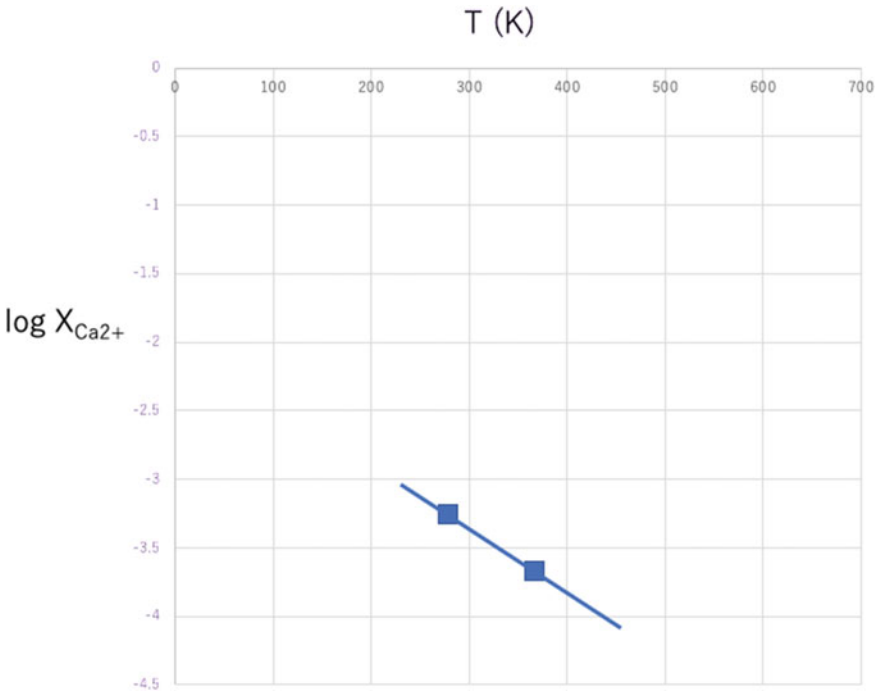

Fig. 3.26 Equilibrium diagram of calcite in the log X_{Ca2+}—temperature of the aqueous solution in the convection system

starting chemistry of down-flow is nearly buffered by sea water as discussed earlier and then it should change according to the dissolution of quartz of the fractured rocks. On the other hand, the starting chemistry of the up-flow must be inherited by the down-flow at the bottom, and then it is probably controlled by the dissolution of relic quartz and after reaching near the top of the up-flow it changes from the dissolution to the precipitation of quartz by its oversaturation derived from decrease in temperature as displayed in Fig. 3.21.

Therefore, it seems to be concluded that the dissolution of quartz of the surrounding fractured rocks should controls the content of the aqueous SiO_2 component in solution and precipitation of the chlorite and muscovite continuously occurs along with the down-flow region. This may result in the continuous increase in porosity of the fractured rocks due to distinctive dissolution of quartz but small amounts of precipitation of chlorite and muscovite. In addition, it is also concluded that in the up-flow region the porosity should increase with decreasing depth but near the top it changes decreasing because of precipitation of quartz. In this up-flow region, the precipitation of albite and muscovite appears instead of chlorite and muscovite as seen in Fig. 3.27.

On the other hand, calcite may be dissolved in the down-flow region, but in the up-flow region, it seems to be precipitated because of oversaturation by high temperature conditions relative to the down-flow temperature. Accordingly, the contrasting mineral assemblages of the permeable convection system of the fractured plate boundary zone are characterized by chlorite–muscovite in the down-flow region and by albite–calcite–muscovite in the up-flow region. The porosity of both regions may continuously increase excluding the top of the up-flow region, for the rate of

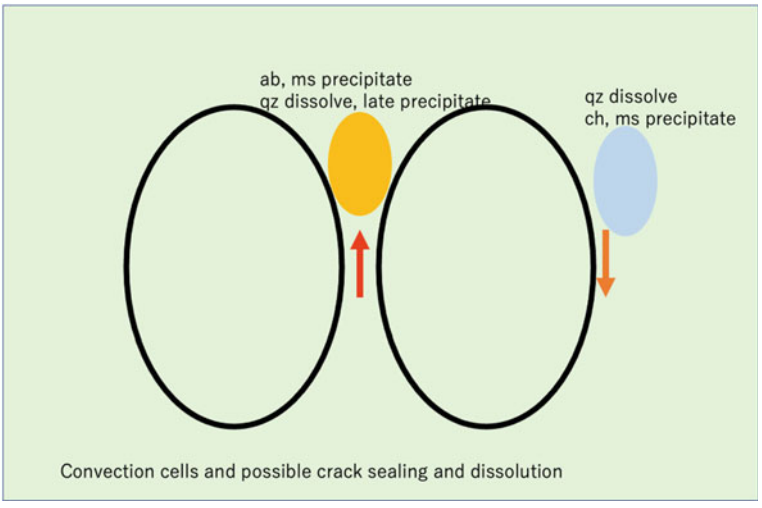

Fig. 3.27 Possible model of mineral precipitation and dissolution showing quartz, muscovite, and albite precipitation at the top of up-flow, and quartz dissolution and chlorite precipitation in the down-flow

precipitation of chlorite and calcite with albite may be less than that of dissolution of quartz. If the rate of this precipitation rate is faster than that of dissolution of quartz, the mechanical coupling changes strong between the accretionary wedge and subducting slab, and thus, it results in the stress accumulation along the plate boundary. This case will be discussed in the later chapter.

References

Aki K, Richards PG (1980) Quantitative seismology: theory and methods, W.H. Freeman, San Francisco, California, p 948

Hacker BR, Peacock SM, Abers GA, Holloway SD (2003) Subduction factory-2. Are intermediate—depth earthquakes in subducting slabs linked to metamorphic dehydration reactions? J Geophys Res 108(B1). 10. 1029/2001JB00129

Hasegawa A, Nakajima J (2017) Seismic imaging of slab metamorphism and genesis of intermediate depth intraslab earthquakes. Prog Earth Planet Sci 4:12. https://doi.org/10.1186/s40645-017-0126-9

Holland TJB, Powell R (1998) An internally consistent thermodynamic data set for phases of petrological interest. J Metamorphic Geol 16:309–343

Hyndman RD, Yamano M, Oleskevich DA (1997) The seismogenic zone of subduction thrust faults. Island Arc 6:244–260

Inui M, Toriumi M (2004) A theoretical study on the formation of growth zoning in garnet consuming chlorite. J Petrol 45:1369–1392

Ishido T, Mizutani H (1981) Experimental and theoretical basis of electrokinetic phenomena in rock-water systems and its applications to geophysics. J Geophys Res 86:1763–1775

Jaeger JC (1964) Elasticity, fracture and flow with engineering and geological applications, Methuen

Kasahara J, Toriumi M, Kawamura K (2003) The role of water in earthquak generation. University Press of Univ, Tokyo

Kitamura Y, Sato K, Ikesawa S, Ikehara-Ohmori K, Kimura G, Kondo H, Ujiie K, Onishi CT, Kawabata K, Hashimoto H, Mukoyoshi H, Masago H (2005) Me´lange and its seismogenic roof de´collement: a plate boundary fault rock in the subduction zone—an example from the Shimanto Belt, Japan, Tectonics, vol 24, TC5012. https://doi.org/10.1029/2004TC001635

Landau LD, Lifshiz EM (1987) Fluid mechanics. Pergamon Press

Moore JC, Vrolijk P (1992) Fluids in accretionary prisms. Rev Geophys 30(2):113–135

Murphy HD (1979) Convective instabilities in vertical fractures and faults. J Geophys Res 84:6120–6130

Nakanishi A, Kodaira S, Park J-P, Kandea Y (2002) Deformable backstop as seaward end of coseismic slip in the Nankai Trough seismogenic zone. Earth Planet Sci Letts 203:255–263

Obara K (2002) Nonvolcanic deep tremor associated with subduction in southwest Japan. Science 296:1679–1681

Okamoto A, Toriumi M (2001) P-T paths of amphiboles by Gibbs method. Contrib Mineral Petrol 141:168–181

Omori S, Kamiya S, Maruyama S, Dapeng Z (2002) Morphology of the intraslab seismic zone and devolatilization phase equilibria of the subducting slab peridotite. Bull Earthquake Res Inst Univ Tokyo 76:455–478

Park J-P, Tsuru T, Nakanishi N, Hori T, Kaneda S, Nakanishi A, Miura S, Kaneda Y (2002) A deep strong reflector of the Nankai accretionary wedge from multichannel seismic data: Implications for underplating and interseismic shear stress release. J Geophys Res 107(ESE3-1):3–16

Schwartz S, Rokosky JM (2006) Slow slip events and seismic tremor at circum—Pacific subduction zones, Rev Geophys 45:RG3004. https://doi.org/10.1029/2006rg000208

Shikazono N (2003) Geochemical and tectonic evolution of arc-backarc hydrothermal systems. Elsevier

Suzuki T (1988) Geochemistry of metabasalts in the Shimanto belt. Mod Geol 12:225–241

Takei Y (2002) Effect of pore geometry on V_P/VS: from equilibrium geometry to crack. J Geophys Res 107(B2):2043. https://doi.org/10.1029/2001JB000522

Toriumi M (1975) Petrological study of the sanbagawa metamorphic rocks—The Kanto Mountains, Central Japan, Univ. Museum, Univ. Tokyo Bull., 9, p 99

Toriumi M (2021) Global Seismicity Dynamics and Data-Driven Science. Springer

Toriumi M, Teruya J (1988) Tectono-metamorphism of the Shimanto belt. Mod Geol 12:303–324

Toriumi M, Arai T (1989) Metamorphism of the Izu-Tanzawa collision zone. Tectonophysics 160(1–4):293–303

Tsuru T, Park J-P, Miura S, Kodaira S, Kido Y, Hayashi T (2002) Along-arc structural variation of the plate boundary at the Japan Trench margin: implication of interpolate coupling. J Geophys Res 107:B12

Yamaguchi A, Cox SF, Kimura G, Okamoto S (2011) Dynamic changes in fluid redox state associated with episodic fault rupture alojg a megasplay fault in a subduction zone, Earth Planet. Sci Lett 302:369–377. https://doi.org/10.1016/j.epsl.2010.12.029

Yamanaka Y, Kikuchi M (2004) Asperity map along the subduction zone in northeastern Japan inferred from regional seismic data. J Geophys Res 109:B07307. https://doi.org/10.1029/2003JB002683

Zhao C, Hobbs BE, Ord A, Peng S, Muhlhaus HB, Liu L (2004) Theoretical investigation of convective instability in inclined and fluid-saturated three-dimensional fault zones. Tectonophysics 387:47–64. https://doi.org/10.1016/j.tecto.2004.06.007

Chapter 4
Rapid Process of Massive Extrusion of Plate Boundary Rocks

Abstract It has been considered that many geological processes having large special scales in the plate boundary zone are long-term phenomena during several to several hundred million years. However, recent development of earth sciences suggests existence of rapid and extremely rapid phenomena within the large-scale orogenic process. The giant earthquakes and large-scale slow slip events show the slip velocity from km/s to 0.01 m/s, and a part of high-grade metamorphic rocks shows the extremely rapid extrusion maintaining the dendritic grains of minerals after peak metamorphism.

Keywords Rapid extrusion of metamorphic rocks · Time scale of geological process · Metamorphic banding · Porosity wave · Metasomatic instability

4.1 Rapid Process of the Subduction Boundary Zone

The geological processes had been thought to be the very slow and long-term phenomena likely to now-ongoing uprising and erosion of mountains and down sinking of large-scale basin. Typical uplift rate of mountain building in the orogenic belts has been at most about several millimeter per year in the Himalayan region although this rate implies only the average value during the several ten million years. It remains yet that there are many unknown mechanisms and that whether there are very rapid processes like high-speed fault movement such as giant earthquakes or not in the orogenic process. Typical rapid phenomenon is probably a volcanic eruption and giant earthquake along the plate boundary region, and the volume of these phenomena extends over 10^6 km^3 during the period from 10 to 10^3 s. Such huge amount of mass movement speeds manifests also the vast amount of massive moment release derived from the earth's gravitational potential. On the other hand, it is still unclear that how many rates of process the geological processes occurred in the complicated orogenic process. In order to infer the rate of the process, it is required that the time scale of the physical process should be estimated quantitatively in the natural geological processes. In this section, the author intends to propose several methods for estimating the time scale of the physical processes, based on the materials sciences and data-driven science.

M. Toriumi, *Geochemical Mechanics and Deep Neural Network Modeling*,
Advances in Geological Science, https://doi.org/10.1007/978-981-19-3659-3_4

The active earth's process is mainly represented by the accretionary and successive deformation processes in the plate boundary zone accompanied with plate subduction toward the deep mantle. In this region, the most rapid deformation process is clearly the giant earthquakes at the plate boundary: in the case of 2011 Tohoku-Oki giant earthquake, the hanging wall crust of the NE Japanese island moved massively eastward about 70 m at the trench axis and the size of the moving mass reaches about 500 km length and 300 km width of 10–20 km thickness during the period of 10 min. As a result, the giant tsunami occurred and attacked widely the coast area of NE Japan.

The geological process in the plate boundary zone represents the exhumation of the huge mass of deep-seated metamorphic rocks which is derived from gravitational negative buoyant force by subducted crustal materials coupled with subducting slab. This exhumation process is apparently likely to the uplift by the giant earthquake but the total amount of uplift of the metamorphic mass reaches about 50–200 km, being much larger than that of even several to several ten events of giant earthquakes. On the other hand, it is commonly found that the deep-seated rock masses appear in the middle of the accretionary prism along on the large faults near the subduction plate boundary. In the northern California region, the Franciscan metamorphic rocks widely occur above the lower-grade metamorphic rocks of Franciscan Group and under the Great Valley Fault. In the case of Sanbagawa metamorphic belt, the metamorphic masses occurred being sandwiched by upper thick sedimentary piles and lower accretionary Shimanto rocks with the largely extended low angle faults. In almost always giant metamorphic belts in the world, the common tectonic features mentioned above appear as noted in the paper of Maruyama et al. (2004). According to the structural similarity of the boundary faults along the deep-seated metamorphic masses and the ongoing spray fault associated with subduction plate boundary, it seems to be considered that some events of the boundary fault movement should took place at the very high slip velocity likely to the seismogenic faults. It is sure that recent studies of the fault zone rock in the old accretionary prism such as Shimanto belt clarified the occurrence of pseudotachylite which contains abundant glass and quench crystals of some variety of rock-forming minerals derived by shear melting of surrounding rocks. Accordingly, the author intends to show the evidence of short-term annealing after formation of microstructure of mineral association in the metamorphic and metasomatic rocks in the old accretionary wedge materials.

4.2 Time Scales of Spherical Shape Transformation and Waveform Grain Boundary During Growth

In the year of 2009, it was surprisingly evident that the dendritic grains of feldspar and biotite together with glass are found in the fine-grained and nano-granite inclusions in metamorphic garnet grains from the granulite rocks of the central India by Caesar et al. (2009), and later, Hiroi et al. (2014) reported in detail the dendritic crystals

and glass of felsite inclusions in garnet from the granulite rocks of central Sri Lanka. The garnet granulite containing nano-granite or felsite inclusion involving quench crystals and glass occur in the central zones of the granulite terrane which is derived from deep lower crust and upper mantle and constitutes the wide and huge orogenic terranes in the stable continents.

These dendritic textures showing quench of the melt inclusions in garnet porphyroblasts have been evident that the granitic hydrous melt phase in equilibrium with garnet and other granulitic assemblages, and furthermore, the extremely rapid growth of feldspar, quartz, and biotite had occurred at the time of dehydration of melt derived from fracture of host garnet grain (Cesare et al. 2009). On the other hand, it should be noteworthy that to remain the quench crystals in inclusions must be required too for the rapid cooling after quenching as noted by Hiroi et al. (2014).

It is a great problem that whether the quenching temperature of this type of inclusions in garnet was high or low enough to cessation of later annealing of dendritic grains. In the case of high temperature annealing, the boundary between angular—dendritic albite and quartz should change rapidly rounded outline, but in the very low temperature less than 100 °C, it should keep the angular outline even in the geological time scales. Caesar et al. and Hiroi et al. (2014) have clarified the quenching temperature to be about 500–600 °C, judging from granitic and felsitic mineral assemblages and glass likely to igneous felsite rocks. Therefore, it is imagined that the annealing time of the garnet granulite rocks manifests very short period after the quenching by dehydration crystallization of felsite inclusion as suggested by Hiroi et al. (2014).

By the way, it may be worth to be noted that the annealing times of the metamorphic texture of spherical grains of quartz inclusions in albite porphyroblastic grains have been estimated for the Sanbagawa high pressure metamorphic rocks, and Ryoke and Abukuma high temperature ones by Toriumi (1979). He concluded that the annealing times above increase clearly with increasing metamorphic temperature although it was very strange for the author that there are abundant rocks containing porphyroblastic albite grains having many of very small and spherical grains of quartz inclusions both in basic and pelitic schists of the highest-grade zone in the Sanbagawa belt.

It is very simple system for consideration of annealing process that the single grains of quartz appear abundant in single large grains of pure albite in metamorphic rocks. It is obvious that the quartz grains must be included by albite during grain growth of albite and the temperature of this inclusion process occurred just after the peak temperature of the metamorphism, judging from the evidence that albite grains contain also mineral assemblages formed at the peak temperature. This temperature was to be about 600 °C. It is very difficult to be understood in the geological sense that this means the very fast annealing after formation of albite–quartz inclusion system during metamorphism.

Therefore, let us introduce a physical model of annealing process of spherical shape transformation of inclusion minerals in host minerals as proposed by Toriumi (1979, 1981).

In Fig. 4.1, the annealing of quartz in albite simple system is shown according to Toriumi (1979), indicating that the initial polygonal grains of quartz with various

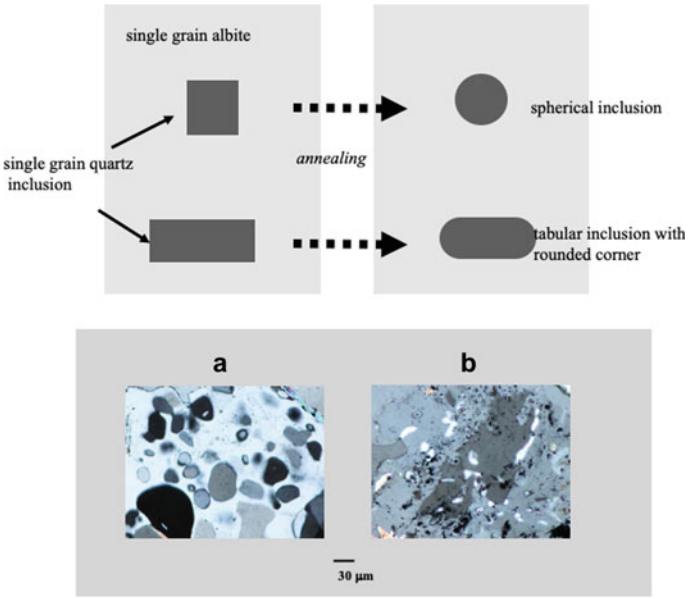

Fig. 4.1 Shape transformation of quartz inclusion in albite and K-feldspar from polyhedral to spherical shapes by annealing process (upper). In bottom figure, the small spherical quartz inclusion and polyhedral inclusion with rounded edges are shown in the albite–biotite zone pelitic schist (**a**) and in the oligoclase–biotite zone pelitic schist (**b**)

size changes to ellipsoidal grains with rounded corner and edge in single crystal of albite. The process of this annealing is governed by the diffusion of slowest oxygen in the volume or along the grain boundary. According to Toriumi (1979), in the low to medium temperature conditions, the grain boundary diffusion of oxygen between albite and quartz is available for the annealing of them. In this case, the controlling equation exhibits as,

$$r^2 \mathrm{d}r/\mathrm{d}t = AD_b/R \tag{4.1}$$

and integrating this equation, it holds,

$$r^3 - r_o^3 = 3AD_b t/R \tag{4.2}$$

$$A = (8/(8-2\pi))\gamma\,\Omega d/kT$$

in which r is the curvature of the corner, r_o is the initial curvature of the polyhedral quartz inclusion, t is the annealing time, and R is the grain size of quartz. In the definition of A term, γ is the interfacial energy between quartz and albite, Ω is the

volume of oxygen vacancy in quartz, d is the thickness of the grain boundary, and k is the Boltzmann's constant.

In the case of plastic deformation of quartz and albite during the annealing, the vacancy flow due to lowering the interfacial energy is also coupled with deformation by diffusion and/or dislocation migration by applied differential stress. This type of shape transformation has been investigated by Toriumi (1987) in the case of syn-metamorphic noncoaxial plastic deformation, and it is controlled by following coupled differential equations (Fig. 4.2),

$$\mathrm{d}L/\mathrm{d}\varepsilon = K\left(1-L^3\right)/\left(1+L^3\right)^{1/2} - (L/2)\ \sin\ 2\theta \tag{4.3}$$

$$\mathrm{d}\theta/\mathrm{d}\varepsilon = (1/2)((1+L^2)/(1-L^2)\ \sin^{-1}2\theta - \tan^{-1}2\theta - \tan 2\theta)/(\tan^{-1}2\theta + \tan 2\theta) \tag{4.4}$$

$$with\ K = 2\gamma\ \Omega d\ D_b/R_o^4\ kT(\mathrm{d}\varepsilon/\mathrm{d}t).$$

in which L is the aspect ratio of quartz inclusion, θ is the angle of ellipsoidal quartz grain against the shear plane, and ε is the shear strain. R_o is the mean grain size of quartz inclusion.

Next, let us move to another candidate of measuring the time scale of geological process which has been developed experimental and theoretical study by the author. In 1977, the author's group (S. Karato, T. Fujii and M. Toriumi) started the experimental investigation of dislocation recovery process of olivine which is major component of the upper mantle in the oxygen fugacity controlled high temperature furnace and issued the recovery rates in the upper mantle condition in order to infer the annealing time scale of the mantle xenolith and massive peridotite during their exhumation. The theory is as follows,

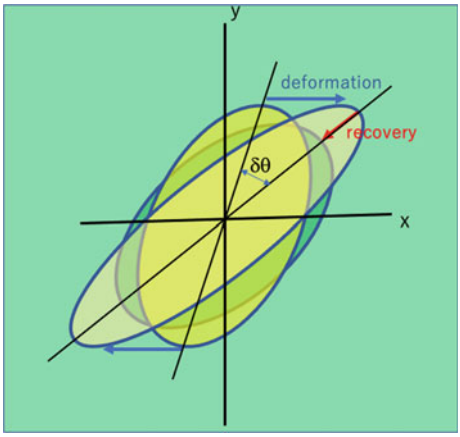

Fig. 4.2 Illustration of noncoaxial deformation and coeval annealing of quartz single inclusion in albite under the shear stress showing the competition between ellipsoidal strain with rotation ($\delta\theta$) and decrease in interfacial energy between inclusion and host

Assuming the dislocation density of initial state to be ρ_o, the rate of annihilation of dislocation pairs becomes,

$$d\rho/dt = -k_d \rho^2 \tag{4.5}$$

integrating the equation, it holds,

$$\rho^{-1} - \rho_0^{-1} = k_d t \tag{4.6}$$

On the other hand, during the annealing process of dislocation annihilation, the grain growth process should take place by reduction of interfacial energy of olivine aggregate. The term of k_d of the annihilation process studied involving the activation term.

The general equation of grain growth becomes (e.g., Karato 2008),

$$d^n - d_o^n = k_r\, t \tag{4.7}$$

in which d is the grain size, d_o is the initial grain size, k_r is the coefficient involving activation term and geometry, and n is the power exponent of the process which is about 2 in most silicates (e.g., Karato 2008).

The stationary state of the relationship between the grain size and dislocation density can be obtained from the steady state relations of them dependent on the applied differential stress as follows,

$$\Delta\sigma = \alpha \mu b\, \rho^{1/2} \tag{4.8}$$

in which μ is the rigidity, b is the length of Burgers vector of dislocation, and α is a constant about 1.

On the other hand, the grain size d is obtained experimentally as a function of the applied differential stress by Karato et al (1980) on olivine as

$$\Delta\sigma = B\, d^{-1} \tag{4.9}$$

In which B is a constant term.

These empirical relations of dislocation density, recrystallized grain size, and differential stress in the steady state deformation and static annealing after deformation bring the time scale of annealing after steady state deformation with active dislocation dynamics and dynamic recrystallization. For the grain growth rate is relatively very slow compared with dislocation annihilation (Toriumi and Karato 1978), the early process of annealing of minerals is certainly governed by the dislocation annihilation, and then, the time scale of the short-term recovery can be estimated from the rate of the annihilation of dislocations. In Fig. 4.3, the successive recovery of dislocation density is displayed in the diagram of grain size versus dislocation density

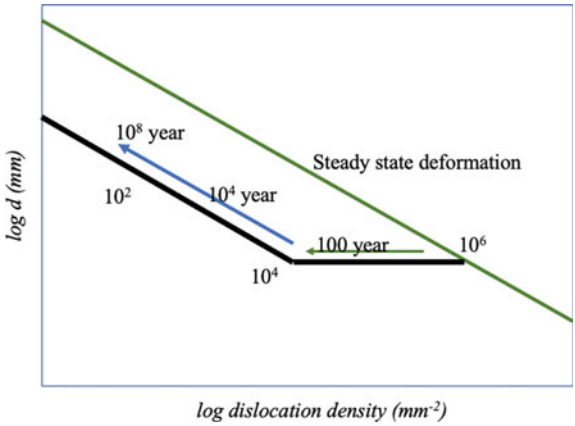

Fig. 4.3 Diagram of dislocation density versus grain size showing the dislocation process during static annealing of polycrystals. Annealing process is composed of dislocation annihilation reducing strain energy and grain growth reducing interfacial energy

together with the relationship between them in the steady state plastic deformation (creep). This diagram is until now possibly applied for olivine aggregates because of experimental data. After some calculations, the relationship between grain size and dislocation density after some extent of annealing of olivine holds,

$$\log d\,(\mathrm{mm}) = -0.5 \log \rho\,(\mathrm{mm}^{-2}) + \text{constant} \tag{4.10}$$

The application of the annealing time by relation of dislocation density and grain size was carried out by Matsumoto and Toriumi (1986) for the magmatic transportation of mantle xenolith in basaltic magma from the upper mantle under SW Japan. The mantle xenoliths are mainly dunite, lherzolite, and harzburgite, and those commonly exhibit a dynamically recrystallized textures showing distinctive high temperature deformation. The dislocation microstructure involving subgrain boundary and dislocation substructure and dynamically recrystallized grains are possibly studied by means of oxidation decoration method and TEM. The data are plotted in the diagram of grain size and dislocation density of various localities in SW Japan, suggesting that there are abundant peridotite xenoliths showing the annealing time within the several ten years.

Next, the time scale of the metasomatic replacement of banding structure of calcite, wollastonite, and garnet in the thermal aureole from basaltic magma intrusion studied by Fukuyama et al. (2006). These mineral bands often display the wavy band boundary formed during the development of metasomatic banding, suggesting that the competitive rate process of boundary advancement and diffusive transportation of constituent components of banding minerals in the grain boundary aqueous solution. This process can be formulated by the Mullins–Sekerka instability which is derived from capillary effect on the growth of minerals from the thin fluid film occupying the grain boundary. In the case of albite and chlorite bands during the metamorphism of the plate boundary rocks, the wavy boundary is also possible to be considered by this MS instability at their metasomatic replacement.

First, the simple system consisting of growing wollastonite band and consuming calcite band is considered in the Hiraodai metasomatic rocks. The waveform boundary between wollastonite and calcite bands is shown in Fig. 4.4, suggesting that the migrating boundary into calcite band becomes unstable resulted from competition between rate of replacement reaction of wollastonite after calcite and diffusion of SiO_2 and CO_2 aqueous components in the intergranular solution. The stability relation between wollastonite and calcite in the metasomatic system could be represented by chemical potentials diagram of SiO_2 and CO_2 (Fig. 4.5).

The chemical potentials of these components are on the equilibrium line with $d\ln X_{SiO_2}/d\ln X_{CO_2} = 1$, because the following chemical equation is satisfied at the equilibrium condition,

$$CaCO_3 + SiO_{2,aq} = CaSiO_3 + CO_{2,aq}$$

In this figure, the chemical composition apart from the boundary should be plotted at the point, W in the wollastonite region and that of the point in the calcite band also plotted at C in the calcite stability region. The chemical composition profile between W and C should not be linear in this diagram but at the boundary equilibrium relation must require $d \ln X_{SiO_2}/d \ln X_{CO_2} = 1$.

Further, let us consider the boundary migration toward the calcite region having V, and then the concentration profiles of CO_2 and SiO_2 change with migration velocity V in terms of diffusion equation with moving boundary as follows,

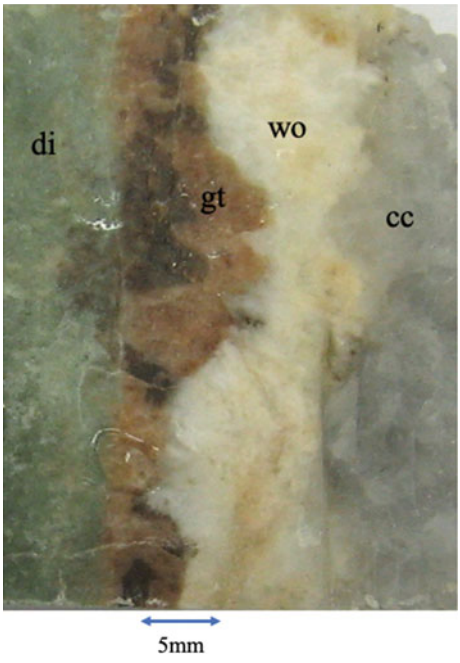

Fig. 4.4 Photograph showing the metasomatic bands between marble (right side) and basaltic dyke rock (left) composed of wollastonite band, garnet band and diopside band (personal communication of Fukuyama). Notice that the boundary of bands displays obviously waveform indicating the growth instability of Mullins–Sekerka type

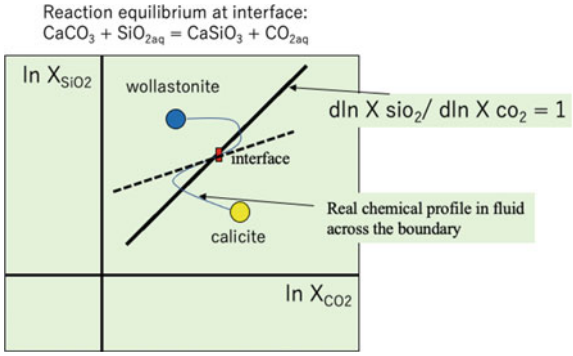

Fig. 4.5 Model of metasomatic instability at calcite and wollastonite boundary in the diagram of logarithmic concentrations of SiO_2 and CO_2 in grain boundary solution. Diffusional condition of their solute components makes decrease in the slope from the equilibrium one between calcite and wollastonite, inducing the instability of the growth interface at the boundary

$$X_i = X_{i,o} \exp(-Vz/D_i) \tag{4.11}$$

and then

$$(\mathrm{d} \ln X_i/\mathrm{d}z)_0 = -V/D_i \tag{4.12}$$

where i is SiO_2 and CO_2 in aqueous phase, D_i is the diffusion constant of i-species in intergranular solution, and z is the distance from the band interface toward the calcite band. Combining X_i with equilibrium relation at the moving boundary, we obtain the following relation,

$$\begin{aligned} \mathrm{d} \ln X\mathrm{sio}_2/\mathrm{d} \ln X\mathrm{co}_2 &= \mathrm{d} \ln X\mathrm{sio}_2/\mathrm{d}z/\mathrm{d} \ln X\mathrm{co}_2/\mathrm{d}z \\ &= (\mathrm{d}X\mathrm{sio}_2/\mathrm{d}z/\mathrm{d}X\mathrm{co}_2/\mathrm{d}z)\,(X\mathrm{co}_2/X\mathrm{sio}_2) \\ &= (X\mathrm{sio}_2,\ o\,V/D\mathrm{sio}_2/X\mathrm{co}_2,\ o\,V/D\mathrm{co}_2)(X\mathrm{co}_2/X\mathrm{sio}_2) \\ &= k\,D\mathrm{co}_2/D\mathrm{sio}_2 \end{aligned} \tag{4.13}$$

In this equation, k is about 1, and ratio of the diffusion constants becomes smaller than 1. Therefore, the above logarithmic concentration ratios take values smaller than the equilibrium one at the band boundary as shown in Fig. 4.5. In this figure, it leads that the calcite stability band near the band boundary becomes stable for wollastonite instead of calcite with increasing V. On the other hand, wollastonite keeps stable in the wollastonite region. In other words, the metasomatic boundary between calcite and wollastonite bands is unstable in the moving boundary condition. The strength of the instability should be proportional to the ratio of diffusion constants of SiO_2 and CO_2 species in intergranular solution.

The instability of the moving boundary must be the rate competing process between boundary migration and capillary effect of the curvilinear boundary in terms of Mullins–Sekerka instability.

The waveform growing interface of polycrystalline aggregate facing with matrix having intergranular solution is very important to infer the growth velocity of metasomatic minerals together with time scale of band formation. Next, the author considers the instability of the growing interface by rate competing of diffusion and growth with capillary effect as Mullins–Sekerka instability (Kurz and Fisher 1985). Here, we will introduce the waveform propagation of the interface as a function of growth velocity citing from Jamtveit and Anderson (1992).

Here, we will use the characteristic wavelength of growth interface as follows.

$$\begin{aligned}\lambda = 1/k &= 2\pi(T_c\gamma D/m\mathrm{Co}V)^{1/2} \\ &= K^{1/2}\,V^{-1/2}\end{aligned} \tag{4.14}$$

where m is the gradient of overstepping of temperature corresponding to the oversaturation from the equilibrium condition of wollastonite in solution, V is the migration velocity of the band, γ is the capillary constant, D is the diffusion constant of soluble component in fluid, and Co is the equilibrium solute concentration.

In this case, the instability proceeds the waveform boundary as,

$$V = K\,\lambda^{-2}, \tag{4.15}$$

and

$$\mathrm{d}z/\mathrm{d}t = V$$

Therefore, we obtain the logarithmic migration velocity

$$\log\ V = \log\ K - 2\ \log\ \lambda \tag{4.16}$$

with $K = K_o \exp(-Q/RT)$.

In this equation, Q is the activation energy of diffusion of aqueous SiO_2, R is the gas constant, and T is temperature. The above equation is clearly scaled by temperature and degree of supersaturation of component ions in grain boundary solution. Therefore, if we can determine the normalized K value, advancing velocity V of the metasomatic bands, and sealing aggregate in the open cracks is possibly inferred from characteristic wavelength of the grain–grain boundary and growth interface.

The relations of growth velocity and parameter K with various wavelength of waveform grain–grain interface are shown in Fig. 4.6. These relations show clearly that the migration velocity of the metasomatic bands can be estimated by measurement of characteristic wavelength of the waveform grain boundary if we obtain

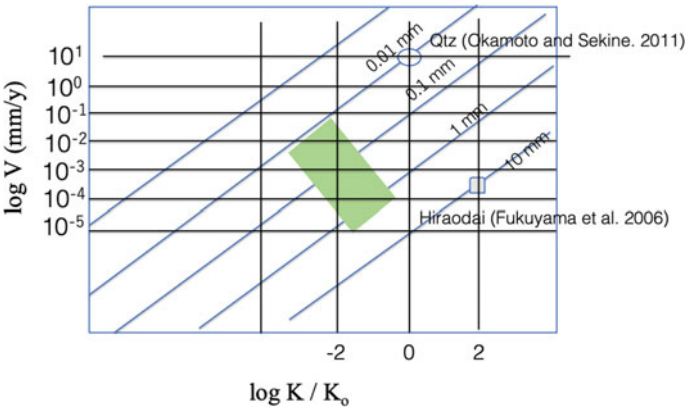

Fig. 4.6 Diagram of the band growth velocity vs wavelength of the boundary derived from Mullins–Sekerka instability using the temperature and cooling time constraints (Fukuyama et al. 2006). The data point of Okamoto and Sekine (2011) is plotted in the diagram for comparison

the activation energy of apparent solute diffusion in grain boundary solution with characteristic wavelength of waveform interface by the metasomatic experiments in hydrothermal system in high temperature conditions.

4.3 Rapid and Extremely Rapid Extrusion of Massive Metamorphic Rocks

The time scale of extrusion process of regional metamorphic rocks can be estimated by shape transformation of quartz inclusion in single grains of metamorphic albite during annealing of the metamorphic rocks. The critical radius defined by spherical quartz inclusion increases is obtained as a function both of temperature and annealing time of the metamorphism. Therefore, in this paper, the author tried to estimate the time scales from the critical radius of spherical quartz inclusions of the Sanbagawa metamorphic rocks, the corner curvatures of quartz grains in nano-granite inclusions of granulite garnet of India, and felsite inclusions of granulite garnet of Sri Lanka; those were about several ten thousand years in the highest-grade rocks of Sanbagawa belt, but were several thousand years and several ten to hundreds years for the Sri Lanka and India granulite rocks, respectively. The available physical model of this extremely rapid metamorphic extrusion should be interpreted by the buoyancy-driven frictional drag extrusion instead of viscous drag extrusion.

Recent studies of very large regional metamorphic belts suggested somewhat strange phenomenon that grains of metamorphic garnet contain abundant nano-granite and felsite inclusions having dendritic textures of quartz, albite and K-feldspar (Cesare et al. 2009; Hiroi et al. 2014). Melt inclusions have been also found in the

same porphyroblastic grains of garnet in the granulites of India and Sri Lanka granulite terrains and of the Variscan orogenic belt, and it shows that these metamorphic rocks had suffered from partial melting of host rocks. It also surely indicates that the metamorphic rocks were partially molten at the high temperature conditions under hydrous environments in the growth stage of garnet (Cesare et al. 2009; Hiroi et al. 2014). Furthermore, the melt inclusions might survive during exhumation but at the instant felsitic melt inclusions should change drastically the aggregate of dendritic quartz and feldspars by decompression of melt inclusions due to cracking of host garnet grains as suggested by Hiroi et al. (2014).

However, it remains somewhat strange that in the exhumation process dendritic grains of quartz and feldspars keep a proper texture as like as a quench crystal. It clearly indicates luck of enough annealing after rapid crystallization of felsite/nano-granite inclusions in garnet, strongly suggesting a rapid cooling of the metamorphic rocks containing garnet grains with felsite inclusions. Cesare et al. (2009) looked at the formation of dendritic grains of nano-granite inclusions and they attributed the texture to the rapid decompression by fracture of garnet grains. On the other hand, Hiroi et al. (2014) suggested that the texture of dendritic quartz and feldspars may indicate a rapid cooling after formation of dendritic nano-granite/felsite inclusions during exhumation of the metamorphic rocks. They noticed that such volcanic rock-like texture is due to the quenching process of the metamorphic rocks (Fig. 4.7).

By the way, the author has proposed the annealing time of metamorphic rocks by means of the characteristic time for shape transformation of the single quartz inclusions in porphyroblastic single grain of albite (Fig. 4.8) and K-feldspar (Toriumi 1979, 1981). He obtained theoretical annealing time required for rounding after polyhedral shape of quartz grain embedded in the single crystal of albite. The mechanism of the shape transformation from the polyhedral to the spherical grain is basically governed by the interfacial diffusion of oxygen between host and inclusion minerals by means

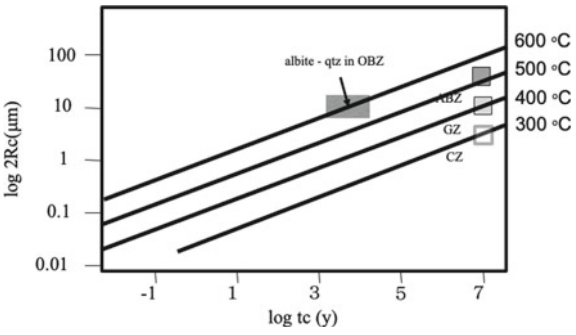

Fig. 4.7 Diagram of annealing time and logarithmic diameter of the spherical transformation process of quartz single inclusion in albite host for various temperature conditions. The data obtained in Toriumi (1979) are shown for schists from various metamorphic zones (different metamorphic temperature) from chlorite zone, garnet zone, albite–biotite zone, and oligoclase–biotite zone of the Sanbagawa plate boundary rocks, indicating the large difference of the annealing time of the oligoclase–biotite zone rocks

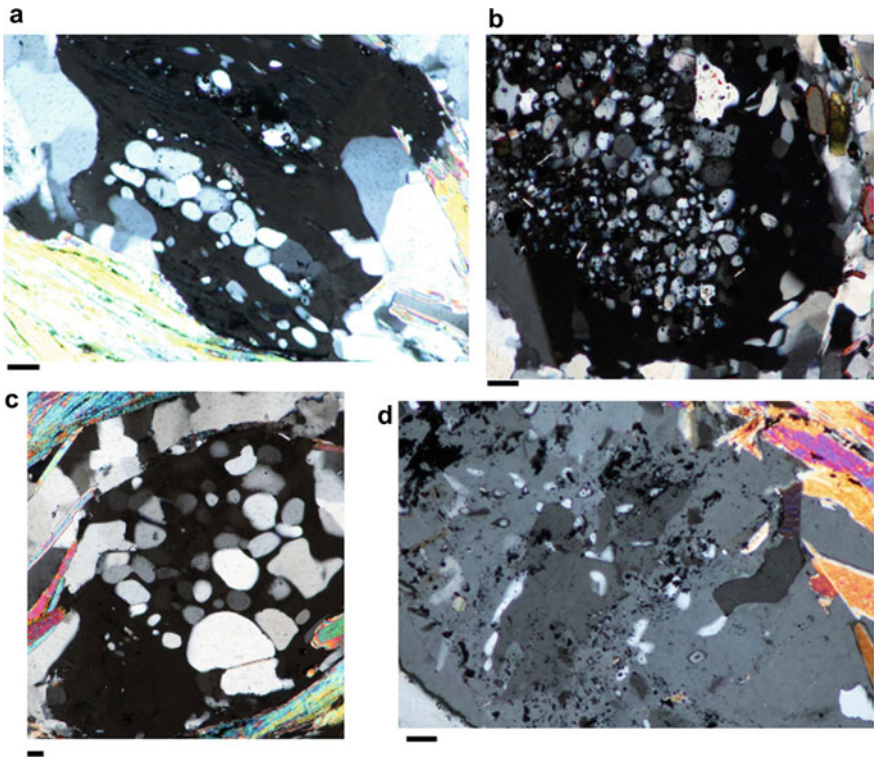

Fig. 4.8 Photographs showing rounded and spherical inclusions of quartz in albite host in the Sanbagawa metamorphic rocks from garnet zone (**a**, **b**), albite–biotite zone (**c**), and oligoclase–biotite zone (**d**)

of interfacial energy reduction as clarified by the author (Toriumi 1979). In the same paper, the author suggested that the estimated annealing times of the highest metamorphic rocks in the Sanbagawa metamorphic belt show somewhat strange values much less than those of surrounding lower-grade rocks. In addition, it may be very strange that the dendritic aggregate inclusions existing in garnet porphyroblasts of the large-scale and high-grade regional metamorphic belts as noted previously. If we apply the shape transformation mechanism for keeping dendritic textures in nanogranite inclusions of metamorphic garnet of high temperature metamorphic rocks, annealing times producing a slightly rounded shape of the corners of dendritic quartz and albite surely suggest an extremely short time far from 1 million years.

In this paper, the author intends to discuss the annealing times of the metamorphic rocks during the retrograde metamorphism using shape transformation mechanism in the inclusion—host bicrystal system and to investigate the mechanism satisfying the short time scale of rapid and extremely rapid exhumation process of the metamorphic mass.

Cesare et al. (2009) and Hiroi et al. (2014) found dendritic microstructures of nano-granites and felsite in garnet porphyroblasts of the high-grade metamorphic rocks, suggesting rapid growth from granitic melt inclusions. The nano-granite inclusions in garnet measure about 10–100 μm in diameter, and in these inclusions, rounded shape of the dendritic grains of albite and quartz with rounded corner and edges about 0.5–1 μ-m critical radius of curvature is commonly found.

The nano-granite and felsite inclusions surely indicate a development of dendritic growth of minerals in the conditions of large degree of oversaturation as being commonly found in volcanic rocks. Dendrites initially show a skeletal shape having angular edge and corner. During annealing process of dendrites, the angular edge and corner must change to a rounded outline because of large interfacial energy. This is because the annealing process takes place through reduction of the interfacial free energy of the mineral boundaries as formulated by the author (Toriumi 1979, 1981).

The process of annealing of the grain boundary is simple in the case of a single quartz inclusion in the albite host. The kinetic model of this annealing of quartz inclusion in single feldspar grain during metamorphism likes as follows: quartz grains are first included as a polyhedral grain by growing albite at the peak or just after the peak of metamorphism (Toriumi 1979), and then they are annealed in the rounding process of polyhedral angular boundary between albite and quartz. During annealing, polyhedral grains of various grain size should change in shape to be spherical grain of small size to rounded ones of large size as shown in Fig. 4.9. There should be the critical grain size that is defined as the maximum spherical grain size of inclusions. According to Toriumi (1979), the time scale (t_c) for spherical shape transformation of polyhedral grains of the mineral inclusion holds,

$$\begin{aligned} t_c &= k D_b R_c^4 \\ &= A R_c^4 \end{aligned} \tag{4.17}$$

and thus

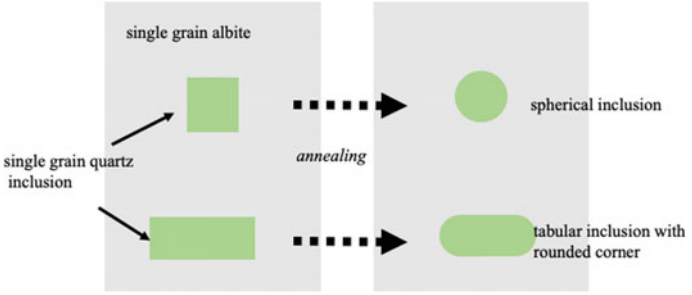

Fig. 4.9 Illustration of shape transformation of inclusion minerals from equigranular and tabular shapes to spherical and rounded ones

$$\log t_c = 4 \log R_c + \log A \tag{4.18}$$

and,

$$A = kD_b = kD_b^o \exp(-Qb/RT).$$

in which R_c is the critical grain size of spherical inclusion, and D_b and k are the grain boundary diffusion constant of oxygen and the material constant, respectively. The author measured the critical radius about 15 μm for 500 °C at the given time scale of annealing about 10 million years, and thus, the term of A should be about 197 (y/μm^4) at 500 °C. If we take 1 μm for R_c, the time scale becomes 197 years at the same temperature of annealing. Further, the activation energy for the annealing process can be obtained by boundary diffusion of oxygen of quartz about 125 kJ/mol (Toriumi 1979). Therefore, the time scales for annealing process from polyhedral to spherical inclusion are estimated as shown in Fig. 4.7.

As described in the previous section, Toriumi (1979) proposed a chronometer of metamorphic duration by shape transformation of inclusion quartz in albite single grain for measuring the critical spherical grain size. In order to show the universal relation of grain size and grain shape feature, the grain size of tabular to equant quartz inclusions was approximated to have flat and rounded segments of the interface: rounded segment shows a same radius of curvature and flat segment does very large one. As illustrated in Fig. 4.10, the sizes of the flat segment and the rounded segment in a single inclusion were measured in several albite grains of the single rock specimens from oligoclase–biotite zone, albite–biotite zone, garnet zone, and chlorite zone along the Asemigawa River which is the representative route across the Sanbagawa

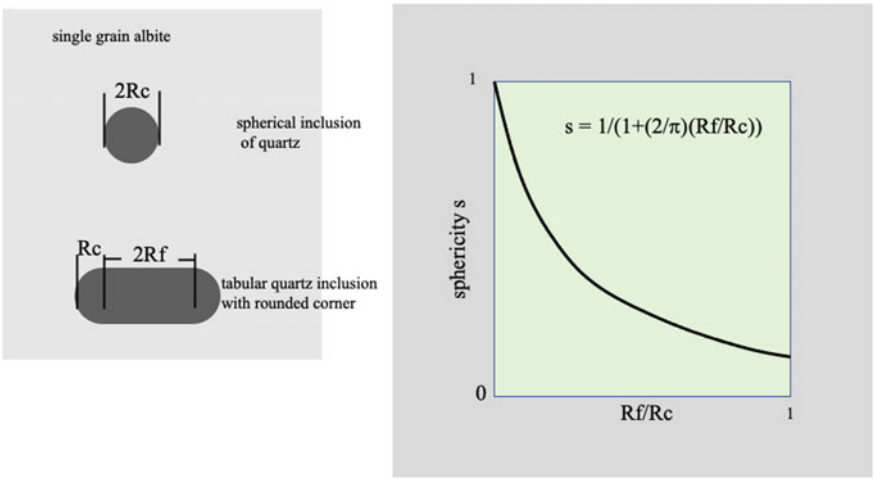

Fig. 4.10 Relation of the sphericity s and rounded and planar size ratio of rounded tabular grains of inclusion quartz in albite host

metamorphic belt in Shikoku (Enami 1983). As indicated in the previous paper (Toriumi 1979), the 3D shape of quartz inclusion in albite changes from initial sharp and angular to partly rounded corner and edge during annealing, and the ratio (R_f/R_c) of the size of the flat segment and the rounded corner is an indicator of the degree of shape transformation. In this case, the R_c should be equal to the critical radius of spherical inclusion of inclusion. Furthermore, the sphericity of the inclusion may be defined as,

$$s = 1/(1 + (2/\pi)(R_f/R_c)) \tag{4.19}$$

Further, the following geometrical relation of the partly rounded tabular grain holds,

$$R/R_c = 1 + k(R_f/R_c) \tag{4.20}$$

here, k is average ratio of short and long diameters of the rounded tabular grains.

In this equation, spherical inclusion may be $R_f = 0$ and $s = 1$, and polyhedral inclusion R_c is nearly zero so that s is nearly zero. The relationship between them is shown in Fig. 4.10.

The results of the measurements are shown in the diagram of average grain size and the ratio of flat and rounded size (Fig. 4.11), suggesting that the small grain clearly appears spherical shape, but the large grain does tabular one with rounded corner and edge. Further, it is obvious that relation of the grain size normalized by R_c versus ratio of R_f/R_c looks like a universal one in every rock of various metamorphic grades in the Sanbagawa metamorphic belt: the relation under $R/R_c = 1$ displays asymptotic at $R_f/R_c = 0$, and that over unity does linear increase with R/R_c as shown in Fig. 4.12. In addition, the frequency diagram of grains with $0 \leq R_f/R_c < 0.2$ against R/R_c ratio shows an abrupt decrease over $R/R_c = 1$.

The critical grain sizes of spherical inclusion of quartz in albite are shown in Fig. 4.13, suggesting clearly that the critical size increases with increasing metamorphic grade (temperature), though those of the highest-grade zone (OBZ) display sharply smaller than those in ABZ and GAZ but similar value of CHZ (chlorite zone). Then, the critical sizes of spherical inclusion of quartz in both pelitic and basic shists collected along the Asemigawa river section are shown in Fig. 4.14, showing clearly that the critical size increases with increasing metamorphic grade from chlorite zone to albite–biotite zone but in oligoclase–biotite zone it sharply changes at very small level as first suggested by Toriumi (1979).

Applying the relation between the annealing time and the critical spherical radius of quartz inclusion proposed by Toriumi (1979), the normal metamorphic duration of the rocks of OBZ is much shorter than that of ABZ, GAZ, and CHZ. The time scales of this metamorphic duration (annealing time after formation of quartz inclusion in albite) are estimated as 1000–10,000 years as indicated in Fig. 4.15. It is quite impressive that this time scale of metamorphic annealing after peak of metamorphism should be estimated from the highest-grade rocks.

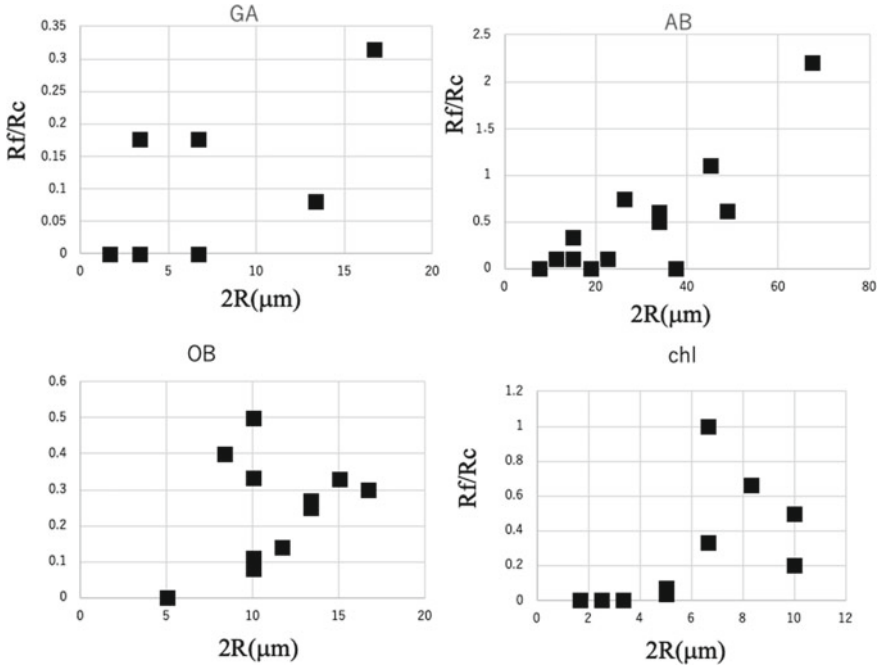

Fig. 4.11 Relations of R_f/R_c and average grain size R of quartz inclusion in albite from chlorite zone (300 °C; CH), garnet zone (400 °C, GA), albite–biotite zone (500 °C, AB), and oligoclase -biotite zone (600 °C, OB)

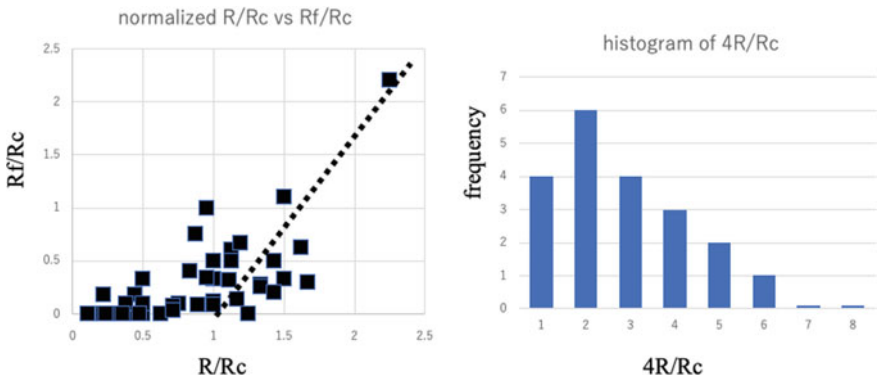

Fig. 4.12 Relations between R_f/R_c versus normalized R/R_c for quartz inclusion in albite of all samples (left) and frequency distribution of $4R/R_c$ of quartz inclusions of the Sanbagawa metamorphic rocks

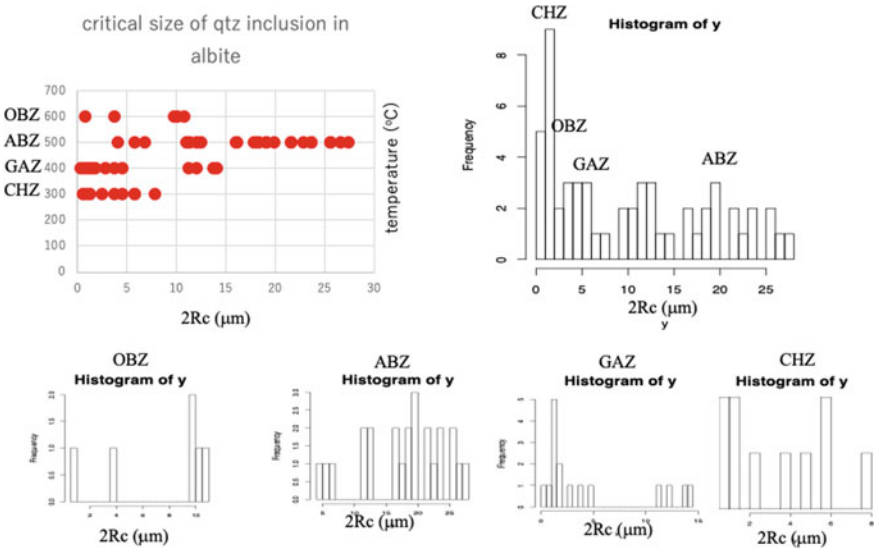

Fig. 4.13 Relations of critical grain size R_c of quartz inclusion and temperature and frequency diagram of them of various temperature zones, showing the decrease in the oligoclase–biotite zone rocks

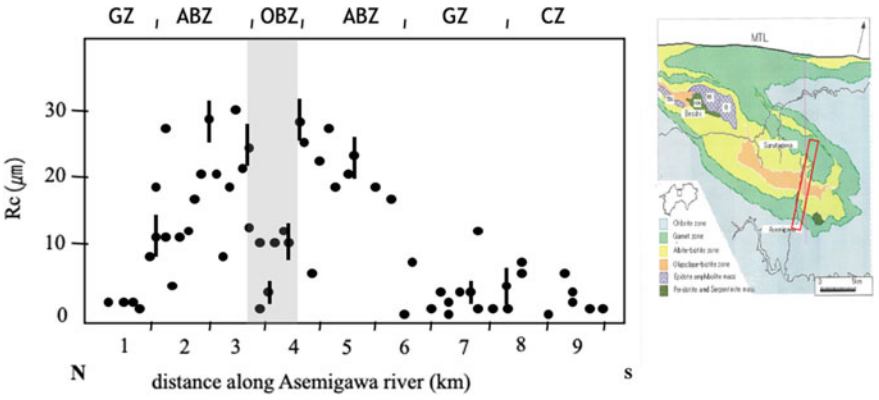

Fig. 4.14 Regional distribution of the critical spherical grain size of quartz inclusion of albite in rocks along the Asemigawa section (right), showing the rapid decrease in the oligoclase–biotite zone. CZ; chlorite zone, GZ; garnet zone, ABZ; albite–biotite zone, OBZ; oligoclase–biotite zone

Considering that the time of retrograde metamorphism of the Sanbagawa belt can be estimated from the several isotopic age determination methods with different closure temperatures. Itaya et al. (2011b, a) summarized the isotopic ages ranging from 90 to 80 Ma, suggesting 10 million years of annealing time in the albite–biotite zone. Therefore, the author assumed 10 million years of annealing time at

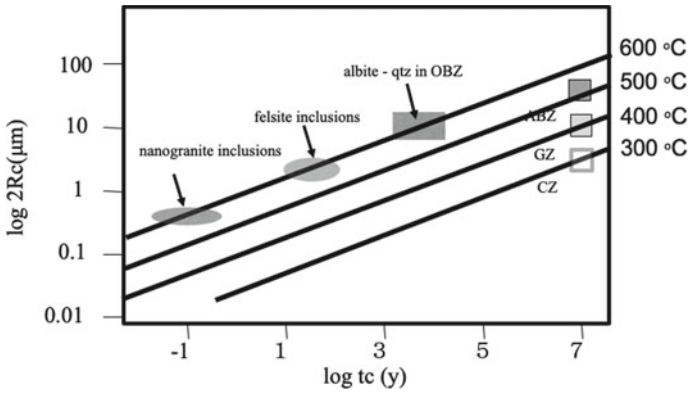

Fig. 4.15 Diagram of the critical grain size of spherical quartz inclusion in albite and the annealing time showing the extremely short annealing times of oligoclase–biotite zone schists, felsite inclusions (Hiroi et al. 2014, Sri Lanka) and nano-granite inclusions (Cesare et al. 2009, central India) in metamorphic garnet of granulites

500 °C using metamorphic P–T paths of Okamoto and Toriumi (2004). For the present metamorphic zones reveals a continuous geologic structure, the very rapid exhumation of the highest-grade rocks surely occurred sharply at the latest time of the lower-grade zones, that is to be 85 Ma.

In this paper, we will infer the annealing time of nano-granite and felsite inclusions in the high-grade metamorphic rocks of the collision type large-scale regional metamorphic belt in order to clarify the very rapid exhumation process of the collision type orogenic belts. The data of critical radii of curvatures of rounded corners of dendritic quartz are measured from photographs of Cesare et al. (2009) and Hiroi et al. (2014). The data are listed in Table 4.1.

Critical radius of the corner curvature of quartz inclusions in albite of nano-granite inclusions is about 0.5 μm for Indian granulite and 2.5 μm for Sri Lanka granulite.

Table 4.1 List of measured critical radius of spherical quartz inclusions

Locality	$2R_c$ (critical diameter μm)	Annealing temperature (°C)
Kerala Khondalite Granulite, India (Cesare et al. 2009)	0.5	600
Highland Granulite, Sri Lanka (Hiroi et al. 2014)	5	600
Sambagawa belt, Shikoku (Toriumi 1979)		
Chorine zone	7	300
Garnet zone	15	400
Albite–biotite zone	30	500
Oligoclase–biotite zone	10	600

The occurrence of dendritic grains of albite and quartz in nano-granites and felsite inclusions suggests that the inclusion grains are to be a part of intergrowth of albite and quartz dendrites against melt inclusion. In such a case, the critical radius of the curvature of quartz grains against albite should be the same value as the data presented here.

As shown in Fig. 4.15, the critical radius of the curvature of quartz in nano-granite inclusions in garnet grains of central India granulite rocks is characterized by very short annealing times ranging from 0.1 to 10 years at 600 °C. On the other hand, the felsite inclusions in garnet of Sri Lanka granulite show about 10–300 years of the annealing times at 600 °C. It should be noteworthy that the larger critical curvatures were not found in studied samples. Furthermore, dendritic inclusions of India and Sri Lanka granulite were only found in the case of aplitic rocks composed of albite, K-feldspar, biotite, and quartz. It suggests that the garnet grain has once included aplitic melt drops in the high temperature stage of the granulite facies and then those were experienced very short time annealing during the ascent of the granulite mass.

As suggested by Hiroi et al. (2014), dendritic felsite inclusions (same as nano-granite inclusion) in garnet are common in high-grade metamorphic rocks in the large-scale metamorphic belts of the world. Nevertheless, enough long time annealed felsite inclusions cannot be found, and thus, the rapid cooling after rapid crystallization of felsitic melt inclusion should characterize the late stage of the exhumation process of the granulite belt.

The important geometry of the metamorphic mass for their exhumation is the length, width and density of the mass. Here, the metamorphic mass is assumed to have a lens-shape during extrusion (Maruyama et al. 2004). If the vertical length of the metamorphic mass is limited in the crust, the buoyant force of the dyke is not sufficient for extrusion to the earth surface because of small density difference between metamorphic rocks and lower crust. At this case, the extrusion direction of the metamorphic mass should be horizontal but not vertical because of its neutral buoyancy. If very large metamorphic mass having a deep root within the mantle is considered, the negative buoyant force is enough large, and thus, the metamorphic mass continues to extrude by vertical intrusion.

The simple model of the metamorphic mass extrusion is based on the force balance during vertical extrusion in the mantle between the buoyant and the drag forces coming from boundary shear within the metamorphic mass.

The buoyant force, F_b, is estimated from the density difference δ_ρ between metamorphic rocks and surrounding mantle rocks, and volume of the metamorphic mass V as follows,

$$F_b = \delta\rho \, V g \tag{4.21}$$

$$V = \pi L^2 w \tag{4.22}$$

in which L and w are the radius and width of the lens-shaped metamorphic mass, respectively, and g is the gravitational acceleration as shown in Fig. 4.16.

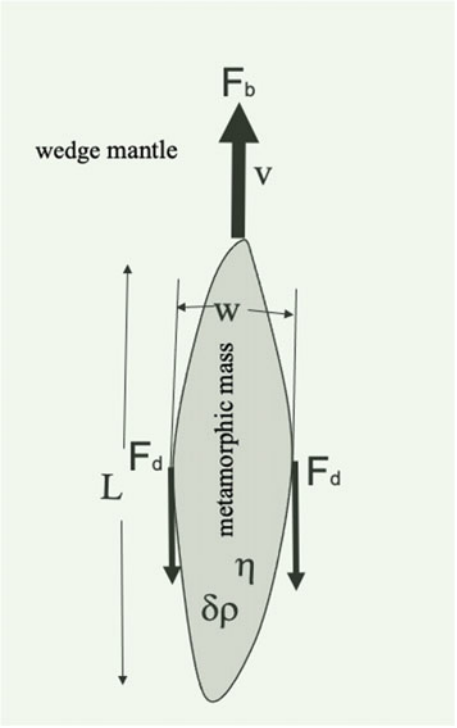

Fig. 4.16 Illustration of a model of rapid extrusion of the metamorphic mass in the upper mantle and crust showing the geometry, density difference and viscosity of the mass, and buoyant and viscous force acting on the mass

On the other hand, the viscous drag force acting on the boundary surface is divided into two types: one is the viscous drag force, and another is the frictional drag one.

First, we consider the viscous drag as follows: the viscous drag, F_v, holds,

$$F_v = \pi L^2 v\, \eta / d \tag{4.23}$$

in which v, d and η are the extrusion velocity, effective thickness, and viscosity of the metamorphic mass, respectively. Here, the effective thickness, w, is approximated to the following equation,

$$d = c\, w \tag{4.24}$$

in which c is about 1.

Therefore, we obtain the velocity of the metamorphic mass as follows,

$$v = c\, w^2 g\, \delta\rho / \eta \tag{4.25}$$

This equation likes that of the magmatic mass velocity obtained by Spence and Turcotte (1985) and Nakashima (1995) for the case of gravitational hydrofracturing.

On the other hand, if the drag force is the frictional stress along on the boundary, we have drag force, F_f, from the simple friction law as follows,

$$F_f = \pi L^2 P \mu \tag{4.26}$$

where P and μ are the effective pressure and frictional coefficient, respectively.

In this case the total force, F_t, acting on the mass becomes

$$\begin{aligned} F_t &= F_b - \pi L^2 P \mu \\ &= \pi \delta\rho L^2 w g - 2\pi L^2 (P_s - P_f) \mu \end{aligned} \tag{4.27}$$

Therefore, we obtain the Newtonian motion as follows,

$$\begin{aligned} \mathrm{d}v/\mathrm{d}t &= F_t/m = F_t/\rho_s \pi L^2 w \\ &= \delta\rho\, g/\rho_s - 2\big(P_s - P_f\big)\mu/\rho_s w \\ &= (\delta\rho\, g/\rho_s)\left(1 - 2\big(P_s - P_f\big)\,\mu/\delta\rho\, g\, w\right) \\ &= \delta\rho\, g/\rho_s \end{aligned} \tag{4.28}$$

Here, we assume very small μ, and P_f is to be nearly equal to P_s because abundant fluid-filled pores along the boundary between the metamorphic mass and the surrounding rocks.

Then, it holds

$$\mathrm{d}z/\mathrm{d}t = v \tag{4.29}$$

Thus, we obtain

$$\mathrm{d}^2 z/\mathrm{d}t^2 = (\delta\rho\, g/\rho_s) \tag{4.30}$$

Consequently, the frictional exhumation should become the accelerating process from the earth interior to the earth surface. Then the average velocity of the frictional exhumation can be estimated from the time scale and the distance of frictional exhumation. The distance of the frictional exhumation, z_o, can be estimated from $F_t = 0$ of Eq. (4.8),

$$z_o = \delta\rho\, w/2\mu\, \rho_s \tag{4.31}$$

Further, we obtain the time scale t_s of the frictional extrusion of the metamorphic mass as,

$$t_s = (w/2g\mu)^{1/2} \tag{4.32}$$

Thus, the average velocity of the metamorphic mass becomes,

$$v_a = z_o/t_s = 0.5\,(w/2g\mu)^{1/2}\delta\rho/\rho_s \tag{4.33}$$

Moreover, the maximum velocity of the metamorphic mass extrusion becomes at the earth's surface as,

$$v_{\max} = (w\,g/2\,\mu)^{1/2}\delta\rho/\rho_s \tag{4.34}$$

Consequently, the maximum velocity of the metamorphic mass reaches about 1–3 m/s for $w = 1$–10 km.

On the other hand, it is also concluded that the average extrusion velocity of the viscous drag regime is proportional to square of the metamorphic mass width, although in the frictional regime it is proportional to square root of the width of the metamorphic mass. The transition of the regime should occur at the depth where the frictional drag is just equal to the viscous one as,

$$\pi\,L^2\,P\,\mu = \pi L^2 w\,\delta\rho \tag{4.35}$$

Thus, we obtain

$$P = w\,g\,\delta\rho/\mu. \tag{4.36}$$

In order to illustrate the relationship between the viscous and frictional drag regimes, the velocities of these two modes are shown in the logarithmic diagram of velocity versus width of the metamorphic mass by Fig. 4.17. The regime transition from the viscous to the frictional drag should be about several ten km because of

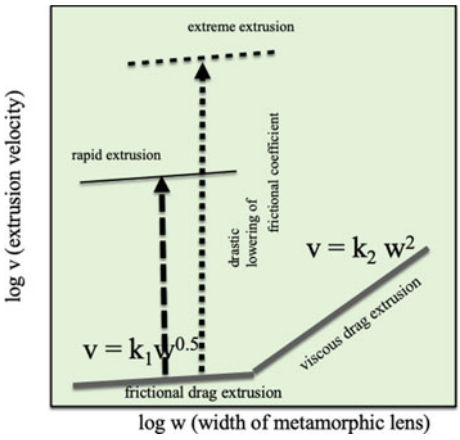

Fig. 4.17 Diagram of extrusion velocity and the thickness of the metamorphic mass showing two modes of the frictional drag and viscous drag along the boundary surface of the mass. The rapid and extremely rapid extrusion needs very small friction of the boundary due to fluid entrainment in the boundary zone

very small frictional coefficient of hydrous condition at the boundary, and it may be in the crust.

The buoyant force of the metamorphic rocks already was evaluated from the mineralogy and density as Irifune et al. (1994) and Ishii et al. (2012) suggested that total buoyant force of the long extended metamorphic mass in the upper mantle appears positive until the front depth over 660 km. The maximum buoyancy is at the front depth of 200 km. On the other hand, the drag force from the slab is governed either by the rheology of the metamorphic rocks, or by the friction between metamorphic rocks and the slab. These both mechanisms yield the strong constraint between the extrusion velocity and the aperture of the metamorphic mass. However, the time scales of the metamorphic extrusion vary from 1 to 10 million years judging from the variations of metamorphic ages in the single metamorphic belts as compiled by Maruyama (1990) and Maruyama et al. (2004). On the other hand, the actual thickness of the metamorphic belts ranges from 1 to 10 km, resulting the extrusion time scale variation of 100 times of magnitude in the case of the viscous drag extrusion.

In the case of the large frictional drag, the extrusion speed of the metamorphic mass is not fast even in the large aperture of the metamorphic mass, being compared with the case of viscous drag as predicted previously. However, that velocity is only proportional to square root of the aperture of the metamorphic mass (Eq. 4.34), and thus, the even small metamorphic mass can continue the extrusive motion. The ratio of the extrusion velocity of the mass having size contrast of about 10 becomes also 3.2 times, suggesting that the small metamorphic mass may extrude to the upper crust within 10 million years if the large metamorphic mass extruded within 10 million years as shown in Fig. 4.17.

In this paper, the author strongly suggested that the highest-grade zone of the Sanbagawa metamorphic belt was extruded into the mass of lower-grade zones within the very short times. Then, it seems that the metamorphic pressure and temperature paths of the highest-grade zone in the retrograde metamorphism should be steeper than those of surrounding lower-grade zones. Okamoto and Toriumi (2004) and Uno et al. (2015) clarified the different retrograde P–T paths from amphiboles and garnet chemical zoning by means of Gibbs method for pressure and temperature path inversion, showing that retrograde P–T paths from amphiboles and garnet are very steep and show rather temperature increase suggesting shear heating by rapid extrusion as shown in Fig. 4.18. They also clarified the large-scale hydration reaction in the retrograde metamorphism from high pressure mineral assemblages to low pressure ones during the retrograde metamorphism.

The rapid extrusion of the high pressure and ultrahigh pressure regional metamorphic belts extruding into lower-grade zones must requires the sudden change from the viscous drag to the frictional drag mechanism as indicated in this paper. It leads that the boundary zones of extruding higher-grade rocks against the surrounding rocks were formed as large hydrous shear zones in the short periods during the exhumation process of the whole metamorphic belt. The formation of such shear zone boundaries is the reason of the drastic decrease of frictional coefficient resulted from accumulation and connection of fluid-filled shear cracks with small aspect ratio along on such boundaries, and the present fluid should be generated from the dehydration

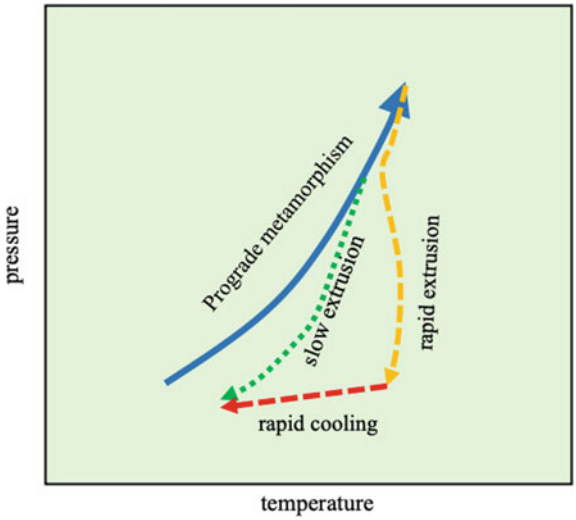

Fig. 4.18 Possible P-T-t paths of the metamorphic masses in the rapid and extremely rapid extrusion modes in the retrograde process, suggesting the frictional heating of the mass in the extremely rapid extrusion mode

reactions in the deeper metamorphism. The large-scale faults near the rocks having nano-granite and felsite inclusions of garnet in granulite may be the high shear zones responsible for the extremely rapid extrusion of the thin high-grade metamorphic masses as shown in Hiroi et al. (2014). The case of the shear faults in the Sanbagawa metamorphic belt may be accompanied with the hydrated damage zones along the boundaries between oligoclase–biotite and albite–biotite zones in Shikoku. Okamoto and Toriumi (2004) and Uno et al. (2015) found the frequent occurrence of large-scale retrograde hydration of the higher-grade zones of the Sanbagawa metamorphic belt. Furthermore, Uno et al. (2015) clarified metasomatic compositional change by large-scale fluid flow through the banded basic amphibolite forming retrograde garnet. It seems that such large-scale metasomatic banding formation in the oligoclase biotite zone due to huge amount of fluid flow should result in rapid and huge lowering the frictional coefficient along the shear zone of the highest-grade zone boundary, being responsible for the very rapid extrusion of the oligoclase–biotite zone of the Sanbagawa metamorphic belt.

4.4 Time Scale of Mineral Banding and Metasomatic Instability with Fluid Flow

Metamorphic banding phenomena are commonly observed in the subduction zone metamorphic rocks. There have been several models interpreting this metamorphic banding in the initially homogeneous basic schists, and the models are possibly classified into three types: one is the mechanical differentiation model proposed by Toriumi (1975), the second is the shear crack sealing by minerals presented in

the previous chapter, and the third is the Liesegang banding model. Classically, the model by general diffusion and reaction dynamics has been proposed by Ortoleva et al. (1987), but it may be possible to interpret the special case of banding but not to be applied for studying the time scale of the process.

On the other hand, the author intends to propose a dynamic model of precipitation and dissolution of minerals in the permeable flow of aqueous solution in the later section. The model includes the effect of porosity change in the space and time, and it is available for application of data science method to obtain the validity of the model. Furthermore, the beautiful banding structure of precipitation of minerals in the coupled diffusion column filled with gelatin has been known as the results of the typical diffusion–reaction nonlinear dynamics (e.g., Izsak and Lagzi 2005). This type of nonlinear dynamics has been investigated by many experiments and simulations and clarified that there are universal laws of the relationship among the band distance, band width, band position, and characteristic time scale of the band. This nonlinear phenomenon of mineral precipitation which is called as Liesegang banding in the diffusion–reaction system is commonly found in the geological process. In this section, the author intends to apply this type of nonlinear dynamics to metamorphic banding with special reference to the time scale of the band formation and migration.

At first, let us summarize the formulation of the Liesegang dynamics in the simple system that the mineral of C is precipitating in the diffusion column of component A and dispersion of B as illustrated in Fig. 4.19. The precipitation rate of the mineral C is governed by the difference of concentration product from equilibrium saturation product $K^o = (X_A X_B)^o$, and thus the differential equations of their concentration and mass of C,

$$\begin{aligned} dX_A/dt &= D\Delta X_A - k_a X_A X_B \\ dX_B/dt &= D\Delta X_B - k_a X_A X_B \end{aligned} \tag{4.37}$$

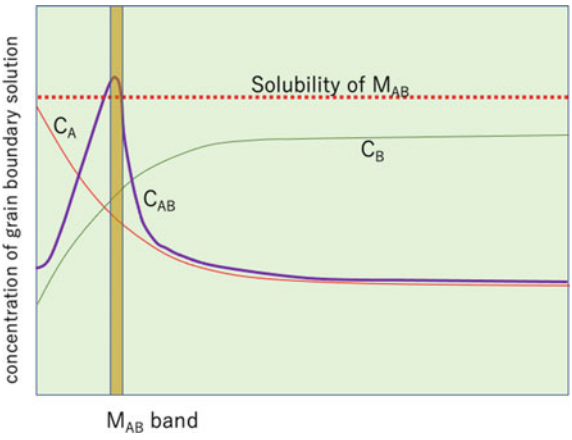

Fig. 4.19 Illustration of a model of mineral band formation in the case of diffusional gradient of C_A and C_B from the jog of the shear crack filled with aqueous solution showing the oversaturation of mineral M_{AB} at a distance from the shear crack like the Liesegang band formation

$$dX_C/dt = k_a X_A X_B$$

$$dMc/dt = k_c(1 + \tanh\ X_C)$$

The reason why the intermediate aqueous component of C is considered in this system is responsible for the fact that the crystallization of C is to be experienced through nucleation and successive grain growth process and the nucleation should need the finite colloidal minute cluster of C component in the aqueous solution (Igzak and Lagzi 2005). In the above equation, the solidification of colloidal cluster of C is followed by the sigmoidal relation against the composition of C as like as term of $(1 + \tanh X_c)$. In the schematic interpretation of the Liesegang banding by these nonlinear dynamics, the product of preexisting dispersive component B and diffusive component of A from the source region is over the critical value and then colloidal cluster of C changes to mineral grain, and thus, the components A and B decrease and diffuse in the surrounding region. This diffusion process of A and B into the crystallizing band of C results in the advancement of the boundary of band successively, and in the band, the grain growth of mineral C takes place continuously. The explanation mentioned above is in the case of the simple experiment such as AgI and NH_4I in gelatin, but in the natural case of metamorphic and metasomatic rocks, how is it real?

There are abundant textures of so-called metamorphic and metasomatic bands which are commonly composed of single to several kinds of minerals such as quartz, albite, chlorite, and calcite as mentioned in this book. Furthermore, it is well known that the metasomatic bands of chlorite, talc and tremolite between serpentinite and pelitic rocks (Oyanagi et al. 2020), and that wollastonite, grossular, diopside bands between marble and basaltic dykes are commonly found in the metamorphic rocks (Fukuyama et al. 2006). Moreover, there should be abundant pores and voids in the metamorphic and metasomatic rocks during recrystallization process because of common findings of open cracks and shear crack jogs in them as indicated in the previous chapters. Therefore, it is natural to be considered that the Liesegang dynamics should operate in the metamorphic reaction and diffusion process including the aqueous fluid flow.

If it is the case, the additional phenomena can be found in the various bands: one is the boundary migration and related waveform structure of the boundary derived from instability through imbalance of migration rate and diffusion rate of components in the matrix, and another is the grain size variation of the bands due to difference in material supply and time scale of grain growth in bands. In the natural occurrence of metamorphic and metasomatic banding, the grain size grading of the metamorphic garnet and albite porphyroblastic grains are commonly found in the plate boundary zone, and it has seemed strange in the long time that the size grading in the common basaltic metamorphic rocks. Considering the metamorphic grain growth process in the permeable flow of aqueous fluid and diffusive flux of ionic species relevant to mineral growth, the Liesegang dynamics operates probably in the natural

metamorphism. Therefore, the grain size grading phenomena in the subduction zone metamorphic rocks will be discussed in this section.

By the way, as mentioned previously, it is well known that there are universal relations among the spacing, width, position, and time of Liesegang bands in the experiments and simulation results as shown in Fig. 4.20,

$$\begin{aligned} X_{n+1}/X_n &= p(\text{spacing rule}) \\ W_{n+1}/W_n &= q = p^{0.95.}(\text{width rule}) \\ X_n^2/t_n &= r \ (\text{timing rule}) \end{aligned} \tag{4.38}$$

And then the following relations are derived from above universal equations,

$$d_n = X_{n+1} - X_n = (p-1)X_n$$

$$\ln(W_n/W_1)/\ln(X_n/X_1) = 0.95 \tag{4.39}$$

$$2.1 \ln W_n = \ln t_n + C$$

$$W_n = A\, d_n^{0.95}$$

in which n means the n-th bands from the diffusion source boundary and d is the distance between neighboring bands. These relationships are available for the natural metamorphic bands to investigate the applicability of the Liesegang dynamics.

In Fig. 4.20, it seems that there appears wide variation in relations of band width and band spacing of monomineralic albite bands in the Sanbagawa metamorphc rocks, suggesting that the process of banding does not represent the simple unidirectional diffusion mechanism, but should involve the advection by fluid flow and later band migration and splitting as discussed by Lagzi (2005). He also proposed the Liesegang dynamics involving advection of fluid flow velocity v and the relation between X_n and t_n is,

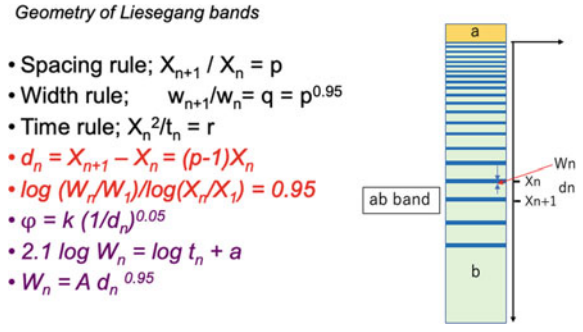

Fig. 4.20 Universal relations of the Liesegang bands showing the band-spacing rule, width rule and time rule, and modified rules between width and band distance and duration time of the Liesegang process. Right figure shows the geometry of the bands

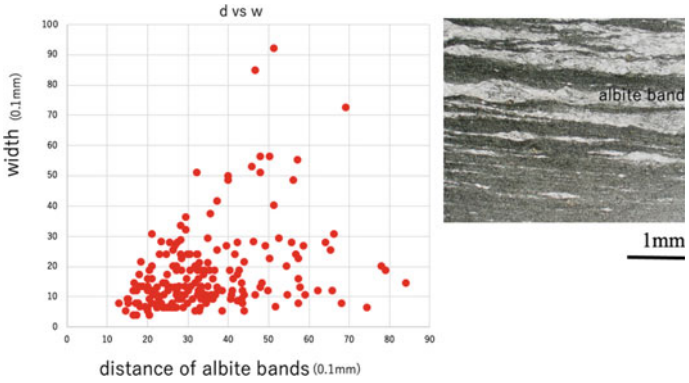

Fig. 4.21 Diagram of the width and distance of neighboring albite bands in the banded basic schists of the single outcrop of the Sanbagawa metamorphic belt. Right figure shows the photograph of the thin section of the banded schist

$$X_n/t_n = r\prime \tag{4.40}$$

in which r' is the constant term.

On the other hand, migration of the Liesegang bands was clarified by simulation and experimental investigation (Lagzi 2005). Therefore, in the diagram of width and spacing of the bands, there is a scattered distribution of the data as like as those for natural bands in Fig. 4.21. Later, the simulation of the system involving diffusion and advection by fluid flow accompanied with permeable flow of aqueous solution which coupled with porosity change, dissolution, and precipitation of minerals will be discussed based on the simulation results to obtain the general relations of width and spacing of the bands with advancing time.

Well, it is noteworthy that the band formation by diffusion–reaction dynamics such as Liesegang phenomenon is almost always associated with mineral growth in the developing bands and the grain size within the bands are strongly dependent on the band position, that is the band width and band spacing. The grain size in this mechanism is probably dependent on the mechanism of grain growth such as Ostwald ripening and or Cahn-Hillard mechanism. The former gives the relation of growth velocity as

$$\mathrm{d}R/\mathrm{d}t = M/R$$

and

$$R = M\,t^{1/2} \tag{4.41}$$

and the latter does,

$$R = k_1\,t^{1/3,1/2} \tag{4.42}$$

And thus, the relations of R and X become in the case of advection control,

$$R_n = k_2 X_n^{1/2} \tag{4.43}$$

or

$$R_n = k_3 X_n^{1/3}$$

On the other hand, in the case of diffusion control, it holds,

$$R_n = k_4 X_n$$

or

$$R_n = k_5 X_n^{2/3, \text{or} 1} \tag{4.44}$$

These simple relations between grain size of solution growth mineral and position of the band manifest the banding of the grain size and/or spatially inhomogeneous but not random grain size distribution of minerals in metamorphic and metasomatic rocks. Therefore, in the case of unidirectional flow of aqueous solution of the plate boundary zone, the grain size grading should appear commonly nearly parallel to the schistosity plane because the microopen cracks are surely aligned normal to the schistosity plane shown in the previous section.

As shown in Fig. 4.22, the grain size grading of albite is possibly recognized in the basic schists of the Sanbagawa metamorphic rocks, and the iso-grain size plane is nearly parallel to the schistosity plane as discussed above. On the other hand, there is rarely found the sporadic very large grains of garnet and albite in basic and pelitic schists which are surrounded by rather small grains of them, thereby suggesting that the diffusional environment around the large porphyroblastic grains seems to be formed during their growth.

The Liesegang like bands of albite are often sandwiched by chlorite and epidote bands, and these bands are mutually invaded by their migration, judging from the wavy boundary of the bands and often including grains of them. In the case of simple experiments of Liesegang bands, the migration of bands is clearly found (e.g., Lagzi 2006). Thereby, let us discuss the band migration velocity by means of the interface instability of the bands due to Mullins–Sekerka instability.

In this study, the metasomatic boundaries between albite and chlorite band are considered; in this case, Di is the diffusion constant of Na^+ and Al^{3+} soluble ions in intergranular solution, and V is the velocity of albite band against matrix chlorite. Possible reactions involving albite and chlorite in basic metamorphic rocks with intergranular solution should be represented by following,

$$Mg_2Al_3Si_3O_{10}(OH)_5 + 3\,Na^+ + H^+ + 6SiO_{2aq} = 2Mg^{2+} + 3H_2O + 3NaAlSi_3O_8$$

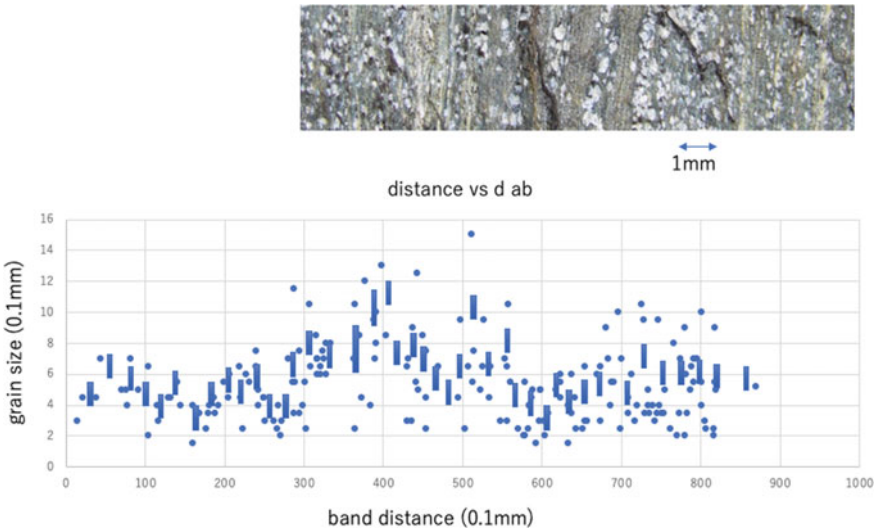

Fig. 4.22 Diagram of the grain size of albite and the distance of the albite rich band showing the grain size grading associated with metamorphic banding in the basic schists of the Sanbagawa metamorphic belt

This chemical equation can give the equilibrium relations between concentrations of Na and Mg ions in solution at a given pH and temperature as following,

$$3 \ln X_{\mathrm{Na}+} - 2 \ln X_{\mathrm{Mg2}+} = A + pH \tag{4.45}$$

where A is equilibrium constant at given temperature and pressure. Let us assume the band boundary velocity V, the difference of diffusivity of Na and Mg ions takes some difference from the equilibrium line proposed above. The difference of concentration gradient from equilibrium one, d in solution is given by

$$\begin{aligned} d &= 2/3 - \mathrm{d} \ln X_{\mathrm{Mg}}/\mathrm{d}z/\mathrm{d} \ln X_{\mathrm{Na}}/\mathrm{d}z \\ &= 2/3 - (1/X_{\mathrm{Mg}} D_{\mathrm{Mg}}/1/X_{\mathrm{Na}} D_{\mathrm{Na}}) \end{aligned} \tag{4.46}$$

From the graphical relations of the metasomatic gradient from equilibrium one, if d is negative, the chlorite matrix near the boundary becomes unstable and albite should be more stable with V even in the chlorite region. If d is positive, the advancing the boundary keeps stable relation at the boundary (Fig. 4.23).

Using the relation of time scale and wavelength of the unstable migration boundary in the previous section, the velocity of the band boundary migration should be inferred from the equation of,

$$\log V = \log K - 2 \log \lambda \tag{4.47}$$

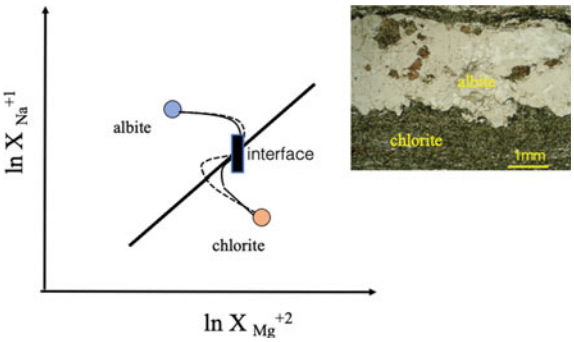

Fig. 4.23 Illustration of a model of interface instability between albite and chlorite band in the banded basic schist showing that oversaturation of albite beside the interface due to imbalance of diffusion and growth velocity in the boundary zone. The right figure shows the thin section of the waveform pattern of the albite and chlorite band boundary

with $K = K_o \exp(-Q/RT)$.

in which Q is the activation energy of boundary migration, V is the velocity of the boundary migration, and λ is the wavelength of the band boundary as obtained in the previous section.

Second, let us consider the polycrystalline aggregate replacing the matrix minerals with the intergranular solution as illustrated in Fig. 4.24. In the figures, the triple junction of the grain–grain–matrix is required for the balancing of grain–grain interfacial tension and two grain–matrix tensions as shown in Fig. 4.24. The geometry of the triple junction must satisfy the conditions that the tangent surface of the average growing interface near triple junction T is normal to the tangent line of grain–grain

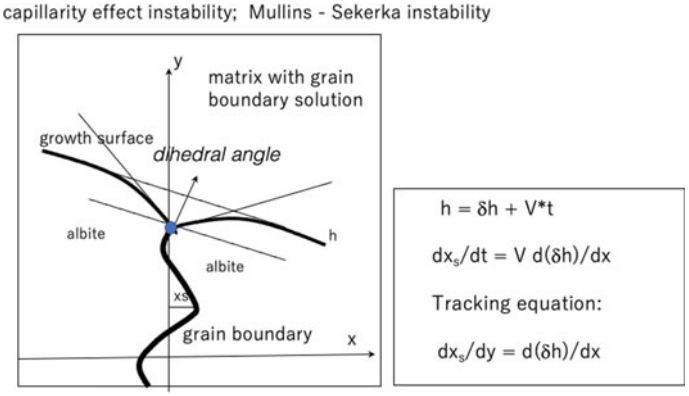

Fig. 4.24 Illustration of a model for waveform growth interface and inherited waveform grain boundary of the aggregate behind the growth front of the albite band

boundary at triple junction because of equilibrium of interfacial energy at T. Therefore, the tracing of the grain–grain boundary must be invariantly normal to the tangent line of the growing interface at the triple junction as shown in Fig. 4.24.

If we consider the flat surface of the growing interface, the tracing of the triple junction T becomes exactly the straight line normal to the growth interface, but in the case of periodical waveform of growth interface, the tracing of the triple junction appears waveform or curvilinear grain boundary. Here, waveform grain boundary should be analyzed in order to infer the growth interface waveform which is responsible for the growth instability related to the growth velocity.

Consider the waveform of grain–grain interface as shown in Fig. 4.24. The grain boundary is approximated to be sinusoidal function as seen in figures. As the time advances, at the growth interface line intersected with above grain–grain interface curve, the tangent line of the growth interface is normal to the tangent line of the grain–grain interface because of the interfacial tension balance described above. Let us assume the following model grain–grain interface in the two dimensions,

$$h(x) = A \sin k\,x \tag{4.48}$$

in which $h(x)$ is the growth interface curve, k is the wave number, and A is the amplitude of the wavy interface.

Along this interface curve, the growth point of the growing interface advances with time as,

$$x\,(t) = V\,t \tag{4.49}$$

in which V is the growth velocity.

At the crossing point of both curves, the tangent lines of them are mutually orthogonal as shown in Fig. 4.24,

$$\mathrm{d}\,h(x)/\mathrm{d}x = \mathrm{d}g(y)/\mathrm{d}y \tag{4.50}$$

where, $g(y)$ is the grain–grain interface, and y is vertical axis in the orthogonal coordinate system.

Applying $h(x) = A \sin kx$, we obtain

$$\mathrm{d}\,g(y)/\mathrm{d}y = Ak \cos kx \tag{4.51}$$

and

$$y = A \sin kx \tag{4.52}$$

Therefore, we obtain the following differential equation,

$$\begin{aligned} \mathrm{d}\, g(y)/\mathrm{d}y &= Ak\, \cos\left(\sin^{-1}(y/A)\right)/k \\ &= Ak\left(1-\sin^2(ky)\right)^{1/2} \\ &= Ak\, \cos\, ky \end{aligned} \tag{4.53}$$

Integrating this equation, we obtain

$$g(y) = A\, \sin\, ky + \text{constant} \tag{4.54}$$

The growing interface followed by adjoint grain–grain interface is, therefore, concluded to appear the sinusoidal waveform having the same wave number and amplitude of the unstably growing interface. It follows that the grain shape of the metasomatic band interior displays a waveform outline like flower shape.

The metasomatic bands are investigated in the basic schists of Sanbagawa metamorphic belt of Shikoku (Fig. 4.25). The bands of basic schists are composed predominantly of albite and of minor chlorite and epidote. The shape of the grain in bands are often flower pattern as shown in Fig. 4.25. The waveform band boundaries are very common, and the albite bands having wavy boundary display commonly both of fold-like and boudin-like patterns in the single rock samples as shown in Fig. 4.25, suggesting that such waveform boundary is not due to the extensive deformation. The wavelengths of the wavy grain–grain interface in the bands from the boundary to the center are measured under the optical microscope as shown in Figs. 4.26 and 4.27. It is obvious that the wavelength increases toward the center of the bands from 0.05 to 0.15–0.2 mm in the rim of the albite grains of the bands. Therefore, it seems that the growth interface making the grain–grain interface within the band appears gradual increase in wavelength suggesting the decrease in replacement velocity of the albite after chlorite. The ratio of the wavelength of the center against the wall

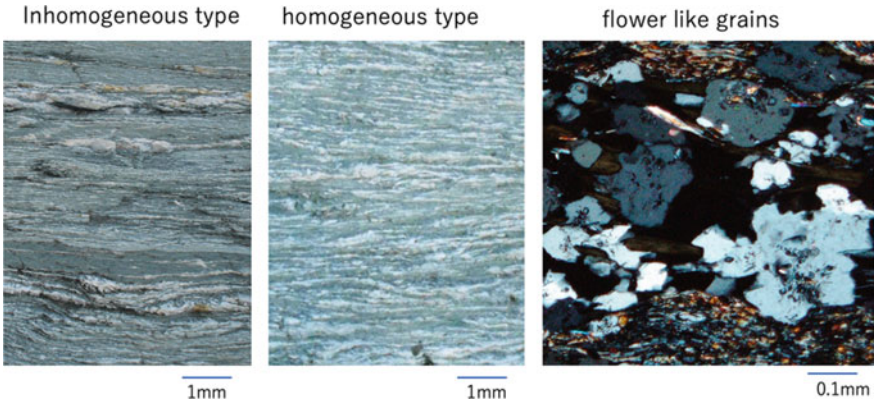

Fig. 4.25 Photographs showing the various features of the albite bands in the outcrops and under the thin section showing the inhomogeneous and homogeneous distribution (left two) and waveform and flower-like grain outline of albite of the band interior (right) under thin section (crossed polar)

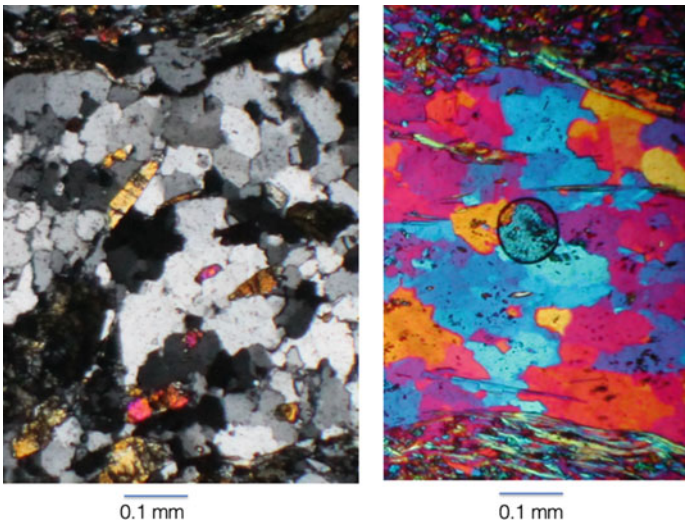

Fig. 4.26 Photographs of the wavy grain boundary of albite aggregate in the albite band of thin section with crossed polar (left) and with sensitive plate (right)

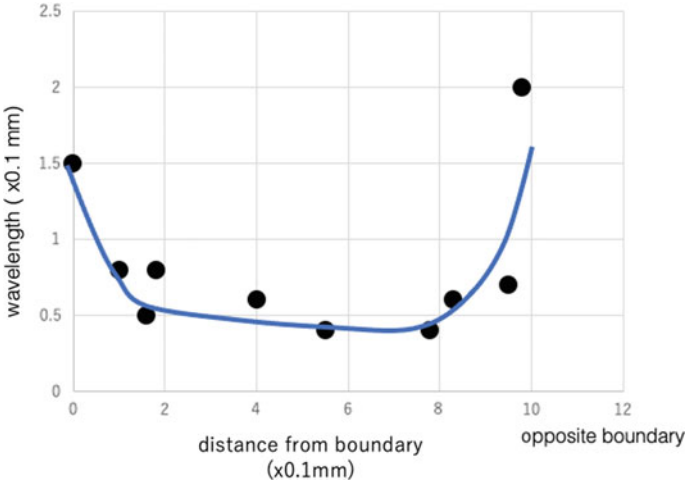

Fig. 4.27 Diagram of the wavelength and the distance from the band boundary showing the gradual increase toward the band boundary

reaches about 2–3, suggesting the ratio of the metasomatic band velocity about 4–9. On the other hand, the average wavelength of the grain boundary of albite is not related to the band width as shown in Fig. 4.28, suggesting the common migration velocity of the albite bands in the basic schists.

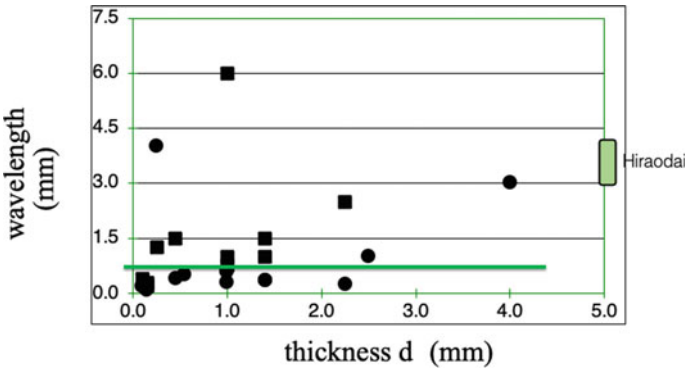

Fig. 4.28 Diagram of the average wavelength of albite grain and thickness of the albite bands showing the value of wavelength indifferent with thickness of band

In order to estimate the absolute velocity of the bands, we need experimental study about growth of the albite band in the basic rock of the hydrothermal system. Okamoto and Sekine (2011) investigated the hydrothermal experiments in the high temperature and high pressure flow system in the granite tube and succeeded in growth of quartz aggregates but not albite on the wall of the tube. The final interface between the aggregate and solution is not the unstable growth front at the instantaneous time, but the grain–grain interface normal to the wall displays clearly a waveform. The changing patterns of the grain–grain interface seems to be likely to the natural cases studied here. The time of this experiments took about 350 h, indicating the average velocity of the growth about 3×10^{-4} mm/h at 400 °C (Okamoto and Sekine 2011). The wavelength of this case was about 0.01 mm (Fig. 4.29), thereby suggesting that the K value normalized by temperature at growth velocity obtained previously is about 3×10^{-8} mm^3/h. On the other hand, Fukuyama et al. (2006) studied metasomatic bands derived from contact metamorphism surrounding granitic mass of Hiraodai, Kyushu. The duration of the metasomatic bands formation of wollastonite is probably about 1000–10,000 years and temperature around 600 °C, judging from the size of basaltic dyke. These data are plotted in the same diagram of metasomatic advancing velocity vs log K with given wavelength and then the value of temperature normalized K is estimated to be about 1×10^{-6} mm^3/h (Fig. 4.30). These known K values and temperatures give possibly the activation energy of K to be about 30 kJ/mol if the activation energy and interfacial energy of wollastonite and quartz related with grain boundary solution are the same order of magnitude.

The sealing time scales of open cracks and shear cracks are very important to discuss the fluid migration in the crust and to discuss the seismic activity associated with slow slip events. Toriumi and Hara (1995) investigated the crack geometries and their distribution patterns in the Sanbagawa metamorphic rocks. Applying the normalized K values, the time scale of open and shear crack sealing of quartz in the plate boundary rocks is possibly inferred by measurement of wavelength of the quartz-quartz grain boundary undulation as shown in Fig. 4.31, suggesting that there

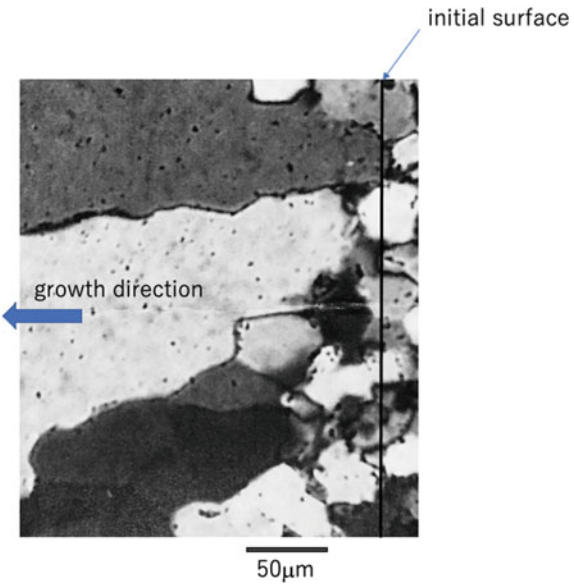

Fig. 4.29 Photographs of the experimental result of grain growth of quartz in the hydrothermal condition through the flow system made by granite tube (personal communication) by Okamoto (2014)

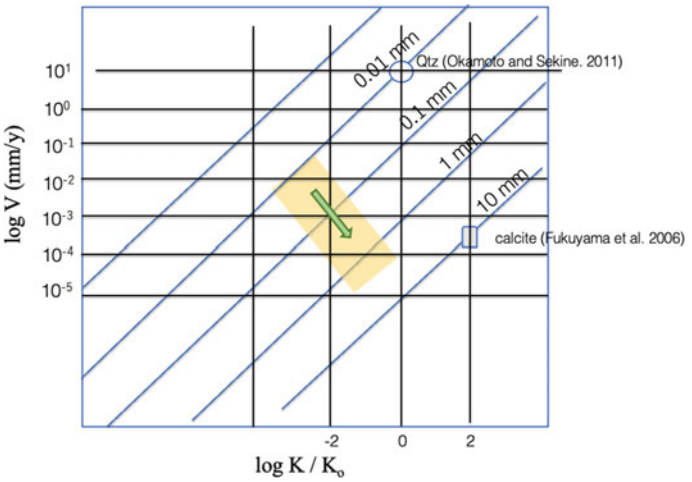

Fig. 4.30 Diagram of the migration velocity of the mineral band and the wavelength with temperature term K (see text) for quartz (experimental data of Okamoto and Sekine 2011) and calcite (Fukuyama et al. 2006) and albite bands in the basic schists of the Sanbagawa metamorphic belt. Arrow indicates the trend of progressive albite band migration in the metamorphic rocks

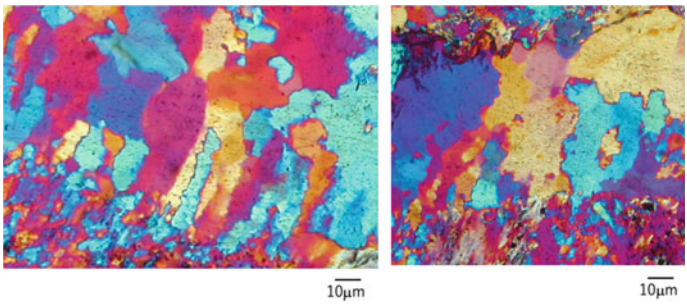

Fig. 4.31 Photographs showing the quartzose band in the pelitic schists of the Sanbagawa metamorphic belt showing the waveform grain boundary of the band interior under the microscope with sensitive plate and crossed polar

are two types of wavelengths—change from the rim to the core of the sealed cracks. One is the comb type, and the other is the granular type (Figs. 4.32 and 4.33). In the case of the comb type sealed cracks, the wavelength of the grain boundary shows oscillatory change near the 2–3 μm, on the other hand, in the granular type it shows a gradual increase from rim to core. Therefore, it seems to be the rapid sealing in the comb type but lowering the sealing velocity of the granular type as shown in Fig. 4.34. Then, the time scales of these sealing may be in the range of 100–1000 years in the conditions of 400 °C, assuming the activation energy about 30 kJ/mol for diffusion of ionic species of Si like that of Al^{3+} in solution (Li and Gregory 1974). But if the activation energy is much smaller than this value and it is assumed to be 10 kJ/mol, the time scales of sealing the open cracks with width of 1 mm become around 10–100 years.

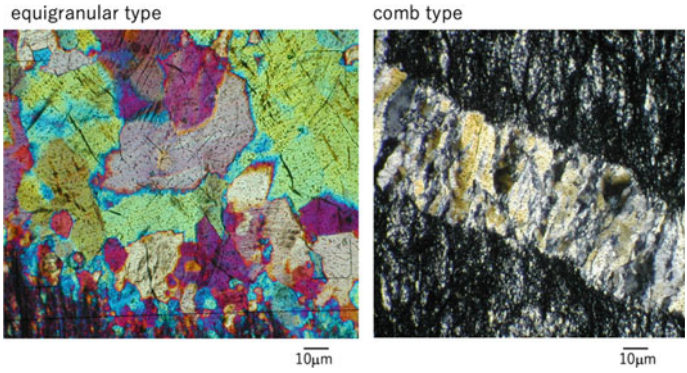

Fig. 4.32 Photographs showing the waveform grain boundary of quartz in two types of sealed open cracks in metachert of Shimanto accretionary prism. Left figure displays granular type and right one does comb type sealed crack

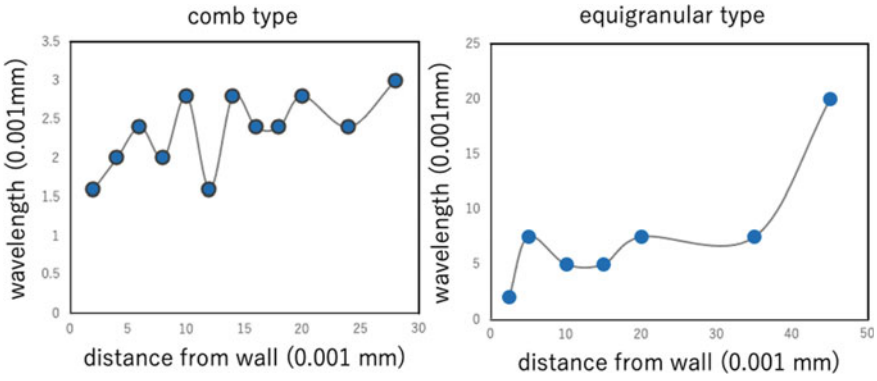

Fig. 4.33 Diagram of the wavelength and distance from wall of comb type sealed crack (left) and granular type one (right)

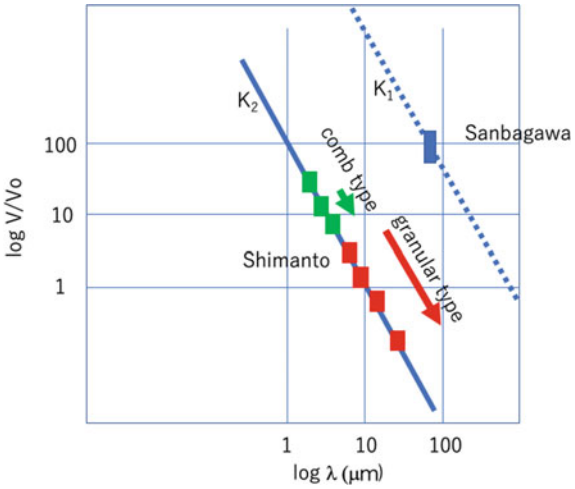

Fig. 4.34 Diagram of sealing velocity of cracks and bands and wavelength of the grain boundary of quartz of the comb type and granular type in Shimanto accretionary prism and the granular type of Sanbagawa metamorphic rocks. Arrows show the temporal trend of the sealing velocity in the prograde deformation

4.5 Dynamics of Porosity Wave and Mineral Banding

Metamorphic and metasomatic banding are very common in the regional and contact metamorphic rocks. Mineral bands are composed mainly of retrograde assemblages of albite, chlorite, epidote, calcite and quartz in basic schists and quartz, albite, chlorite, calcite in pelitic schists of the low-grade zones, although in the medium-grade zones, albite, epidote, garnet, and amphiboles are common in basic schists. In many

cases, bands both pelitic and basic schists together with low-grade and medium-grade metamorphic rocks exhibit monomineralic to bimineral coarse-grained texture compared with matrix. Besides, there is a significant difference in crystallographic orientation in matrix and bands. For examples, tabular grains of epidote occur commonly perpendicular to the band boundary, suggesting the geometrical growth in the bands from the band wall.

By the way, in metamorphic bands, abundant pores coated by oxides and hydroxide minerals appear in the central zone of the band. Those are considered to have been fluid filling pores but not pore after dissociation of carbonates, because of common existence of druse mineral of euhedral acicular quartz. Considering the periodic and parallel distribution of these metamorphic bands, it seems that there is a layered structure of fluid filling pore distribution during the retrograde metamorphism. Besides, such pores are surely considered to be the paths of metamorphic fluid. The pores in these bands also are thought to be derived from dissolution of constituent minerals.

In this paper, the author would like to propose a theoretical model of banding distribution of the fluid filling pores during the metamorphism and metasomatism. It suggests that the banding distribution of these pores in the metamorphic rocks may result in the strain instability forming shear localization and large-scale faults in the plate boundary metamorphic rocks.

As noted previously, the pores after metamorphic minerals are surely formed by dissolution and precipitation derived from fluid flow through metamorphic rocks. How can we obtain the banding structure of high and low porosity layering in the simulated model? In this question, the author intends to propose a model of porosity layering and its wavy behavior.

First, assuming the dissolution and precipitation process of metamorphic /metasomatic minerals in the homogeneous rocks under the differential stress condition. In the deviatoric stress conditions, homogeneous rocks have many microcracks of type I which are aligned to be perpendicular to minimum stress orientation as shown in Fig. 4.35. These microcracks commonly occur along the grain boundary of constituent minerals. Toriumi et al. (1986) clarified common occurrence of these microcracks filled with fluid by means of TEM. According to their studies, there are abundant lens like pores along the grain boundary which are filled with fluid. The orientation of these lens is normal to the minimum stress orientation, and, thus it suggests that the permeability of fluid flow should be anisotropic and keeps maximum along with the direction of the maximum stress. It seems that the large fluid flux is to be perpendicular to the schistosity and stretching lineation of the schists. Therefore, it leads that fluid flow, dissolution, and precipitation of constituent, minerals and resultant pore population change are simplified to be 1D spatial variation of porosity with time as shown in Fig. 4.36.

Let us formulate the dissolution and precipitation kinetics introduced by Lasaga (1998). The compositional change by mineral dissolution in pore solution along the grain boundary holds

$$\partial(\phi C_i)/\partial t = k(A/M)\Sigma_i(C_i - C_{i,e}) - \partial(qC_i)/\partial z \quad (\text{mass balance of } i - \text{component})$$

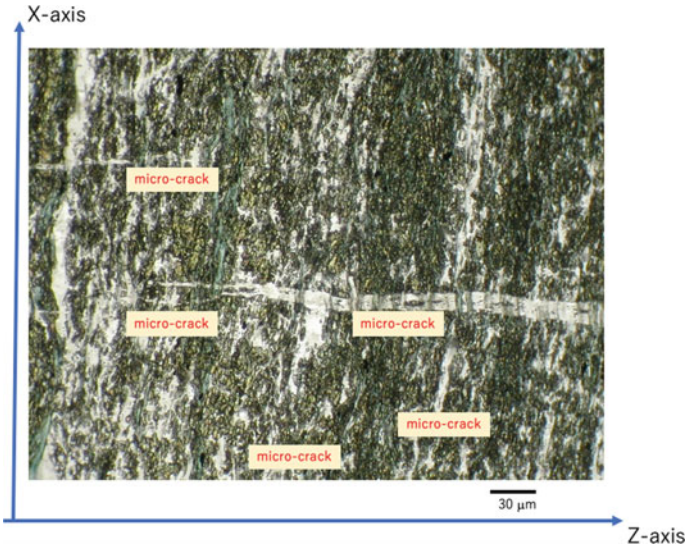

Fig. 4.35 Photograph showing the sealed microcracks in the basic schists of the Sanbagawa metamorphic belt. Notice that the open cracks display the alignment perpendicular to the schistosity plane (//shortening orientation; *z*-axis)

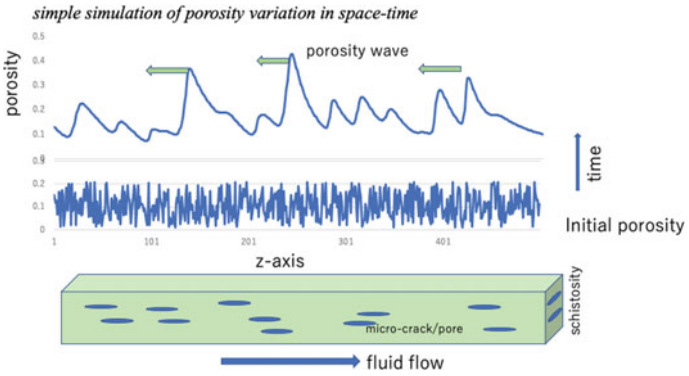

Fig. 4.36 Initial condition (random distribution of porosity) and simple one-dimensional model of dissolution of quartz and formation of pore in the flow system of grain boundary aqueous solution along the shortening axis (*z*-axis) through open microcracks showing the upward migration of developing porosity wave (see text)

$$\partial\phi/\partial t = -\partial(q\phi)/\partial z + \phi(\partial C_i/\partial t) + D\Delta\phi \quad \text{(mass balance of water)} \qquad (4.55)$$

and

$$A/M = 2\phi/\rho_s ar \text{ (geometrical relation)}$$

Here, A and M are the total pore surface and present rock volume, ϕ is the porosity, a and r are the aspect ratio and average radius of pore, and C_i and $C_{i,e}$ are the concentration of solute ion i and equilibrium concentration of i-th ion of present mineral, and D is the diffusion coefficient.

The change of pore volume ($\mathrm{d}V_p$) by dissolution of minerals is constrained by the change of dissolution mass ($\mathrm{d}M_i$) of minerals and concentration change above as follow

$$\mathrm{d}Mi = m_i V_p \, dC_i/v_i \tag{4.56}$$

in which mi and vi are molecular weight and molecular volume of dissolution minerals, respectively.

On the other hand, pore volume change becomes

$$\begin{aligned} \mathrm{d}V_p/\mathrm{d}t &= (v_i/m_i)\,\mathrm{d}M_i/\mathrm{d}t \\ &= V_p\,(\mathrm{d}C_i/\mathrm{d}t) \end{aligned} \tag{4.57}$$

and because it is $V_p/V = \phi$, then we have,

$$\mathrm{d}\phi/\mathrm{d}t = \phi(\mathrm{d}C_i/\mathrm{d}t) \tag{4.58}$$

Therefore, we have

$$\mathrm{d}\phi/\mathrm{d}t = k\,\phi^2 \delta C_i \tag{4.59}$$

On the other hand, pore is filled with solution, and flux of solution q_{sol} is controlled by Darcy's law as

$$q_{\mathrm{sol}} = k_1 \phi^2 \mathrm{grad}\, p_f \tag{4.60}$$

and volume change of fluid due to accumulation of fluid is

$$\begin{aligned} \partial\phi/\partial t &= -\partial q\phi/\partial z + D\Delta\phi \\ &= -K\,\mathrm{d}(\phi^2\,\mathrm{grad}\,p_f)/\partial z + D\Delta\phi \end{aligned} \tag{4.61}$$

On the other hand, grad p_{f} becomes,

$$\mathrm{grad}\, p_f = (\mathrm{d}\phi/\mathrm{d}z)\,(\mathrm{d}p_f/\mathrm{d}\phi) \tag{4.62}$$

Then, the total change of porosity becomes,

$$\partial\phi/\partial t = K\prime_1\phi^2\delta C_i - K\prime_2\partial(\phi^2(\mathrm{d}\phi/\partial z)(\mathrm{d}p_f/\mathrm{d}\phi))/\partial z + K'_3\Delta\phi \tag{4.63}$$

Here, $V_p\, p_f = V\,\phi\, p_f =$ constant, because of pore filled with fluid and very small porosity, and small degree of the oversaturation. Then,

$$\mathrm{d}p_f/\mathrm{d}\phi = \text{constant} \times 1/\phi$$

$$\partial\phi/\partial t = K_1\,\phi^2 + K_2\Delta\phi + K_3(\mathrm{grad}\,\phi)^2 \tag{4.64}$$

This is the master equation for porosity change in the single dissolution–precipitation process in the pores.

Next, let us consider the system that pore formation by dissolution of mineral and mineral banding by precipitation in the solution flow through pores and microcracks. Basically, the pores in the metamorphic rocks should be filled with fluid phase and fast path of the fluid flow during metamorphism. Further, the pores are formed both by dissolution of minerals into solution and by crack opening by differential stress condition. In accordance with change of pore volume by dissociation and subcritical crack growth, the volume of fluid phase changes by fluid flow through pores and microcracks. Then the volume of fluid phase (solution) is approximated to be the volume of pores and microcracks, indicating the mass balance equation of fluid phase equivalent to the phase balance of pores involving microcracks.

The fundamental equations are composed of conservation laws of fluid, dissolution and precipitation components, and momentum.

The conservation conditions with dissolution and precipitation of minerals become,

$$\partial\phi/\partial t + \partial\phi q/\partial z = D\Delta\phi + \phi\,\partial(C_d/k_3 + C_p/k_4)/\partial t \quad \text{(water conservation)}$$

$$\partial\phi C_d/\partial t + \partial(\phi C_d\, q)/\partial z = k_1\, A/M\,\phi\,(C_d - C_{d,e})C_{d,e} + D_1\Delta(C_d\phi) \tag{4.65}$$

$$\partial\phi C_p/\partial t + \partial(\phi C_p\, q)/\partial z = k_2\, A/M\,\phi\,(-C_p + C_{p,e})/C_{p,e} + D_2\Delta(C_p\phi)$$

$$\phi\partial C_p/\partial t = k_3\,\partial v_p/\partial t$$

$$\phi\partial C_d/\partial t = k_4\partial v_d/\partial t$$

and, momentum equation is,

$$q = k_5\phi^2\mathrm{grad}\,p_f \tag{4.66}$$

geometrical relation becomes,

$$A/M = k_6\phi$$

In these equations, ϕ is porosity, q is flux of fluid, v_p and v_d are volumes of precipitation and dissolution minerals, C_p and C_d are concentration of their components in solution, and $C_{p,e}$ and $C_{d,e}$ are equilibrium concentration of them. The terms of k_1 to k_6 are the constant coefficients, and D_1 and D_2 are diffusion coefficients of p and d components.

Assuming small perturbation of flux d_q and small concentration of C_p and C_d, the equations become by ignoring the second order of small values,

$$\begin{aligned}(1 + C_d)\partial C_d/\partial t &= \partial C_d/\partial t \\ &= K_1(C_{de} - C_d)/C_{de} - K_3 q_o \nabla C_d - C_d(\partial C_p/\partial t) \\ &\quad + K_5 \Delta C_d\end{aligned}$$

$$\begin{aligned}(1 + C_p)\partial C_p/\partial t &= \partial C_p/\partial t \\ &= K_2\left(-C_{pe} + C_p\right)/C_{pe} - K_4 q_o \nabla C_p + C_p(\partial C_d/\partial t) \\ &\quad + K_6 \Delta C_p\end{aligned}$$

$$\partial\phi/\partial t = \phi\,\partial(C_d/k_3 - C_p/k_4)/\partial t - K_7\nabla\phi$$

$$q = q_o + \delta q$$

$$\phi\partial C_p/\partial t = k_3\partial v_p/\partial t$$

$$\phi\partial C_d/\partial t = k_4\partial v_d/\partial t \tag{4.67}$$

in which K_1 to K_7 is the constant term, and q_o is the average flux of aqueous fluid.

In order to obtain the characteristic features of the time–space variation of the dissolved minerals, precipitated mineral, and porosity in the simple aqueous flow with small velocity perturbation, simulation study of above equations will be carried out in the one-dimensional system with periodic boundary condition and equal constant terms between minerals using simple discrete time and space method. The results are shown in Fig. 4.37, thereby suggesting that the amounts of porosity and precipitating mineral develop with time and space as the waveform appearance, and thus in this book, these are called as porosity wave and mineral band hereafter, respectively.

It is also noteworthy that the porosity wave and mineral bands migrate toward the upstream of the aqueous flow as displayed in Fig. 4.37. Furthermore, it is obvious that the band width of the large bands and distance between neighboring bands increase with simulating time and consuming the surrounding small band. Thereby, the characteristic features of the dynamics studied here are inferred possibly to be the distance

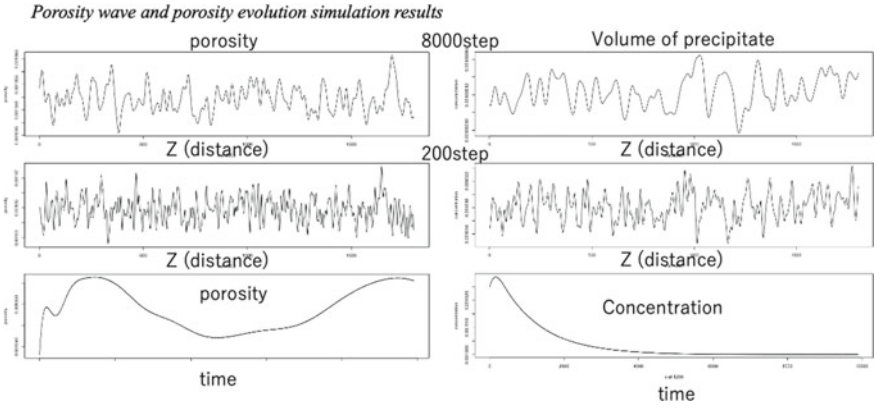

Fig. 4.37 Simulation results of the one-dimensional model involving porosity, dissolution dominant mineral and precipitation dominant mineral showing the evolution of the porosity distribution and of the mineral precipitate against the distance of the flowing column and displaying the temporal variation of the porosity and concentration of component ions in solution

between mineral bands and their band width, suggesting the possible application for natural metasomatic bands described in the earlier sections to investigate the time scale for the migrating mineral bands (Fig. 4.38).

As seen in Fig. 4.39, it is clarified that the mineral bands and the band distance simulated here are classified into two clusters: one is the ratio about 1 of the band width by the band distance, and the other the ratio about 0.1. This means probably that the former seems to be migrating and growing bands and the latter does the isolated bands.

Next, the author will try to study the behavior of the porosity change of 1D system, because the permeability by lens like pores along the grain boundary shows anisotropic features of orientation perpendicular to the schistosity plane as described in the previous section. In this simulation study, the 1D axis is taken to be parallel to the highest permeability orientation.

First, we consider the initial condition that the random porosity distribution appears along the 1D section perpendicular to the schistosity plane as shown in Fig. 4.36. The simulations in the case of various K_1 and K_2 were performed in order to obtain the general trends of the solution of above equation. The representative results of simulations reveal the advancing wave with increasing amplitude and wavelength and the distinguishing wave with small amplitude and wavelength as displayed in Fig. 4.37. It shows that the porosity wave is repeating function on time and space. As shown in Fig. 4.37, the porosity of the given position changes repeatedly with time in the range of 0.1–0.3, and the porosity wave migrates gradually toward the upper portion of the solution flow in the ine-dimensional coordinate. Furthermore, it concludes that the initial randomized variation of porosity diminishes after 200–400 steps in the simulation. Thus, the periodic wave of the porosity change should be the stable solution of the present nonlinear PDE.

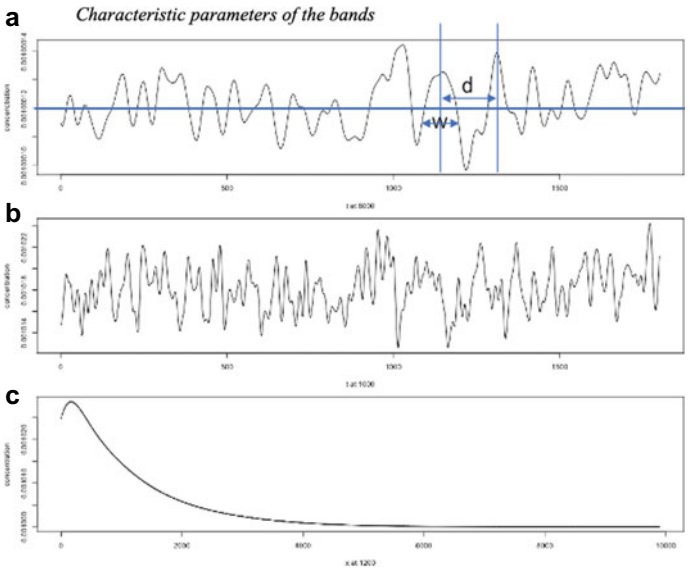

Fig. 4.38 Characteristic feature parameters of the simulation results to be compared with the natural mineral bands of the plate boundary rocks. **a** Enough developed mineral band pattern, **b** early stage of simulation results of mineral band pattern, **c** temporal variation of ionic concentration in solution. The parameters are width d and distance d between neighboring bands

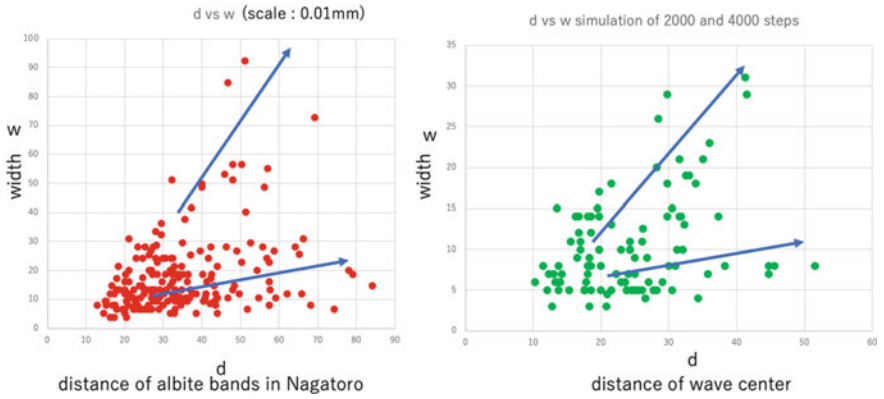

Fig. 4.39 Comparison between the albite bands in natural (left) and the precipitate bands in simulation (right) showing two patterns of developing bands. It is noticed that the distance of the natural albite band means the distance between the neighboring band walls but in the simulation result, the distance does that between the neighboring precipitate wave center, and thus, the slope of two trends in both figures is the same with each other

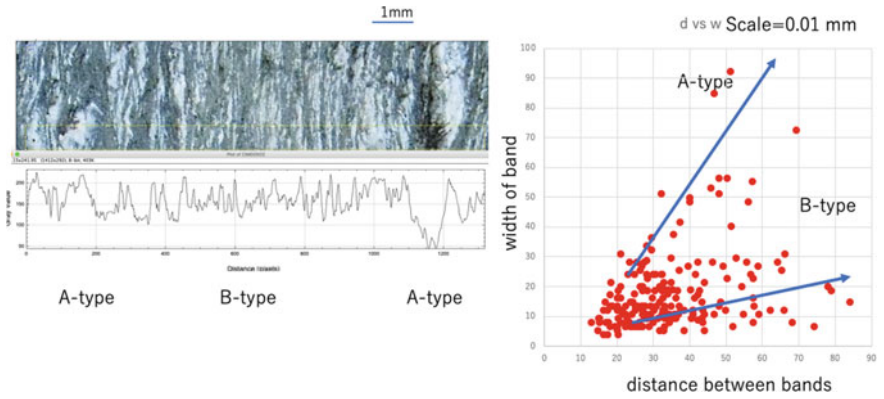

Fig. 4.40 Classification of two types of band dynamics: one is the A-type showing the thick and small density of bands and B-type thin and frequent bands. Left figure shows the photographs of their occurrence in the outcrop

In Fig. 4.37, the spatial pattern showing the various porosity waves also varies with advancing time: the porosity waves having short wavelength become adsorbed by neighboring large porosity wave which grows its amplitude and wavelength. In this figure, it seems that there are several types of porosity wave with different migration velocity. Many of large porosity wave show the large migration velocity toward the upper stream. But the small wave shows rather low velocity, and thus, it disappears in the large one.

According to this tendency, it should be considered that there exists relationship between the wavelength and distance of peak to peak of the neighboring porosity wave. In order to clarify the present relationship between them, simulations of 2000 samples for x-axis have been performed and the peak-to-peak distance and width of porosity wave were measured as shown in Fig. 4.38. In Figs. 4.39 and 4.40, the representative relationship between them can be classified into two patterns: one shows sharp increase of width with increasing distance of neighboring peaks and the other keeps small width even with increasing peak-to-peak distance. In this paper, the former is called as the type A porosity wave, and the latter as the type B porosity wave. It seems that the type A porosity wave belongs to the migrating one, but the type B may be the immobile to very slow porosity wave, judging from annihilation and growth of porosity wave being clarified by simulation experiments.

By the way, the mineral bands of albite and chlorite are very commonly observed in the plate boundary metamorphic and metasomatic rocks such as Sanbagawa and Shimanto belt in SW Japan as described in the earlier sections. In this section, the relations of the band width and band distance mentioned above will be investigated, for the metamorphic and metasomatic banding which is parallel to the schistosity plane and nearly to the shear crack orientation. Judging from the finite strain pattern of these metamorphic rocks determined by the deformed radiolarian fossils abundant in metamorphosed chert and mudstone (Toriumi and Noda 1986; Toriumi and Teruya

1988), the permeable flow of aqueous solution is almost always perpendicular to the schistosity plane. It is also supported by the lens like micro pores commonly oriented normal to the schistosity plane in the grain boundary of minerals under the transmission electron microscope (Toriumi et al. 1986).

It is clear in Fig. 4.40 that there are two types of the relationship between the band distance and band width in the Sanbagawa metamorphic rocks in SW Japan, being likely to the relations obtained by the simulation studies above. Therefore, it seems to conclude possibly that the metamorphic mineral bands of albite and chlorite together with epidote which are parallel to the schistosity plane are formed by the porosity—precipitation—dissolution dynamics with aqueous fluid flow which is mainly perpendicular to the schistosity plane of the plate boundary rocks.

4.6 Time Scale of Konpeito-Like Flower Grain Growth and Fluid Flow

Mineral grains display various shape from euhedral to anhedral grain shape. This morphology of the mineral grains in the metamorphosed rocks from igneous to sedimentary rocks means their growth mechanism almost always controlled by the replacement of preexisting mineral grains through aqueous fluid. As shown in the previous chapters, the author stressed that the metamorphic and metasomatic reactions in the plate boundary zone is strongly governed by the aqueous fluid flow with dissolution and precipitation of relevant minerals in rocks and the fluid comprises with micro to nano-scale pores and voids associated with shear crack jog and open crack. Therefore, it is clearly obvious that the permeable flow of aqueous solution should be controlled by the porosity and open crack density and their connectivity.

The grain boundary of constituent minerals in metamorphic rocks is partly occupied with small lenses of aqueous solution as observed by TEM and exemplified by the occurrence of pressure shadow around garnet and magnetite filled by quartz and chlorite. Thus, during the metamorphic reactions among preexisting minerals, it should take place that the grains of metamorphic minerals grow through the aqueous solution in the grain boundary. If it is the case, the morphology of that grain should be controlled by the diffusivity of soluble components, fluid flow rate, and degree of supersaturation of minerals.

There appears common occurrence of flower-like shape of garnet, albite, and quartz which is surrounded by the matrix minerals such as chlorite, micas, and amphiboles in the regional metamorphic rocks, and dendritic grains of cordierite, garnet, staurolite and plagioclase in the contact metamorphic rocks of thermal aureole. The latter is probably due to the rapid growth under the high degree of supersaturation, but the former is surely derived from the growth instability as like as the formation of icicle and hail which is characterized by regular spikes. This type of grain shape appears in the Japanese classic sugar ball something like small cake called as

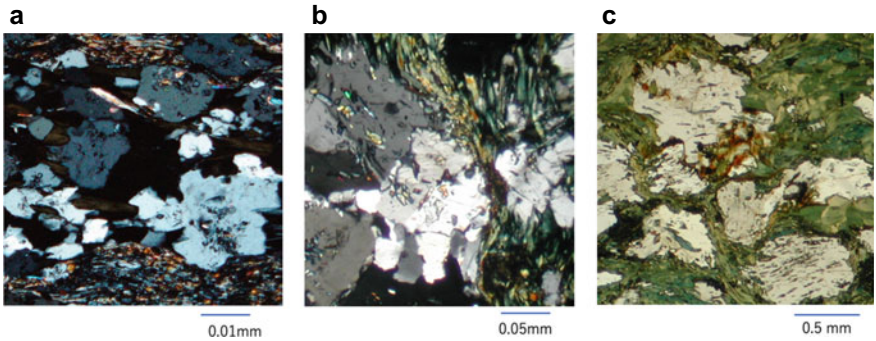

Fig. 4.41 Photographs showing the flower-shaped grains of albite in albite band **a** matrix albite, **b** and porphyroblastic albite, **c** in Sanbagawa basic schists

konpeito in Japan which has also the periodic spikes on the surface. In this book, the author intends to call this type of flower-like grain as the konpeito grain hereafter.

In the earlier sections, the metasomatic instability of the albite bands replacing surrounding chlorite bands and grain growth of quartz and albite in the open cracks were discussed in terms of the instability of the growth interface by the rate competing of surface tension and oversaturation degree through diffusion and growth velocity contrast which is called as the Mullins and Sekerka instability.

In the case of konpeito growth of porphyroblastic garnet and albite grains in the fluid assisted metamorphism, the waveform of growing interface should be due to this MS instability relevant to the aqueous fluid flow during metamorphism. In this context, it is possible that the growth time scales of konpeito-like porpyroblastic grains of albite and garnet are inferred from the characteristic spike distance depending upon the growth velocity with capillary term as seen in the previous chapters.

First, let us look at the morphology of the porphyroblastic grains of garnet and albite in metamorphic rocks in the Sanbagawa belt. As seen in Fig. 4.41, the porphyroblastic grains of albite display the flower-like and konpeito-like grain shape, and these are surrounded by mainly chlorite. Considering that the grain growth of albite should advance with its replacement after surrounding chlorite, the waveform of interface between them is responsible for the mechanism like metasomatic instability development between albite and chlorite bands discussed in the previous sections.

As same as the case of interface instability of albite and chlorite bands, the stability map of albite and chlorite is determined by the following chemical reaction involving aqueous solution,

$$2NaAlSi_3O_8 + 3Mg^{2+} + 2H_2O = Mg_3Al_2Si_3O_{10}(OH)_4 + 2Na^+ + 4H^+ + 3SiO_2$$

$$\begin{aligned} \Delta G/RT &= \ln\ K \\ &= \ln\ X^3_{Mg2+}/\left(X^2_{Na+}X^4_{H+}X^3_{SiO_2}\right) \end{aligned}$$

$$= 3 \ln X_{Mg2+} - 2 \ln X_{Na+} - 3 \ln X_{SiO_2} + 4pH \tag{4.68}$$

and then it holds,

$$\ln X_{Mg2+} = 2/3 \ln X_{Na+} + \ln X_{SiO_2} - 4/3 pH + 1/3 \Delta G/RT \tag{4.69}$$

in which K and ΔG are the equilibrium partition coefficient and Gibbs free energy change of this chemical reaction. According to above equation, it is obvious that the linear relation between ln X_{Mg2+} and lnX_{Na+} shift with changing ln X_{SiO_2} and pH or temperature and pressure. Therefore, the interface between albite and chlorite becomes unstable by changing the concentration of aqueous SiO_2 and pH, and if diffusion of Na^+ is much faster than Mg^{2+} in the aqueous solution, the slope of the d ln X_{Mg2+}/d lnX_{Na+} is larger than that of equilibrium line defined by above equation as shown in Fig. 4.23. In the case, the Mullins–Sekerka instability should take place in the interface, and it results in development of the waveform boundary showing the characteristic wavelength as like as that in the case of metasomatic instability discussed in the earlier section as,

$$\lambda = k V^{-1/2} \tag{4.70}$$

in which V is the interface migration velocity, and k is a constant depending on the temperature and degree of oversaturation about the equilibrium boundary in the ln X_{Mg2+} and ln X_{Na+} diagram. In the isothermal condition, the change of X_{SiO_2aq} and pH in aqueous fluid controls the degree of oversaturation at the interface between chlorite and albite bands.

In the model of MS instability for the interface waveform, the wavelength should be governed by the interface migration velocity so that the spatial inhomogeneity in growth velocity of albite and garnet porphyroblastic grains is possibly investigated by the wavelength measurements of the konpeito-like grains of them in the rocks. In order to study the inhomogeneous distribution of the grain growth rate in the rocks accompanied with fluid flux, the general relations between the grain size and wavelength of wavy interface of porphyroblastic albite and garnet are to be required. In Fig. 4.42, the logarithmic relations between grain diameter and wavelength of konpeito-like grains of albite and garnet are shown, thereby displaying that the relations appear obviously linear between them as like as the case of typical konpeito growth of sugar and hail (Sakai and Hayakawa 2006).

As being indicated above, the wavelength of the waveform interface in the case of konpeito and flower-like grains of albite and garnet increases with the inverse of square of the growth velocity, and so that the very slow boundary migration rate results in the growth by flat interface of singular surface of minerals showing the euhedral shape of minerals. On the other hand, if the growth velocity is very high, the interface of the rapid growth of the grain shows so-called rough interface, and in some cases, it appears probably a dendritic shape.

As is seen in Fig. 4.43, there seems to be a linear relation with slope of 0.9 between

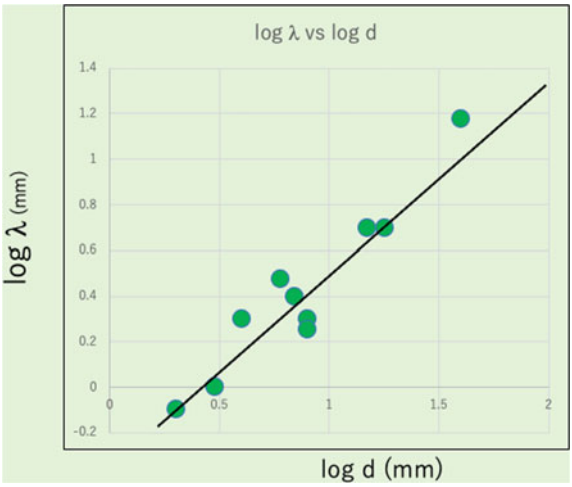

Fig. 4.42 Diagram of the logarithmic average distance of spikes and the grain size of the flower-like albite of the Sanbagawa basic schists showing the linear relation between them

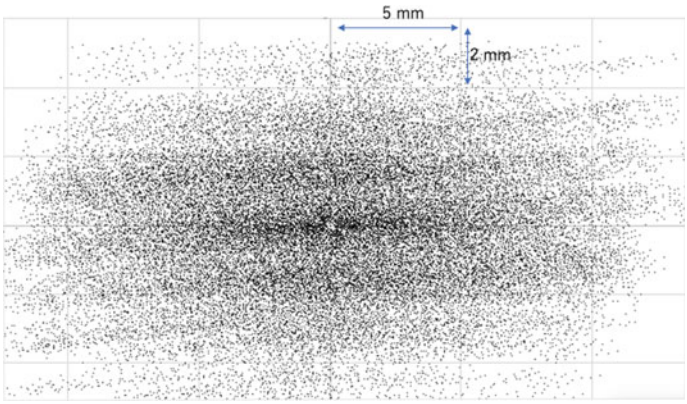

Fig. 4.43 Map of the center-to-center correlation of the porphyroblastic grains of albite in basic schist of the Sanbagawa metamorphic belt, showing the layer structure and oblique small cluster of them

the wavelength (λ) of the interface between albite and chlorite and grain diameter (D) of albite in the logarithmic diagram, thereby indicating that the growth velocity of them seems to be governed by the power law of growth as,

$$\log \lambda = 0.9 \log D - 3.6 \tag{4.71}$$

and then, because of $\lambda = k V^{-1/2}$, it holds,

$$\mathrm{d}D/\mathrm{d}t = A D^{-1.8} \tag{4.72}$$

where A is constant.

Therefore, the grain growth law of albite porphyroblast becomes,

$$D^{2.8} - D_o^{2.8} = k\,t \tag{4.73}$$

in which k is a constant term.

On the other hand, the actual velocity V should be inferred from the boundary migration of the albite bands discussed in the previous chapter. Applying the relations of the wavelength of the albite band against chlorite band shown in Fig. 4.30, the growth velocity of the poryphyroblastic grains of albite is possibly obtained to be about 10^{-3} mm/y. Therefore, the time scale of the porphyroblastic grains of albite with diameter of 1 mm is commonly estimated to be around 1000 years. This time scale of common grains of albite porphyroblast seems likely to that of the albite bands in the lower temperature zones of the Sanbagawa metamorphic rocks.

By the way, it should be noteworthy that the grain growth law of the albite mentioned above is not likely to that by Ostwald ripening mechanism that satisfies the relation of $\mathrm{d}R/\mathrm{d}t = MR^{-1}$ (R is grain size and M is mobility). On the other hand, the diffusion limited growth is required for the $\mathrm{d}R/\mathrm{d}t = KR^{-2}$, and thus, it seems probable that the kompeito growth of albite should be governed by growth mechanism controlled by diffusion, being consistent with the Mullins–Sekerka process of capillary effect of growth. On the other hand, is it possible weather this model can explain the formation of grain size grading texture of the albite porphyroblast in the metamorphic rocks?

First, let us look at the occurrence of porphyrobastic albite grains in the plate boundary metamorphic rocks. As shown in Fig. 4.22, the banding structure of layers rich in albite porphyrobastic grains in basic and pelitic schists is nearly parallel to the schistosity plane. The modal composition of the albite grains in the single layers gradually decreases toward the upper and lower boundaries of albite rich layer. In addition, there are commonly found the albite-rich clusters in these single layers, forming the platy aggregate oblique to the layer and lenses parallel to the layer. This type of feature can be clearly found in the center-to-center correlation map as shown in Fig. 4.43, displaying the distinctive layer structure and clusters in the layer.

According to the kompeito growth model of albite porphyroblast mentioned above, the instability is probably responsible for the water–mineral reaction between chlorite and albite with limited diffusion of aqueous species of SiO_{2aq}, Na^+, Mg^{2+} even under the constant temperature and buffered pH. Especially, it seems that the instability of this metasomatic reaction is responsible for the high Na^+ and low Mg^{2+} ionic diffusion in aqueous pore fluid and the concentration gradient of X_{SiO_2aq} across the albite rich layer. As indicated in the previous sections, the aqueous solution reacting with minerals flows through pores and grain boundary toward the orientation perpendicular to the schistosity plane. Therefore, the degree of supersaturation defined by X_{SiO_2aq} related to the above albite and chlorite reaction should vary in the direction perpendicular to this schistosity plane, thereby suggesting that the boundary

migration rate between chlorite and albite should also change together with variation of the supersaturation degree, as shown in Fig. 4.23.

Therefore, the pattern of grain size grading may be a potential indicator of the concentration patterns of SiO_{2aq} so that the relationship between the distance from a fixed point to the layer rich in albite and the grain size of the porphyroblastic grains was measured as shown in Fig. 4.19. It suggests that the grain size of albite shows the pattern like waveform in the spatial coordinate normal to the schistosity plane suggesting the waveform concentration pattern of X_{SiO_2aq} and/or pH because of coeval mineral reaction between albite and chlorite with aqueous solution in the rocks. This pattern of the concentration of aqueous components may be due to advection of aqueous solution and accompanied diffusive migration of their components. The simulation results of the dissolution—precipitation—advection of aqueous solution model discussed in the previous section look like the one-dimentional pattern of the grain size grading above, thereby being consistent with the above interpretation of the grain size grading phenomena.

Moreover, it will be possible that the advection velocity of aqueous fluid across the schistosity plane is inferred by application of time scale rule of Liesegang bands as mentioned previously and grain growth of konpeito grains of albite (1000 years for 1 mm diameter) as,

$$V_f = X_R/t$$

$$R^3 = k\,t$$

and

$$V_f = k\,X_R/R^3 \tag{4.74}$$

in which X_R is the characteristic distance of large albite rich layer, k is the grain growth coefficient for diffusion limited growth of albite, and V_f is the velocity of fluid.

For 1 mm of albite and 10 mm of characteristic distance, it takes 1000 years as estimated in the previous section. Thus, k is approximated to be $k = 10^{-3}$ mm^3/year, and then, V is estimated to be about 10^{-2} mm/y (3.2×10^{-10} mm/s). If fluid flow across the large earthquake shear fault is the case of this permeable flow, the time scale of 100 m migration of fluid into the shear fault seems to be required about 1000 years which is comparable for recovery time scale of the giant earthquake.

On the other hand, there is common occurrence of grain size grading, and konpeito-like grains of garnet in the plate boundary metamorphic rocks (Fig. 4.44). Garnet occurs commonly as euhedral shape in pelitic and basic metamorphic rocks, and it sometimes appear the waveform interface on (110) singular surface as like as small growth spike (Fig. 4.45). Furthermore, garnet display the distinctive compositional zoning across the core to the rim. This compositional zoning is commonly imaged

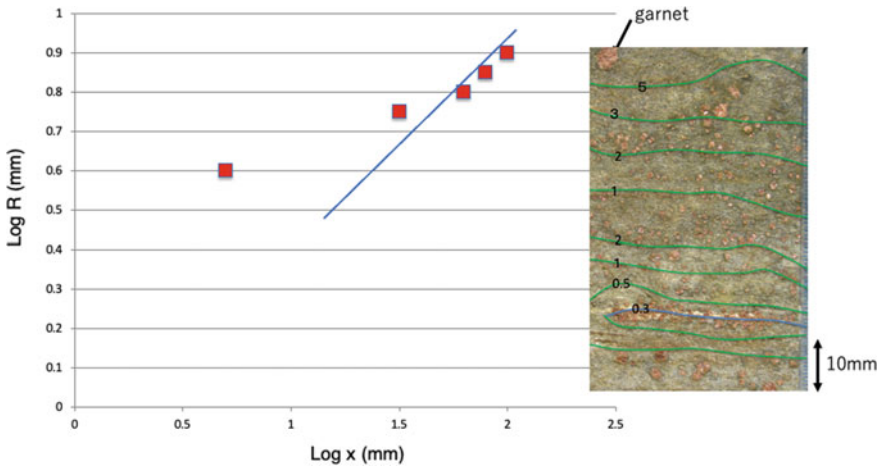

Fig. 4.44 Photograph of size grading of garnet grains in the Sanbagawa metamorphic schists and diagram of the grain size and distance between garnet rich layers in the logarithmic diagram. Number in the photograph is average grain size of garnet

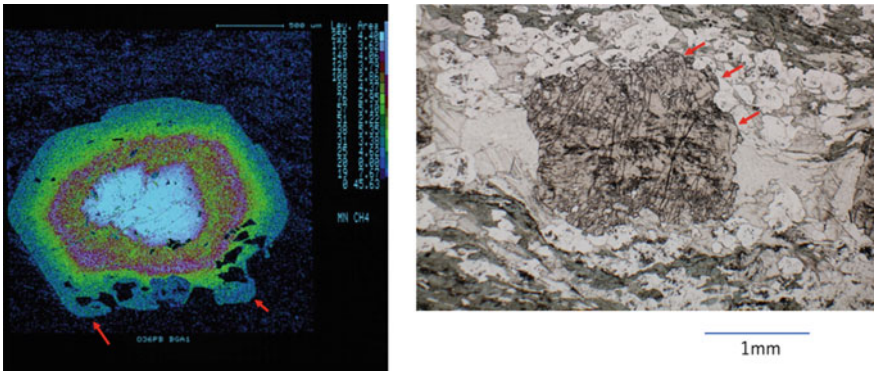

Fig. 4.45 Map of Mn concentration of garnet (left) showing small spikes of inner growth interface identified by color contrast and the photographs of large and flower-like grain of garnet in the basic schists of the Sanbagawa metamorphic belt

by electron probe microanalyzer on the cutting plane, and the image of Ca often manifests the growth interface assigned by the sharp contrast of (110) with low spike in the schists metamorphosed in the condition lower than the amphibolite facies (about 600 °C). These grains of garnet also show commonly wavy outline of near (110) and (111) surface against chlorite, quartz, and micas, even though these appears roughly euhedral. The undulated spiked surface of the porphyroblastic garnet grains were measured and the diagram of grain size vs spike distance of peak to peak of undulation as shown in Fig. 4.46, indicating the slope about 0.88 on logarithmic grain diameter vs wavelength diagram. This slope is likely to that of the case of

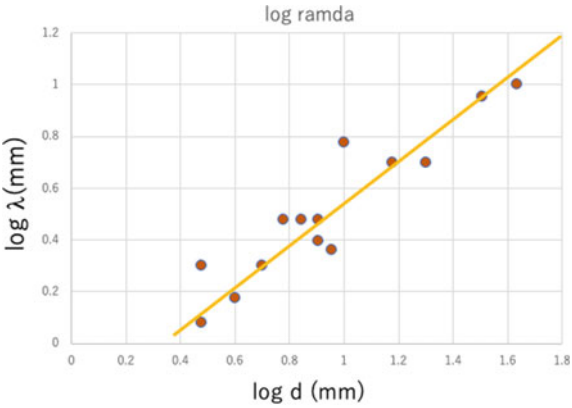

Fig. 4.46 Diagram of the spike spacing and diameter of flower-like grain of garnet in logarithmic diagram showing the linear relation between them

albite porphyroblastic grains. In the case of garnet growth by consuming chlorite, the reaction with aqueous solution appears as,

$$\underset{\text{garnet}}{Fe_2MnAl_2Si_3O_{12}} + 2Mg^{2+} = \underset{\text{chlorite}}{Mg_2FeAl_2Si_3O_{10}(OH)_4} + Fe^{2+} + Mn^{2+} + 2H_2O$$

$$\Delta G/RT = \ln\left(X^2_{Mg2+}/X_{Fe2+}X_{Mn2+}\right)$$

in which chemical compositions of garnet and chlorite are assumed to be constant for simplification of the reaction. If it is necessary, the activities of end components of garnet and chlorite should be involved in the equation above.

In the diagram of $\ln X_{Mg2+} - \ln X_{Fe2+} - \ln X_{Mn2+}$, the phase relation appears as equilibrium line with slope = 2. Therefore, when the concentrations of X_{Fe2+} and X_{Mn2+} in aqueous solution change locally by advection (fluid flow), garnet or chlorite should grow at the expense of chlorite or garnet, respectively. Further, as there is a difference of diffusivity among Mg^{2+}, Fe^{2+}, and Mn^{2+}, the boundary between them should be unstable in the case of rather rapid growth velocity. Then, as like as the case of albite, the MS instability should appear in the growing interface of garnet with characteristic wavelength against grain size relevant with growth velocity.

Therefore, the growth velocity becomes,

$$dR/dt = A\,R^{-1.76} \tag{4.75}$$

and thus, the growth law holds,

$$R^{2.76} - R_o^{2.76} = k_g t \tag{4.76}$$

in which k_g is a constant that depends on temperature and supersaturation degree.

Garnet, however, in many metamorphic rocks is considered to grow in the process of increasing temperature and pressure, judging from that the compositional zoning of garnet shows the increase in Mg and Fe contents but decrease in Mn content from the core to the rim. Applying the differential thermodynamics for the equilibrium conditions of garnet, chlorite, quartz, albite, biotite, and magnetite in the multicomponent system, the growth zoning of the garnet grains clearly indicates the gradual increase of temperature and pressure from the core to the rim (Inui and Toriumi 2002). On the other hand, it seems strange that this type of pressure–temperature path estimated by large grains of garnet is just likely to that done by small grains. It apparently suggests the grain growth velocity of large grains faster than that of small ones. If the grain size distribution of garnet should show spatially random pattern, a homogenous temperature and pressure change in the single rock specimen might still produce a various grain size distribution. However, instead of such spatial distribution of grain size, there is common occurrence of layered structure of grain size of garnet called as grain size grading in this book in the various plate boundary metamorphic rocks, thereby implying that the layered structure of the grain size should be due not to the temperature and pressure but to the concentration variation of aqueous components such as Mg^{2+}, Fe^{2+}, Mn^{2+}, SiO_{2aq}, and others.

On the other hand, it remains that the time scale of garnet growth during the process with increase in temperature and pressure is inferred to be the order of 10^5 years because of pressure difference of the core and rim about 0.4–0.5 GPa (Inui and Toriumi 2002). This time scale is much larger than that of albite porphyroblastic grains. It should be considered that the grain size grading pattern as shown in Fig. 4.44 was formed in the process governed by intermittent and unidirectional aqueous fluid flow accompanied with diffusion of aqueous components around growing garnet grains arising the different growth velocity in each layer. If it is the case, it may be found that the grains of garnet are often experienced by reverse reaction (resorption) to chlorite by the way of their growth process. As is shown in Fig. 4.45, the compositional images of garnet grains by EPXMA display commonly the irregular contour of Ca content and rapid increase of Mn content (so-called reverse zoning) and this fact probably suggests the event of resorption of garnet at once. Therefore, the time scale of the intermittent fluid flow is probably considered to be the same as that of the grain size grading of albite mentioned previously. The intermittent fluid flow was inferred from the rate of growth volume of garnet against the unit pressure change derived from the pressure–temperature path and volume ratio of garnet grains at the finite pressure difference as shown in Fig. 4.47 by Toriumi and Inui (2001).

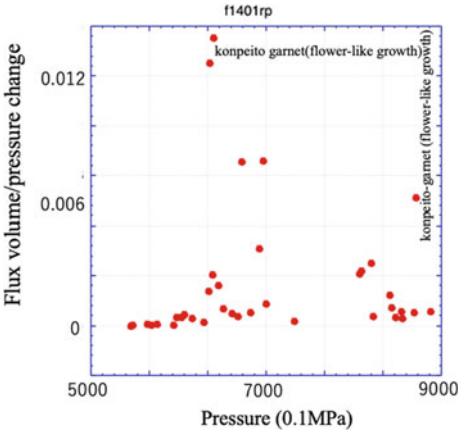

Fig. 4.47 Diagram of fluid flux and pressure showing flower-like growth of garnet at the periods of the high fluid flux rate by unit pressure increase inferred from the chemical zoning of the garnet grains and grain size distribution (see text) showing the high aqueous fluid flux corresponding to flower-like growth of garnet

References

Aoya M, Uehara S, Matsumoto M, Wallis S, Enami M (2003) Subduction stage pressure-temperature path of eclogite from the Sanbagawa belt: prophetic record for oceanic-ridge subduction. Geology 31(12):1045–1048

Cesare B, Ferrero S, Salvioli-Mariani E, Pedron D, Cavallo A (2009) "Nanogranite" and glassy inclusions: the anatectic melt in migmatites and granulites. Geology 37:627–630

Enami M (1983) Petrology of politic schists in the oligoclase–biotite zone of the Sanbagawa metamorphic terrain, Japan: phase equilibria in the highest-grade zone of a high-pressure intermediate type of metamorphic belt. J Metamorph Geol 1:141–161

Fukuyama M, Nishiyama T, Urata K, Mori Y (2006) Steady-diffusion modeling of a reaction zone between a metamorphosed basic dyke and a marble from Hirao-dai, Fukuoka, Japan. J Metamorph Geol 24:153–168

Hiroi Y, Yanagi Y, Kato T, Kobayashi B, Prame T, Hokada M, Satish-Kumar M, Ishikawa T, Adachi Y, Osanai YM, Shiraishi K (2014) Supercooled melt inclusions in lower-crustal granulites as a consequence of rapid exhumation by channel flow. Gondwana Res 25:226–245

Igzak F, Lagzi I (2005) A new universal law for the Liesgang pattern formation. J Chem Phys 122:184707

Inui M, Toriumi M (2002) Prograde pressure–temperature paths in the pelitic schists of the Sanbagawa metamorphic belt, SW Japan. J Metamorph Geol 20:563–580

Inui M, Toriumi M (2004) A theoretical study on the formation of growth zoning in garnet consuming chlorite. J Petrol 45:1369–1392

Irifune T, Ringwood AE, Hibberson WO (1994) Subduction of continental crust and terrigenous and pelagic sediments. An experimental study. Earth Planet Sci Lett 126:351–368

Ishii T, Kojitani H, Akaogi M (2012) High-pressure phase transitions and subduction behavior of continental crust at pressure–temperature conditions up to the upper part of the lower mantle, Earth Planet. Sci Lett 357–358:31–41

Itaya T, Tsujimori T, Liou JG (2011b) Evolution of the Sanbagawa and Shimanto high-pressure belts in SW Japan: insights from K-Ar (Ar-Ar) geochronology. J Asian Earth Sci 42:1075–1090

Itaya T, Tsujimori T, Liou JG (2011a) Evolution of the Sanbagawa and Shimanto high-pressure belts in SW Japan: insights from K-Ar (Ar-Ar) geochronology. J Asian Earth Sci 42:1075–1090

Jamtveit B, Anderson TB (1992) Morphological instabilities during rapid growth of metamorphic garnets. Phys Chem Miner 19:176–184

Karato S (2008) Deformation of earth materials: an introduction to the rheology of solid earth. Cambridge University Press
Karato S, Toriumi M, Fujii T (1980) Dynamic recrystallization of olivine single-crystals during high-temperature creep. Geophys Res Lett 7(9):649–652
Kurtz W, Fisher DJ (1986) Fundamentals of solidification. Trans Tech Publications Switzerland, 249p
Lagzi I (2005) Liesegang patterns: complex formation of precipitate in an electric field, Pramana. J Phys Indian Acad Sci 64(2):291–298
Lasaga A (1998) Kinetic theory in the earth sciences. Princeton Univ, Press
Li Y-H, Gregory S (1974) Diffusion in ions in sea water and in deep-sea sediments. Geochim Cosmochim Acta 38:703–714
Maruyama S, Masago H, Katayama I, Iwase Y, Toriumi M (2004) A revolutionary new interpretation of a regional metamorphism, its exhumation, and consequent mountain buildings. J Geogr 113:727–768
Maruyama S (1990) Exhumation mechanism of high-pressure metamorphic belt. Geol Soc Jpn 484 (abs.)
Matsumoto K, Toriumi M (1989) Mechanical states of the upper mantle under the island arc as inferred from the microstructures of peridotite xenoliths. In: Karato S, Toriumi M (eds) Rheology of solids and of the earth. Oxford University Press, 374–392
Nakashima Y (1995) Transport model of buoyant metamorphic fluid by hydrofracturing in leaky rock. J Metamorph Geol 13:727–736
Okamoto A, Sekine K (2011) Textures of syntaxial quartz veins synthesized by hydrothermal experiments. J Struct Geol 33:1764–1775
Okamoto A, Toriumi M (2004) Optimal mixing properties of calcic and subcalcic amphiboles: application of Gibbs' method to the Sanbagawa schists, SW Japan. Contrib Mineral Petrol 146:529–545
Okamoto A, Kikushi T, Tsuchiya N (2008) Mineral distribution within polyminerali veins in the Sanbagawa belt, Japan: Implications for mass transfer during vein formation. Contrib Miner Petrol 156:323–336
Ortoleva P, Chadam J, Merino E, Sen A (1987) Geochemical self-organization, I: the reactive-infiltration instability. AM J Sc 287:1008–1040
Oyanagi R, Okamoto A, Tsuchiya N (2020) Silica controls on hydration during serpentinization of olivine: Insights from hydrothermal experiments and a reactive transport model. Geochim Cosmochi Acta 270:21–42
Sakai I, Hayakawa Y (2006) Shape selection of kompeitoh. J Phys Soc Jpn 75(10):104802
Spence DA, Turcotte DL (1985) Magma-driven propagation of cracks. J Geophys Res 90 https://doi.org/10.1029/JB090iB01p00575,575-580
Toriumi M (1979) A mechanism of shape-transformation of quartz inclusions in albite of regional metamorphic rocks. Lithos 12:325–333
Toriumi M (1981) Rounded mineral inclusions in upper mantle peridotites. Phys Earth Planet Inter 27:39–46
Toriumi M (1987) Progressive deformation and annealing of quartz inclusion in porphyroblastic feldspar during synmetamorphic non-coaxial deformation. J Jpn Assoc Miner Petr Econ Geol 82:123–131
Toriumi M (1990) The transition from brittle to ductile deformation in the Sambagawa metamorphic belt, Japan. J Metamorph Geol 8:457–466
Toriumi M, Hara E (1995) Crack geometries an deformation by crack-seal mechanism in the Sambagawa metamorphic belt. Tectonophysics 245:249–261
Toriumi M, Inui M (2001) Pressure–temperature–water production rate paths in the subduction metamorphism. Bull Earthq Res Inst Univ Tokyo 76:367–376
Toriumi M, Karato S (1978) Experimental studies on recovery process of deformed olivine and mechanical state of upper mantle. Tectonophysics 49(1–2):79–95

Toriumi M, Noda H (1986) the origin of strain patterns resulting from contemporaneous deformation and metamorphism in the Sanbagawa metamorphic belt. J Metamorph Geol 4(4):409–420
Toriumi M, Teruya J (1988) Tectono-metamorphism of the Shimanto belt. Mod Geol 12:303–324
Toriumi M, Teruya J, Masui M, Kuwahara J (1986) Microstructures and flow mechanisms in regional metamorphic rocks in Japan. Contrib Miner Petrol 94:54–62
Uno M, Iwamori H, Toriumi M (2015) Transition from dehydration to hydration during exhumation of the Sanbagawa metamorphic belt, Japan, revealed by the continuous P-T path recorded in garnet and amphibole zoning, Contrib Miner Petrol 170:33. https://doi.org/10.1007/s00410-015-1185-9

Chapter 5
Mechanics by Synchronous GRACE Gravity, Earth Rotation, Plate Velocity, and Global Correlated Seismicity

Abstract Recent development of earth observation by satellite system and very long baseline interferometry shows enigmatic global change of the gravity, earth rotation, sea level rise, and plate velocity during some decades. Looking their monitoring data, it should be surprising that their temporal variations show the likewise secular trends and annual to near-annual periodic changes suggesting the global change in the fluid earth. On the other hand, the global correlated seismicity as shown in the previous book suggests the likewise temporal variations.

Keywords GRACE gravity C20 · Length of day · VLBI plate velocity · Global correlated seismicity

5.1 Global Monitoring Data and Seismicity

Satellite observatory is now developing as a great monitoring system on the solid earth phenomena, and it especially continues to take a massive data on the precise change of gravitational field, geodesical positioning, and topographic data of sea surface. Especially, the GRACE satellite (Gravity Recovery and Climate Experiment) has founded on 2002 by US-German joint research program to investigate the precise change of gravitational field by global precipitation loading, global ice loading, sea surface degradation and elevation, and global heterogeneity of mass distribution in solid earth (e.g., Chen et al. 2000). Concerning the solid earth elastic and plastic deformation, the GRACE data involve the long-term solid earth deformation which is physically decomposed to the spherical function series, and the mode II of them displays the change of elliptical flattening component of the earth called as the elliptical deformation index. Chen et al. (2005) first estimated the time series of the elliptical index from 1980 to 2002 using the satellite data before the GRACE satellite. After foundation of GRACE, they obtained the time series of them after 2002–2020 and proposed the full times series of the mode II variation from 1990 to 2020 which is quite important to compare the correlated global seismicity rate defined in the previous book of the author (Toriumi 2021).

Furthermore, it is also very important to investigate the solid earth mechanics partially controlled by the astronomical interaction of earth, moon, and sun system

M. Toriumi, *Geochemical Mechanics and Deep Neural Network Modeling*,
Advances in Geological Science, https://doi.org/10.1007/978-981-19-3659-3_5

through their gravitational force that the precise time of the earth rotation because of seismic effect on it from the change in the angular momentum of the rotational earth, and because of elliptical deformation change as mode II gravitational field. Recent length of day (LOD) variation shows the long-term drift with annual variation due to the tidal variation in the earth–moon–sun system. These variations should be relevant to the global and regional correlated seismicity together with the real seismicity as manifested by near-annual periodicity of the correlated seismicity temporal variations (Toriumi 2021), although Chanard et al. (2018) suggested annual periodicity of GNSS variation derived from snow and rainfall precipitation loading and unloading.

As discussed in the previous book (Toriumi 2021), it seems to be available that the long-term variation of the global correlated seismicity can be expressed by a kinetic model in terms of nonlinear differential dynamical phase equations having stable and unstable nodes. In addition, the global correlated seismicity dynamics is possibly decomposed of three to four modes of network systems in the global subduction zones as previously proposed in the book. However, it is afraid that the physical modeling of these empirical representation has not been founded yet. Thus, it is surely required to understand the physical behavior of the earth mechanics network showing the relations between the correlated global seismicity and deformation by solid earth tide, ice and precipitation loading, and evaporation unloading together with global plate motion and related ridge magmatism.

In order to survey the correlation among these global mechanical characters, the huge amounts of accumulating satellite gravity time series, very long baseline interferometry (VLBI) time series, and earth rotation time series are needed for their regression and synchronization of their time series. These time series data are taken by the different sampling time span and associated with different noises. Therefore, in this book, the Gaussian-type regression method with Bayesian parameter fitting (hyperparameter leaning) is adopted for the most likelihood approximation of native data.

The Gaussian regression with Bayesian model (Bishop 2006) in this study holds as,

$$g(t) = \sum w_i g_i(t) = \sum w_i \exp(-(t-t_i)^2/\sigma^2) \tag{5.1}$$

Optimization of weight parameter, w_i should be determined by minimization of following evaluation function of

$$E(w) = 1/2\left(\sum \left(g\left(t_j\right) - g_j^o\right)^2 \right. \tag{5.2}$$

Thus, it becomes,

$$\mathrm{d}E/\mathrm{d}w_i = \sum g_i\left(t_j\right)\left(\sum w_k g_k\left(t_j\right) - g_j^o\right) = 0 \tag{5.3}$$

Therefore, w is obtained as,

$$w = (g(t)_T g(t))_{-1} g(t)_T g^o \tag{5.4}$$

$$g(t) = \{g_i(t_j)\}$$

in which subscript of T means transposed matrix and that of -1 does inverse matrix.

Thus, the weight parameter vector w should be estimated by data matrix of g_{ij} above with Bayesian scheme.

5.2 Gaussian Regression of the GRACE Gravity Data

Earth gravity data are continuously taken from the two special purpose satellites by 10 times per month from 2002 to nowadays, and these data are possibly connected with the previous gravity time series estimated by Chen et al. (2016) using pre-GRACE satellite data. The gravity data by GRACE over the whole earth should be decomposed by spherical harmonic function, and the mode I means the intensity of gravity of the spherical surface, and mode II means the intensity of flattening of the earth as

$$\begin{aligned} f &= (a-c)/a \\ &= \left(a^2/c^2 + c/2a\right)(A-C)/Ma^2 \\ &\quad + (a^2 c\omega^2/\mathrm{GM})/2 \\ &= 3J2/2 + m/2 \end{aligned} \tag{5.5}$$

in which A and C are the principal moments concerning the axis passing through the equator and pole, respectively, and f is the flattening intensity of the earth. The a and c are the equatorial and polar radii, respectively, and w is the earth rotation. Term of m means in this equation, the centrifugal acceleration at the equator.

$$V = -\mathrm{GM}/r + \mathrm{GMR}^2 J_2(3\cos^2\theta/2) - 1/2)/r^3(\theta = \pi/2 - \phi) \tag{5.6}$$

and

$$W = (\mathrm{GM}/R)\sum\sum (R/r)^{l+1} P_{lm}(\sin\phi)\left(C_{lm}^w \cos m\lambda + S_{lm}^w \sin m\lambda\right) \tag{5.7}$$

by Hofmann-Wellenhof–Moritz (Barthelmes 2013).
and

$$W = (\mathrm{GM}/R)\sum (R/r)^{l+1} P_l(\sin\phi) C_{l0}^w \text{ at } m = 0 \text{ (for zonal pattern)}$$

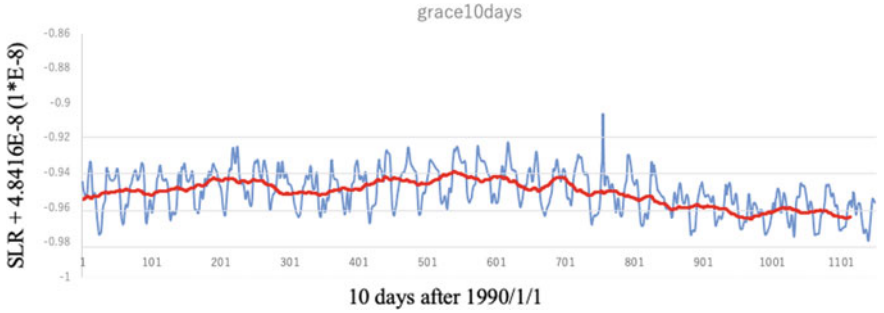

Fig. 5.1 Temporal variation of C20 satellite gravity with sampling time of 10 days by Gaussian regression with Bayesian processing of machine learning. Data are cited from database of Chen and Ries (2017)

$$\mathrm{J2} = \mathrm{K\,C20} = 2f(1 - f/2)/3 - m(1 - 3m/2 - 2f/7)/3 \tag{5.8}$$

Further, it holds (Chen and Wilson 2003),

$$\Delta \mathrm{J2} = 2.236\,\Delta \mathrm{C20} \tag{5.9}$$

On the other hand, Chen and Wilson (2003) obtained the time series of flattening index C20 before 2002 (GRACE start) from the time series of the length of day (so-called LOD). In this book, to compare quantitively the time series between the correlated global seismicity and the gravity variation J2 (C20), the regression of the time series of LOD (daytime) and C20 with every time step of 10 days is needed. The regression model used here is the Gaussian basis Bayesian regression model mentioned above, because the data involves naturally the Gaussian noises in observed data. The Python 3 code of this GBRM is listed in Appendix I.

As shown in Fig. 5.1, it shows that the C20 time series from 1990 to 2019 indicates apparently two components that are the seasonal variation and the long-term secular variation. The seasonal variation displays sharply the peak in August to September, and the secular variation does not indicate the clear periodicity, but it slowly increases from 1990 to 2006 and decreases to 2019 with several years undulation (Fig. 5.1). Judging from the seasonal periodicity of C20 during 1990–2019, it seems sure that the gravity J2 = −2.326 C20 change showing the zonal pattern of geoid is derived from the total atmospheric and ocean mass migration between polar and equatorial region as proposed by Chen et al. (2005). However, it remains still unclear that the rapid change of the J2 from 1990 to 1992 and it is not responsible for the atmosphere and ocean mass (AOM) change involving land ice melting into ocean as suggested by Dumberry and Bloxham (2004). They proposed thus the outer core torsional oscillation mechanism resulting the J2 sub-decadal change with its several years rapid change, although they failed to explain the actual amplitude of J2 change. However, they pointed out that the geomagnetic jerk (third time-derivative of geomagnetic

intensity) shows a sudden change at the same time of above rapid increase of J2, suggesting the outer core torsional oscillation model mentioned above.

In this study, it should be noteworthy that the C20 variation pattern from 1990 to 2019 is correlated with the global correlated seismicity change during that period as shown the next section. It suggests that the long-term C20 variation probably contributes to the global seismic activity of the plate boundary, or it is partly controlled by the mass migration between polar and equatorial region. Judging from no distinctive signals in C20 at the time of giant earthquakes such as 2004 and 2011, the latter process is probably not the case. Then, it is required to know that length of day (LOD) variation from 1990 to 2019 correlates with the variation of C20 and global correlated seismicity.

To investigate the correlation between the LOD and global correlated seismicity, the data of the LOD time series given by open source (IERS) may be transformed into the time series of 10-day sampling by means of Gaussian regression with Bayesian model as same as that in the previous section. The time series of the LOD from 1990 to 2019 is then shown in Fig. 5.2, suggesting the long-term variation as like as the C20 and the global correlated seismicity z_1 and z_2.

As shown in Fig. 5.2, the variation of LOD displays several components: One is annual component, and second is the long-term drift with several to several ten years undulation.

The polar orientation also changes in several modes that contain the Chandler wobble derived from triaxial shape of the earth and tidal migration of atmosphere, ocean, and fluid core (e.g., Chanard et al. 2018). The International Earth Rotation and Reference Services (IERS) supports the earth orientation parameters (EOP) variations, suggesting that this type of wobble motion of the earth contributes the short-term periodic variations in the LOD change as proposed by Chen and Wilson (2003), although the long-term variation of the LOD is seemingly not the case. Therefore, the long-term trend of the LOD variation should be investigated for comparison with the correlated global seismicity.

In this study, the 10-day sampling data of the 365-day migration average of the LOD variation from 1990 to 2019 are obtained from the IERS data centers. The numerical data were obtained from data processing on Image J by graphical data

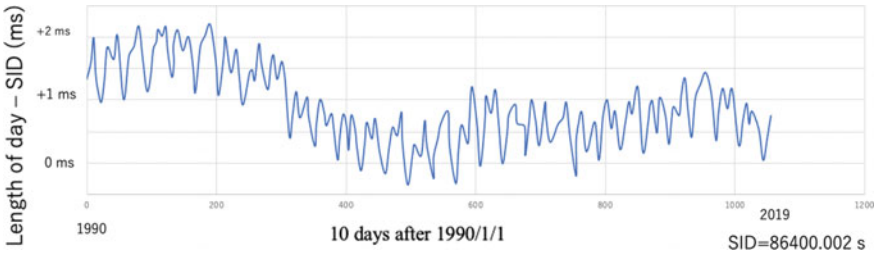

Fig. 5.2 Temporal variation of length of day (LOD) with sampling time of 10 days by Gaussian regression with Bayesian processing of machine learning. *Data source* IERS database

of 365-day migration average. The pattern of the time series of this LOD shows the fast rotation stage during 1990–2005 and slow undulation stage from 2005 to 2019, suggesting the long-term drift with slightly periodic feature. This pattern is the secular trend of the LOD time series, but the annual variation has the same variational intensity as that of the secular trend mentioned above, thereby suggesting that the long-term variation of LOD should be derived from the large-scale migration of the mass as like as the atmosphere and ocean mass migration involving land ice melting. It does not seem to be possible explanation that the large-scale coherent very slow slip events of the subducting slab may be potential to contribute the correlated plate subduction reaching to the mantle transition layer from 410 to 550 km depth and penetrating down to the lower mantle. Recent giant earthquakes occurred of Sumatra and Tohoku-Oki yields only about 2 microgals (Matsuo and Heki 2011), and thus, if the several giant slow slip events reaching Mw about 9, it is not enough to be satisfied for the secular change of C20 components in gravitational potential.

5.3 Temporal Variation of the Global Correlated Seismicity

Next, let us investigate the global correlated seismicity change from 1990 to 2019 cited from the previous book (Toriumi 2021). In this study, the author intends to compare the long-term variation of the correlated seismicity change with the change of zonal gravity patterns of C20 and length of day (LOD) variations, so that the 300-day migration average of the global correlated seismicity time series should be estimated. As shown in Fig. 5.3, it is obvious that the time series of z_1 and z_2 represent the different mode of variation that the z_1 contains the over 30 years secular trend and displays the peak near 2005–2006, but the z_2 component does rather near periodical change within 20–30 years having rapid change in 2011. On the other hand, z_3 and z_4 appear obviously the periodical variations of 10–5 years, respectively, and have sharp signals of giant earthquakes of Sumatra, Tohoku-Oki, and Chile, suggesting that such rapid signals at giant earthquakes should be derived from the post seismic signals in the regions of these giant earthquakes. Thus, it seems that such rapid signals in correlated seismicity are removed from the z_1 and z_5 to z_{10}, though z_2 to z_4 include the rapid signals associated with giant earthquakes as seen in Fig. 5.3.

In the diagram of z_1 to z_3 showing the phase correlation between them (Fig. 5.4), it should be noteworthy that the episodic increase of them from 1990 to 2003 is observed and the stagnant clusters of them are identified as A, B, and C regime. The C cluster, however, shows a wide scattering and it involves the periods of huge amounts of annual seismic moment release rate. As discussed in the previous book, the mechanical state of the global seismicity dynamics represented by z_1 and z_3 parameters may be relevant to the critical conditions formulated by the tangential relation between null cline of dz_1/dt and dz_3/dt because of very large fluctuation of z_3.

On the other hand, the phase diagram of higher components of z_6 to z_{10} appears central dense cluster and surrounding circular tracks showing the strong coherent

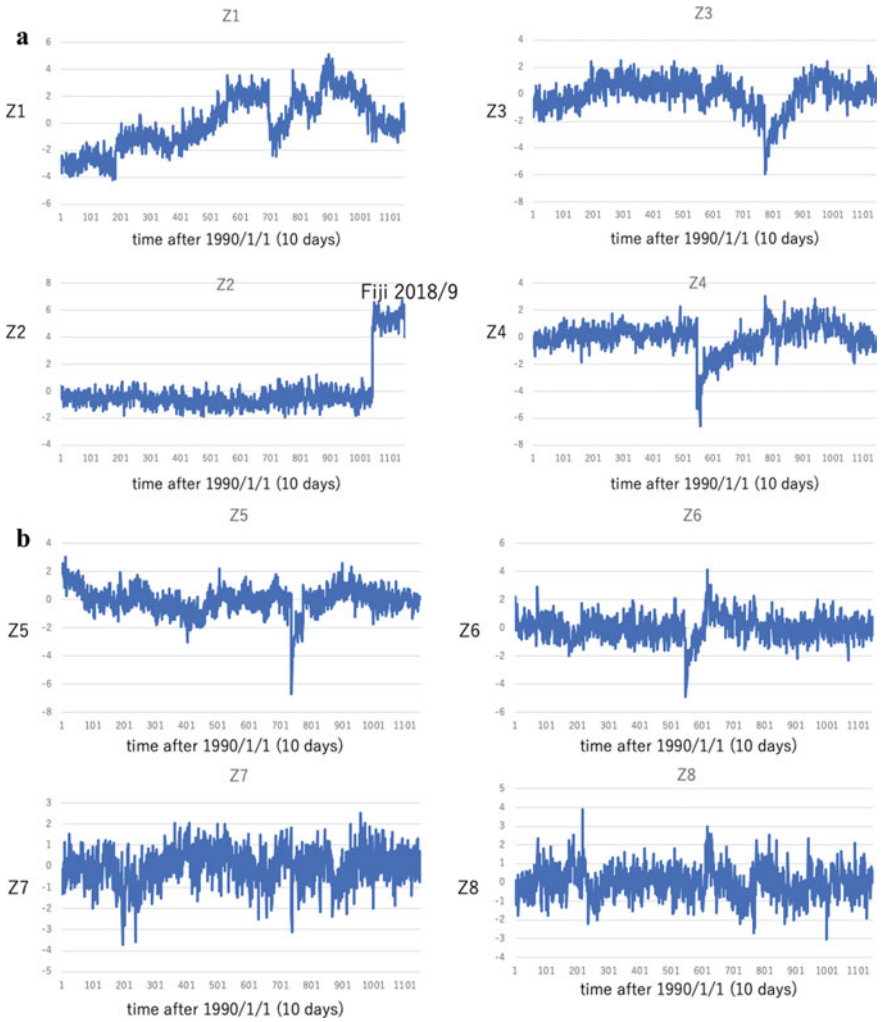

Fig. 5.3 **a** Temporal variations of the global correlated seismicity z_1 to z_4 from 1990 to 2021/6 with sampling time of 10 days. **b** Temporal variations of the global correlated seismicity z_5 to z_8 from 1990 to 2021/6 with sampling time of 10 days

cyclicity with some degree of phase shift. But, in the diagram of z_9 and z_{10}, the central cluster is obvious and surrounding subsidiary tracks display spike like extension from the central cluster as shown in Fig. 5.5. The intensity of these spike and cyclic change in z_6 to z_8 reaches about 0.5–1.0, though that of the z_1 and z_2 does about 3–4, thereby indicating the contribution of the higher-order correlated seismicity is less than 20–30% at most.

On the other hand, the correlated global ridge seismicity manifests the variation likely to those of the global subduction zone as displayed in Fig. 5.6. It is obvious

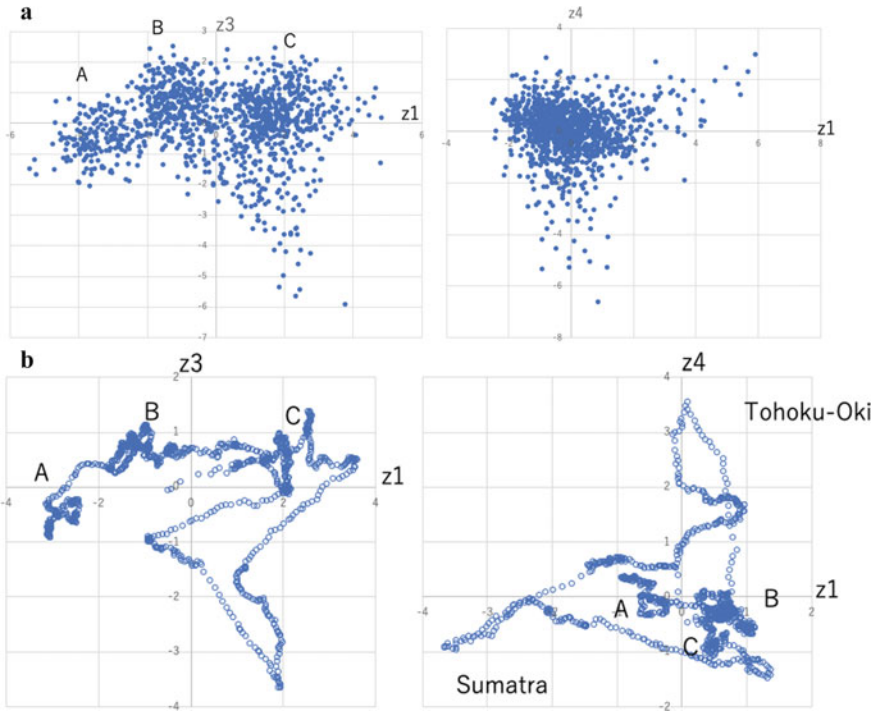

Fig. 5.4 **a** Maps of z_1 versus z_3 and z_1 versus z_4 global correlated seismicity rates, and **b** map of their 36-step migrating average time series, showing the clusters of A, B, and C

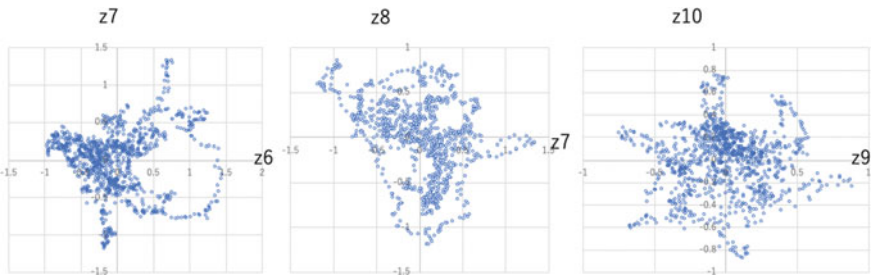

Fig. 5.5 Maps of higher global correlated seismicity z_6 to z_{10} showing the single cluster at the center and spikes from the cluster

that above variation shows the step like increase of z_1 until 2003, and then, it does large fluctuation until nowadays. As pointed out in the previous book, the phase map of the correlated global seismicity z_1 in ridge and subduction zone appears the dense clusters of A and B, but scattered C cluster, suggesting the coherent motion of the divergence and convergence of the oceanic plate. Considering that the seismic moment release rate increases abruptly after 2004, the scattered cluster C mentioned

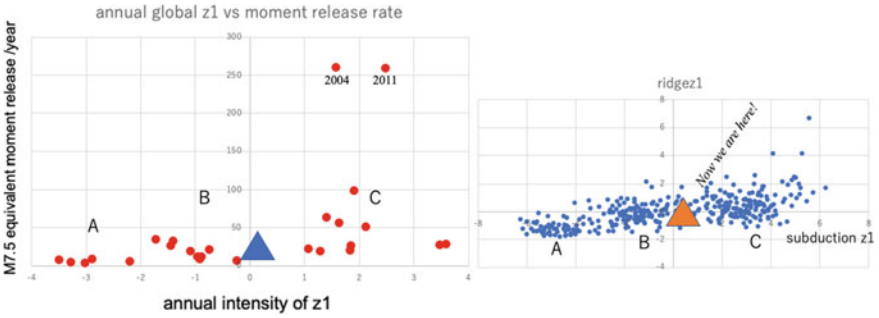

Fig. 5.6 Relationship between the global correlated seismicity z_1 and annual moment release rate by large earthquakes, and between the global correlated seismicity z_1 between the subduction zone and global ridge zone

above means probably the active period of the mechanical behavior in terms of surficial seismicity of the earth.

By the way, the orthogonal decomposition method yields the correlated seismicity localities of the gridded subduction and ridge zones associated with the characteristic feature z_i variations. The orthogonal rotation matrix defines the correlated seismicity locality vector of each z_i and it is relevant to the mechanically cooperative network of the plate boundary as discussed in the previous book (Toriumi 2021). In Fig. 5.7, it suggests that the major components of correlated global seismicity z_1, z_2, and z_3 are identified with each other, and that the z_1 appears the wide connection of many gridded localities such as IBM (Izu-Bonin-Mariana), TK (Tonga-Kermadic), CP (Chile-Peru), Ak (Alaska), NEJ (Northeast Japan), and JS (Java-Sumatra) segments. On the other hand, the z_2 and z_3 display the high intensity of mechanical states of NEJ, Sumatra, and Chile and correlated locality segments (Fig. 5.8). These characteristics of the global connection styles shown by the intensity of eigencomponents of the orthogonal basis vector of the data matrix determine near-invariant parameters of the global seismicity network. However, it is required that the successive change of the mechanics network of the global correlated seismicity is possibly inferred from the spectrogram expression of the correlated seismicity z_i especially z_1 to z_4 as shown in the previous book. In this section, judging from clustering in the z_1 to z_2 phase map (Fig. 5.4), then, it is needed that the global correlated seismicity should be taken in the periods of A, B, and C clusters of the z_1 and z_2 time series.

As shown in Fig. 5.9, it seems that there is weak difference in the intensity pattern of the locality cells seismicity among the clusters of A, B, and C: All of them show the coeval seismic activity in Izu-Ogasawara, Tonga-Kermadic, New Zealand, Chile, Mexico, Alaska, Kuril, and NE Japan, and Taiwan, Philippine, Java-Sumatra, and Himalaya, though their intensity ratios vary with small amounts in the cluster A, B, and C, thereby suggesting the increase of global seismic activity in the wide regions of subduction boundary zone in the period of cluster C. In this period, as seen in the variance distribution of z_1 and z_2 and global moment release rate (Toriumi 2021), the fluctuation of the global seismic activity appears very large, and therefore, it is

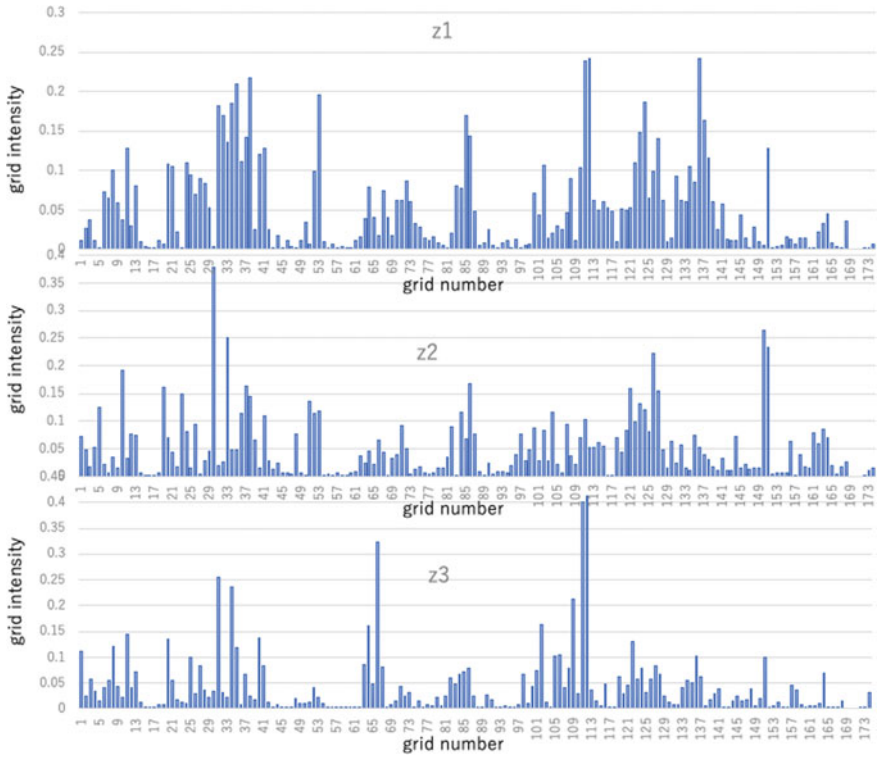

Fig. 5.7 Diagrams of the weight intensity of the grided localities of the global subduction zone for the global correlated seismicity z_1 to z_3

apparently related to the globally active period in seismicity of the plate boundary. Thus, it is to be shown that how appears the mode change in the global correlated seismicity in the boundary zone with advancing the time.

In Fig. 5.10, it seems obvious that the progressive variation of the global correlated seismicity from the cluster A to C through B is represented by the change between the localization and the homogenization of the global seismic activity, which can be assigned by the change in z_1 and z_2. In the period of A and B, the localization shown by high intensity of active seismicity in Chile to Peru and NE Japan to Kuril changes to the homogenization into the whole region of the plate boundary. In addition, from B to C cluster, the global correlated seismicity z_1 changes from homogeneously active situation to the localization into the Sumatra and Java region, NE Japan region, and Chile. Furthermore, it is probably seen that the localization of the global correlated seismicity z_1 changes progressively from Sumatra to Chile through NE Japan in the C cluster. It is noteworthy that the time scale of the change between homogeneous and localized correlated seismicity is different in z_1 and z_2: The time scale of z_1 change is longer than that of the z_2 (Fig. 5.11). These characteristic features of the

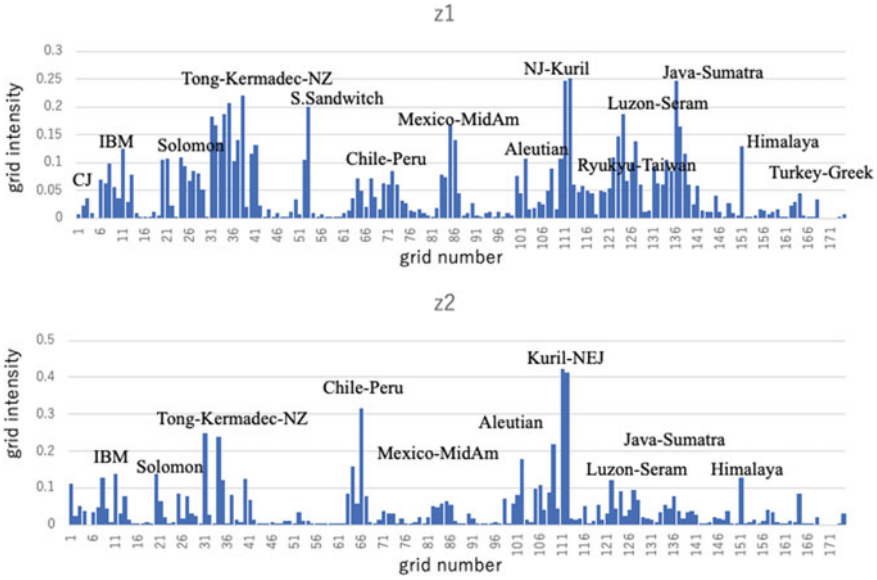

Fig. 5.8 Diagrams of the weight intensity of the grided localities of the global subduction zone for the global correlated seismicity z_1 and z_2, showing the different network pattern in z_1 and z_2

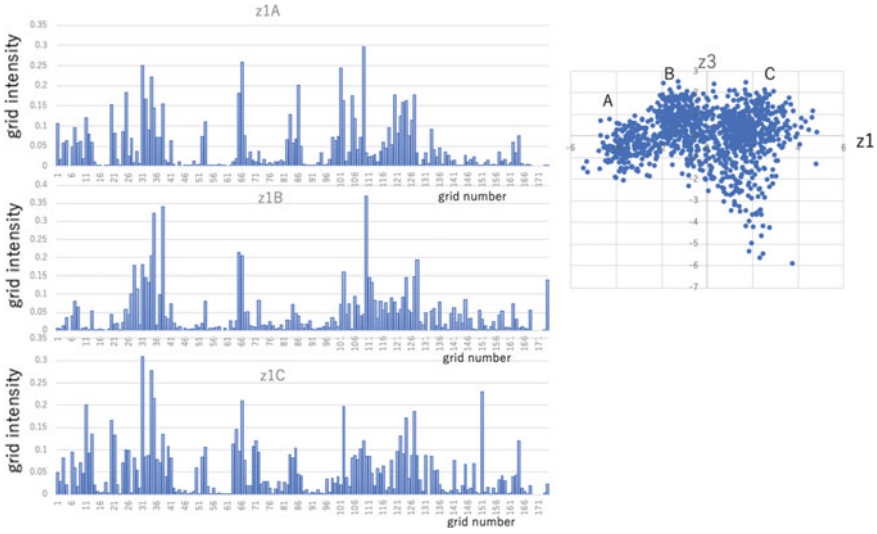

Fig. 5.9 Diagrams of the weight intensity of the grided localities of the global subduction zone for z_1 in the cluster A, B, and C shown in right figure

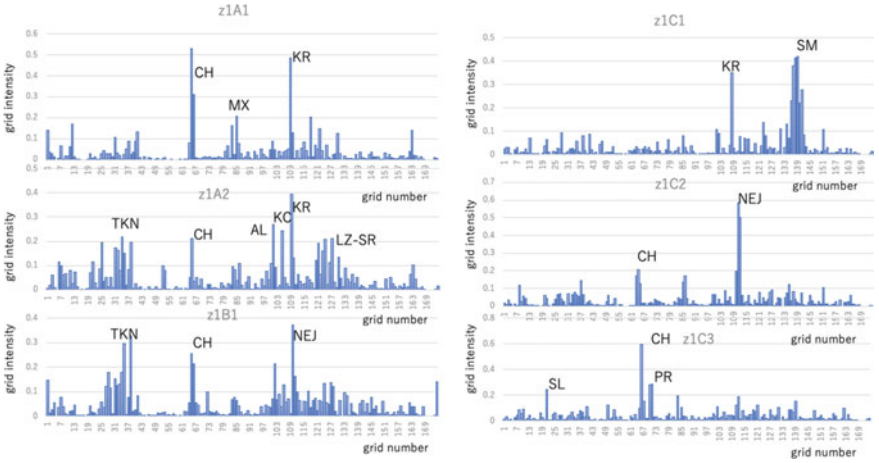

Fig. 5.10 Diagrams of the weight intensity of the grided localities of the global subduction zone for z_1 in the subdivided A1, A2, B1, C1, C2, and C3 clusters with advancing the time, showing the change in pattern of intensity

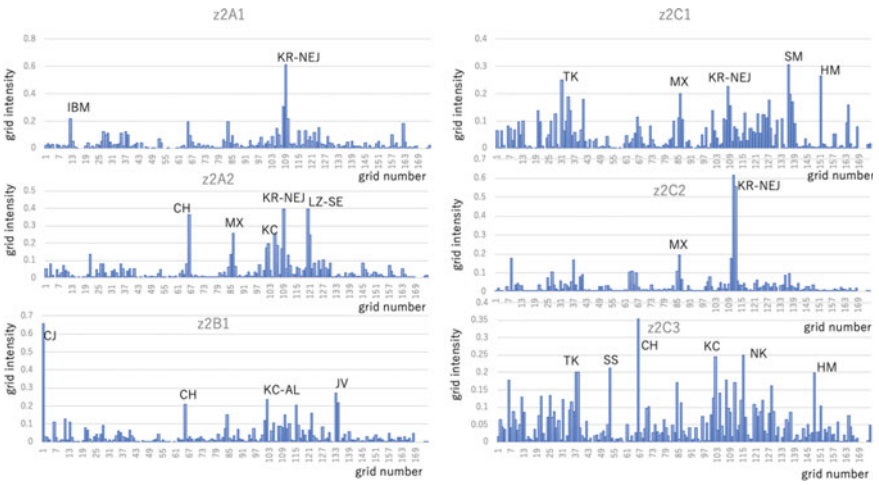

Fig. 5.11 Diagrams of the weight intensity of the grided localities of the global subduction zone for z_2 in the subdivided A1, A2, B1, C1, C2, and C3 clusters with advancing the time, showing the change in pattern of intensity

mode change in z_1 and z_2 may appear the modulation of the large-scale failure of the plate boundary in the global earth as discussed in the next chapter.

5.4 Synchronous Change of the Global Satellite Gravity, Earth Rotation, and Correlated Seismicity

In the previous sections, it is stressed that J2 or C20 of the mode II gravity change with time should be decomposed into the annual variation and secular change. Furthermore, it is also suggested that the sub- to overannual variations may be observed in the global correlated seismicity change in z_1 to z_4, and in the previous book it is also stressed that the partial *b*-value change and z_1 to z_4 of the regional correlated seismicity also appear the periodic variation with sub- to tri-annual repeating cycle (Toriumi 2021). Therefore, it may be natural that the annual variation of the C20 is surely related to that of the global and regional correlated seismicity z_1 to z_4 and correlated partial *b*-value change.

By the way, the annual change of the C20 and thus J2 of the gravitational potential is thought to be responsible for the total atmosphere and ocean mass (AOM) migration by climate dynamics (e.g., Tapley et al. 2004). The length of day (LOD) also clearly appears the annual and secular change, and the former is obviously synchronized with that of the C20 annual change, suggesting that the AOM migration involving land ice melting governs both C20 and LOD annual variation.

On the other hand, it is very difficult to be considered that the correlated global seismicity change of the plate boundary zone is directly governed by the fluid earth dynamics because earthquakes occur in fracture mechanics of the solid earth. It is also difficult to image that the variation of the C20 and LOD may be due to the large-scale and short-term subduction of the plate such as slow slip event and giant earthquake because even giant earthquake of Sumatra 2004 results in only change of gravity less than the 0.001 times of the annual variation (Mastuo and Heki 2011). Nevertheless, as there is near synchronous variation among C20, LOD, and correlated global seismicity (see Figs. 5.1, 5.2, and 5.3), it may be concluded that the correlated seismicity should be derived from the global loading change due to migration of sea water and land ice melting. The secular variation of the correlated global seismicity too is controlled by that loading change as well as the annual variation of C20 and LOD as shown in Fig. 5.12.

Therefore, it should be checked whether the regions of the highly active correlated seismicity are consistent with the regions of high sea level rise and geoid high in the zonal component of gravitational potential or not. It seems available that the largest geoid height around equatorial zone may correspond to the highly active correlated seismicity zone located at the Java-Sumatra, Solomon, Luzon-Seram regions which are the region of high sea level rise too, as shown in Fig. 5.13. The active regions of Kuril-NEJ and Tonga-Kermadic-New Zealand are the medium latitudinal zone, which are also the region of high rate of sea level rise by means of global sea level change map (NOAA 2021). Furthermore, it is important that the average sea level change by satellite razer measurement shows the rapid change is responsible for the adding of sea water by land ice melting as shown in Fig. 5.13, thereby suggesting the secular trend of the correlated global seismicity possibly derived from water loading and unloading as well as the case of seasonal variation. The rate of SLR (sea

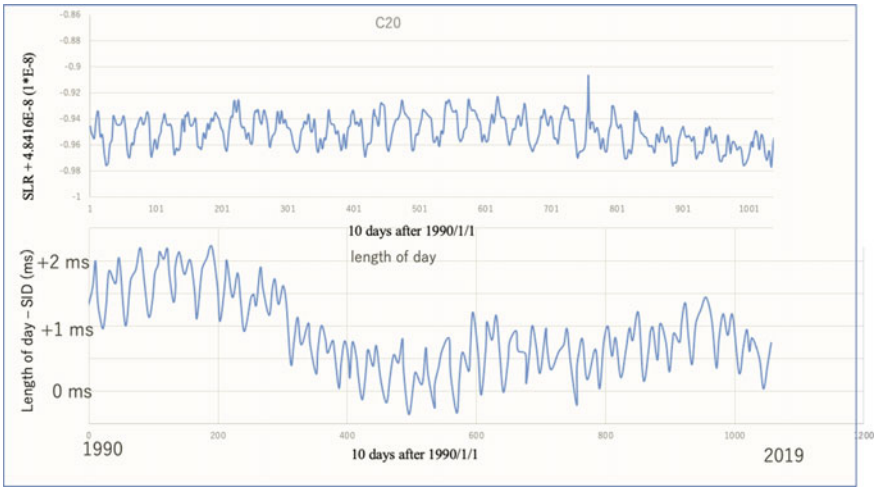

Fig. 5.12 Comparison of temporal variation of the C20 satellite gravity from GRACE (top) and the length of day (LOD; bottom) showing the strong correlation of annual variation of them

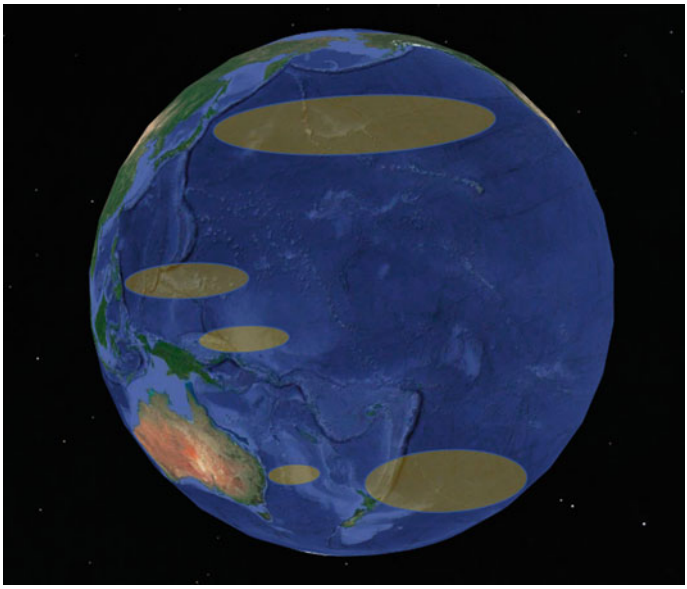

Fig. 5.13 Global distribution of the zone of large sea level rise (SLR > 15 cm) from 1993 to 2018 in the intermediate latitudinal zones modified from NOAA climate database (NOAA 2021)

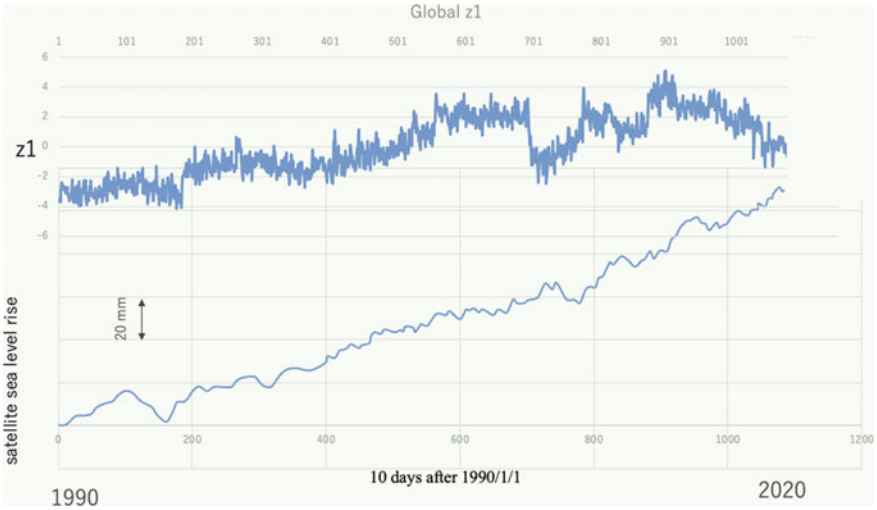

Fig. 5.14 Comparison of the temporal variation in the sea level change (NOAA 2021) and global correlated seismicity z_1, showing the similar secular trend between them

level rise) reaches about 5 mm/year (NOAA 2021), and it corresponds to the rate of sea water loading pressure as 0.5 kPa/year. In the periods of rapid SLR, it seems to reach about 1 kPa/year. Seasonal variation by ocean tide also adds to this stress on the solid earth. These loading pressure increase associated with fluid pressure rise should affect the critical resolved shear stress on the small to large-scale shear cracks which may be growing by chemically assisted subcritical crack growth as discussed in the previous chapter.

By the way, it has been clarified that SLR estimated by the global climatology model is consistent with the SLR by the satellite observation with razer altimetry (Fig. 5.14), which appears the gradual increase of SLR from 1995 to 2021 (NOAA 2021), thereby suggesting that the correlated seismicity z_1 may appear a gradual increase to the next decade, being stagnant in the C cluster of z_1 and z_3 in the global seismicity (Fig. 5.15).

In the previous book, the author discussed the sub-annual to tri-annual variation of the correlated regional seismicity and its partial *b*-value change in Japanese islands region to be attributed not to the snowy and rainy loading and unloading proposed by Heki (2010), because there is no difference in correlated seismicity patterns between the snowy and nonsnowy regions of Japanese islands. However, such short-term periodic variations of regional correlated seismicity may be due to the change in the global SLR around Japanese islands region. Moreover, it seems clear that there are obvious relations in the correlated seismicity between the global subduction zone and Japanese islands region as well as the Northern California region.

Furthermore, it is probable that the sub-periodic slow slip events occurred along on the subduction plate boundary in the world may take place due to the water pressure increase by SLR on the plate boundary zone absorbing the sea water. In

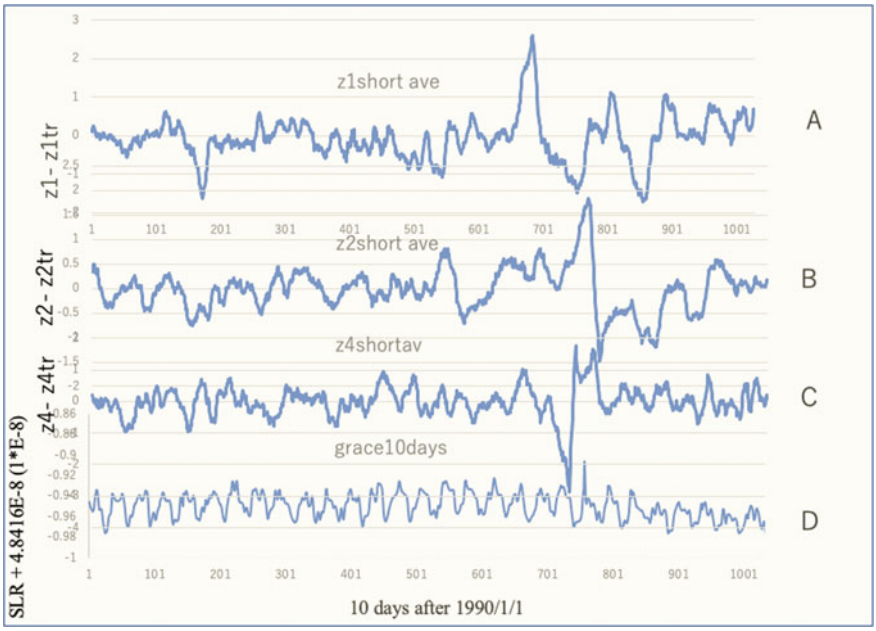

Fig. 5.15 Comparison of the temporal variations among short-term z_1, z_2, and z_4 of the global correlated seismicity and sea level rise (SLR) from satellite observation showing the different periodicity and phase shift between them

Cascadia subduction zone, the synchronous events of SSEs and abundant tremors are very clear, thereby showing the tremor activity is synchronous with the seasonal variation of the global SLR and thus with the variation of gravity and solid earth rotation (LOD).

5.5 Synchronous Change of the VLBI Geodesical Data and Correlated Seismicity

As discussed in the previous section, it shows that the correlated global seismicity change is mainly contributed by those of Java-Sumatra, Tonga-Kermadic, Chile, and Kuril-NE Japan. These regions seem to correspond to the region with large rate of sea level rise, thereby indicating that the global change of the correlated seismicity is responsible for the sea water loading and unloading on solid earth together with oceanic tide. Furthermore, it is probable that the plate motion by sub-periodical SSEs along on the plate subduction boundary may be coherent with the global correlated seismicity z_1 to z_4 as well as the C20 and LOD. Thus, let us look at the coherency of variation in the length of the very long baseline between Japan (Tsukuba) and

Australia (Hobart, Tasmania) by means of the very large baseline interferometry (VLBI) from 2012 to 2018.

In Fig. 5.16, the variation of the distance between the Tsk (Tsukuba, central Japan) and Hbt (Hobart, Tasmania) is shown by plotting the data read by ImageJ of open-source image data of VLBI results from 2012 to 2019. The data are fitted by Gaussian regression with Bayesian model (GRBM) as described in detail in the previous section. The data sampling was estimated every 10 days interval as same as that of the correlated seismicity and LOD. The variation of the distance appears slightly periodic feature of the time series from 2012 to 2017. Therefore, the velocity of the relative motion of the Tsk-Hbt is calculated from above data as shown in Fig. 5.16, and it obviously shows that the present velocity appears clearly annual periodicity as like as the LOD and C20 gravity as mentioned previously. In addition, it is very important that the time of the high velocity of the relative motion is coincided with that of the high rotation velocity of the earth. If this is not the case of the measurement drift by earth rotation in the VLBI, this synchronicity between the plate motion and the earth rotation has an important meaning that the long-term drift of the earth rotation speed and gravitational potential are both controlled by the plate velocity change or inversely, the plate motion is controlled by the earth rotation speed. Judging from that the earth rotation speed and gravitational variation are derived from the sea level change with land ice melting, the correlated seismicity change with short- and long-term variation is probably due to the plate velocity change resulted from climatological variation of regional ocean volume.

By the way, the phase relation of the correlated global seismicity and the velocity of relative motion of the Tsk-Hbt distance is shown in Fig. 5.17, suggesting no apparent dependency between them. However, above relation is in the range of 2012–2018, and the large difference in the correlated global seismicity z_1 is in the range from 1990 to 2018, that is the range of the z_1 and z_2 clusters of A, B, and C. Thus, as seen in the phase relation between the LOD and the correlated global seismicity

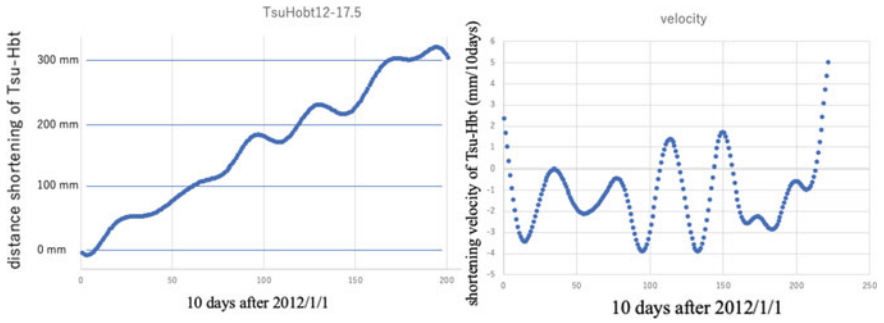

Fig. 5.16 Temporal variations of distance by the very large baseline interferometer (VLBI) between Tsukuba, central Japan and Hobart, eastern Australia and the velocity of plate convergence between North American Plate and Australia Plate. The large disturbance by giant earthquakes is possibly ignored in the time range from 2012 to 2019. It is noticed that the velocity fluctuation near the initial and terminal time series should be error from finite size of the VLBI data

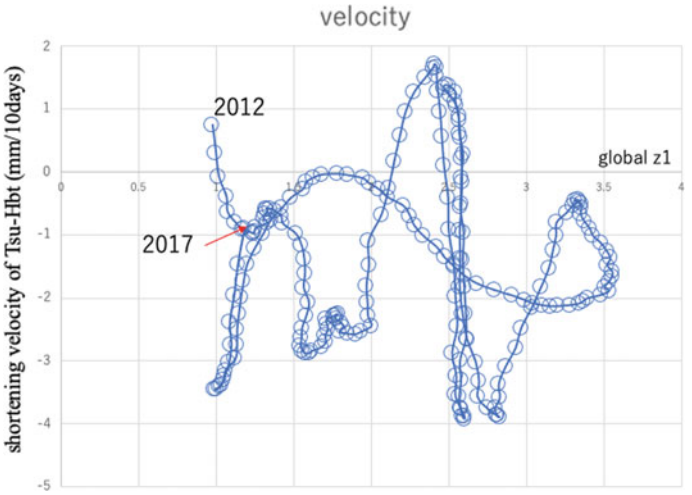

Fig. 5.17 Diagram of the phase relation between the time series of the convergence rate in VLBI data and the global correlated seismicity z_1 showing the correlation between them

(Fig. 5.18), it is obvious that the low-speed earth rotation stage appears in A and B cluster stages, and the high-speed one is satisfied in the C clusters of high seismic activity. Therefore, it is concluded that the high-speed plate motion period coincides with the high correlated seismicity one.

The baseline between Tsk and Hbt runs across the Australian Plate, Philippine Sea Plate, and eastern end of North American Plate. Thus, the change of the baseline length should involve the variation in migration of the Australian Plate and Philippine Sea Plate and total strain rate of these plate themselves. Then, it remains that the high velocity of shortening between Tsk and Hbt is probably due to the elastic deformation of these plate produced by solid earth tide but not the subduction velocity. In the

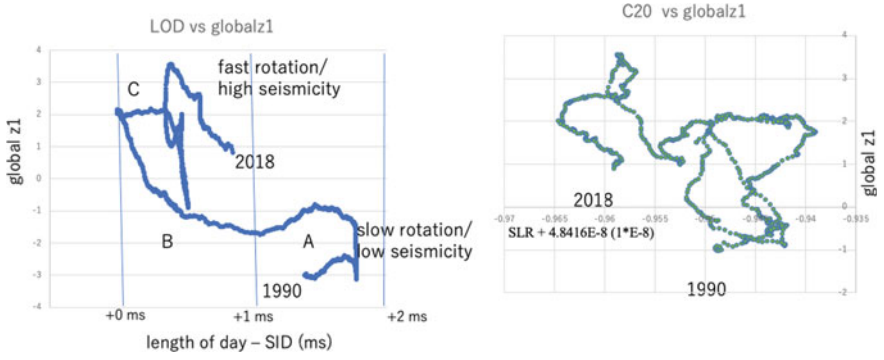

Fig. 5.18 Phase relations of the distance between Tsukuba–Hobart of VLBI data (left), C20 of GRACE data (right), and the global correlated seismicity z_1 showing the strong correlation of them

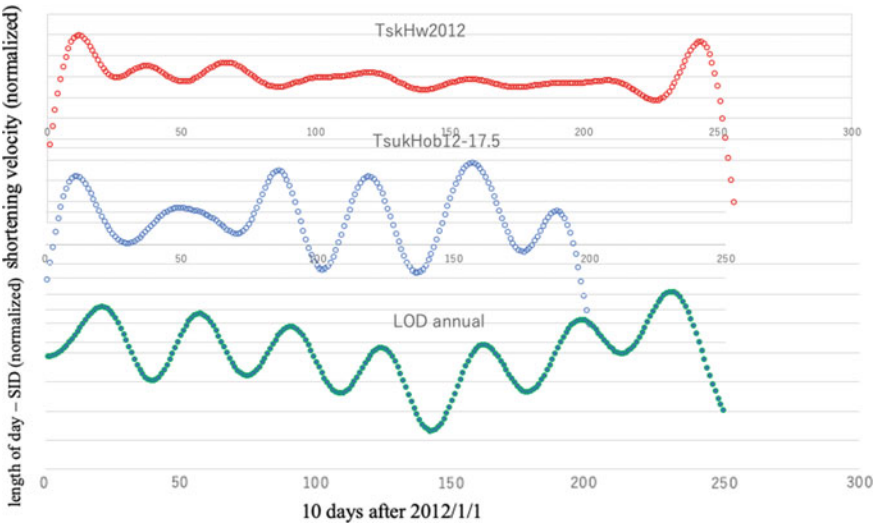

Fig. 5.19 Comparison of temporal variations of the plate velocity between Tsukuba–Hawaii (top) and Tsukuba–Hobart (middle), and the annual variations of the length of day (LOD) from 2012, showing the strong correlation between them

case of tidal deformation, it should be expected that the minimum length appears at March equinox and maximum at September equinox every year. However, the LOD and migration velocity of the baseline of Tsk-Hbt attains the peak in June and the minimum in January, suggesting no match of the earth tidal pattern. In addition, as shown in Figs. 5.19 and 5.20, the fact that the periodical change of the plate velocity change and the LOD displays the change in phase shift of them with time advance, despite near-annual periodicity of both variations seems to manifest the plate velocity change due not to the elastic deformation by solid earth tide. Therefore, it is probable that the plate velocity change appeared in baselines of Tsk-Hawaii (KK) and Tsk-Hbt is responsible for the AOM change derived from climatological large scale circulation involving land ice melting. In Fig. 5.21, it shows that the phase map between C20 and the plate velocity between Tsk-Hbt appears the strong correlation with antisynchronous relationship of their phase, suggesting the coherent mode of temporal change of them, and short-term plate velocity changes with atmosphere and ocean mass (AOM) temporal variation.

5.6 Periodic Variation of Correlated Seismicity and Global C20 of the Japanese Islands Region

As shown in the previous book, the time series of the residual time series of the correlated seismicity minus secular variation of the correlated seismicity of Japanese

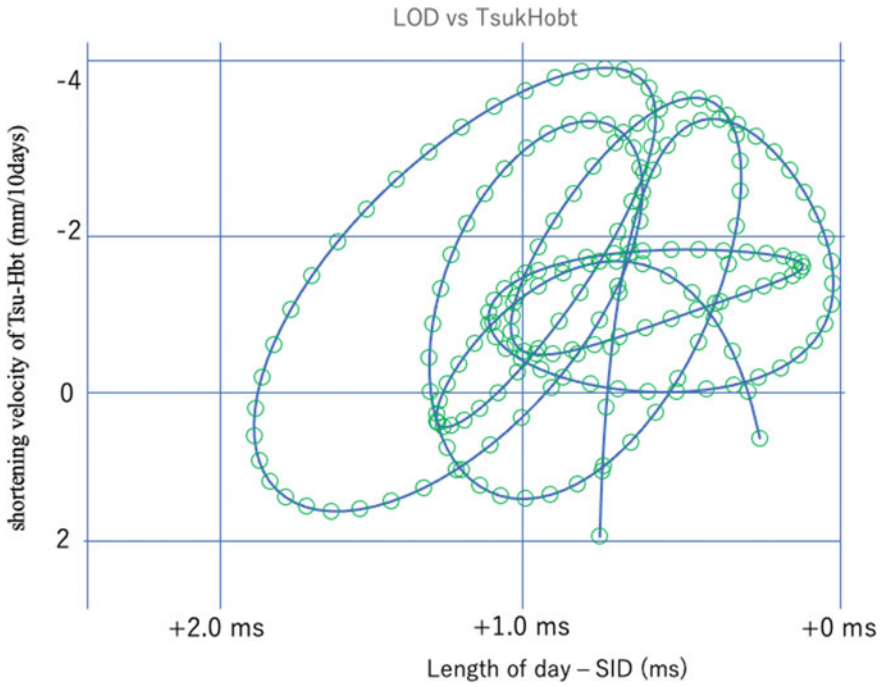

Fig. 5.20 Phase relation of the temporal variation between the plate velocity of Tsukuba–Hobart and the length of day showing the strong correlation of them

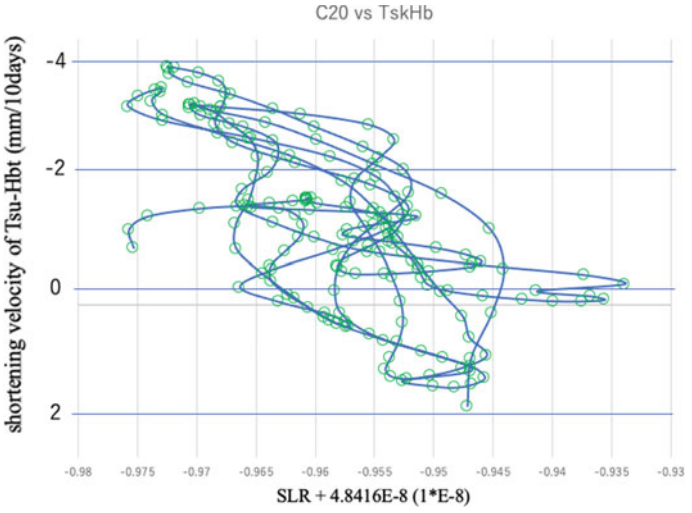

Fig. 5.21 Phase relation of the temporal variation between the satellite sea level rise and the plate velocity of Tsukuba–Hobart suggesting the strong correlation between them

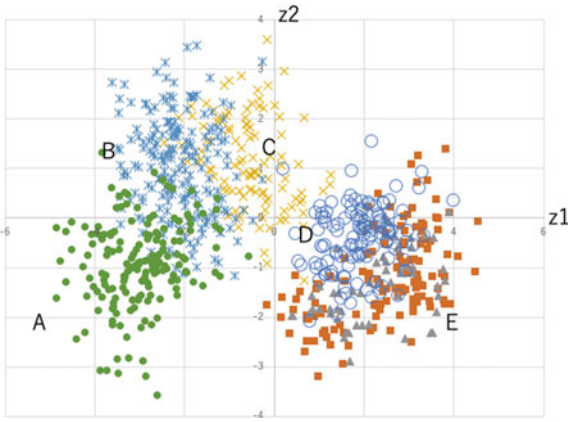

Fig. 5.22 Diagram of phase relation between the regional correlated seismicity z_1 and z_2 of the Japanese islands region from A, B, C, D, and E clusters in the advancing order of the time

islands regions manifest distinctively sub-annual to tri-annual variation, and these variations seem likely to that of the slow slip events along on the subduction boundary (e.g., Schwartz and Rokosky 2006). In this study, the time series of the gridded seismicity extends from 1998 to 2021 instead of 1998 to 2018 in the previous book, and the phase map of the correlated seismicity z_1 and z_2 of the Japanese islands region is carried out in the present time range as shown in Fig. 5.22.

As shown in Fig. 5.23, it is obvious that the time series of the correlated partial *b*-value seismicity of the Japanese region appears secular variation and short-term temporal variation having sub- to several years periodicity as like as those in the period from 1998 to 2018. The short-term temporal variation of the correlated partial *b*-value seismicity is clearly shown by the difference between the migration average and the correlated seismicity time series as shown in Fig. 5.23, thereby suggesting that there is apparently complicated periodicity from sub-annual to tri-annual one as suggested in the previous book (Toriumi 2021).

As discussed in the previous sections, it suggests that the global correlated seismicity of the subduction zones contains the secular variation and the short-term temporal variations with sub- to tri-annual periodicity, and it appears to be synchronized with the LOD and C20 (or J2) gravity time series. Therefore, it needs to be studied whether the regional correlated seismicity time series displays a synchronized pattern with the temporal variation of the satellite gravity and the length of day (earth rotation). In Fig. 5.24, the comparison among these different time series is displayed, and thus, it is clear that the synchronous patterns of the regional correlated seismicity, C20 gravity, and the partial *b*-123 value time series defined previously. It is very important that the short-term temporal variation of the correlated seismicity of the Japanese region is not derived from the local variation of them, but from the global variation of the gravity and earth rotation (LOD). This is strongly supported by the evidence that the correlated seismicity of the Northern California region appears the same annual periodicity as that of the Japanese region.

By the way, it seems that the secular variations and seasonal ones of the LOD and C20 are responsible for the global distribution change of the total ocean mass

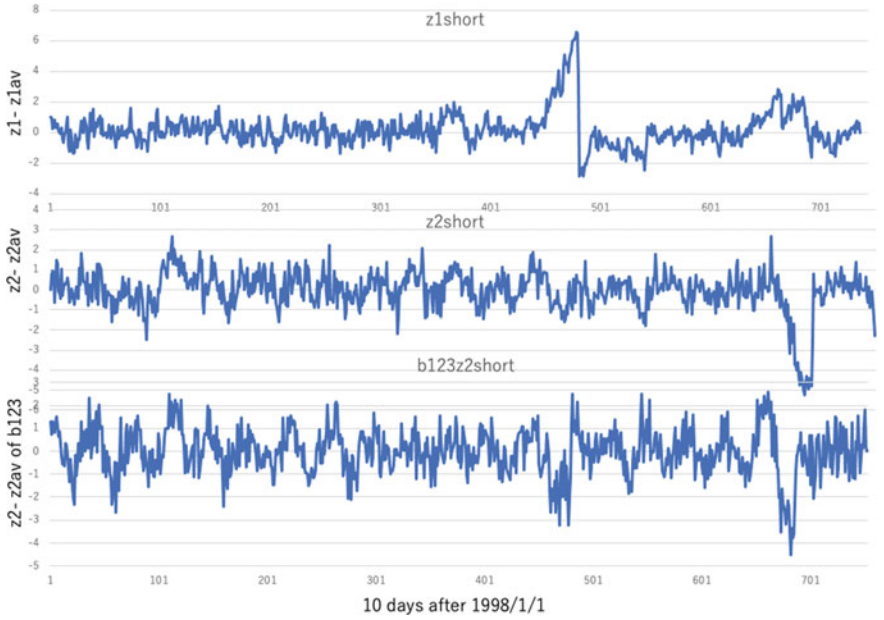

Fig. 5.23 Comparison of the periodical temporal variations among short-term z_1 and z_2 of regional correlated seismicity and z_2 of partial *b*-value in the Japanese islands region

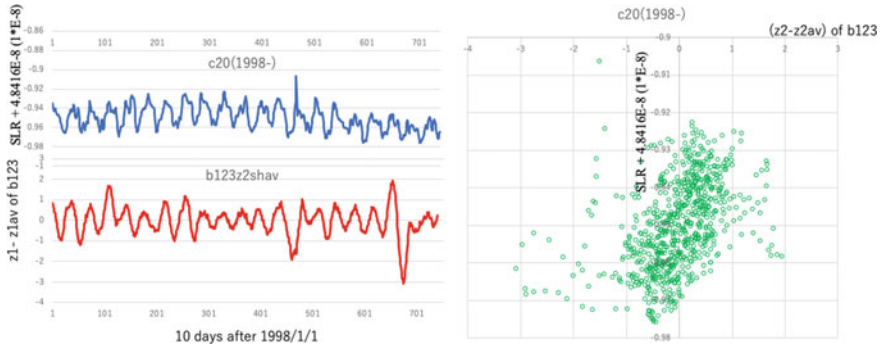

Fig. 5.24 Comparison of the periodical temporal variations between the C20 gravity and z_2 of the partial *b*-value of the regional correlated seismicity of Japanese islands region. Right figure shows the phase relation showing the strong correlation of them

and the variation of the total polar and land ice mass (e.g., Chen et al. 2016). The temporal change in the C20 satellite gravity component which is called as the zonal component of the geoid height probably means that of the angular moment due to the mass distribution change of the outer ocean mass derived from tidal force and the global climatological variation including global ocean circulation change. Therefore,

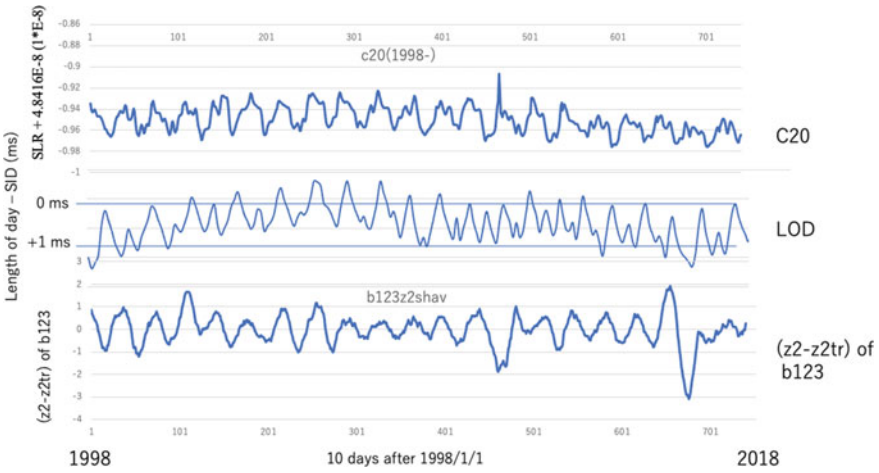

Fig. 5.25 Comparison of the resembling periodical temporal variations of global sea level rise, length of day (earth rotation), and regional correlated partial *b*-value z_2 of Japanese islands region from 1998 to 2018

the temporal variation of the present zonal component (C20) should be coherent with the length of day of the earth as shown in Fig. 5.25.

Consequently, for there is a synchronized near-annual variation of the regional correlated seismicity and the LOD, it may conclude that both global and regional correlated seismicity and partial *b*-value changes are largely controlled by the mass distribution change of global ocean and land ice, and precipitation. It appears that the long-term temporal variation of these correlated seismicity depends probably upon the secular change of the global climate. Therefore, it seems that the rapid change of Pearson's map of the correlated seismicity of Japanese islands region appears after 2015 is partly due to the global climate change as seen in C20 and LOD. In the change of the seismicity network dynamics of the subduction zone system, it is noteworthy that the dominant relevant network is represented from the Nankai–Ryukyu, Ryukyu–Tohoku, and Nankai–Tohoku to their dense connection network after 2015, as discussed in the next chapter.

5.7 Nonlinear Dynamics of Earth Rotation and Global Correlated Seismicity

In the preceding sections, it has been clarified that the temporal variation of the global correlated seismicity displays the synchronous behavior with those of earth rotation (length of day) and satellite gravity C20, suggesting the global seismicity dynamics is partly responsible for the centrifugal and gravitational force, although

even giant earthquakes in 2004 (Sumatra Earthquake) and 2011 (Tohoku-Oki Earthquake) did not change the earth rotation in the level of the secular variation (e.g., Heki 2010). In order to clarify the controlling process of the earth mechanics in earthquake activity, the relation of the characteristic features of the global and regional correlated seismicity and the angular velocity change of the earth are investigated in the following.

The characteristic features of the regional and global correlated seismicity display the periodic variation having the sub-annual to tri-annual periodicity as is seen in the time series subtracted the long-term secular trends of them (Fig. 5.26). Then, the change of the periodicity of the seasonal variation of the regional correlated seismicity of the crust and the mantle in the Japanese islands region against the rotation rate of the earth is shown in Fig. 5.27, indicating that the periodicity increases with increasing the earth rotation rate $d\Delta\Omega/dt$. It suggests that the correlated seismicity is

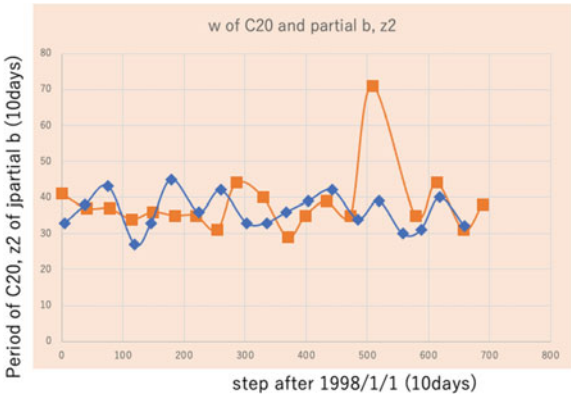

Fig. 5.26 Temporal variation of the periodicity in the regional correlated seismicity b123 of crust in the Japanese islands (blue) and GRACE gravity C20 (red) from 1998 to 2018

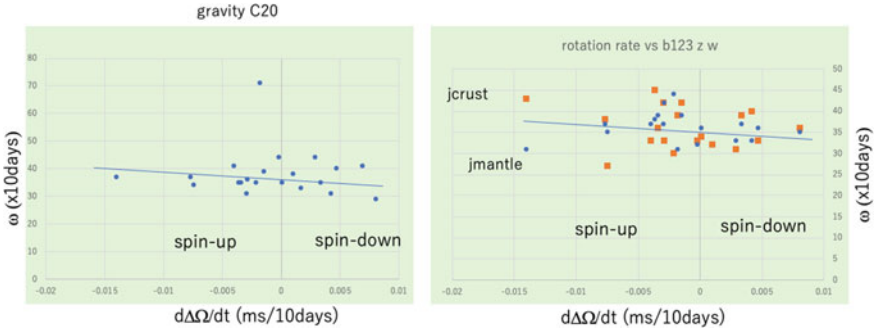

Fig. 5.27 Diagram of earth rotation rate and periodicity of the satellite gravity C20 (left) and regional correlated seismicity of b123 in the crust (red, right) and mantle (blue, right) of the Japanese islands, showing the slight decrease in the spin-down of the earth rotation

partly controlled by the global earth rotation rate, and thus, the momentum change due to the change of mass redistribution of the fluid earth affects the seismicity of the solid earth as discussed previously.

Therefore, let us investigate the relations of the earth rotation rate and the global correlated seismicity in the next. In Fig. 5.28, it is obvious that the global correlated seismicity z_1 tends to be a function of the rate of earth rotation in the period of the 1990–2021, and that in the spin-down region, there are two regimes, but in the spin-up region the single regime appears. It seems that the transition of the dynamical process of the earth rotation and global correlated seismicity takes place at the transient regime between them. It should be considered this type of dynamical transition to be the so-called pitchfork bifurcation in the nonlinear dynamics.

Furthermore, it is very important that the giant earthquakes in 2004 and 2021 took place in the transitional region of the pitchfork bifurcation as shown in Fig. 5.29. In addition, the spin-down and high correlated seismicity trend begins after giant

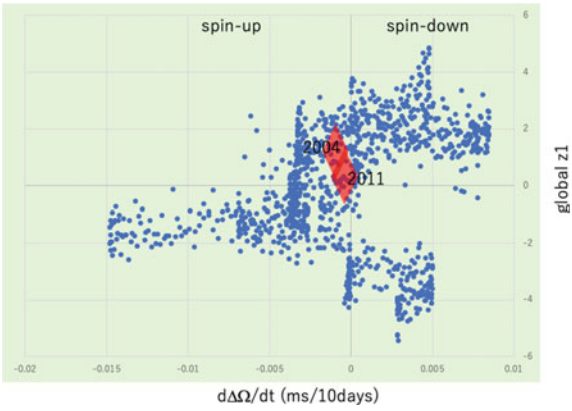

Fig. 5.28 Diagram showing the relations between the earth rotation rate and the global correlated seismicity z_1 from 1990 to 2018, showing the pitchfork bifurcation pattern in the global correlated seismicity dynamics related to earth rotation rate. Red triangles show the plots of giant earthquake events (see text)

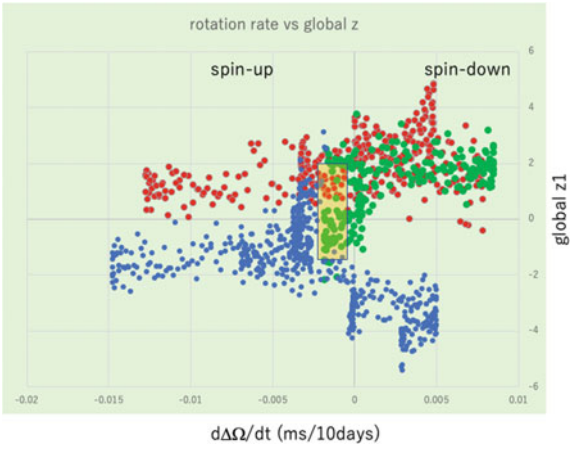

Fig. 5.29 Diagram showing the pitchfork bifurcation of the earth rotation-controlled global correlated seismicity and transition from single stability in the spin-up region to double stable states in the spin-down region. The transition region exhibits the giant earthquake zone (red shadow zone)

earthquake events. As noted previously, the giant earthquakes give only the almost always very small change of the earth rotation speed under the 0.001 times of the present level, and therefore, it is probable that it should be considered that the start of the spin-down of earth rotation may induce the giant earthquake failure of the plate boundary.

By the way, the pitchfork bifurcation of nonlinear dynamics is represented by the nonlinear ordinary differential equation (e.g., Kuramoto 2003) of

$$dz/dt = Kz - z^3 \tag{5.10}$$

in which K is the control parameter represented here by

$$\begin{aligned} K &= a(d\Delta\Omega/dt + 0.003) \\ z &= z_1 + 1 \end{aligned} \tag{5.11}$$

in which z_1 is the first global correlated seismicity and a is the constant term.

As the spin rate of the earth changes repeatedly likely to the periodical function together with earth rotation Ω as shown in Fig. 5.30.

Therefore, in the period of $K < 0$, the above ODE has a single stable solution of $z = 0$, on the other hand, in the condition of $K > 0$, it has double stable solution of $z = \pm K^{1/2}$.

In the previous book (Toriumi 2021), the author suggests the minimal model of the global correlated seismicity dynamics governed by nonlinear ODE involving z_1 and ${z_1}^3$ terms. In that model, the control parameter is taken to be z_2 which shows periodic variation. This is surprisingly consistent with the present pitchfork bifurcation model proposed above! Therefore, it may be evident that the global and the regional correlated seismicity dynamics is governed by the angular momentum change represented by the earth rotation rate as like as the gravitational variation and sea level rise as noted previously.

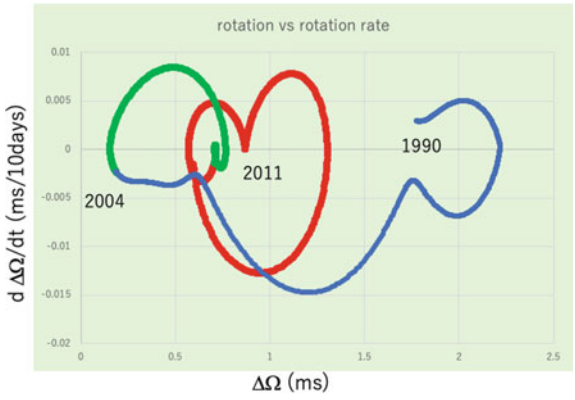

Fig. 5.30 Diagram of the earth rotation and the rotation rate (rotation derivative) from the 1990 to 2021, showing the transition from one loop to another loop at the giant earthquake events (2004 Sumatra, and 2011 Tohoku-Oki)

The important points of this simple model appear the timing of the giant earthquake events as mentioned previously. The onset of the pitchfork bifurcation in the z space is just at the giant earthquakes of Sumatra and Tohoku-Oki (Fig. 5.29), and this implies the synchronous relationship between the giant earthquake event and the critical point of the earth rotation rate, that is the earth spin rate. Considering that the spin rate is controlled by the angular momentum such as mass redistribution of the fluid earth (air, ocean, and outer core) and their boundary friction, and that the observed spin rate shows the sinusoidal temporal variation with several to several ten years cycle, it may be reasonable that the spin rate change is probably derived from the combination of climate change and celestial dynamical effects such as Chandler wobble (Blagoveshchenskaya et al. 2019). Soon, this problem should be discussed.

References

Barthelmes F (2013) Definition of functionals of the geopotential and their calculaiton from spherical harmonic models, Scientific Technical Report STR09/02. http://icgem.gfz-potsdam.de/ICGEM/

Bishop CM (2006) Pattern recognition and machine learning. Springer, New York

Blagoveshchenskaya E, Lyskova E, Sannikov K (2019) Variation of seismic activity caused by the Chandler wobble. In: E3S web of conferences 127, 03007, solar-terrestrial relations and physics of earthquake precursors. https://doi.org/10.1051/es3conf/201912703007

Chanard K, Fleitout L, Calais E, Rebischung P, Avouac J-P (2018) Toward a global horizontal and vertical elastic load deformation model derived from GRACE and GNSS station position time series. J Geophys Res, Solid Earth 123(4):3225–3237

Chen MK, Ries JC (2017) The unexpected signal in GRACE estimates of C20, J Geodesy. https://doi.org/10.1007/s000190-016-0995-5, https://doi.org/10.1029/2004GL019920

Chen JL, Wilson CR, Eanes RJ, Tapley BD (2000) A new assessment of long wavelength gravitational variations. J Geophys Res 105(B7):16271–16278

Chen JL, Wilson CR (2003) Low degree gravitational changes from earth rotation and geophysical models. Geophys Res Lett 30(24):257. https://doi.org/10.1029/2003GL018688

Chen JL, Wilson CR, Tapley BD, Famiglietti JS, Rodell M (2005) Seasonal global mean sea level change from satellite altimeter, GRACE, and geophysical models. J Geodesy 79(9):532. https://doi.org/10.1007/s00190-005-0005-9

Chen JL, Wilson JL, Ries JC (2016) Broad-band assessment of degree-2 gravitational changes from GRACE and other estimates, 2002–2015. J Geophys Res 121:2121–2128. https://doi.org/10.1029/2015JB012708

Dumberry M, Bloxham J (2004) Variations in the earth's gravity field caused by torsional oscillations in the core. Geophys J Int 159(2):417–434. https://doi.org/10.1111/j.1365-246X.2004.02402.x

Heki K (2010) Co-seismic gravity changes of the 2010 earthquake in central Chile from satellite gravimetry. Geophys Res Lett 37:24306. https://doi.org/10.1029/2010GL04335

Kuramoto Y (2003) Chemical oscillations, waves, and turbulence. Dover, 340p

Matsuo K, Heki K (2011) Coseismic gravity changes of the 2011 Tohoku-Oki earthquake from satellite gravimetry. Geophys Res Lett 38:7

NOAA (2021) https://tidesandcurrents.noaa.gov/strends

Schwartz S, Rokosky JM (2006) Slow slip events and seismic tremor at Circum-Pacific subduction zones, Rev Geophys 45:RG3004. https://doi.org/10.1029/2006rg000208

Tapley BD, Bettadpur S, Watkins M, Reigber C (2004) The gravity recovery and climate experiment: mission overview and early results. Geophys Res Lett 31:L09607. https://doi.org/10.1029/2004GL019920

Toriumi M (2021) Global seismicity dynamics and data-driven science. Springer

Chapter 6
Gaussian Network Model of Global Seismicity

Abstract The plate tectonics needs the direct stress continuity between the far-distant subduction zones within the travel time of the elastic wave through the rigid plate. Therefore, the plate boundary zones in the globally connected western and eastern Pacific regions possibly form some kinds of mechanical network system in which the global correlated seismicity of the subduction zones is coherent with each other. The dynamics of this type of globally connected seismicity network should be controlled by the rotation-invariant potential energy with connectivity matrix (Kirchhoff matrix).

Keywords Gaussian network of global seismicity · Kirchhoff matrix · Network transition

6.1 Phase Transition and Fluctuation in Gaussian Network Dynamics

In the previous chapters, the basic mechanisms of crack growth and propagation and its distribution were discussed in the simulation and natural occurrence and materials scientific process of chemical weakening of cracks and aqueous solution flow through them were also pointed out for applying their basics to earth mechanics. In this book, the author called the relevant field of earth science as the geochemical mechanics.

On the other hand, even in the rock mass with about 100 m size, the shear and open cracks filled with fluid show the inhomogeneous distribution patterns and thus the mechanical strength and permeability of such rock mass should be controlled by their density and connectivity distribution, that is the network dynamics. In the cases of global and regional seismicity patterns, the author has proposed the network model of the transition of the global seismicity and regional seismicity pattern by means of the correlated seismicity rate. In the previous book, the transition of global seismicity network from the region of western Pacific and eastern Indian Ocean to the Eastern Pacific with NEJ can be identified in the correlated seismicity model that took place rapidly and repeatedly. In this book, the author will try to propose a dynamic model of Gaussian network model (GNM) of the global seismicity dynamics.

M. Toriumi, *Geochemical Mechanics and Deep Neural Network Modeling*,
Advances in Geological Science, https://doi.org/10.1007/978-981-19-3659-3_6

GNM is a newly founded model for investigating the function of the bio-giant molecules such as ribosome and proteins with DNA and RNA. This is based on the simple assumption that the potential and potential fluctuation of the node and its connection are formulated by the sum of apparent elastic energy by displacement of position of atom from the regular position measured by X-ray structure analysis (e.g., Rader et al. 2006, Felice and Mancini 2015). That is,

$$\begin{aligned} Ub &= h/2 \sum \left(\Gamma_{ij} \left(\Delta R_{ij} \right)^2 \right) \\ &= h/2 \Delta R^T \Gamma \Delta R \end{aligned} \tag{6.1}$$

in which Γ_{ij} is the connectivity matrix (Kirchhoff matrix) and ΔR_{ij} is the fluctuation of distance between i and j atoms.

In this study, the potential of the seismicity network along the plate boundary zone is assumed to be a fluctuation in strain energy release rate estimated from logarithmic seismicity rate as

$$U_k = h X^T \Gamma^k X \tag{6.2}$$

in which X and Γ^k are the logarithmic seismicity rate and Kirchhoff network matrix (connectivity matrix) of the kth network, respectively, and subscript T means the transposed matrix. U_k is the potential related to the shear crack strain of the mode kth network characterized by Γ^k, and h is the constant parameter related to the interaction term. In this binomial summation for the potential, so as to the U_k displays the multidimensional ellipsoid depending on the Kirchhoff matrix Γ^k in the (x_1, x_2, …, x_n) space, the minimum condition of U_k should be satisfied at the condition that the maximum dispersion ellipsoid of xi is approximated with the U_k ellipsoid, thereby indicating that the given {xi} should make the available Gaussian network of nodes Γ^k as illustrated in Fig. 6.1. In other words, the correlated seismicity matrix Z for the given data matrix X determines the Kirchhoff matrix Γ^k.

In this system, the X of the network system behaves as fluctuation with Gaussian probability density and Kirchhoff matrix characterizes the network mode which is represented by the connection patterns of nodes. Let us consider the potential difference between the kth and lth network as,

$$\begin{aligned} \Delta U &= U_k - U_l \\ &= X^T \left(\Gamma^k - \Gamma^l \right) X \end{aligned} \tag{6.3}$$

Because Kirchhoff matrix is symmetric matrix with each component of 0 or 1, the different matrix of Kirchhoff matrix is to be symmetric. Therefore, this matrix can be decomposed by eigenmatrix and rotation one. On the other hand, the above potential difference between two different network modes is expressed by sum of several $x_i x_j$ term. In order to obtain the minimum condition for the fluctuation of x_i,

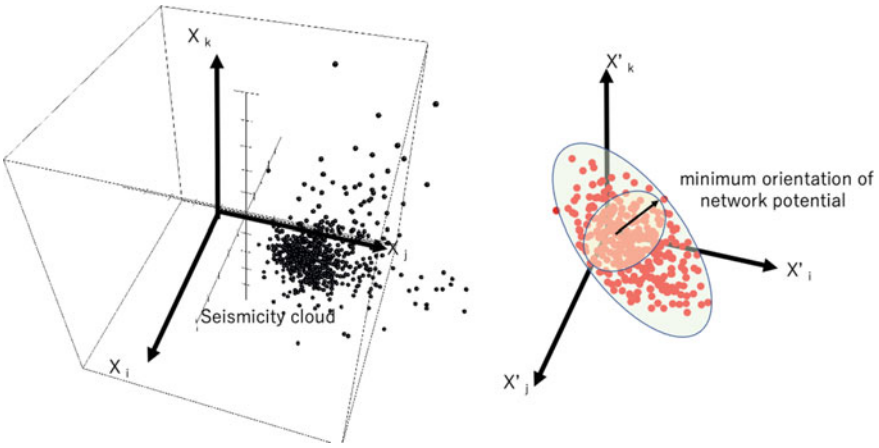

Fig. 6.1 Illustration of the data cloud of the logarithmic seismicity of gridded locality and minimum network potential ellipsoid in the representative localities diagram (see text)

the first derivative of ΔU should be zero together with equilibrium condition. Then, it holds,

$$\begin{aligned} \Delta U &= 0 \\ d\Delta U/dx_i &= 0 \end{aligned} \tag{6.4}$$

Further, the intensity of fluctuation at the transition from kth to lth network of the global seismicity can be estimated by the second derivative of ΔU as,

$$\beta_{\mathrm{ij}}^{-1} = d^2\Delta U/\mathrm{dx}_i\mathrm{dx}_j \tag{6.5}$$

In which β_{ij} is the susceptibility matrix of the ΔU against x_i and x_j.

Let us look at the case of artificial six-node system that contains two stable network patterns as shown in Fig. 6.2. The Kirchhoff matrixes of present two networks are represented as,

$$\Gamma^1 = \begin{pmatrix} 1\,0\,0\,0\,0\,1 \\ 0\,1\,1\,0\,0\,0 \\ 0\,1\,1\,0\,0\,1 \\ 0\,0\,0\,1\,0\,1 \\ 0\,0\,1\,0\,1\,1 \\ 1\,0\,1\,1\,1\,1 \end{pmatrix}$$

and,

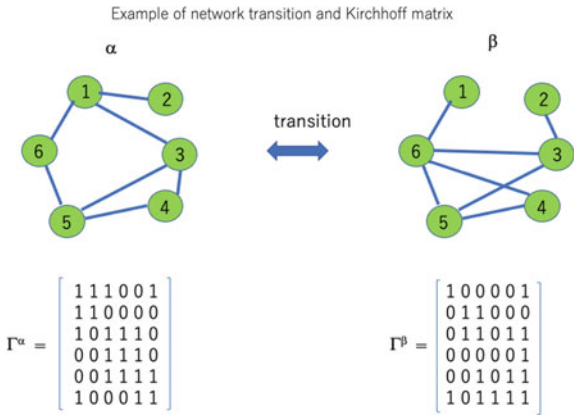

Fig. 6.2 Illustration of transition in the model networks with six nodes and representation of their Kirchhoff matrix

$$\Gamma^2 = \begin{pmatrix} 1&0&0&0&0&1 \\ 0&1&1&0&0&0 \\ 0&1&1&0&0&1 \\ 0&0&0&1&0&1 \\ 0&0&1&0&1&1 \\ 1&0&1&1&1&1 \end{pmatrix}$$

And thus, the *difference of them is,*

$$\Delta\Gamma^k = \begin{pmatrix} 0&1&0&0&0&0 \\ 1&0&-1&0&0&0 \\ 1&-1&0&1&0&-1 \\ 0&0&1&0&1&-1 \\ 0&0&0&1&0&0 \\ 0&0&-1&-1&0&0 \end{pmatrix} \tag{6.6}$$

Therefore, the difference of potential energy of the network becomes,

$$\begin{aligned} \Delta U/2 &= (x_1x_2 + x_1x_3 - x_2x_3 + x_3x_4 - x_3x_6 + x_4x_5 - x_4x_6) \\ &= x_2(x_1 - x_3) + x_4(x_3 + x_5 - x_6) + x_3(x_1 - x_6) \end{aligned} \tag{6.7}$$

Now, when the above potential may be differentiated by x_2 and x_4 and be equal to zero, it would become,

$$\begin{aligned} &d\Delta U/2dx_2 = x_1 - x_3 = 0 \\ &d\Delta U/2dx_4 = x_3 + x_5 - x_6 = 0 \\ &\text{other derivatives} = /0 \end{aligned} \tag{6.8}$$

and,

$$\begin{aligned} x_1 &= x_3 \\ x_3 + x_5 &= x_6 \end{aligned} \tag{6.9}$$

Inasmuch as xi is stochastic variable with Gaussian probability function, then it is concluded that the transition from the 1-network to 2-network due to the fluctuation of isolated nodes 2 and 4 occurs at the above conditions with synchronization of x_1, x_3, and x_6.

Next, let us discuss the global seismicity network system along the subduction zone shown in the previous book (GSD). As indicated in the book (GSD), the network of the global seismicity of the gridded subduction zone is mainly composed of two networks with six nodes that are grids of Northeast Japan (NJ), Sumatra (SM), Tonga-Kermadec (TK), Chile (CH). These nodes are mutually connected by the correlated seismicity variation, and then the bonding potential of them is possibly defined by the product of their logarithmic seismicity rate $x_i x_j$ as defined in the previous book. Two types of their Gaussian network are shown by the network geometry as indicated in Fig. 6.3, suggesting that there is important difference between them in the connection modes of the SM and CH. The network mode changes with advance of time from 1990 to 2021 from NJ-CH-TK to TK-SM-NJ, and NJ-TK to 5:CH-NJ as shown in Fig. 6.3.

Above change of the network mode of the global seismicity from 1 to 2 is possibly expressed by the Kirchhoff matrix (symmetric matrix) as like as

$$\Gamma^1 = \begin{pmatrix} 1 & 1 & 1 & 0 \\ 1 & 1 & 1 & 0 \\ 1 & 1 & 1 & 0 \\ 0 & 0 & 0 & 1 \end{pmatrix}$$

and

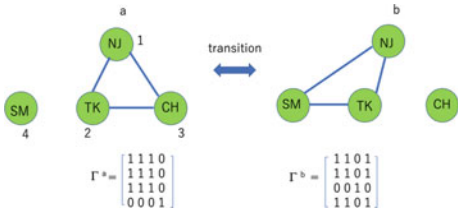

Fig. 6.3 Illustration of transition in the global correlated seismicity in the subduction zones and their Kirchhoff matrix. Abbreviations are follows: SM; Sumatra, TK; Tonga-Kermadec, NJ; Northeastern Japan, CH; Chile

$$\Gamma^2 = \begin{pmatrix} 1 & 1 & 0 & 1 \\ 1 & 1 & 0 & 1 \\ 0 & 0 & 1 & 0 \\ 1 & 1 & 0 & 1 \end{pmatrix}$$

Therefore, their difference becomes,

$$\Delta\Gamma^{1,2} = \begin{pmatrix} 0 & 0 & 1 & -1 \\ 0 & 0 & 1 & -1 \\ 1 & 1 & 0 & 0 \\ -1 & -1 & 0 & 0 \end{pmatrix} \tag{6.10}$$

Therefore, it seems that the potential difference of the two modes of Gaussian seismicity network of the global subduction is formulated by the following equation.

$$\begin{aligned} \Delta U &= 2x_1x_3 - 2x_1x_4 + 2x_2x_3 - 2x_2x_4 \\ &= 2x_1(x_3 - x_4) + 2x_2(x_3 - x_4) \end{aligned} \tag{6.11}$$

Thus, equilibrium condition at the transition of two modes holds,

$$\begin{aligned} d\Delta U/dx_1 &= 0 \\ d\Delta U/dx_2 &= 0 \end{aligned} \tag{6.12}$$

Then, the following conditions are satisfied as

$$x_3 = x_4 \tag{6.13}$$

As every xi contains a secular trend and fluctuation term with Gaussian probability density function, the time variation of x_1 sometimes satisfies above condition, but the linear relation of x_2 and x_{53} is larger than 0 at the same time. In this situation, the transition from one network type to another may happen gradually in the second-order phase transition style because both second derivative and first derivative of seismicity potential are zero. Therefore, it may be suggested that the seismicity of localities (gridded locality) which controls largely the global seismicity dynamics are those of SM, TK, CH, and NJ.

6.2 Geometrical Transformation of Gaussian Network of Global Seismicity

In the previous book (GSD), the author proposed the important network of the correlated global seismicity composed with NEJ, KR, TK, SS, CH, SM and the transition from the western Indian Ocean mode to Pacific Ocean mode. In addition, it seems

that the NEJ and TK are the keystone connecting both of Indian and Pacific modes. In the previous section, the network potential represented by binomial summation of logarithmic seismicity of gridded locality gives the important parameter of the transition of global seismicity network from Indian mode to Pacific mode mentioned above by means of taking the minimum of the present potential against NEJ and TK seismicity. As a result, it seems that the synchronization of the KR, CH, and SM seismicity should induce the network transition mentioned above.

Next, let us look at the change of the correlation pattern in the logarithmic seismicity rate time series of the global subduction zone in terms of Pearson's diagram of major components of the gridded localities on the correlated global seismicity as illustrated in Fig. 6.5. Pearson's diagram is obtained by the correlation matrix of the representative time series of the logarithmic seismicity rates of the global subduction zone, and that matrix is commonly shown by gridded pseudo-color presentation. In this investigation, the representative time series are those of loc.3, loc.10, loc.14, loc.25, loc.34, loc.66, loc.85, loc.111, loc.124, loc.138, and loc.156 (19 localities) as shown in Fig. 6.4, being selected by means of locality intensity patterns of z_1 correlated global seismicity in the previous book. Timestep for Pearson's correlation coefficient of the time series is taken to be 1000 days, and total time series of them are from 1990/1/1 to 2021/6/30.

It seems obvious that Pearson's diagrams from no.1 to no.13, as shown in Fig. 6.6, display the distinctive pattern change from weakly correlated pattern in the early stage to rather strongly correlated one in the later stage and even in the present days. Furthermore, it is possible to say that the local correlation pattern starts at the single locality and then rather correlation localities split apart from the starting locality in both side in the early periods from 1990 to 2016. In the later periods from 2016 to 2021, the whole region of the subduction zone is activated in the synchronic seismicity with weak correlation of seismicity during 2018. This tendency in Pearson's diagram is likely to the secular trend of the correlated global seismicity as shown in Fig. 6.6, and it shows also that the large moment release rate by large earthquakes appears in the later period from 2004 to 2018 as discussed in the previous book.

In terms of the seismic network system mentioned above, as seen in Pearson's mapping (e.g., Yang et al. 2005), the pattern of Pearson's maps is classified into three types: one is the diagram displaying the high correlation grids aligning parallel to the diagonal grids, second is the alignment of high correlation grids along single or double set of row and column, and third is the whole grids of Pearson' matrix showing the rather high correlation (Fig. 6.7). The last type of Pearson's matrix displays surely the high seismic activity of whole subduction zone. On the other hand, the second type displays the local synchronicity of the seismic activity and the first does the regional synchronic activity of seismicity in the subduction zone.

The seismic network of the gridded subduction zone is relevant to the above pattern that appeared in Pearson's diagram: strong correlation of configured grids obviously represents some degree of network connection, and weak correlation does loss of the connection of the seismicity network. Therefore, the synchronic activity of seismicity in the whole subduction zone manifests the global coherence in connectivity of the seismicity network, thereby suggesting the high mechanical activity of the solid earth.

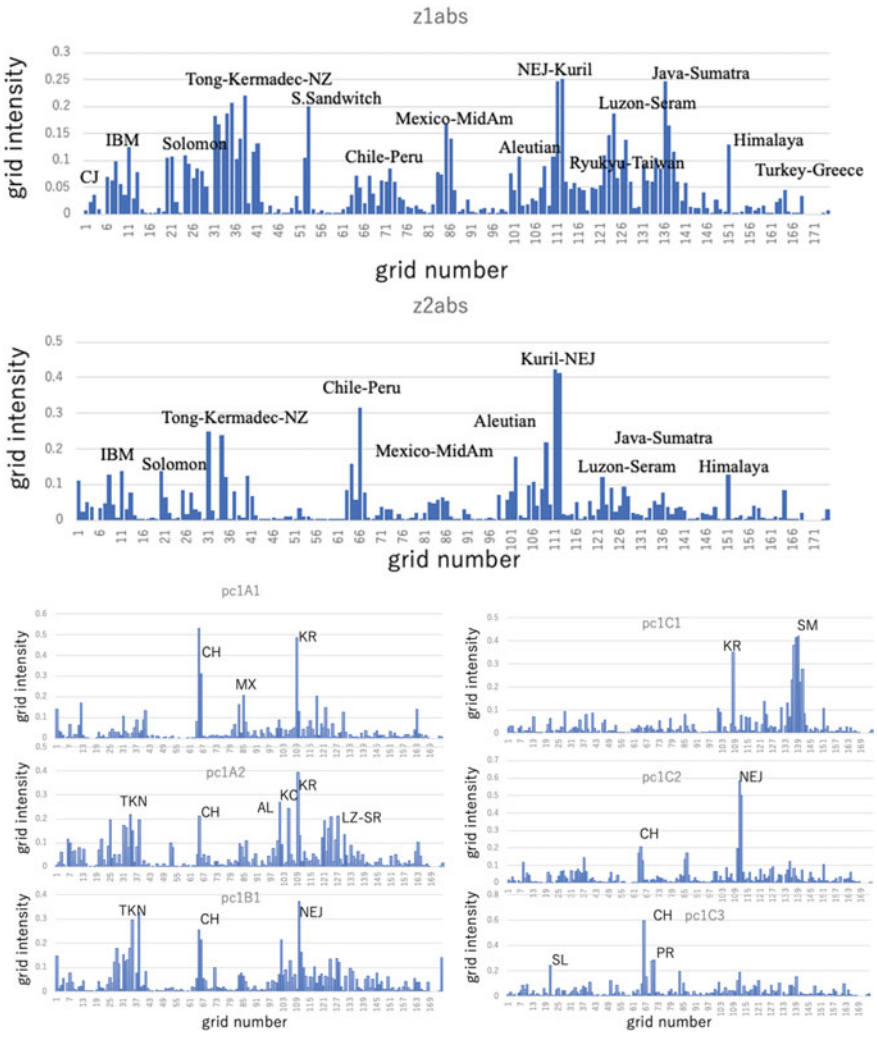

Fig. 6.4 Weight intensities of gridded localities in the global correlated seismicity z_1 and z_2 and details classified by stages of temporal variation of z_1, showing the high intensity localities in the subduction zone

After 2004 of Sumatra and 2011 Tohoku-Oki earthquakes, it should be considered that the subduction system changes global—mechanical exciting state and this state continues at present days.

Next, let us look at the detailed connection of the network in the global subduction zone in terms of Pearson's map. As seen in Fig. 6.6, it seems to be clear that the seismicity connectivity of the gridded locality of the subduction zone is possibly represented by the pseudo-color intensity in the map. If we take the 2-digit expression from Pearson's map, the map manifests the Kirchhoff matrix itself in the selected

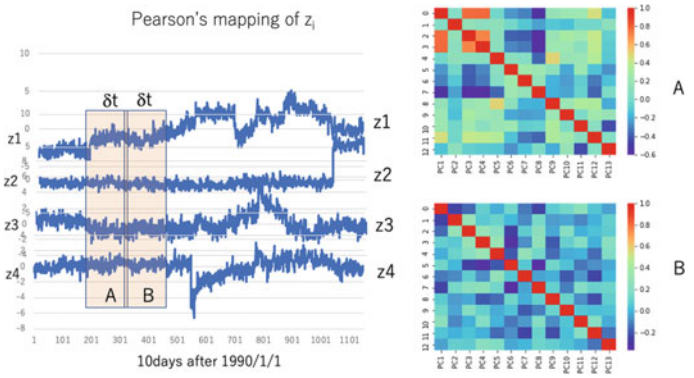

Fig. 6.5 Illustration of the Pearson diagram of studied time series of the logarithmic seismicity rates Xi and their correlated seismicity z_i in the subduction zones. The Pearson matrix is calculated from the correlation matrix of the segmented time series z_1–z_k (left), and it is shown by pseudo-color representation of the matrix value (right)

nodes. Therefore, it is obvious that the detail pattern of the seismicity network, that is the mechanical coupling network, is shown by Pearson's map change with advancing the time from 1990 to 2021.

It is allowed to be concluded that the key grids of the seismicity connection in the global subduction zone are the Northern Japan (NJ), (Tonga-Kermadec (TK), Chile (CH), and Sumatra (SM), and subsidiary the Mexico (MX), Kamchatka (KM), Java (JV), Luzon–Taiwan (LZ), and Himalaya (HM). These are likely to those inferred from the correlated global seismicity zi, though Pearson's map displays local connectivity intensity together with regional to global connectivity. As displayed in Fig. 6.7, it appears that the high correlation grids aligned along the horizontal row are represented by the regional far-distant connection of the seismic activity, but high correlation grids clustered near the diagonal domains of the map are related to the local connection of them. For example, it seems that there is rather strong correlation among TK, CH, NJ, and SM in Pearson's map of 4–6 and 8–10. On the other hand, the widely obvious-correlated pattern of most grids can be found in 10, 11, and 13 of Fig. 6.6, suggesting that the global correlated seismic activity appears in whole region of the subduction zone. It seems that the plate motion in this period is globally active in the solid earth.

In addition, it is noteworthy that the local correlated pattern of CH, SM, and NJ appear in nos. 6, 8, and 9 of Pearson's map (Fig. 6.6), thereby suggesting the isolated—localization of the correlated seismicity at the time of giant earthquakes associated with noncoherent activity of seismicity around high correlation grids. This type of grid pattern of Pearson's map displays the entrainment of the strain energy into the large earthquake region before and after the earthquake event. It seems that there are weak signals before the large earthquakes surrounding the grids of later earthquake as seen in Fig. 6.6.

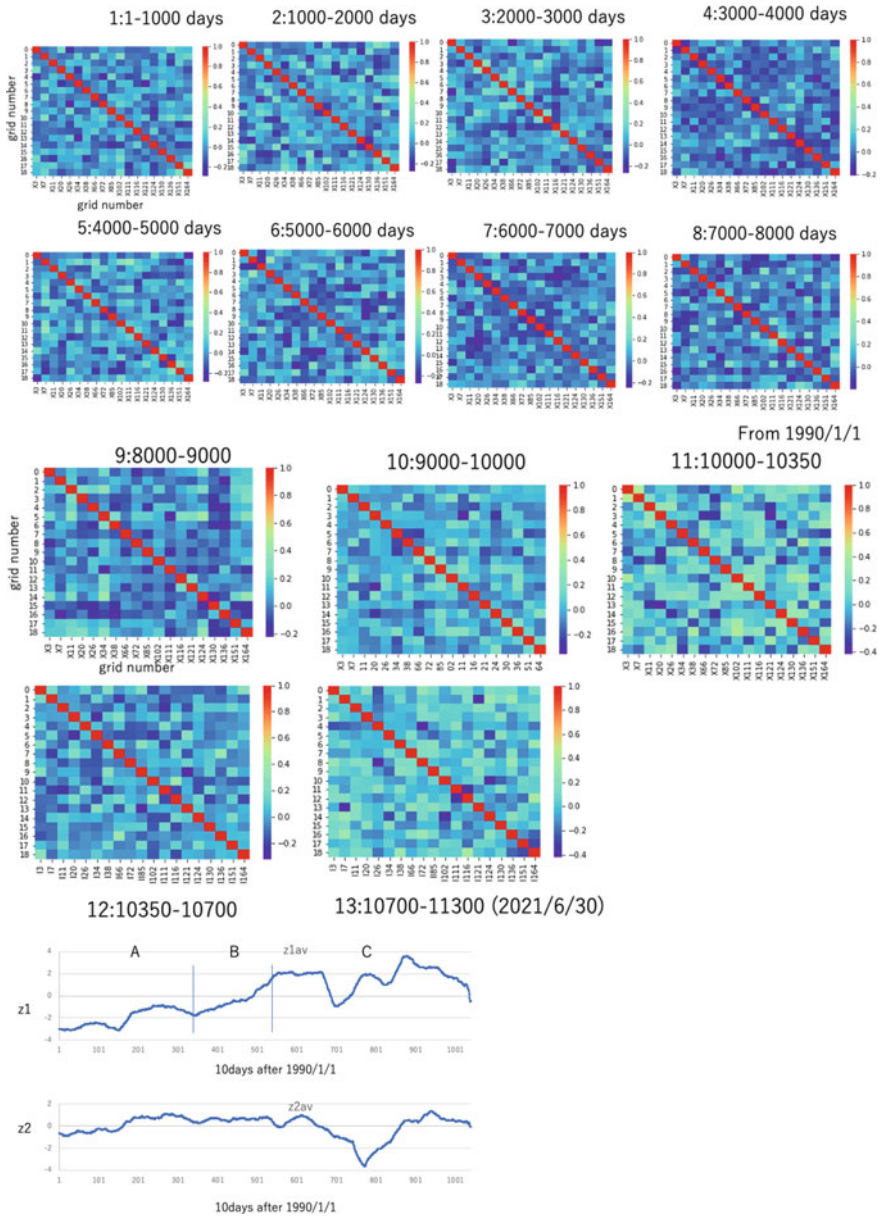

Fig. 6.6 Series of Pearson diagrams of global logarithmic seismicity of high-weight gridded localities in the global subduction zone from 1990/1/1 to 2021/6/30 in the 1000 days step. The bottom figures show the time series of annual average of z_1 and z_2 of the global subduction zone

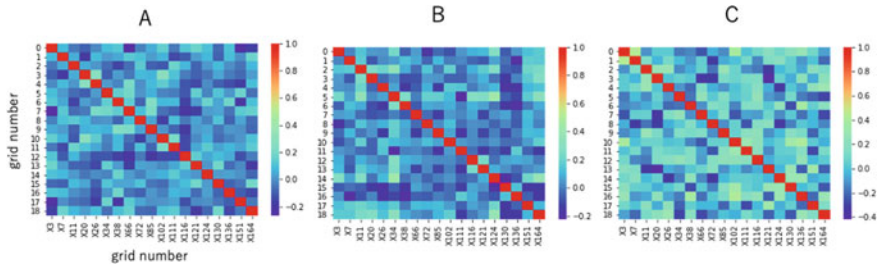

Fig. 6.7 Pearson diagrams of logarithmic seismicity of gridded localities for the clusters in the global correlated seismicity z_1 and z_2 diagrams A, B, and C, showing the wide correlation in the C cluster

Furthermore, it is suggested that there is a sequence in connection strength in the order of TK-NJ, CH-NJ, CH-TK, SM-TK, TK-NJ, and TK-SM. This sequence of rather strong connectivity in seismicity manifests the migration of the mechanical interaction in global network dynamics of the subduction zone involving Pacific Plate, Cocos Plate, Philippine Sea Plate, and Indian Ocean Plate as illustrated in the model of Fig. 6.3. Besides, it is probable that the seismic connection of SM-LZ, NJ-IZ SM-HM, TK-NZ, CH-MX, and NJ-KM appears subsidiary associated with the major connections described above.

It should be concluded that the Gaussian network dynamics of the subduction seismicity represent the transition from the NT-CH-TK to the SM-NT-TK-CH system through the SM-TK as shown in Fig. 6.3.

Furthermore, it is obvious that Pearson's diagram of the global correlated seismicity z_i displays the strengthened patterns of correlation from z_1–z_{12} and their temporal variation as shown in Fig. 6.8. It suggests that there are mainly two patterns showing the correlation of many components of z_i and the pattern of weak correlation among z_i, suggesting the difference of the network types as mentioned previously.

6.3 Gaussian Network Dynamics of the Japanese Region

Japanese islands region shows a very active seismicity from 1990 to 2021 as seen in the previous sections, and that is the key locality of the Gaussian network dynamics of the global seismicity in the subduction zone. It is surely found that as the network subsystem of the global network the seismicity and correlated seismicity of the Japanese islands region is very controlled by the global seismicity network behavior. In the previous section, it is clarified that the long-term variation of the network system appeared in Pearson' s map displays the transition from the heterogeneous correlation patterns to the global correlation one after 2016 and the repeating change from Pacific region to Pacific–Indian Ocean region. Therefore, it is to be clarified that in the Japanese islands region the long-term trend of the subsystem network of

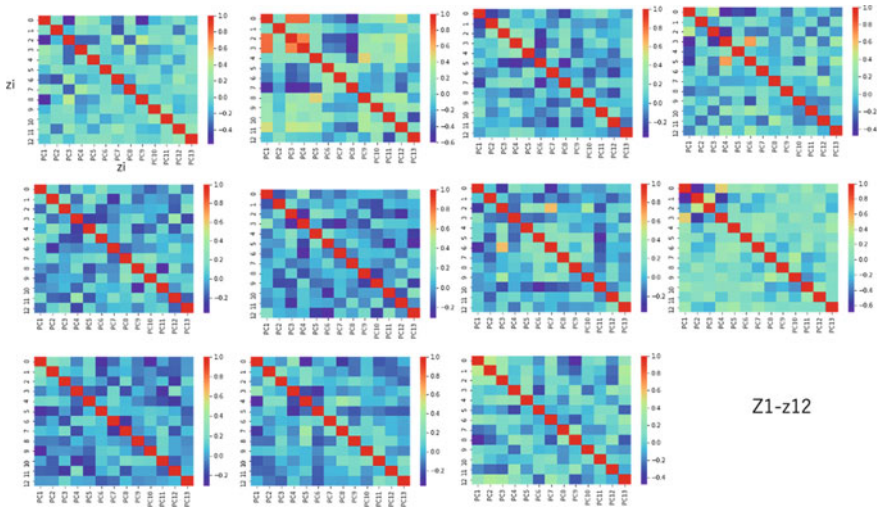

Fig. 6.8 Series of Pearson diagrams of the global correlated seismicity z_1–z_{12} (pc_1–pc_{12} in figure) from 1990/1/1 in the 1000 days step

this region also shows the transition from local change to regional variation in the correlation map after 2010.

First let us look at the sparse modeling of the Japanese seismicity dynamics by means of SVD method as in the previous book. The correlated seismicity of Japanese islands region obtained by SVD on data matrix of logarithmic seismicity rate of gridded localities is estimated in the period from 1998/1/1 to 2021/7/5 using the JMA1 stored in the database of National Institute of Earthquake Disaster (NIED) as well as those in the previous book (Toriumi 2021). The sparse modeling is obtained from the important coefficients of the eigenvectors of the covariant matrix of the logarithmic seismicity data of gridded localities for the several large eigenvalues, that is the correlated seismicity $z1$–$z4$ as same as in the previous book. In the previous book, the author investigated the seismic data from 1998 to 2018, but in this text, he studied the data from 1998/1/1 to 2021/7/5 as shown in Fig. 6.9.

As shown in Fig. 6.6, numbers of important grids for estimating the correlated seismicity of Japanese islands region are at most about 16 from Okinawa to Hokkaido region. Those are loc.3, loc.7, loc.10, loc.14, loc.28, loc.36, loc.44, loc.54, loc.62, loc.68, loc.74, loc.79, loc84, loc.88, loc.96, loc.103 (Fig. 6.10). Thus, Pearson's maps of them which indicate the grid pattern of correlation intensity between every seismicity density of these grid localities in Japanese islands region are shown from 1998 to 2021 in the time span about 100 steps in Fig. 6.11. It shows that there is a clear change of grid patterns showing the correlation of each time series in Pearson's map. In this figure, the correlation intensity is relevant to the strength of the connectivity of each grid, that is the seismicity network intensity of the locality nodes in the Japanese islands region.

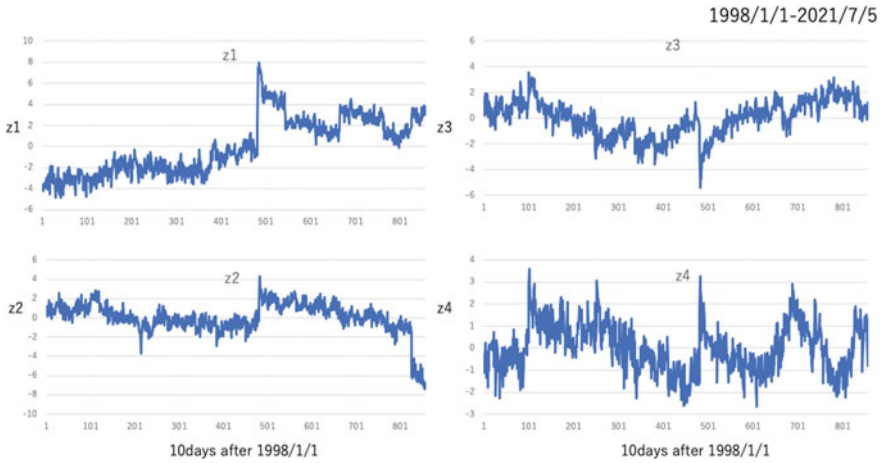

Fig. 6.9 Time series of the regional correlated seismicity z_1–z_4 from 1998/1/1 to 2021/7/31 of the Japanese islands region

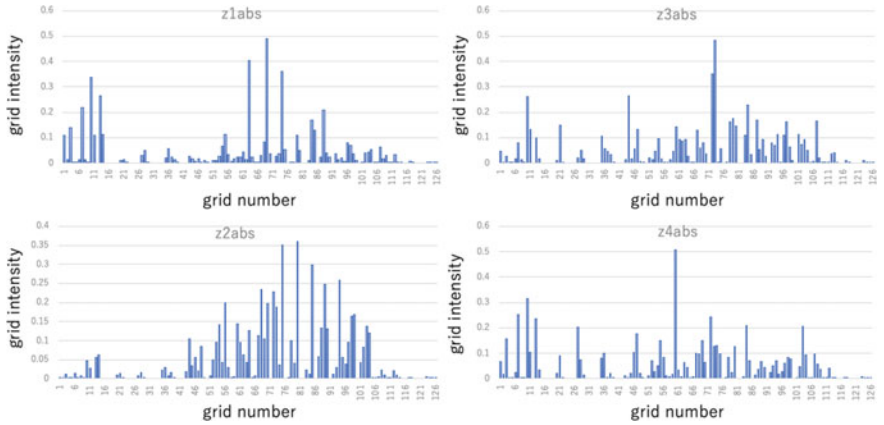

Fig. 6.10 Weight intensity of the regional correlated seismicity z_1–z_4 of Japanese islands region showing the important gridded localities v3 to v103

Therefore, in this study, it is available that the comparison of Pearson's map may allow us to classify the network connection pattern and the actual nodes in the Japanese islands region. As shown in Fig. 6.12, it should be said that there are several characteristic patterns in the rather high correlation in the distant grids. One is the connection of the northeast Japan and Okinawa region, second is that of Nankai and northeast Japan, and third is that of the northeast Japan and Hokkaido region. In Pearson's map, there should be classified into two types: one is the distant connections separated with each other and another is the distant connections bonded with each other. Therefore, the typical network structures are the nearly whole connected

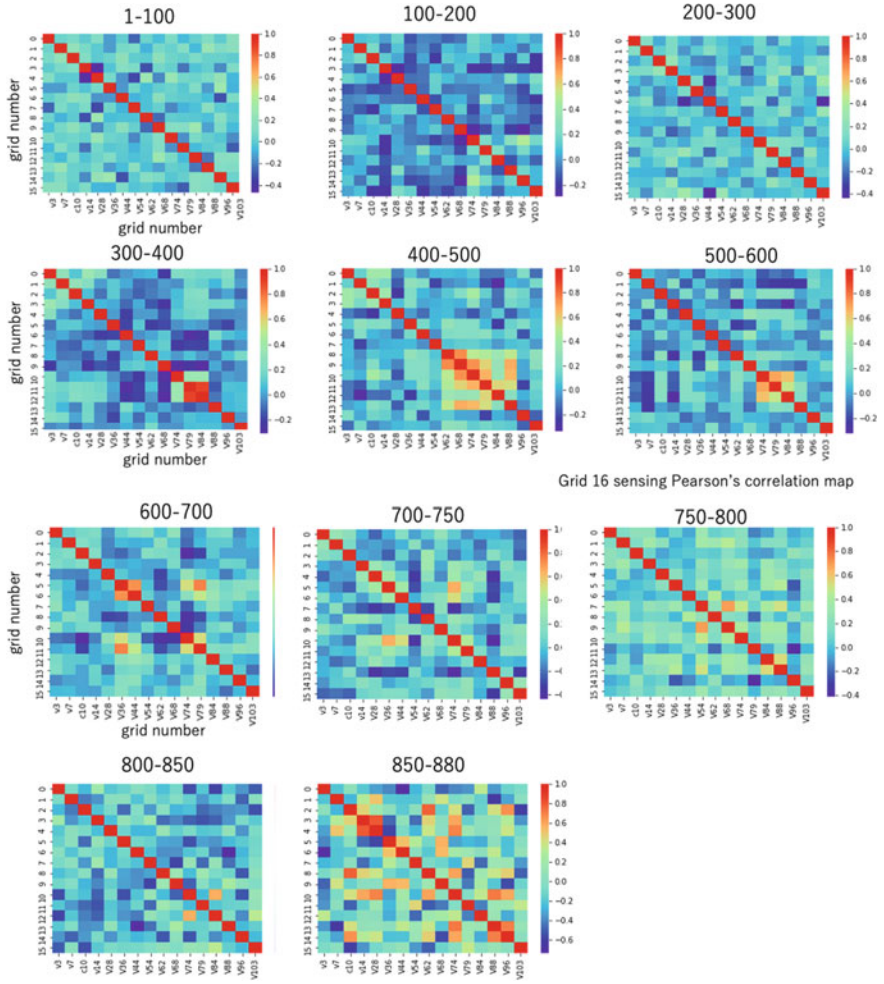

Fig. 6.11 Series of Pearson diagrams of the logarithmic seismicity in the 16 gridded localities of Japanese islands region from 1998/1/1 to 2021/7/31. Number shows the step after 1998/1/1 in the 10 days unit

network and partially connected one as represented in Fig. 6.13. In these network systems, the geometrical phase transition is possibly expressed by the following Kirchhoff matrix difference,

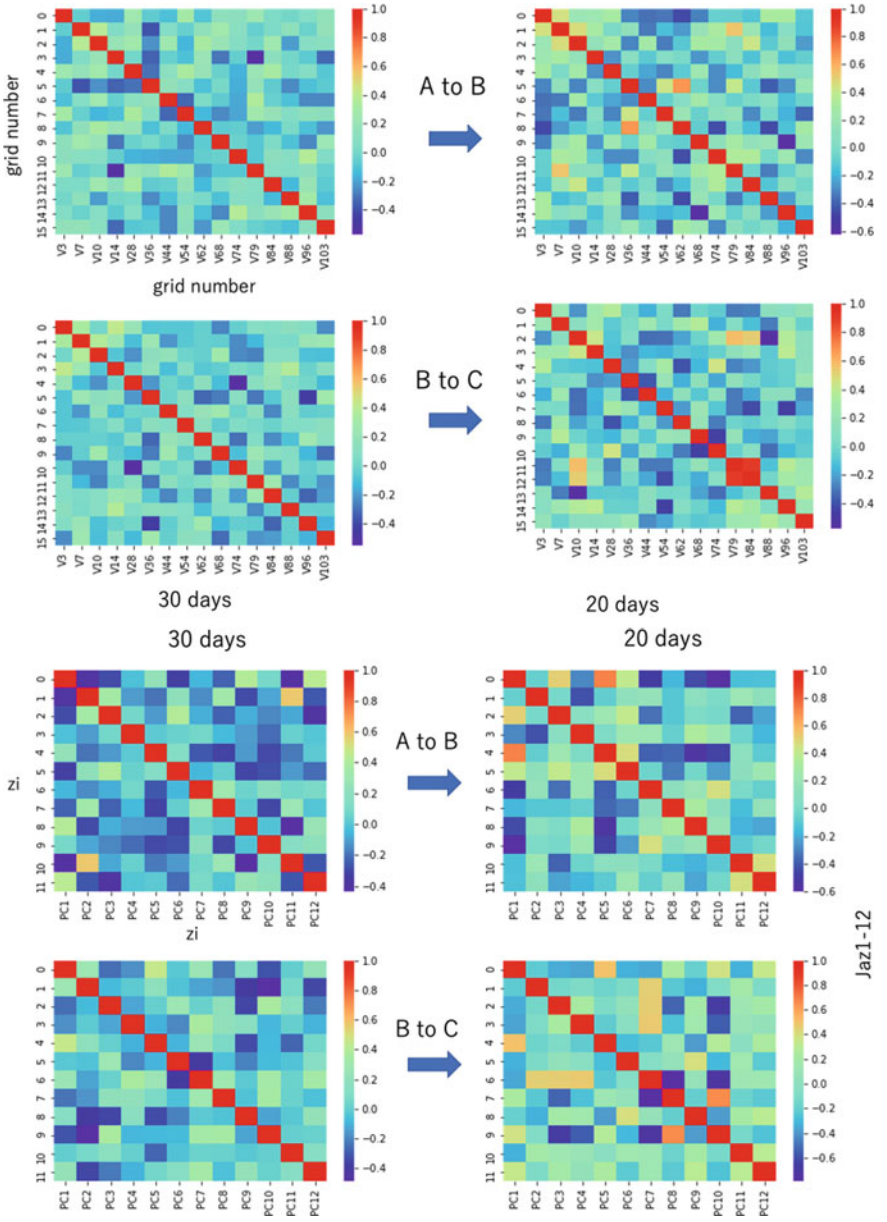

Fig. 6.12 Transition of Pearson diagrams in the clusters A, B, and C shown in bottom diagram of phase relation in the z_1 and z_3 of the regional correlated seismicity of Japanese islands region. Top; Pearson diagrams of logarithmic seismicity, Middle; Pearson diagrams of correlated seismicity

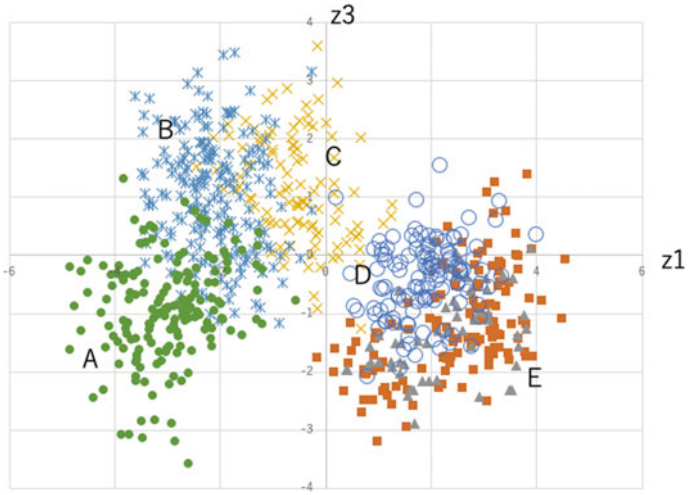

Fig. 6.12 (continued)

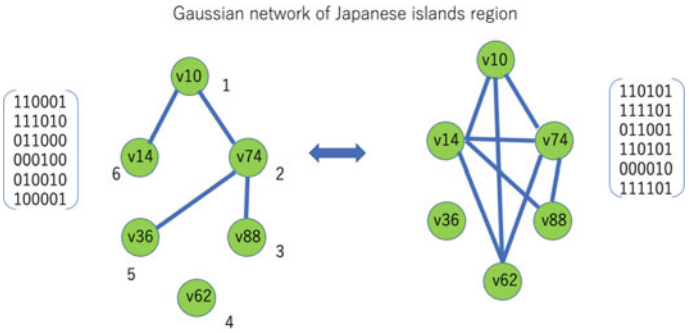

Fig. 6.13 Illustration of network transition and Kirchhoff matrix of the 6 nodes system of Japanese islands region in Pearson diagram series from 750 to 800 step in Fig. 6.11 in the period 2015–2016

$$\Delta\Gamma = \begin{pmatrix} 1&1&0&1&0&1 \\ 1&1&1&1&0&1 \\ 0&1&1&0&0&1 \\ 1&1&0&1&0&1 \\ 0&0&0&0&1&0 \\ 1&1&1&1&0&1 \end{pmatrix} - \begin{pmatrix} 1&1&0&0&0&1 \\ 1&1&1&0&1&0 \\ 0&1&1&0&0&0 \\ 0&0&0&1&0&0 \\ 0&1&0&0&1&0 \\ 1&0&0&0&0&1 \end{pmatrix}$$

$$= \begin{pmatrix} 0 & 0 & 1 & 0 & 0 & 0 \\ 0 & 0 & 0 & 1 & -1 & 1 \\ 0 & 0 & 0 & 0 & 0 & 1 \\ 1 & 1 & 0 & 0 & 0 & 1 \\ 0 & -1 & 0 & 0 & 0 & 0 \\ 0 & 1 & 1 & 1 & 0 & 0 \end{pmatrix} \tag{6.14}$$

Therefore, the transition condition becomes,

$$\begin{aligned} \Delta U = X^T \Delta \Gamma X &= (x_1 x_4 + x_2 x_4 - x_2 x_5 + x_2 x_6 + x_3 x_6 + x_4 x_6) \\ &= 2x_2(x_4 + x_6 - x_5) + 2(x_1 x_4 + x_3 x_6 + x_4 x_6) \end{aligned} \tag{6.15}$$

Thus, it holds,

$$d\Delta U / dx_2 = x_4 + x_6 - x_5 = 0 \tag{6.16}$$

other derivatives are not 0.

This condition means logarithmic seismicity of loc.14 and loc.62 is equal to that of the loc.36. As far as the logarithmic seismicity is the Gaussian type probability variable and it changes with time (Toriumi 2021), the sum of those of loc.14 and loc.62 also behaves as Gaussian fluctuation with time together with that of the loc.36 having different phase parameter. Therefore, it seems that the above transition condition should be satisfied at the available time as seen in Pearson's map after 2017.

By the way, if the time series of seismicity densities of their localities are periodic, the transition condition proposed above should display the behavior of the wave modulation that shows periodic time series with different frequencies. It is still unclear that the natural seismic network dynamics of Japanese islands region appears such periodic transition. However, it is worthy to be noted that the global seismic network dynamics also displays the similar network transition from localized connection pattern to whole connection pattern after 2016, thereby suggesting that the seismicity network transition in Japanese islands region is followed and strengthened by the global network transition.

On the other hand, it is to be noted that Pearson's map manifests the continuous change from giant earthquake of 3.11 Tohoku-Oki showing the diffusive enlargement and shrinkage of the seismic region during 200 steps, and that the area of the enlargement reaches to the Okinawa and southern Kyushu regions without the effect on Shikoku and Chugoku regions. Furthermore, as far as in Pearson's map, it seems that the giant earthquake does not induce the whole active network seismicity occurring in the later stage, but the entrainment of the seismic activity of surrounding regions may take place before the giant earthquake.

Next, let us compare the seismicity correlation in the plate boundary seismic activity of the subduction boundary zones of Ryukyu Trench, Nankai Trough, and Japan Trench by means of Pearson's map discussed previously. The tectonics of the

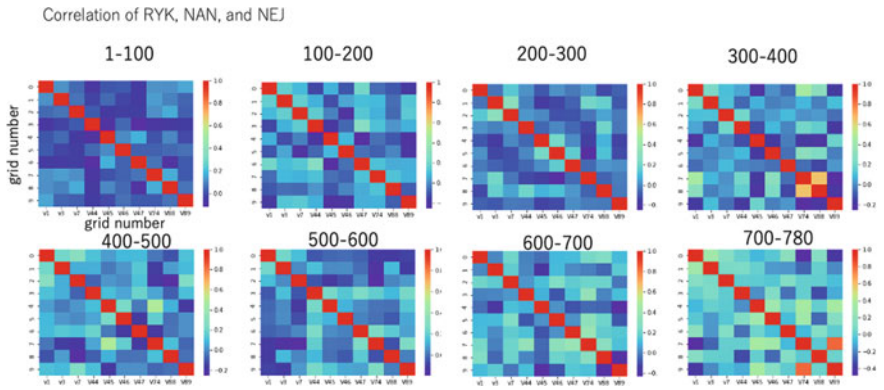

Fig. 6.14 Series of Pearson diagrams in the correlation of Ryukyu, Nankai, and Japan subduction zones in the small number of grids from 1998 to 2021, showing the drastic change after 600 steps

Japanese islands region is characterized by the triple junction of the subduction zones and the boundary zone juxtaposed by the Asian Plate, North American Plate, Philippine Sea Plate, and Pacific Plate. It is very important in the viewpoint of modeling of plate dynamics that the intensity of mechanical coupling of the subduction zones of Ryukyu Trench, Nankai Trough, and Japan Trench segments is possibly investigated by the correlation of seismicity time series of these subduction zones in terms of Pearson's map (Fig. 6.14).

As seen in the previous sections, it is obvious that the secular change of Pearson's map of the logarithmic seismicity of gridded Japanese islands region is possibly represented by the pattern transition from the localization of the seismicity to the wholly correlated seismicity map from 1998 to 2021. The localization pattern of the seismicity involves the diffusional extension from the large earthquake grid and shrinkage toward that one of the seismicity after the Tohoku-Oki 2011 earthquake. Therefore, it is natural to be considered that there should be a transition from isolated subduction zone seismicity pattern to cooperative one in the long-term variation of Pearson's map.

As shown in Fig. 6.15, it may be concluded that the pattern of Pearson's map changes from high correlation of NA—RY to NJ—RY, and from NJ -RY to NA—NJ and then to NJ—NA—RY. This pattern transition in Pearson's map should be summarized in the network transition of the subduction zone seismicity as illustrated in Fig. 6.8. It should be noticed that at the transition stage of each network mode, the large earthquakes took place in the present subduction boundary. According to the mechanical continuity of the subduction zones of Ryukyu and Nankai by Philippine Sea Plate, it may be strange that the correlation between Ryukyu and Nankai becomes disappeared at the second and third stages of Fig. 6.15. It is probable that the mechanical activity of the Nankai subduction zone is mainly covered by the slow slip and stable slip along the subduction boundary as discussed in the previous book (Toriumi 2021). However, it remains that there appears rather strong connection

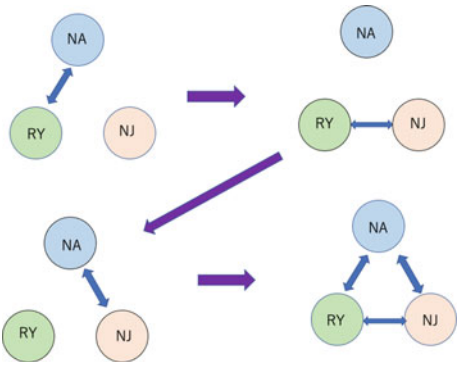

Fig. 6.15 Progressive change of the network structure of the logarithmic seismicity in nodes of Ryukyu (RY), Nankai (NA), and Northeast Japan (NJ) subduction zones from 1998 to 2021

between them in the early and latest stages studied here. It may be possible that the mechanical coupling with active seismicity seems to show an intermittent nature by the flux of the aqueous flow into the plate boundary plane as suggested by previous book.

By the way, as far as the correlation patterns mentioned above of gridded regional seismicity vary with time and space among the different plate boundary zones, it is possible to be considered that the correlated seismicity defined in the previous chapters also shows the characteristic pattern and its change in Pearson's map. Thus, the similar data processing of the correlated seismicity z_i of Japanese islands region will be investigated in the next.

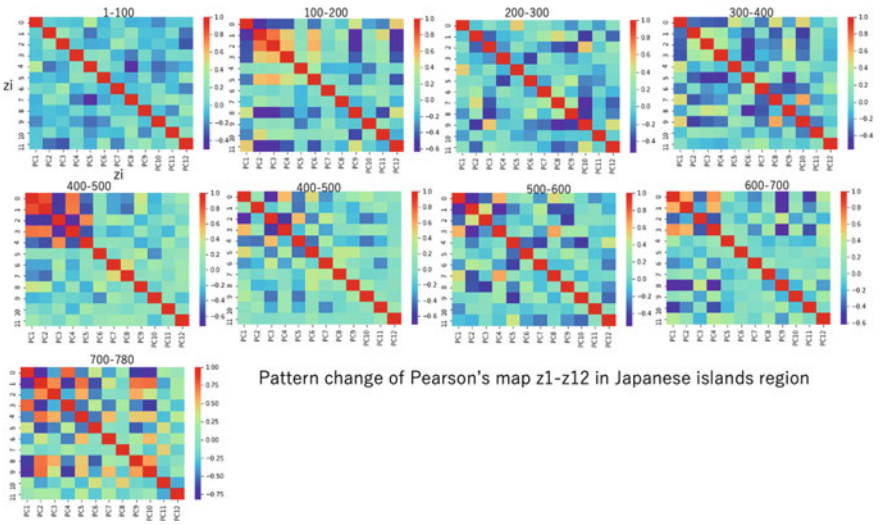

Fig. 6.16 Progressive pattern change of Pearson diagram of the regional correlated seismicity z_1–z_{12} of Japanese islands region from 1998 to 2021

In Fig. 6.16, it shows that the lower order (z_1–z_4) of the correlated seismicity z_i is distinctively changes repeatedly from synchronous correlation associated with antiphase (negative) correlation to rather random pattern as like as in the case of seismicity change in Pearson's map (Fig. 6.11). This is due to the reason why the correlated seismicity is the linear combination of gridded seismicity by the unique rotational matrix. Therefore, it is available that the characteristic network change of the gridded seismicity is favorable for the investigation and identification of the network structure of the regional and global mechanical system as discussed previously.

Basically, the correlated seismicity zi space is compliment with the original logarithmic seismicity data space of the gridded region, and new axes orthogonal are taken from the eigenvectors of the data matrix, that is the orthogonal projection. Therefore, the segmented time series of the correlated seismicity is also equivalent to those of the original seismicity of the gridded localities. Thus, it is obvious that the correlation pattern transition represented by Pearson's map in the correlated seismicity matrix is equivalent to that in the real seismicity data matrix.

Therefore, let us compare the pattern changes of the z and x space in the case of Japanese islands region. In Figs. 6.11 and 6.16, the pattern transition before and after the Sumatra (2004) or Nankai (2004 large eq) and Tohoku-Oki (2011) giant earthquakes are displayed. It is probable to conclude that there seems some change in patterns before and after Tohoku-Oki and Sumatra earthquakes in z space. In the case of the Tohoku-Oki, the pattern changes from the weak correlation pattern to the rather strong correlation around z_1–z_4, suggesting that the coherent seismicity appears in the whole Japanese island region after the Tohoku-Oki and maybe after the Sumatra (or Nankai eq). On the other hand, Pearson's map of the x space in the selected (sparse) grids shows the similar change from spatially random before the Tohoku-Oki earthquake to localized pattern after that event as shown in Fig. 6.11.

By the way, as seen in the correlation seismicity diagram of z_1 versus z_2, there are several clusters A–E in the ascending order of the time (Fig. 6.17), and the transition from one cluster to another one is commonly sharp and rapid. Therefore, it is to be

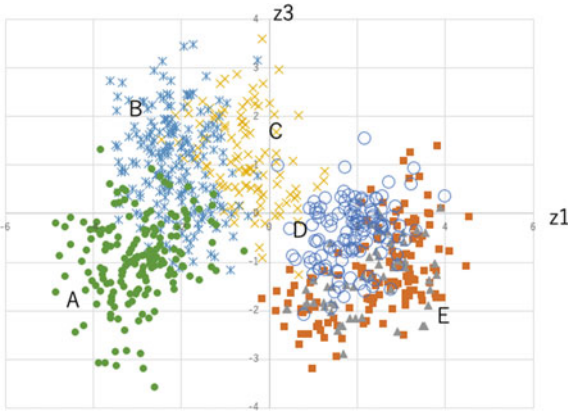

Fig. 6.17 Phase relation of the regional correlated seismicity z_1 and z_3 of Japanese islands region, showing the progressive change of clusters from A to E through B, C, and D

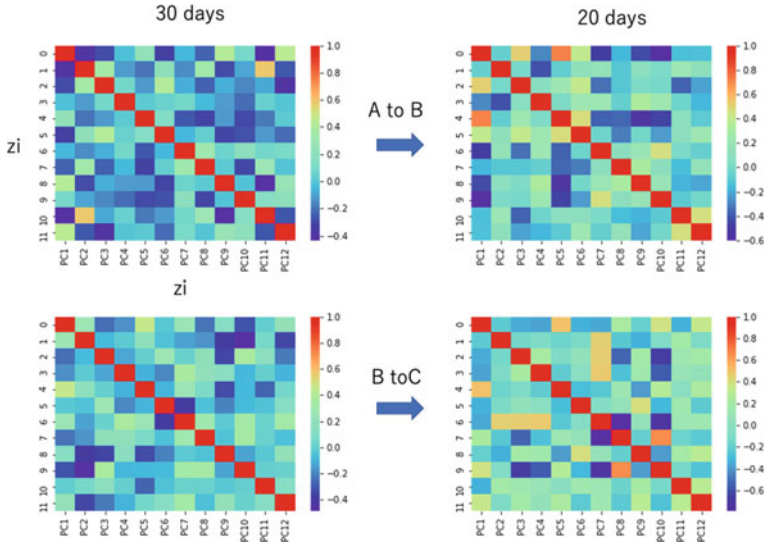

Fig. 6.18 Pattern change of Pearson diagram of the correlated seismicity z_1–z_{12} from A to B and B to C of the clusters in the regional correlated seismicity z_1 and z_3 shown in Fig. 6.17

checked that there is the sharp change in the correlation pattern. In Fig. 6.18, the correlation pattern change in Pearson's map shows a sharp transition that displays the random pattern before the transition to rather strong correlated pattern after the transition. It suggests that no correlation pattern changes to correlation one at drastic transition from A to B in Fig. 6.18, thereby showing that the initial state of the new pattern of the correlated seismicity system is represented by the whole network seismicity grids, and that the final state before transition shows the nearly random correlation state.

The similar change in Pearson's map can be found in the slider block system as discussed in the later section. It is obvious that, in the case of slider—block model for the plate boundary mechanics, the elementary block behaves as the complex oscillator connected by spring with side by side and upper boundary and linked by viscous (velocity-dependent) force with bottom plate and then the multiple linked oscillators should move intermittently in the synchronous and antisynchronous modes and in many times in the randomly nonsynchronous mode. The change to the intermittent synchronous mode comes drastic from random mode but that from synchronous mode to the random one is often continuous and slow. Therefore, it seems that the pattern transition of the seismicity and correlated seismicity resembles that of the slider block system, suggesting the similar operating dynamics between them.

By the way, in the previous book, the author proposed the model of transition in the correlated seismicity dynamics in terms of the nonlinear bistability dynamical differential Langevin equation having double minimum potential. It is,

$$\begin{aligned} dz_1/dt &= dU/dz_1 + \text{Noise} \\ U &= az_1^2 - bz_1^4 + cz_3 z_1 \\ dz_1/dt &= 2az_1 - 4bz_1^3 + z_3 \end{aligned} \tag{6.17}$$

In these equations, z_3 changes periodically.

By taking the null cline of the above equation, it holds,

$$z_3 = 2bz_1\left(6z_1^2 - a/b\right) \tag{6.18}$$

and,

$$z_3 = c \sin wt$$

However, if the Gaussian network system is considered as discussed in the previous discussion, the potential U becomes

$$U = a\left(x^T T x\right) - b\left(x^T T x\right)^2 + N(0, m) \tag{6.19}$$

Thus, the bistable system of the correlated seismicity z_1 is required for the second higher order of scalar product of logarithmic seismicity x.

References

Felice D, Mancini S (2015) Gaussian network's dynamics reflected into geometric entropy. Entropy 17:5660–5672. https://doi.org/10.3390/e17085660

Rader AJ, Chennubhotla C, Yang LW, Bahar I (2006) Gaussian network model: application and theory, BICH, pp 41–64

Toriumi M (2021) Global seismicity dynamics and data-driven science. Springer

Yang LW, Liu X, Jursa CJ, Holliman M, Rader AJ, Karimi HA, Bahar I (2005) iGNM: a database of protein functional motions based on Gaussian Network Model. Bioinformatics 21(13):2978–2987. https://doi.org/10.11093/bioinformatics/bti469

Chapter 7
Prediction Testing of Plate Boundary Earthquake by Global DCNN and VAE-CNN Modeling

Abstract Scientific prediction of natural phenomena occurring in near future is basically required for the numerical model based on the physical processes containing the basic equations and huge amounts of various parameters and initial/boundary conditions, even if they are very complicated and tangled within the basic processes. However, considering such complex and complicated nature of the earth's processes, as being like to the successive framework of the deep neural network modeling, there is surely a route of the probabilistic prediction science for the large earthquake, and it is absolutely needed for the sustainable community of human being. In this chapter, the author intends to try the large earthquake prediction testing by means of neural network modeling applying for the huge amounts of monitoring data from the regional and global seismic networks.

Keywords Prediction testing of large earthquakes · Deep neural network modeling · Timestep and time-shift modeling · Seismicity universal diagram · Slow and very slow slip events

7.1 Possibility of Probabilistic Prediction of the Large Earthquake

In the previous chapters and sections, the characteristic features of the earth mechanics relevant to the seismic phenomena have been proposed in terms of the interaction of aqueous solution and various cracks in the solid earth, and it is clarified that the micro- and small earthquakes are derived from the shear crack propagation after subcritical growth enhanced by flow-in of the aqueous solution into the cracks. Most shear cracks are associated with jog, kink, and micro-open cracks that are grown by absorption of aqueous solution, and these are successively sealed by metamorphic and metasomatic minerals precipitation. Furthermore, the formation of the jog and subsidiary open cracks makes an increase of actual porosity of the rocks and thus of the permeability of fluid. Therefore, it concludes that the shear cracks propagation resulting to the earthquake generation is strongly controlled by the geochemical behavior of the migrating aqueous solution.

M. Toriumi, *Geochemical Mechanics and Deep Neural Network Modeling*,
Advances in Geological Science, https://doi.org/10.1007/978-981-19-3659-3_7

On the other hand, the aqueous solution in the plate boundary zones is derived from the dewatering by compaction of sediments in the shallow parts and from the dehydration of the subducted materials and oceanic plate through metamorphic reactions in the deeper parts of the subduction zone. The fluid circulation along the plate boundary zone, therefore, is coupled with mineral precipitation along the shear crack jog and voids, and the dehydration reaction of the minerals due to the change of the chemical and physical conditions of the rocks and percolating fluid. Thus, the seismicity dynamics should be dependent on the geochemical and hydrological characteristics of the circulating aqueous fluids and hidden various types of micro- to small cracks.

Recently, Fukao et al. (2021) found the rapid slow slip event (rSSE) in the plate boundary and discussed the systematic relation from regular earthquakes to common SSE in the diagram of moment magnitude and duration time with stress drop and slip velocity. It seems that this type of the universal relation in the earth mechanics is possibly extended to the fluctuated plate motion proposed in the previous chapter and the more slowly possible SSE along on the plate boundary. The possible universal relations of them are shown in Fig. 7.1, suggesting the appearance of clear relationships between the slip velocity versus seismic moment, and the moment release rate versus seismic moment. In the diagram of average moment release rate and seismic moment of Fig. 7.2, it is expected that the universal relationship between them is possibly applied to the plate velocity fluctuation mentioned in the previous chapter. In this diagram, the relations of the glacier flow are plotted near the above universal relation (e.g., Thogelsen et al. 2019).

By the way, it is clarified that the variations of the global geophysical data are strongly related to the global seismicity and correlated seismicity of the plate boundary zones. It has been discussed also in detail that the mechanical network system of the global seismicity dynamics proposed in the previous book is possibly

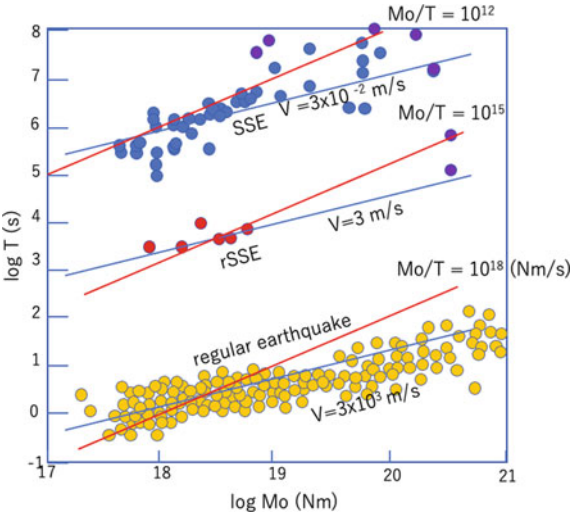

Fig. 7.1 Possible universal relations of seismic duration and seismic moment for various slow slip events (SSE) and common earthquakes based on the diagram by Fukao et al. (2021). Blue, red, and yellow dots are cited from Fukao et al. (2021) and purple dots are from Ide (2009). The diagram shows the systematic relations of slip velocity and average moment release rate against seismic moment

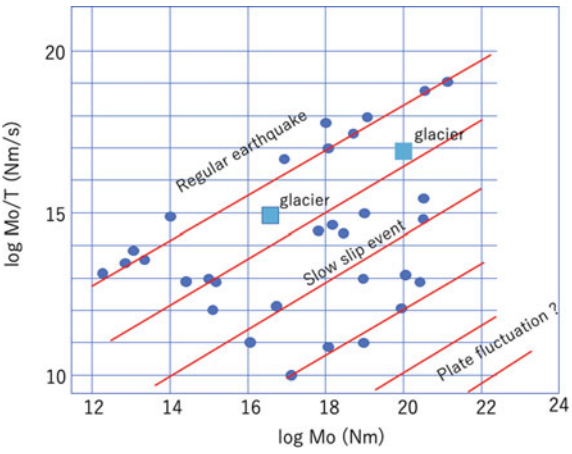

Fig. 7.2 Possible relations of the seismic moment and the moment release rate of regular earthquakes and various slow slip events together with plate velocity fluctuation shown in the previous chapter. The case of land glacier is shown in the same diagram. This diagram may be called as the seismicity universal diagram. Data are referred from Fukao et al. (2021) and Ide (2009)

dealt with the Gaussian network dynamics through sparse modeling of the global correlated seismicity dynamics. In this GND modeling, the network system is characterized by the Kirchhoff matrix, and the present Kirchhoff matrix is inferred by the minimization of the potential energy related to the logarithmic seismicity. Furthermore, the transition from one network to another network system is possibly defined by the minimization of the difference of the above scalar-valued potential energy characterized by the Kirchhoff matrix as discussed in the previous chapter.

On the other hand, it has been clarified that the correlation patterns of the short segments of time series of the logarithmic seismicity in the important nodes of the Gaussian seismicity network are possibly investigated by the Pearson's map of them, and that the transition of the network mode is associated with the rapid change from the random and incoherent pattern to the highly coherent one. In addition, it seems that the large earthquake event gives aftershock effect as the forcible synchronous seismicity on the wide region surrounding the hypocenter. It seems that the foreseismic signals of the large earthquakes in the Gaussian seismicity network appear probably in the change of correlation patterns of the Pearson's map that the nearly random noisy patterns change slightly to the coherent patterns near the coming large earthquake locality. However, this is not clear yet, and it seems that this weak signal before the large earthquake is not potential to prediction of the earthquake.

By the way, the author proposed the data-driven scientific method available for the new framework of understanding the global seismicity dynamics of the solid earth in the previous book (Toriumi 2021). By means of the data-driven scientific method, it is possible that the global seismic phenomena in the solid earth manifest the long-term secular variation and the short-term near-annual variation (seasonal variation). Furthermore, it is also suggested that the secular trends of the global correlated seismicity changes from low activity to high activity period after 2003 before Sumatra giant earthquake of 2004.

In the Pearson's map of the global subduction zone and of the Japanese island region too, it is obvious that Pearson's correlation map shows the distinctive change

from repeating of the weak and local coherent pattern to the wholly coherent (maybe synchronous) pattern after 2016, though the time of this transition does not coincide with the time of the drastic change of the correlated seismicity mentioned above. However, the present pattern change of the global subduction zone is coeval with that of the Japanese island regional system, thereby suggesting that the secular trend of the seismicity and correlated seismicity of the regional system is governed largely by that of the global solid earth system.

In this chapter, the author intends to propose the new method of probability prediction of the large earthquake and discusses the availability of the method using deep machine learning with neural network model. In this study, the method is still in the way of the foundation, and thus, it is the test case of the probability prediction of the large earthquake, though there is available method of regression of seismicity time series that is the ETAS model by Ogata (2015). The proposed testing model for probability prediction of the earthquake is based on the machine learning with neural network model. The large earthquake event is intermittent and very rare phenomenon, and thus, it is difficult to investigate the signals before earthquake though there are distinctive aftershock signals. In the previous book, the regression of the correlated seismicity time series of the global and regional system is possibly determined by the recurrent neural network, convolution neural network and simple dense neural network models, and the testing using the large number of parameters from the former data matrix to the latter one by means of the separation of whole data matrix. This validation is called as the cross-validation method, and it verifies the prediction of the several steps ahead of the correlated seismicity (Toriumi 2021). Therefore, in this chapter, it is needed that whether the deep learning with neural network modeling is available for the probability prediction of the large earthquakes by means of the global and regional correlated seismicity and relevant geophysical big data from the satellite observatories and VLBI monitoring. The author also intends to propose a new method in order to perform a stochastic prediction of large earthquakes in the global earth mechanics system by means of DCNN-VTT with labeling modeling together with variational autoencoder with CNN (VAE-CNN) with labeling modeling.

7.2 Preprocessing of Seismic Source Data

Seismicity rates used here are obtained from USGS Earthquake database center after 1990/1/1 to 2021/6/30 and sorted in the gridded localities of the global subduction and ridge zones (Fig. 7.3 top). The magnitude of earthquakes studied here is ranged from M4 to M5 and M7–M9.5 of the global subduction zones, because of keeping sample homogeneity. In studying the seismicity rates in the Japanese islands region, the hypocenter data of M1 to M4 are cited from JMA-1 database in Japan Meteoric Agency and NIED in the time range from 1998 to 2021 because precise digital seismometer network has been established by 1998 in Japanese islands region.

The data matrixes of logarithmic seismicity rate in the unit volume and time interval along the subduction zone and in the Japanese islands region are introduced

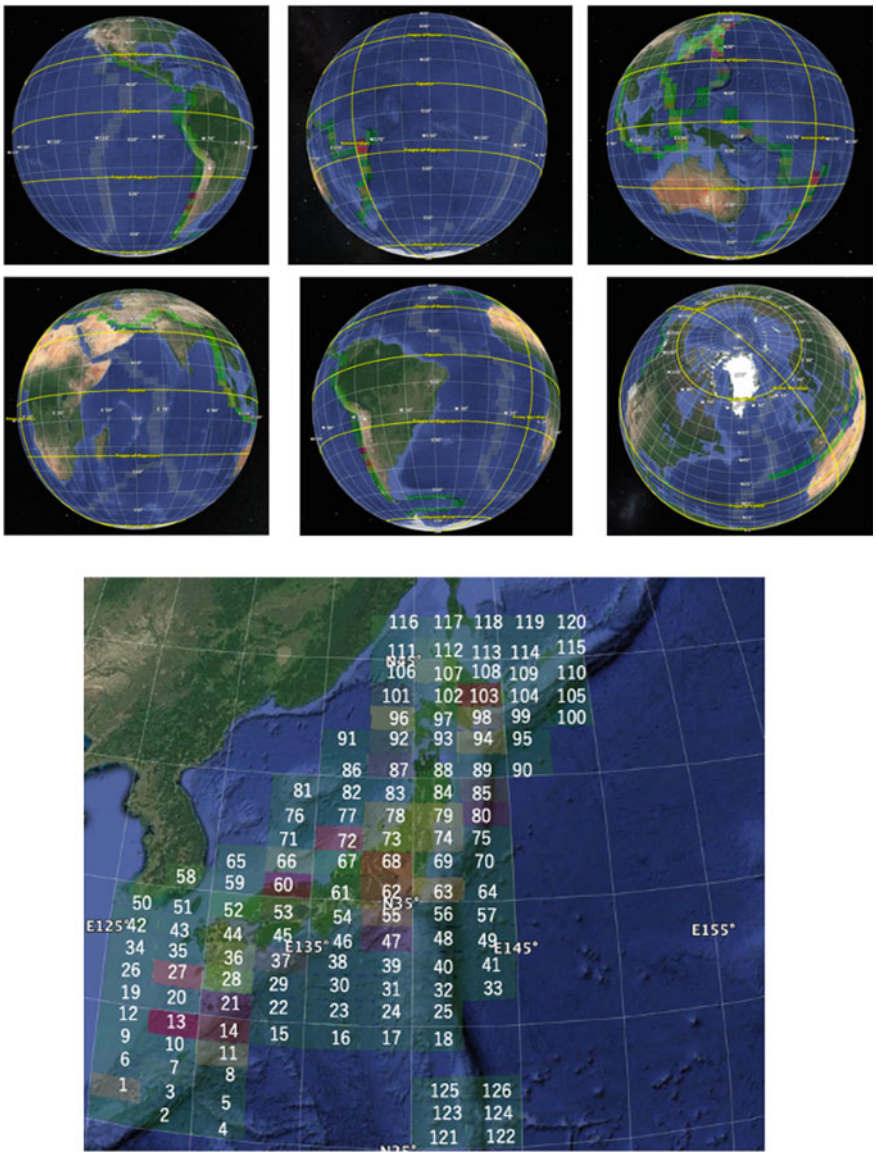

Fig. 7.3 Top, Google Earth Map showing the gridded localities of global subduction and ridge zones studied in this book. Bottom, Google Earth Map showing the gridded localities in the Japanese islands region

as same as those in Toriumi (2021), and they are

$$x(i, j) = \log(1 + n(i, j)) \tag{7.1}$$

here, $n(i,j)$ and $x(i,j)$ are number densities per unit volume and time interval and their logarithmic values of seismic events of magnitudes M4–5 in the global subduction zones, and magnitudes M1–2 and M2–3 in the Japanese islands region, respectively, as shown in Fig. 7.3. The unit volume is the 2.5° of latitude and 5° of longitude, and it is corrected by the latitude, and depth range of 0–700 km in the global subduction zones, and in Japanese islands region the depth ranges are of 0–30 km (crust) and 30–700 km (mantle). The time interval studied here is 10 days because of enough event density available for analyses described later.

The data matrixes of logarithmic seismicity rates are defined by

$$X = \{x(i, j)\} \tag{7.2}$$

in which i is the timestep from 1990 to 2021 in the global subduction zone but from 1998 to 2021 in the Japanese island region, and j is the locality number in this study. The correlated seismicity rates are calculated by singular value decomposition method (Fig. 7.4) of X as,

$$X = Z\,W + N(0, s^2) \tag{7.3}$$

in which Z is the correlated seismicity rate matrix and W the orthogonal rotation matrix with $W^{-1} = W^{\mathrm{T}}$. This decomposition matrix W is uniquely determined by

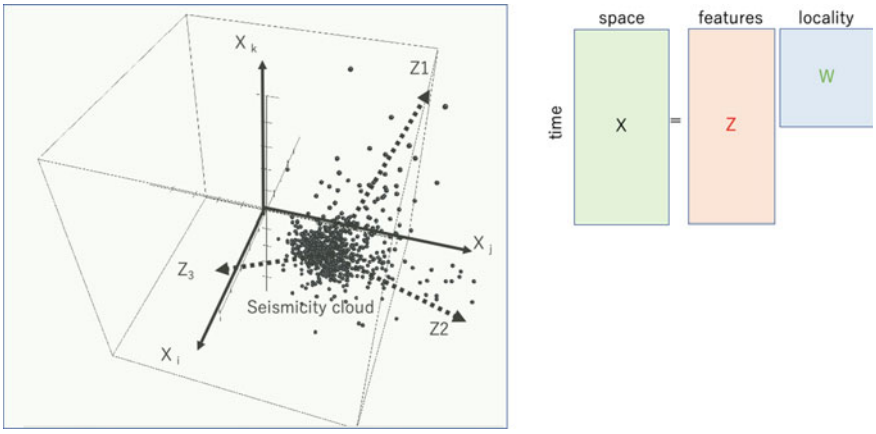

Fig. 7.4 Illustration of the logarithmic seismicity cloud in the diagram of X_i, X_j, and X_k and the correlated seismicity z_1 to z_3 (left). The singular value decomposition of the data matrix is shown in the right figure

eigenvectors of covariant symmetric matrix of X, and thus, z_j in Z matrix implies the time series of characteristic parameters, that is, so-called the feature parameter in terms of the machine learning.

Then, Z becomes,

$$Z = X\,W^{-1} \tag{7.4}$$

If we consider the full set of X and Z, then the logarithmic seismicity rates matrix, $\{x_{ij}\}$ should be estimated exactly from the Z matrix by W, as the perfect inverse matrix. However, as noted in the following sections, the higher components of feature parameters Z appear noisy with small S/N ratio, and so it seems that the inverse matrix W^{-1} shrinks its dimension. Therefore, the logarithmic seismicity X should be estimated as the probability value with some amount of the variance from the feature parameter matrix Z.

On the other hand, it is possible that the coherent patterns of the correlated localities about seismicity in the global earth and in the regional district of Japanese islands by displaying the intensity of W components in the map. In other words, the intensity of weight coefficients of eigenvector components indicates the strength of seismic correlation among localities, though it is no appearance in the raw seismicity as proved by Toriumi (2021).

Conventional representation of data matrix of the logarithmic seismicity rates can be shown by plotting them in 3D diagram of logarithmic seismicity rates of representative three localities as discussed in the previous work (Fig. 7.4). In that book, it is worth noting that data cloud defined by multiple clusters in high-dimensional space containing dense core and scattering spines which often extend to the large earthquake events can be identified in the rather long-term period. Therefore, it seems probable that there should be embed the foregoing seismic signals with largely fluctuated noise in the data cloud. To undermine these signals, the correlated seismicity rates Z of transformed data cloud by W are necessary for processing in more detail by means of machine learning methods (Bishop 2006).

The author already proposed the neural network regression method of correlated seismicity time series for extending the several steps ahead prediction and obtaining the available data extension of probabilistic prediction. In this work, therefore, the author would intend to propose a new method for near future stochastic prediction of large earthquake in the global subduction zones from the correlated seismicity time series by the deep CNN, RNN, and LSTM (Chollet and Allaire 2018) with labeling models as illustrated in Figs. 7.5, 7.6, 7.7, and 7.8.

The data matrix applied for the prediction testing of the large earthquake event should be concatenated with labeling matrix of the large earthquake events. If the locality of the earthquake prediction test is the single one, the labeling matrix is the vector consisting of 1 and 0. On the other hand, the multiple prediction testing needs for multiple labeling and their matrix has dimension of $(n \times m)$ in which n is number of timestep and m is number of locality grid for earthquake prediction. However, the labeling vector consisting multiple digits with 0, 1, and 2 to k representing the locality grid is also possible to apply for the present testing method as shown in Fig. 7.5. In the

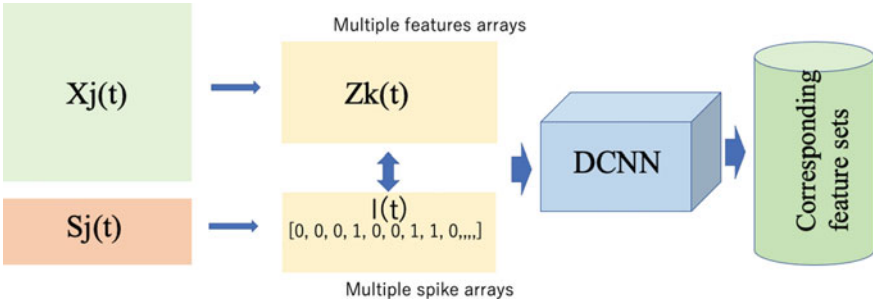

Fig. 7.5 Illustration of the multilabeling method by convolution neural network modeling (CNN) using the logarithmic seismicity matrix $X_j(t)$ and large earthquake labeling 1D matrix $S_j(t)$ for j-grid locality

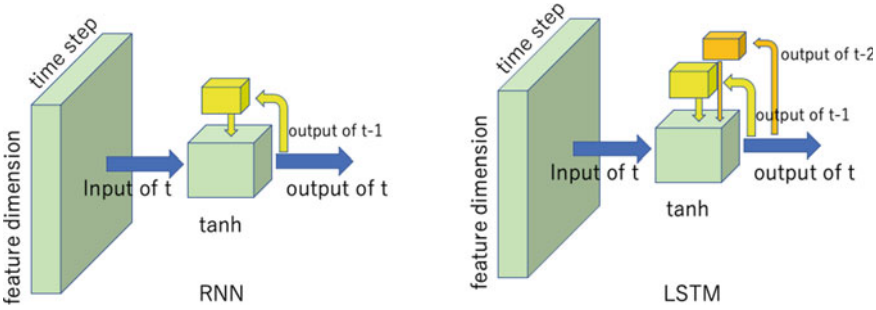

Fig. 7.6 Illustration of the recurrent neural network model (RNN) and long short-term RNN model (LSTM), showing the input data into node containing recurrent schemes

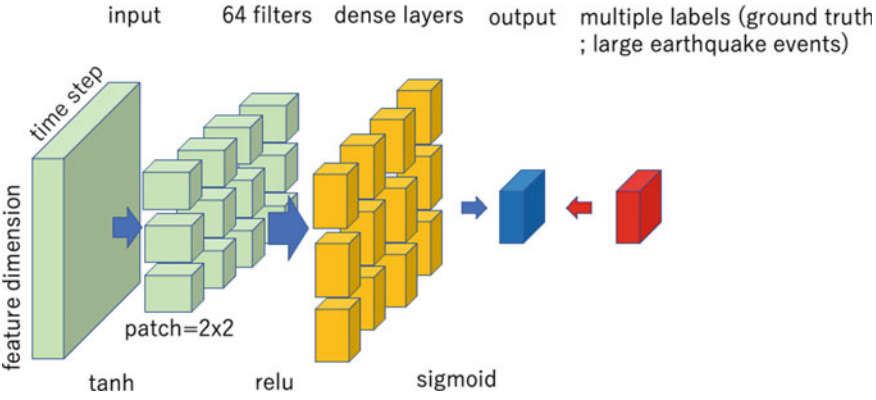

Fig. 7.7 Illustration of the convolution neural network model (CNN) for single target label (ground truth; event of large earthquake)

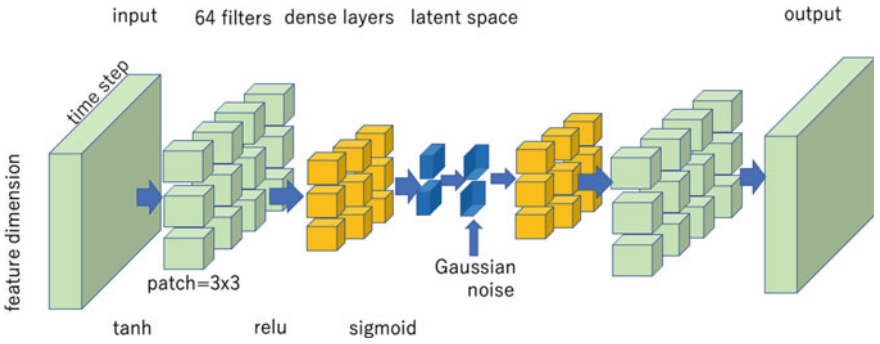

Fig. 7.8 Illustration of the variational autoencorder with CNN model showing the projection of the multivariant data on the latent space (two-dimensional space in the figure) and addition of the Gaussian noise on latent space to produce the generative images (decording) by inverse CNN processing

former case, the final neural net layer must be multiple nodes because of estimation of probability in each earthquake event, but in the latter case the final neural net layer is the single node because of mapping of the data matrix to the identifying digits of the locality grids. In the case of generative variational autoencoder (GVAE; Fig. 7.8), the labeling matrix is used to be the latter case.

The input data for the RNN, LSTM, CNN, and VAE methods applying for the present multivariate time series should be prepared as two matrixes by means of splitting the data matrix with labeling vector using the splitter codes on python 3.0. In this study, the training of the DNN is performed in the data matrix of the former part of the multivariate time series 1–800 and the testing is done in the later part 801–1150 in the global subduction zones. On the other hand, the training is carried out in the 1–500 steps and the testing in the 501–850 steps. The timestep for the DNN is used as 3–13.

7.3 DCNN with Multilabel Modeling Analysis of Large Earthquake Event

Within this century, two giant earthquakes and associated tsunamis occurred in 2004 and 2011 in the world. These geological disasters took huge amounts of damages on human society and infrastructures of the Asian and African countries. To avoid the deep damage by those natural disasters, it is obvious that available information on near-future large earthquakes is required for resilience and stability of the human society.

Because of rare occurrence and complicated phenomena of large earthquakes in the global earth, nature of large earthquakes has been still enigmatic in modern sciences, though those are derived from the stress accumulation and successive

unstable slippage of the plate boundary and large-scale fault boundaries. Especially, although prediction of large to giant earthquakes is deeply required for human society in modern earth sciences, available model of earthquake physics has not been established for a long time. Moreover, the predictable model of large earthquake has not been established yet, although the statistical treatment of time series of large earthquake activity of aftershock seismicity has been proposed as ETAS and modified ETAS models (e.g., Ogata 2015) which are potential predictable regression method of the time series of intermittent occurrence of large earthquake events in a specified locality.

The huge amounts of seismic data of both global earth and regional areas accumulate continuously in the open accessible databases in the world. Many seismologists access the database to investigate the tomographic survey of the earth interior using huge amounts of waveform data but not to study the seismic dynamics using big time series seismicity data stored in the databases. Most recently, the author issued the book entitled as global seismicity dynamics and data-driven science in which he clarified decomposition method of big data matrixes and DRNN and DCNN regression studies of huge seismicity time series stored in the databases available for manifestation of some invariances of global and regional seismicity dynamics. In the book, the author also proposed the correlated seismicity as the feature characteristics both in the global and regional earth mechanics transformed from logarithmic seismicity rates along the plate boundary zones, which is obtained from singular value decomposition of logarithmic seismicity time series.

The correlated seismicity time series of global subduction and oceanic ridge zones change coherently with each other, and they show several stationary nodes and unstable overshoot inducing the giant earthquakes as shown by Toriumi (2021). Furthermore, the major mechanical behavior of the global plate motion is represented by the large moment release rates during 2004–2011 along the subduction boundary as suggested by Ekstrom (2007). The correlated seismicity rates of the global subduction and ridge zones also are plotted in three clusters, and the one of these clusters contains the abnormally scattered extension with large variances as shown in Fig. 7.9,

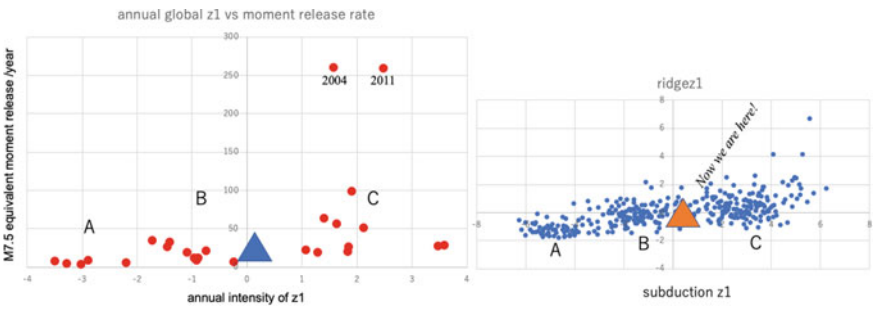

Fig. 7.9 Diagram of the annual moment release rate and the global correlated seismicity z_1 (left) and the phase map of the global correlated seismicity z_1 of the subduction and the ridge zones, showing the data predicted by state-space modeling in Toriumi (2021)

being cited from the above book. This scattered extension involves the huge amounts of moment release rates in 2004 and 2011 (Toriumi 2021), suggesting that the giant earthquakes are characteristic in the cluster of the correlated seismicity with coherent activity between global subduction and oceanic ridge zones. In this book, it is noted that during recent several decades after 2018 the global correlated seismicity rates are possibly predicted by means of state-space modeling (SSM) and deep learning recurrent neural network modeling (DRNN modeling), being plotted within the border area of the high global moment release rate cluster. Therefore, it is very required to know the signal showing transition from quiet period to the giant earthquake one around that cluster.

7.4 Deep Convolution Neural Network and Recurrent Neural Network with Labeling Model

As described in the previous section, the correlated seismicity rates transformed from logarithmic seismicity rates have large number of time series together with large variance noisy signals. These multivariate time series also surely contain some amounts of foregoing signals of large earthquakes. Therefore, introduction of CNN and RNN models applying for multivariate correlated seismicity time series is needed first as follows: The machine learning by CNN and RNN is performed by combination of input data and target data prepared from multivariate time series of Z and logarithmic seismicity X. In this processing, the 1-dCNN and RNN (LSTM) modeling are used for machine learning and then the serial data sets of several timesteps cut from the time series and target data must be prepared as illustrated in Fig. 7.4. If the regression of the time series is the case, the target data are the single data posterior to the input data sets with timesteps. This type of regression by RNN with LSTM was investigated in the previous book (Toriumi 2021).

In this paper, the author intends to investigate the possible foregoing signals of large earthquakes and then he tries to construct the new method of targeting object as follows: The target time series of large earthquakes must be expressed by the series of labeling by 1 (event) or 0 (no event) and corresponding input data of correlated seismicity rates with given timesteps are associated with this target data. Machine learning is performed by output single data by sigmoid type activation function that should be compared to give available parameters fitting with target label 0 or 1 using Adam (adaptive optimizer of first and second moments) optimizer (Fig. 7.7).

The procedure of DCNN, KERAS, and TENSORFLOW system on python platform (Chollet 2017) is used for construction of one-dimensional convolution neural network modeling (1dCNN) at cloud computing system of Google Colaboratory. In this system, the timesteps are selected as 3–13 steps corresponding to 30–130 days, and number of multivariate correlated seismicity time series varies from 3 to 10 to obtain the cross-validation evaluation of the model (Fig. 7.10). To compare the testing results, the modeling by recurrent neural network (RNN) and long short-term

Fig. 7.10 Illustration of the machine learning validation by input data splitting of training and testing subsets of input data. The prediction from the testing data is validated by comparison with target earthquake event in the testing region

memory (LSTM) method is investigated in the same input data matrix. It is noteworthy that the RNN (and LSTM) contains the RNN layer receiving its output data together with input data though the 1dCNN does not involve such recurrent input system (e.g., Chollet and Allaire 2018).

The total DNN architecture is composed of two components: the one is the 1dCNN or RNN and the other the dense NN layers. The 1dCNN has one and two layers with Maxpooling layers with 64 filters (32 filters) and kernel size = 2 (and 4), and activation function of 'relu'. On the other hand, the dense NN component has two or three layers having 32 (64) nodes where the final layer has single node and 'sigmoid' type activation function in the case of single labeling model as illustrated in Fig. 7.5. The repeating number of processing called as epoch number reaches 1000 but error becomes minimum before 200–500 epochs.

In these procedures of RNN and 1dCNN, the experiments were carried out by two steps: one is the training and the second the testing after training. Although common training and testing are repeated several times for cross-validation (Chollet 2017), in this study it is preferable that the cross-validation should be made by changing the multivariate correlated seismicity time series sets and training can be down for the earlier sets of them and testing for the later ones. Furthermore, it should be also checked that correct and error output depend on the timestep number of CNN procedure. In this testing, the number of correct and error output of the DCNN is read from the output within three steps and 90% reliability referred from the ground truth labeling as shown in Fig. 7.7. Exact comparison between them should be carried out by the output and input lists of the labeling data.

On the other hand, the experimental results by the RNN and long short-term memory (LSTM) RNN are also shown in Fig. 7.11, indicating that the similar scoring of the correct output of the prediction testing as those of 1dDCNN. However, it seems that there is some difference among the input data matrix selecting from the sets of

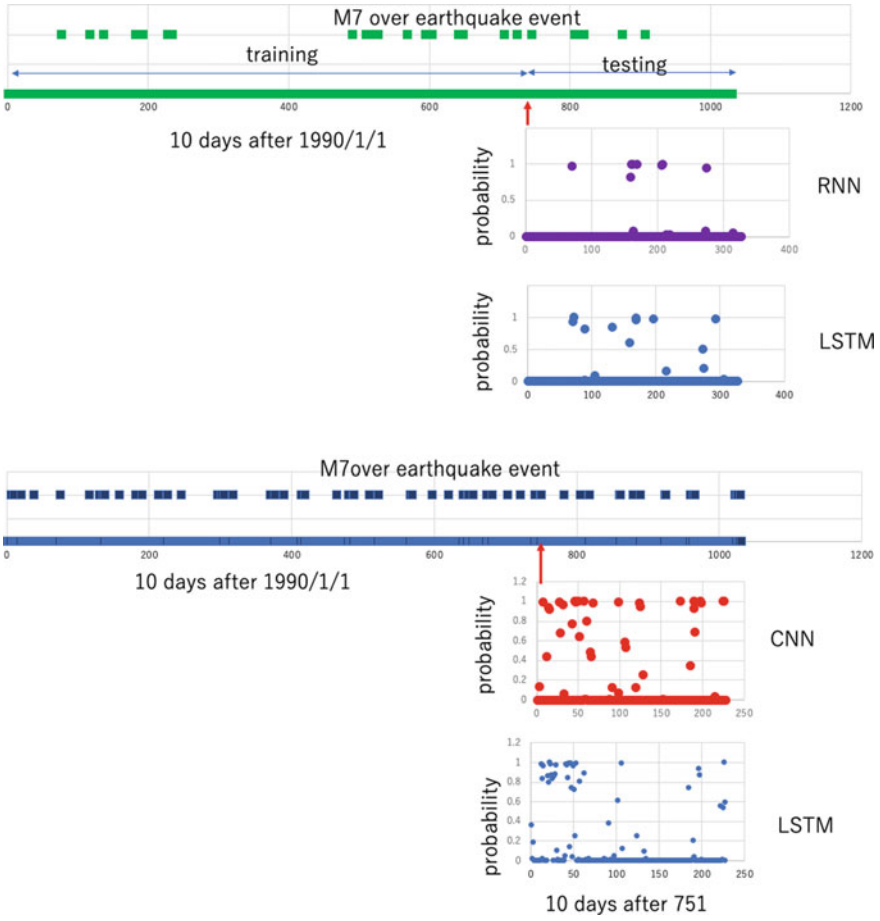

Fig. 7.11 Examples of prediction testing of M7 over earthquakes in the NEJ-Kuril region from the global correlated seismicity z_2 to z_6 with 5 timestep matrix in the training of 1–700 steps and testing of 701–1031 steps by RNN and LSTM (top) and in the western Pacific region by CNN and LSTM (middle)

the correlated seismicity z_1 to z_{12} of the global subduction zones. As mentioned in the following sections, it shows that the z_3–z_9 set of them is available for prediction testing from deep learning by CNN, RNN, and LSTM modeling. On the other hand, it is clarified that the above machine learning from the logarithmic seismicity X is not available for the prediction testing of the target large earthquake as shown in Fig. 7.12, showing no correct prediction results in the case of X.

Moreover, it should be noticed that the number of timestep as the model parameter required is also important factor controlling the accuracy of the prediction testing both in the global and regional subduction zones. As the timestep means the length of the time series segments used in the neural network modeling of the data procession,

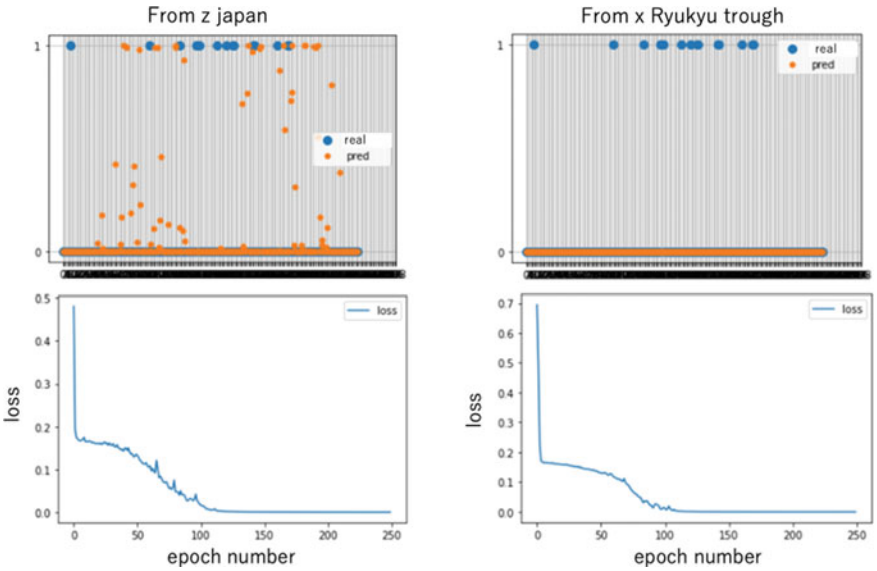

Fig. 7.12 Comparison of prediction testing using the input data of regional correlated seismicity matrix (left) and the logarithmic seismicity matrix of Ryukyu subduction zone, showing the preferable input of correlated seismicity

it seems that their short segments available for the practical prediction testing contain some degree of the signal/noise ratios. Therefore, the intensity of their *S*/*N* ratio may be clarified by scanning the timestep in the neural network modeling. As stated in the following section, the available timestep of the DNN is mostly about 5–6 steps (50–60 days), judging from the cross-validation test of various timestep execution of the modeling.

In this study, the author tries to propose the new method of CNN and RNN using the new parameters of the time-shift called as variational timestep and time-shift modeling (VTTM) available for the practical use of prediction testing of the large earthquake both in the global and regional subduction zones as shown in Fig. 7.13. To construct a prediction system for large earthquake in near future, it is required that the geophysical signals during various time before the earthquake should be investigated in the huge amounts of monitoring data from the global and regional network of geophysical observatories. In specifically respect, it is very important that from when the preseismic signals can be found and after that time whether the accuracy of the prediction testing does increase toward the time of earthquake event or not. Thus, the systematic investigation of the change of accuracy in prediction test depending on the lag time of the input data matrix before the present earthquake is very required. Thus, in this context, the variational time-shift and timestep method for DCNN and DRNN is applied for the prediction testing of the large earthquake as described in detail in the following sections.

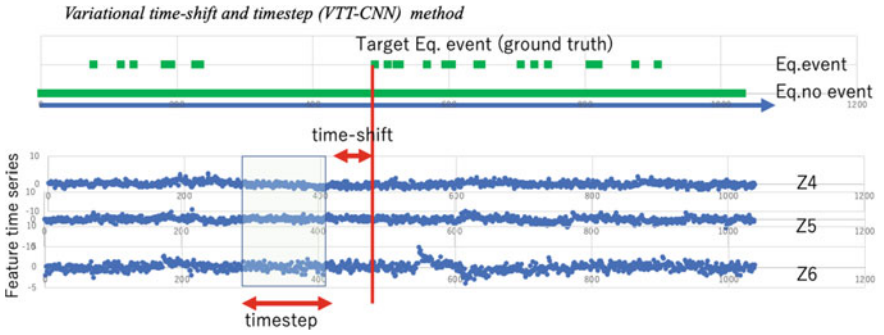

Fig. 7.13 Illustration of the variational time-shift method (VTTM) for prediction testing having various lag time before the target large of the earthquake event

7.5 Prediction Testing of the Large Earthquakes in the Global Subduction Zones

The time series of the global correlated seismicity shows characteristic feature patterns of global subduction mechanics derived from plate motion, and major components of them display different modes of coherent seismic activity of different regions along the plate boundaries. The time series of correlated seismicity z_1 to z_4 from 1990 to 2021 is shown in Fig. 7.14, indicating that z_1 to z_4 show the long-term changes, but z_5 to z_{10} do the short-term ones involving 1000–1500 days cyclic variation as seen in Fig. 7.15.

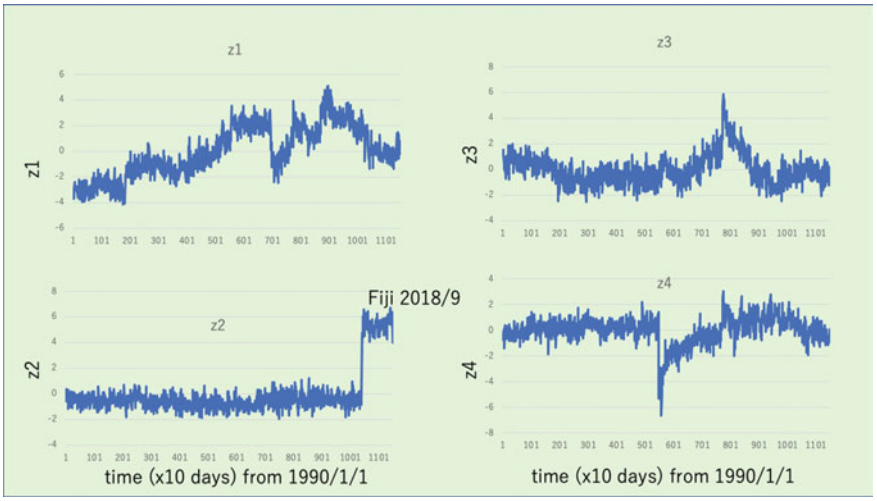

Fig. 7.14 Temporal variations of the global correlated seismicity z_1 to z_4 from 1990/1/1 to 2021/6/30

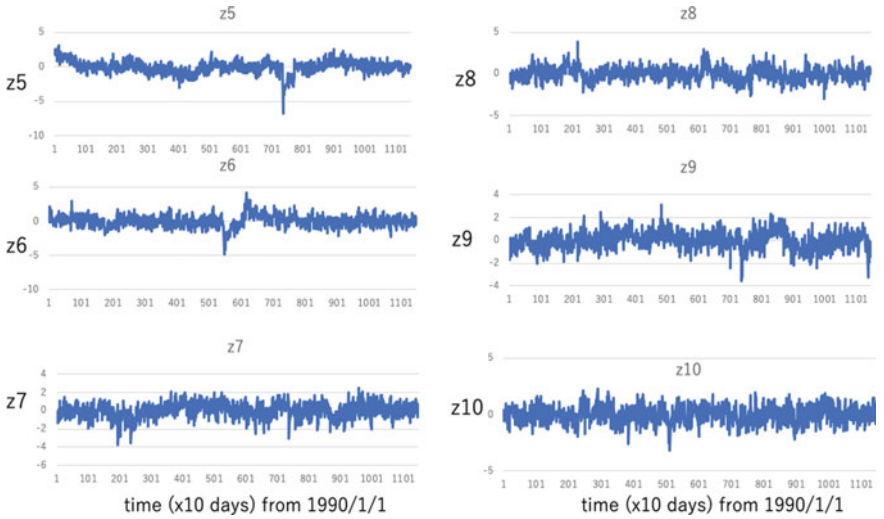

Fig. 7.15 Temporal variations of the global correlated seismicity z_5 to z_{10} from 1990/1/1 to 2021/6/30

The z_1 indicates a coherent seismic activity connecting Indo-Australian plate and Pacific Plate boundary region, although z_2 does a coherent activity of the western Pacific Plate boundary regions as shown by Toriumi (2021). On the other hand, z_4 shows coherent activity of eastern Pacific Plate boundary regions including Chile–Peru and Mexico region. The western Pacific and Indo-Australian Plate coherency is typical in the Northeast Japan region (NEJ) as clarified by Okada et al. (2017) and Toriumi (2021).

Higher-order correlated seismicity z_5 to z_{10} has large fluctuation noises which are nearly Gaussian noise with various variance as indicated in Toriumi (2021). However, as shown in the following sections, there seem to be important signals with very small *S*/*N* ratios, judging from several peaks of histograms of z_i in the global subduction zones. Furthermore, in the Japanese island region, there are obvious sub-annual to tri-annual variations in the z_5 to z_{10} time series, suggesting the importance of the higher-order terms of the correlated seismicity.

In the higher-order correlated seismicity time series, there remain some important information concerning preseismic signals of large earthquakes that should appear in the data processed by DCNN. Therefore, the input matrix for DCNN processing should be expanded into 3–10 components of the correlated seismicity, and 3–13 timesteps matrix, that is 3×3 to 10×13 matrix dimensions targeting the signals of earthquake over M7 (and M5 over in the case of Japanese region) label (0 or 1) at the one-step ahead. The application of regularization of the input data, data splitter and combination set of input data and target data are carried out on Python 3 for preprocessing before DCNN as illustrated in Fig. 7.16.

First, machine learning in training of the correlated seismicity time series was carried out in the period from 1990 to 2005 of the global subduction zones: the

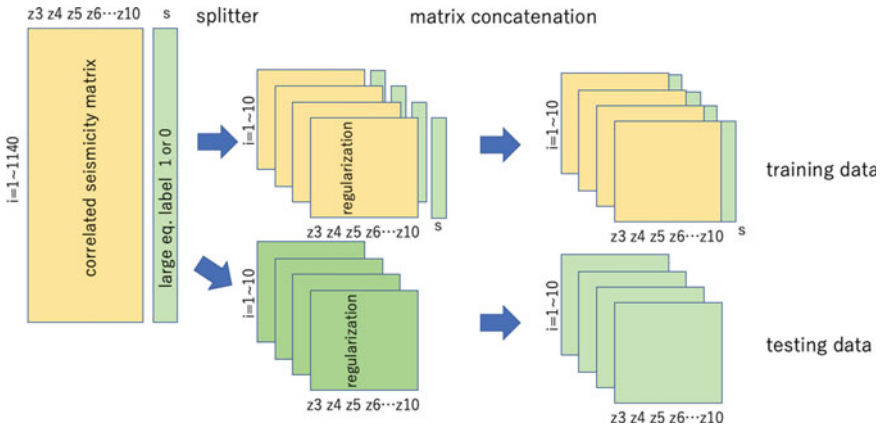

Fig. 7.16 Illustration of the input data and validation by data splitter into training and testing of CNN and VAE modeling

target label time series are made on Northeast Japan and Hokkaido (NEJ-HKD), Chile–Peru, and Sumatra regions as shown in Fig. 7.17. In that time range, there are not many earthquake events of M7 over, and thus, the efficient machine learning of DCNN with labeling model is probably not expected enough.

In Fig. 7.18, the training results targeting the actual large earthquake label sequence and their regression results by DCNN from 1990 to 2005 are shown together with regression MSE loss errors against repeated epoch number in the case of western Pacific region. It shows clearly the error value decreases rapidly with increasing the

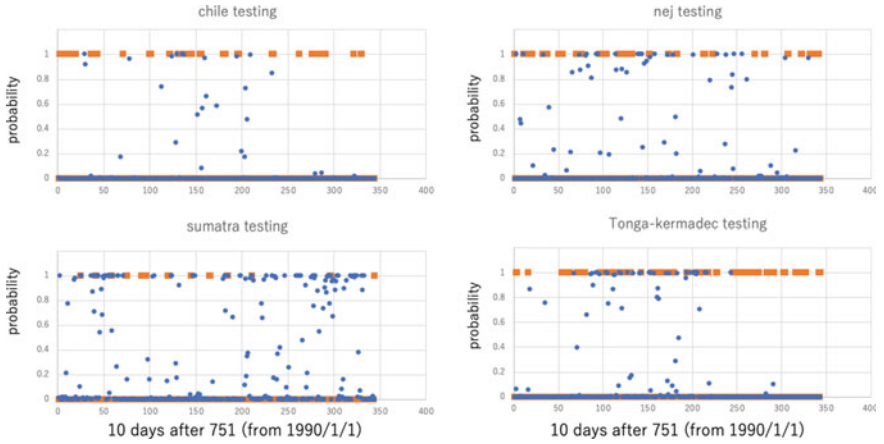

Fig. 7.17 Results of prediction testing for large earthquakes in Chile, Sumatra, Northeast Japan and Tonga-Kermadec regions by CNN

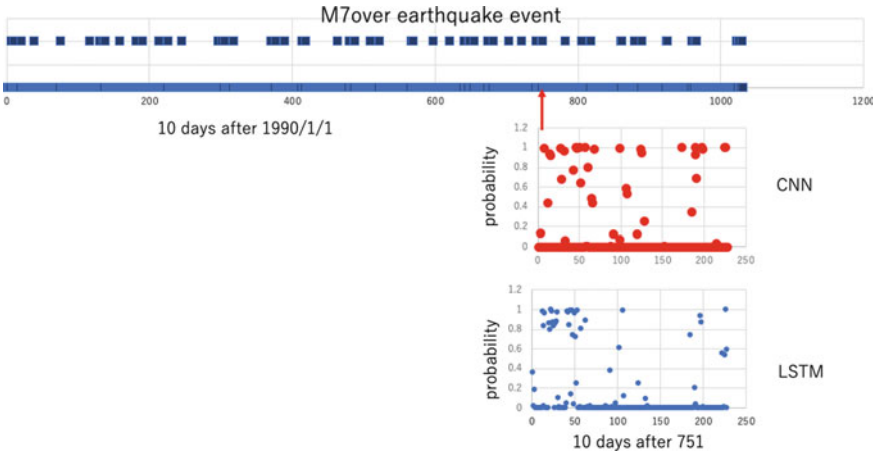

Fig. 7.18 Comparison of prediction testing experiments of M7 over earthquakes in the western Pacific region by CNN and LTM models. Training of 1–750 step and testing of 751–1031 step. Upper figure shows the target events, and lower two figures are testing results

epoch number and reaches minimum level at about 200 epochs. The regression probabilities of M7 over events are almost always near 1, suggesting a good coincidence with natural timestep of the earthquake event.

In Fig. 7.18, the prediction testing results are shown in the timestep from 701 to 1027 in the cases of western Pacific regions by CNN and LSTM modeling. In these figures, the predicted events are compared with natural earthquake labels of M7 over. It is regrettable that the prediction results of them scarcely coincide with real earthquake events. This may be the reason why the machine learning of training was carried on small number of events of M7 over earthquakes.

On the other hand, when we use the correlated seismicity of higher orders such as z_3 to z_{13}, the prediction results are different from those in the case of various correlated seismicity input data: the coincidence between predicted and natural earthquakes become better in the case of the input data of z_3 to z_9 rather than those in the case of other combination sets involving z_3 to z_{13} as indicated in Fig. 7.19. Therefore, it seems that the correlated seismicity rates of z_3 to z_9 should contain important signals of precursor before large earthquakes over M7.

On the other hand, it should be tried that extensive wide region of the target to be predicted is possibly applied for the machine learning in order to increase the number of events to be learned: The regions of the subduction zone from NEJ to Mariana and Southwest Japan are taken into investigation of the test research of prediction. As shown in Fig. 7.20, it is obvious that the prediction scores of the testing results become increasing drastically rather than the case of narrow region events. In this figure, it is necessary to be noticed that there is a shift of timing about 5 steps of the prediction and real events resulting from the timestep parameter in the DCNN modeling as same as those seen in the previous regression study.

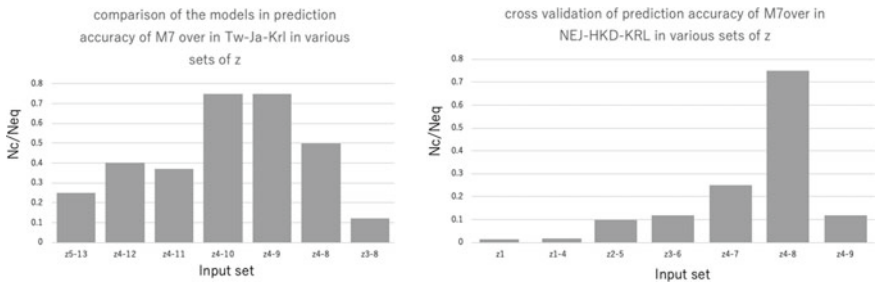

Fig. 7.19 Comparison of the prediction testing results of M7 over earthquakes in Taiwan–Japan–Kuril region and Northeast Japan–Hokkaido–Kuril region for various input data sets of the global correlated seismicity of the subduction zone

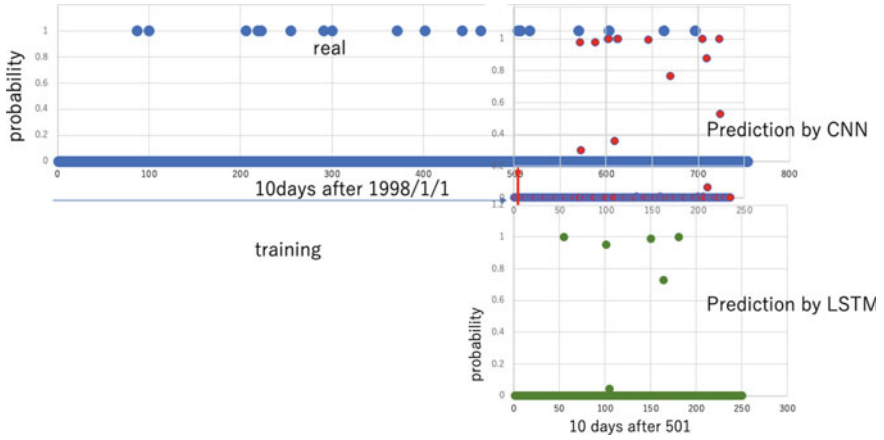

Fig. 7.20 Comparison of the prediction testing results of M7 over earthquakes in NE Japan-SW Japan- Izu-Ogasawara-Bonin region from the regional correlated seismicity z_4 to z_8 of Japanese islands region. Training; 1–500 step, testing; 501–756 step

In the machine learning investigation of M7 over earthquake labeling (i.e., ground truth), various methods of deep neural network modeling were performed for cross-validation test using simple RNN, long short-term memory neural network (LSTM), and convolution neural network (1dCNN). The comparison of them was shown previously in Fig. 7.11, suggesting the relative high performance of 1dCNN with dense connection of nodes rather than RNN and LSTM. Considering that the 1dCNN modeling with labeling for large earthquake is possibly potential prediction method, the partial sequence of correlated seismicity time series denoted by the timestep parameter in DCNN may be classified into random and precursor signals by targeting the large earthquake event as ground truth. In Fig. 7.19, the results of prediction testing for 701–1030 steps in the DCNN are shown by correct and incorrect prediction with

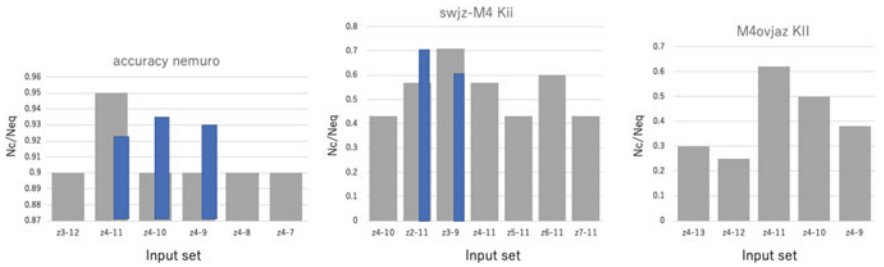

Fig. 7.21 Prediction testing results of various input data sets of the correlated seismicity in the Japanese islands and Southwest Japanese region for the M5 over earthquakes of Nemuro (left) and M4 over of Kii (right). Gray shows the ratio of the prediction number against actual earthquake number, and blue does the incorrect prediction against actual earthquake event

labeling of ground truth in the various input data of z_4 to z_8 of the global correlated seismicity.

On the other hand, prediction testing of rather large earthquakes in the Japanese islands region will be carried out for the case of Kii Peninsula and Nemuro of the subduction zone. In this study, the input data from 1998/1/1 to 2021/6/30 are used. Furthermore, the large earthquake events in those regions over magnitude 4 are labeled as the ground truth because of much training by machine learning and testing. The data of seismic hypocenters are acquired from USGS data center and NIED database and processed by the methods in the previous book (Toriumi 2021). The comparison of the testing results for the correlated seismicity of Japanese islands region shows the available sets of z_4 to z_{11} as shown in Fig. 7.21.

The preprocessing of the data which contains multiple labeling for the above localities and partitioning of the post-earthquake signals and pre-earthquake ones in the input correlated seismicity matrix is needed because nominal 1dCNN model does not identify straightforwardly them. To avoid the post-earthquake signals in the correlated seismicity for prediction testing, the two boxes of the event label that in one box at the timing of the earthquake event it takes digit 1, and in another box at the same time digit 0 is entered, and furthermore, it is needed that at the next timings the digit 0 is to be entered in one box and digit 1 to be in another box. The repeat number of this preprocessing is known by comparison between the parameter timestep and the number density of the large earthquake events over M6 in the studied localities mentioned above. In the case of ignoring this above preprocessing of labeling, the prediction testing is not available enough in terms of the test accuracy.

By the way, the input data of the neural network modeling are the correlated seismicity zi in many cases, but sometimes these are the logarithmic seismicity of the related localities and the correlated partial *b*-value (*b*-123) denoted in the previous book. However, in many results estimated by using the *b*-value and logarithmic seismicity, the accuracy of the testing is not satisfactory as the machine learning, being compared with that by using the correlated seismicity z_i (Fig. 7.22).

On the other hand, it is required to know that how many characteristic features of the correlated seismicity z_i are available as the input data for the effective prediction

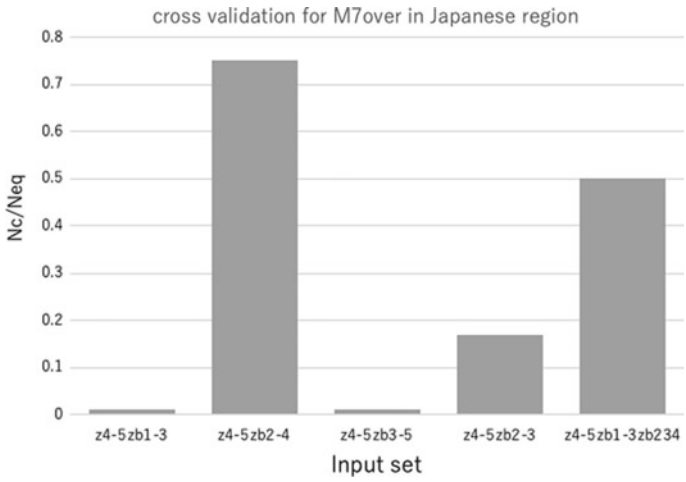

Fig. 7.22 Comparison of the prediction testing results (N_c/N_{eq}) for the M over earthquakes in the Taiwan–Japan–Kuril region of various input data sets of z_4, z_5 and correlated partial b-values z_1–z_5 of $b123$ and $b234$ of the Japanese islands region

testing of large earthquake event. As already discussed previously, the sets of the input data including z_1 and z_2 are not available for the testing, though the reason for this is not enough known yet, it may be partly due to its secular trend of the global and regional seismicity.

In the case of Japanese islands region, it seems that the machine learning data set of the correlated seismicity z_4 to z_9 is available for the prediction testing as well as the case of testing from the global subduction system, judging from comparison among other sets involving z_{10} to z_{13}. Moreover, it is concluded that the input data sets for machine learning containing logarithmic seismicity and partial b-values (and their correlated partial b-values defined previously) do not give the accurate testing results. Therefore, in the book, it may be concluded that both in the case of the global and regional prediction testing of large earthquake, the correlated seismicity set of z_4 to z_9 should be applied as the input data matrix for the prediction testing study by means of DCNN (Fig. 7.23).

7.6 DCNN with Variational Timestep and Time-Shift Method (VTTM) Modeling

As described previously, the input data matrix of DNN modeling should be the correlated seismicity time series z_4 to z_9 (in same cases z_2 to z_6 are used for convenience) from 1990 to 2021 for the global subduction zone and 1998–2021 for the Japanese islands region. However, it remains that to estimate the probability of the future event of large earthquake, the future correlated seismicity time series with length of the

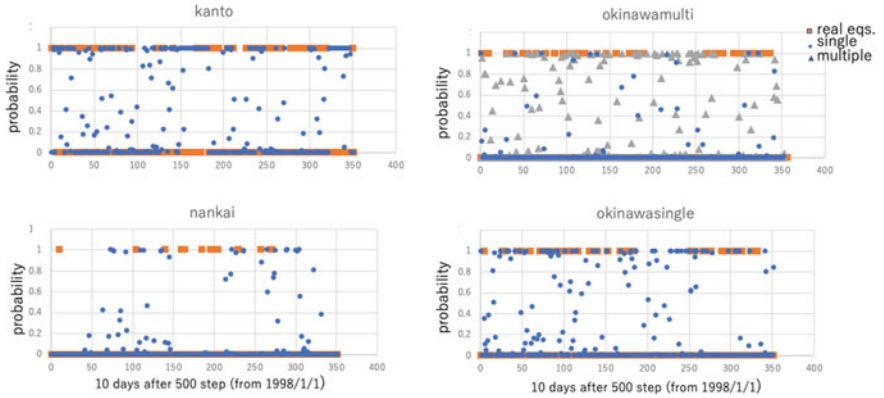

Fig. 7.23 Comparison of the prediction testing results for the Kanto, Nankai, and Okinawa region from the regional correlated seismicity z_4 to z_7 in the Japanese islands region by CNN modeling. Training; 1–500 step, testing; 501–756 step. Red square shows the actual large earthquake event, and multiple does the multiple events

input data matrix should be also predicted precisely from the known correlated seismicity by means of other modeling something like DNN and space-state modeling (SSM) as investigated in the previous book (Toriumi 2021).

By the way, considering the time series of the correlated seismicity that should contain some of signals before the large earthquakes, it is possible that there should be various input data matrix with a constant timestep having the duration of some ten days (steps) interval before the present large earthquake. In this new method, the interval between the input data matrix with a timestep is called as the time-shift as illustrated in Fig. 7.24. This new parameters of the DNN model empirical projection on the earthquake event label are quite convenient for direct prediction testing for future large earthquakes by means of single known correlated seismicity

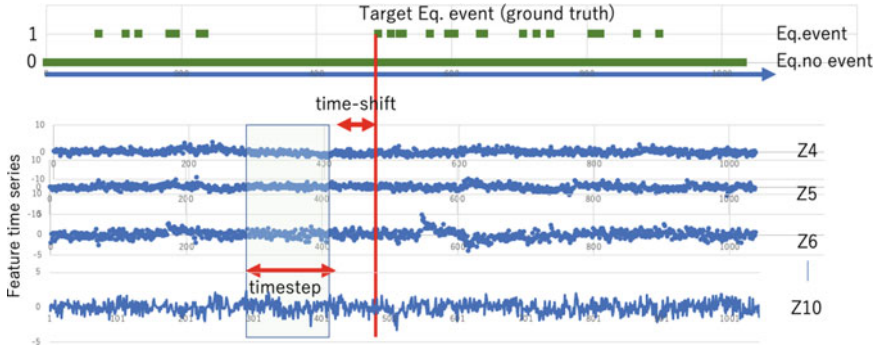

Fig. 7.24 Illustration of variational time-shift method for prediction testing of large earthquake. Upper figure shows the target event, and the time-shift is the lag time between the input data matrix and target event

time series, because the prediction probability should change with decreasing the time-shift approaching the just relevant event. The author, therefore, calls this method as the various timestep and time-shift modeling (VTTM) hereafter.

In the common use of DCNN, RNN, LSTM, and VAE modeling, the cross-validation is performed by K-separation method for multivariate time series as described in Chollet (2017), but in this study the cross-validation has been carried out by the various input data assemblages of the correlated seismicity time series of z_3 to z_{13}. Furthermore, in this study, accuracy of their testing data for prediction has been evaluated by the ratio of the correct prediction time (step) by that of real large earthquake event and by number of the incorrect prediction case, as well as the case of global seismicity mentioned previously. Then, the number ratios N_c/N_{eq} and N_c/N_t are introduced for convenient scores of prediction testing, where N_c, N_t, and N_{eq} are the number of correct prediction case within three steps, that of total prediction case, and number of real large earthquake event as a ground truth (target of testing). The data are plotted in this diagram (Fig. 7.25), for various timestep and time-shift in the Boso of Japanese island region and Taiwan–Japan–Kuril zone from the global correlated seismicity z_3 to z_6 as input data matrix.

In Fig. 7.26, the prediction testing results of time-shift and timestep experiments for DCNN show the cross-validation test of the input assemblage of z_2 to z_6 of

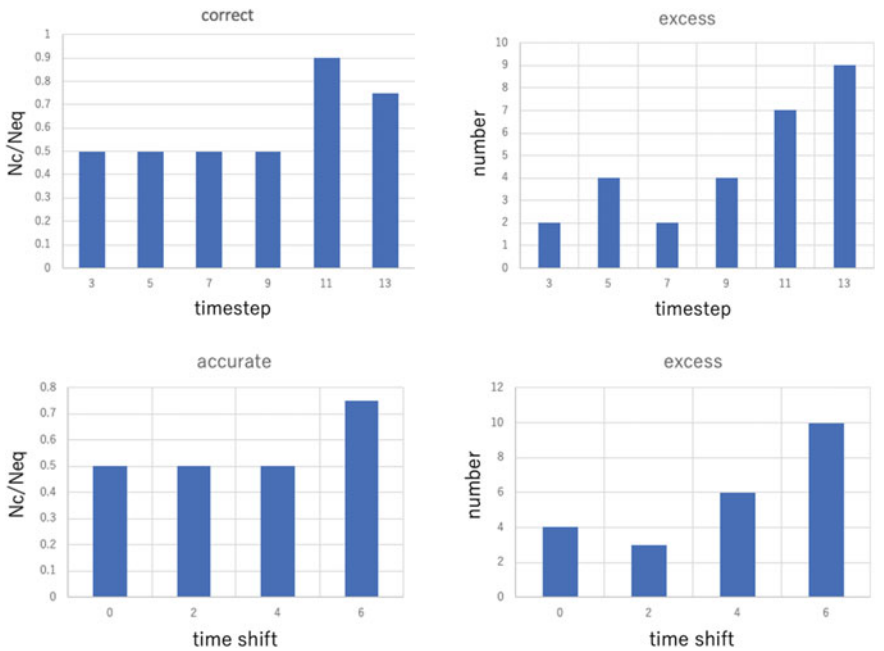

Fig. 7.25 Comparison of the prediction testing score (N_c/N_{eq}) of CNN model with various timestep (top) and CNN with various time-shift (bottom) of M7 over earthquakes in the Northeast Japan region from the global correlated seismicity z_2 to z_6 accuracy diagram

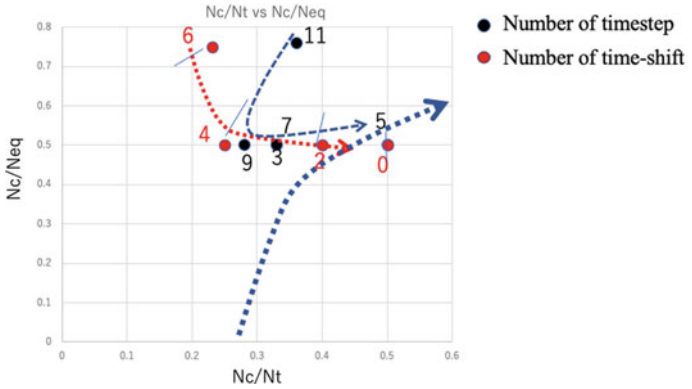

Fig. 7.26 Diagram of the relation between the correct and incorrect prediction of M7 over earthquake in the Northeast Japan region from the global correlated seismicity z_2–z_6, showing the evaluation of various timestep and time-shift of CNN modeling. Red-dotted arrow shows the increasing scores of predictions by decreasing time-shift and blue broken arrow does by changing the timestep suggesting the high scores at timestep about 5. Bold-dotted arrow is the general trend of the prediction scores in the studied cases

the global correlated seismicity. The diagrams display the correct and incorrect prediction results both in the time-shift and timestep change. In the experiments, the timestep is commonly used in the 1DCNN time series analyses, but the time-shift method is original in this study, and it means the difference in the timestep between input data matrix and the labeling time. It, therefore, represents the large earthquake prediction ability before enough time, suggesting the available prediction method for the practical use.

The above results of the variational timestep and time-shift method (called as VTT-DCNN hereafter) in this study are displayed in Fig. 7.26, suggesting obviously that the timestep decrease shown by arrow induces minimum of incorrect prediction as indicated by $(1 - N_c/N_t)$, and that of decrease in the time-shift (red dotted arrow) does minimum one. It implies the gradual decrease of incorrect prediction of earthquake with decreasing the time-shift, suggesting the available prediction development with approaching the near earthquake time-point.

7.7 Prediction Testing of M5 Over Earthquakes in the Japanese Region by Correlated Seismicity

In the Japanese islands region, there are dense seismic station networks (Hinet and Fnet) and ocean bottom geophysical observation network (DONET and SNET) for precise monitoring of earthquakes and volcanic eruption together with the investigation of the structure of crust and mantle. The correlated seismicity rates of small earthquakes after 1998–2018 have been investigated and they are potential indicator

of the mechanical state of both crust and upper mantle of the Japanese island region by Toriumi (2021). In this book, it has been clarified that the major correlated seismicity time series display periodic variations with several to several ten years intervals and that the correlated partial *b*-value time series of ratios of M1-2 by M2-3, called as partial *b*-value, also shows the clear cyclic variations with sub- to tri-annual periodic change. Therefore, it is suggested that there may appear the preseismic signals before large earthquakes in the continuous time series of the correlated seismicity in the Japanese island region.

The DCNN modeling with input data of multivariate time series of the correlated seismicity in the Japanese island region will apply for prediction testing of local large earthquakes in the subduction zones involving Japan Trench and Nankai Trough regions. The lists of the large earthquakes over M7 and over M5 are taken from the USGS earthquake database center because of uniform data in the global subduction zone. The target labels of the M7 over earthquakes from 1998/1/1 to 2018/8/29 are made in the time window of 10 days. If there are more than two earthquakes in the unit time window, the label is taken as digit 1 for the simple labeling CNN model. The number of the epoch calculations is enough for reaching minimum loss by using 'mse' (mean square error) and 'binary-crossentropy' as a loss function. The optimizer 'adam' of the calculation is also used as well as the case of global seismicity. The number of filters of initial CNN layer is 64–32, and kernel one is 2–4 in this study. The dimension of the input data matrix varies from 3×5 to 12×5 as number of the feature parameter $\times$ timestep. The layer constitution of the DCNN models is composed of two or three sets of Conv1D, Maxpooling, and flatten layers, and it is sequentially connected with the dense NN having two or three layers with 128 and 64 nodes. To take a cross-validation by different number of layers both in CNN and dense NN units, three to four layers of both are tried and compared with the accuracy of the testing results of the latter time series of the target labels from 501 to 740 steps (5010–7400 days after 1998/1/1). The results of multiple layers model showed less accuracy of prediction test in the three- and four-layer models of CNN with dense NN, being compared with simple layer model. Therefore, it is available that the simple minimum structure of the DCNN and two layers of dense NN with final single node for labeling is preferable for prediction testing in this study. The activation functions of input layer, intermediate layers, and final layer are 'tanh' (hyperbolic tangent), 'relu' (rectified linear unit), and 'sigmoid' (logistic sigmoid), respectively.

In the common use of DCNN and DRNN, the cross-validation is performed by K-separation method for multivariate time series as noted in Chollet (2017), but in this study the cross-validation has been carried out by various input data assemblages of the correlated seismicity time series of z_1 to z_{13} as illustrated previously. Furthermore, the accuracy of prediction testing has been evaluated by the ratio of number of the correct prediction case by that of real large earthquake event and by number of the incorrect prediction case, as well as the case of global seismicity mentioned previously.

First, we will see the results of prediction testing for M7 over earthquakes in the selected wide regions of Tw (Taiwan)-Ja (Japan)-Krl (Kuril) and Boso Peninsula

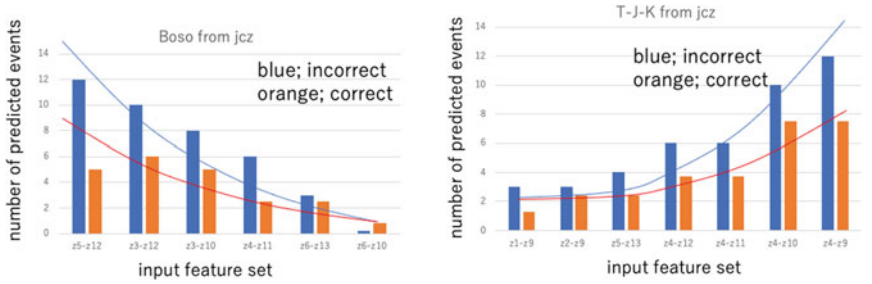

Fig. 7.27 Diagram of prediction number of correct and incorrect cases of the M5 over in Boso from Japanese correlated seismicity and of M7 over in Taiwan–Japan–Kuril region from the global correlated seismicity by various input feature matrix sets of z_3–z_{13}

using the input data of the regional correlated seismicity time series of Japanese island region (Fig. 7.27). The prediction testing was performed in the training of 1998–2011 and testing in the 2011 to 2018. It is very important that the accuracy (N_c/N_{eq}) of the DCNN prediction for the z_1 single and z_1 involving input is very low, compared with other cases of input time series. It suggests that the highest accuracy appears at the case of the input data set (z_4 to z_9) to be about 0.75 as shown in Fig. 7.27. Although these time series contain slightly large noises, it shows that these noisy time series involve the somewhat signals of precursor of large earthquakes. In addition, the z_1 to z_3 components should hidden such signals because of large intensity change.

Next, let us show the prediction testing results of several localities in the Japanese island region from various sets of the correlated seismicity time series of Japanese island crust. In Fig. 7.28, the prediction testing results of Nemuro, Boso, Kanto, and Nankai regions are shown, suggesting that the peaks of accuracy of them appear in the case of input features of z_3 to z_9. Moreover, it is suggested that the tests of Nemuro and Kanto are very high scores of N_c/N_{eq} around 0.9 but those of Kii and Boso are very low near 0.1–0.3. The latter case seems to be due to very small number of large earthquakes to make enough machine learning.

In order to obtain more accuracy (N_c/N_{eq}) of prediction testing in Nankai, that is available to prediction testing of large earthquake along the Nankai Trough, the author tried to investigate deep machine learning by input data of the correlated seismicity of southwest Japan crust as shown in Fig. 7.29. From this figure, it seems that the deep learning with M4 over earthquakes as target labeling is not enough to take available accuracy scores rather than that with M4 over earthquakes as the target. Further, the available multivariate time series for prediction testing are of z_3 to z_9 of the SW Japanese island region system as seen in Fig. 7.29, and the accuracy (N_c/N_{eq}) reaches about 0.7 in the testing of M4 over earthquakes during 2011–2018.

On the other hand, it is necessary to check the incorrect prediction in the practical application of earthquake prediction testing. In order to investigate the available prediction study from the correlated seismicity, the ratio of incorrect and total prediction number ($1 - N_c/N_t$) should be introduced together with the ratio of N_c/N_{eq} as

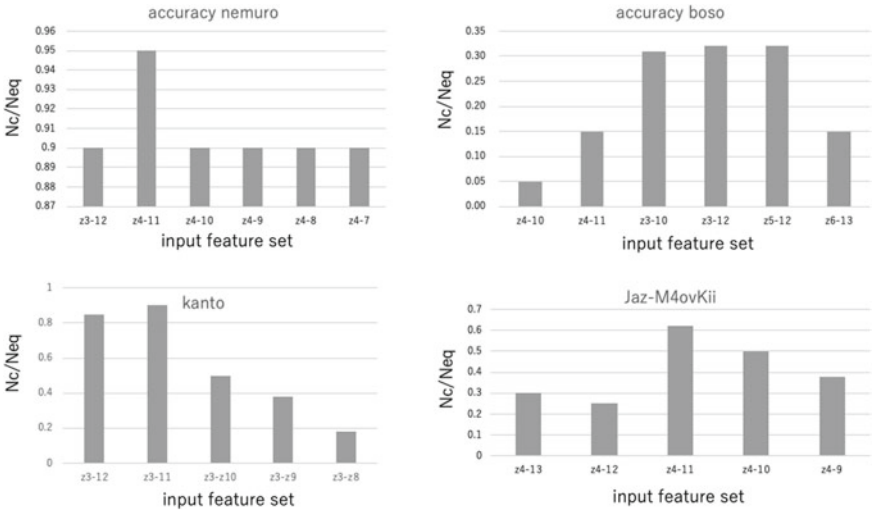

Fig. 7.28 Comparison of the prediction testing results of M5 over earthquakes in the Nemuro, Boso, Kanto, and Kii (M4 over earthquake) from various regional correlated seismicity matrix sets of z_3–z_{12} of the Japanese islands region

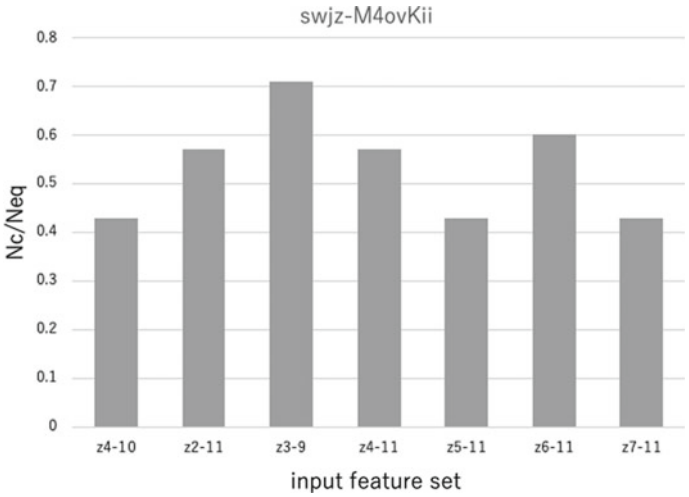

Fig. 7.29 Comparison of the prediction testing results of M4 over earthquakes in the Kii from various correlated seismicity sets of z_2–z_{11} of the Southwest Japan region

defined earlier. Here N_c, N_{eq}, and N_t are the correct number of prediction result, event number of target earthquake, and total number of incorrect and correct prediction ones, respectively. Then, the index of practical accuracy of the prediction is possibly defined as their product, $(N_c/N_{eq})(N_c/N_t)$. The results are shown in Fig. 7.30, showing

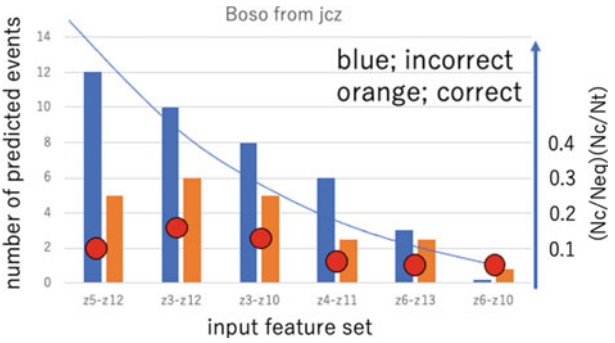

Fig. 7.30 Comparison of the prediction testing for various correlated seismicity sets showing the number of correct and incorrect prediction and preferable condition of prediction by $(N_c/N_{eq})(N_c/N_t)$ (red circle) where N_c, N_{eq}, and N_t are correct number of prediction within three steps, total number of actual large earthquakes, and total number of correct and incorrect prediction in the testing

that the practical accuracy is satisfied at the input data of z_3 to z_{12}.

In summary, the degree of the practical accuracy by N_c, $N_{eq,}$ and N_t can be displayed in the diagram of N_c/N_{eq} versus N_c/N_t as shown in Fig. 7.31. Many results of the prediction testing in the various cases seem to be roughly increasing trend with increasing N_c/N_t ratio which shows the degree of incorrect prediction. In this figure, the trend of the dotted red line arrow indicates an increase in practical accuracy of the earthquake prediction testing by DCNN with labeling.

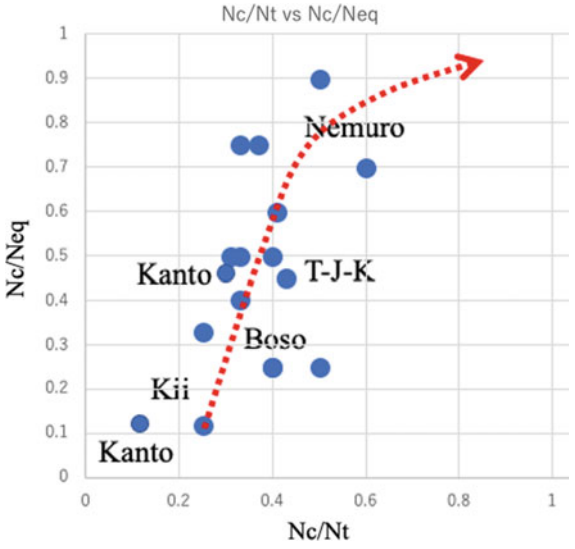

Fig. 7.31 Diagram of the N_c/N_{eq} versus N_c/N_t of the prediction testing experiments for various regions from the global and regional correlated seismicity by 1dCNN modeling with constant timestep and time-shift condition, showing the general trend of the increasing availability of the actual prediction of large earthquakes from the correlated seismicity time series

The correlated seismicity time series both of global and regional systems seems to be extrapolated by means of state-space modeling (SSM) with Kalman filter and smoothing and of deep neural network modeling based on RNN and CNN as proposed by the author (Toriumi 2021). He has studied step-by-step prediction by one-step ahead calculation from input time series of the correlated seismicity rates, using Helske's model (Helske 2018) of SSM which is based on simple random walk model with drift term.

On the other hand, investigations by RNN (LSTM) and CNN modeling of the correlated seismicity time series are also possible to be applied for the prediction study by means of repeating one-step ahead estimation from input data as shown by Toriumi (2021). The algorism for repeating prediction and input of one-step ahead is carried out by sequential modeling of DCNN with targeting the one-step ahead and its repeating.

The predicted time series of the correlated seismicity in near future is seemingly potential input data available for DCNN prediction with large earthquake labeling of which machine learning of huge amounts of parameters has been already learned. In order to evaluate the accuracy of prediction of the correlated seismicity in near future, the simple way as previously proposed in the prediction testing of large earthquake may be the VTT-DCNN direct method for near future possibility of earthquake studied here, instead of the near future estimation of the correlated seismicity by SSM and DCNN.

In order to develop the more practical prediction testing of large earthquake, it is required that the prediction testing is to be performed straightforwardly by the correlated seismicity monitored by active regional and global seismicity networks. Then, various time-shift and timestep method called as VTTM-DCNN with labeling model should be available for the practical prediction testing of near-future large earthquake. Therefore, in the present study, the author newly developed the VTTM modeling using DCNN for prediction testing of large earthquake in the global and regional cases as described in the previous sections.

Furthermore, this VTTM method shows a strong possibility of direct prediction from the available monitoring signals of most recent 5 timestep can give a prediction of possibility of near-future large earthquake, and one-step (10 days) ahead possibility of earthquake should be forecasted by the 50 days signal segment of the correlated seismicity time series before 10–100 days at the present time as shown in Fig. 7.31. It is also important that the prediction of two months before earthquake seems to be possible in practice and then following continuous notice on the present prediction may be added before 20 days. However, it should be noted that the present prediction is limited at most in the case of large earthquakes of about M5 because there is so rare in M7 over earthquake to enough training by machine learning from the studied correlated seismicity from 1990 to 2020.

7.8 Feature Mapping of DCNN Intermediate Layer Output

By the way, the VTTM studies may show a manifestation of something like preseismic signals of large earthquake embedded in the correlated seismicity time series. Thus, the author will intend to study the feature patterns of the second CNN and dense NN layers of DCNN and latent space of variational autoencoder with CNN (VAE-CNN) in order to look for the preseismic signals. In Fig. 7.32, the output data of the second layer having 32 × 1 dimension are shown by diagrams of features in the several filters. In addition, the right-hand diagrams display attractor expression of filter data such as filt.22 versus filt.20, suggesting that the data labeled by digit 1 are plotted in the region encircled, though there are data labeled by digit 0 in the circle (Figs. 7.33 and 7.34). Therefore, preseismic signals are not unique in the feature parameters of the second layer of DCNN with labeling model.

The predicted time series of correlated seismicity in near future is seemingly potential input data available for DCNN prediction with large earthquake labeling of which machine learning of huge amounts of parameters has been already learned. In order to evaluate the accuracy of prediction of the correlated seismicity in near future, the simple way as previously proposed in the prediction testing of large earthquake may be the VTT-DCNN direct method for near future possibility of earthquake studied here, instead of the near future estimation of the correlated seismicity by SSM and DCNN.

In order to develop the more practical prediction testing of large earthquake, it is required that the prediction testing is to be performed straightforwardly by the correlated seismicity monitored by active regional and global seismicity networks. Then, various time-shift and timestep method called as VTTM-DCNN with labeling model should be available for the practical prediction testing of near-future large earthquake. Therefore, in this paper the author newly developed this type of VTTM modeling of DCNN for prediction testing of large earthquake in the global and regional cases as described in the previous sections.

Furthermore, this VTTM method shows a strong possibility of direct prediction from the available monitoring signals of most recent 5 timestep can give a prediction

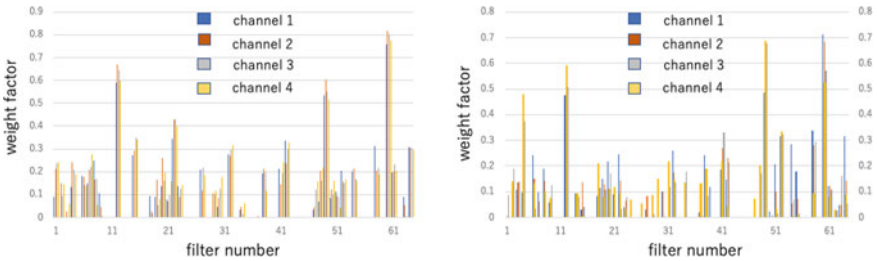

Fig. 7.32 Diagrams of the intensity of weight factor and filter number in the first layer of the Conv1d (1dCNN) with four channels for training experiments of Kanto region with 1–500 steps, showing the filter patterns in different timesteps 100 and 400

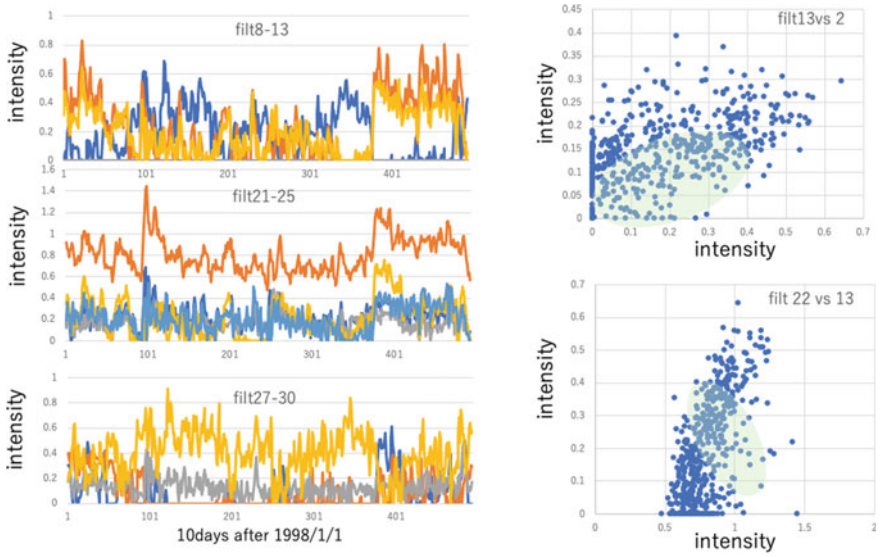

Fig. 7.33 Temporal variation of the intensity of weight factor of filters from 1 to 64 (8 × 8) in the first layer of 1dCNN (left) and phase maps of filter 2 versus 13 and filter 13 versus 22 of label 1 (shaded region) and 0 (nonshaded) in the case of training of Kanto region

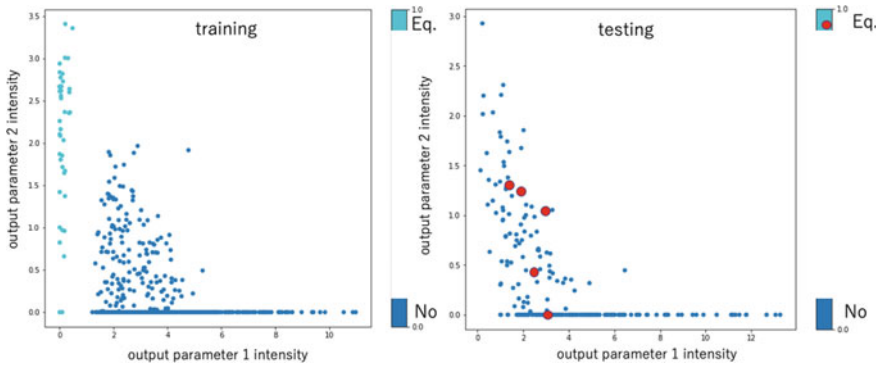

Fig. 7.34 Maps of the output parameters in final layer of CNN modeling of training (left) showing the separated clusters of large earthquake labeling (light blue), and testing experiment (right) showing mixture of earthquake (red circle) and nonearthquake labeling in the Kanto region

of possibility of near-future large earthquake, and one-step (10 days) ahead possibility of earthquake should be forecasted by the 50 days signal segment of the correlated seismicity time series before 20 days at the present time as shown in Fig. 7.25. It is also important that the prediction of two months before earthquake seems to be possible in practice and then following continuous notice on the present prediction may be added before 20 days. However, it should be noted that the present prediction

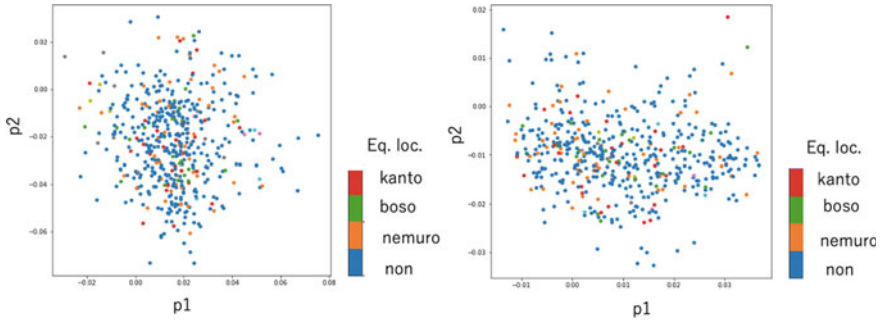

Fig. 7.35 Maps of the latent space parameters p1 and p2 in the multi-labeling model of VAE-CNN modeling of Kanto (red), Boso (green), Nemuro (orange), and nonearthquake label (blue) of the M5 over earthquake in the training (left) and testing condition (right). Timestep and z are 7×7

is limited at most in the case of large earthquakes of about M5 because there is so rare in M7 over earthquake to enough training by machine learning from the studied correlated seismicity from 1990 to 2020.

The author intends to investigate the feature patterns in the latent space projected in the VAE-CNN with labeling model by 2dCNN. The latent space expression is obtained from output of two dimensions mean and variance values of Gaussian distribution by machine-learned from input data matrix of $5 \times 5 \times 1$, $7 \times 7 \times 1$, and $9 \times 9 \times 1$ dimension. The feature patterns of the processed data in the latent space are shown in Fig. 7.35 in the case of $(7 \times 7 \times 1)$ input data, respectively. It is not sure that the data cloud of the large earthquake labeling of Nemuro in Hokkaido, Boso and Kanto regions of the central Japan is not identified by those of no earthquake labeling in the latent space expressions. It seems that there are not distinctive patterns showing the preseismic signals in the diagram of latent space of the VAE-CNN.

Furthermore, the feature parameter diagrams of the dense NN layer output which is the input of final layer with single node connected by sigmoid activation function are shown in Fig. 7.34. In this figure, the left diagram displays the feature pattern of the training process, and the right one does that of the testing process. It shows that the feature diagram of the training process displays clear classification of earthquake labeling and nonearthquake one but in the testing process the earthquake labeling data plot in the region of nonearthquake region denoted by the training data. Therefore, it is still unknown whether the preseismic signals are possibly identified from the global and regional correlated seismicity time series monitored or not.

In this study, the author investigated the prediction testing of large earthquakes by means of one-dimensional DCNN with labeling method based on the correlated seismicity in the regional and global earth. This method is carried out by multil-abeling and single labeling of large earthquake time-point with multivariate time series of global and regional correlated seismicity of the higher order than z_1 and z_2. Furthermore, the author proposed new method of prediction testing by various timestep and time-shift of input data and label series called as VTTM by author. This

VTTM method can apply for the prediction testing by ongoing monitoring of global and regional seismicity and correlated seismicity in the practical use.

The accuracy of prediction testing of large earthquake reaches at most 0.5 to 0.7 even though there are several degrees of incorrect predictions that increase with increasing apparent accuracy score. Therefore, the correct and incorrect prediction results are mutually the trade-off, and the optimal prediction testing should be proposed as the maximum accuracy under the minimum condition of the incorrect prediction number.

The prediction testing by means of VTTM method is quite practical availability because of possible forecasting at 30–60 days before large earthquake. It concludes, therefore, that the widescale monitoring of seismicity of regional and global system is much useful for the actual prediction of large earthquake through the global and regional correlated seismicity studied in this paper. However, the level of the prediction is still low around 0.5–0.7, and thus, it is needed that global and regional satellite gravity data and network GPS data may be incorporated in the input multivariate time series into the processing of DCNN with labeling model of the large earthquake prediction testing.

The preseismic signals in the global and regional correlated seismicity time series were investigated by means of output feature patterns in the DCNN second layer and dense NN layer of the DCNN with labeling method, together with latent space diagram in the VAE-CNN autoencoder model of the correlated seismicity. It is regrettable still unclear that whether there is distinctive preseismic signal in the correlated seismicity time series although there is positive prediction testing of large earthquake from DCNN with labeling method of the global and regional correlated seismicity.

7.9 Feature Mapping in Latent Space of Generative Variational Autoencoder (GVAE-DNN, VAE-CNN)

The feature mapping by DCNN intermediate layer output matrix does not display the distinctive feature patterns of the preseismic signals of large earthquake labels yet though there is some positive probability prediction of the relevant earthquake. Thus, the author intends to take a latent space mapping by generative variational autoencoder (GVAE) with DNN and CNN to investigate the possibility of clustering of event and no-event signals in the low-dimensional latent space. As shown in Fig. 7.8, the GVAE modeling is also performed by deep machine learning of training data like input data matrix of CNN based on labeling of earthquake event and no event as the target ground truth through the encoder and decoder layers connected by the low-dimensional latent space adding the mean value and variance of Gaussian noise. The present latent space appears clearly the characteristic features identified by digit labels of 0 (no event) and 1 (earthquake event). Therefore, it is expected that the feature parameters v1 and v2 of the latent space of vast amounts of samples should make different clusters corresponding to the label 0 and 1.

In the case of GVAE modeling, the multilabeling of 0 to digit m for the instantaneous multiple grids is carried out possibly by dimension reduction into two or three dimensions of mean value and variance. Here, the number of grids n is assigned as the nth locality of earthquake event, and no event and it is the target of the training of many inputs' matrix $7 \times 7 \times 1$ of the correlated seismicity z_3 to z_9 with timestep 7. In this study, the localities of Nemuro, Kanto, Boso, Nankai, and Ryukyu are investigated, but the multilabeling modeling is performed on the Nemuro, Kanto, and Boso districts as the testing case. The results are shown in Fig. 7.35, and it seems that there are no distinctively identified clusters for the earthquake occurrence of each locality, though there is a vague appearance of different scattering patterns of their localities as seen in distribution of different color dots.

Furthermore, in the case of single labeling for the regions of Kanto, Nankai, and Ryukyu areas, latent space mapping by two methods was carried out after enough training by input data: one is the output data of final dense layer before reference single output node of DCNN and other is the VAE-CNN latent space output as illustrated in Fig. 7.36. It is clear that the output mapping for training data by DCNN final layer output which is constituted basically with 500×16 (sample number $\times$ characteristic features) matrix manifests two separated clusters with label 0 and 1, that is no earthquake signals and earthquake ones after training and testing, thereby suggesting that the training by CNN for 1–500 steps performed enough to learn the transformation by NN from the correlated seismicity matrix to label 0 and 1. However, the mapping of testing data at the same time does not appears always two clusters of labels 0 and 1 as shown in Fig. 7.37, and then it seems that the characteristic patterns of the training data matrix do not match with the testing data matrix.

On the other hand, the latent space mapping by VAE-CNN (and VAE-DNN) does not appear the obviously separated clusters but does nearly a single cluster in both cases of training data and testing one as shown in Fig. 7.37. In this case, it possibly concluded that the generative VAE is not available for the augmentation of random

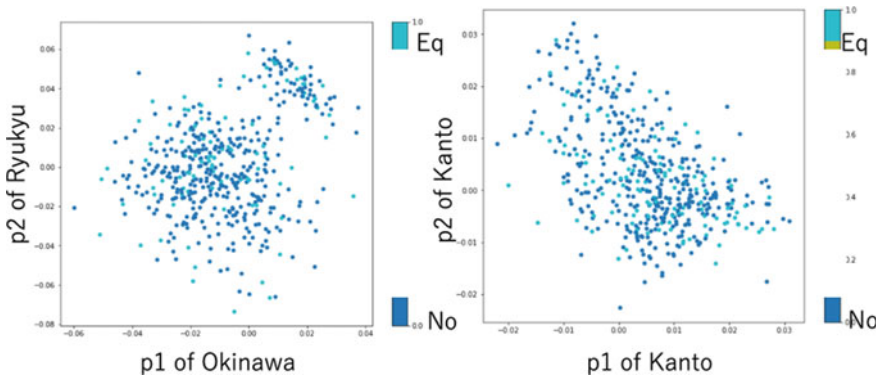

Fig. 7.36 Comparison of the latent space mapping of the VAE-CNN modeling of Okinawa and Kanto regions in the training stage showing the mixing of the earthquake and nonearthquake labels in the map

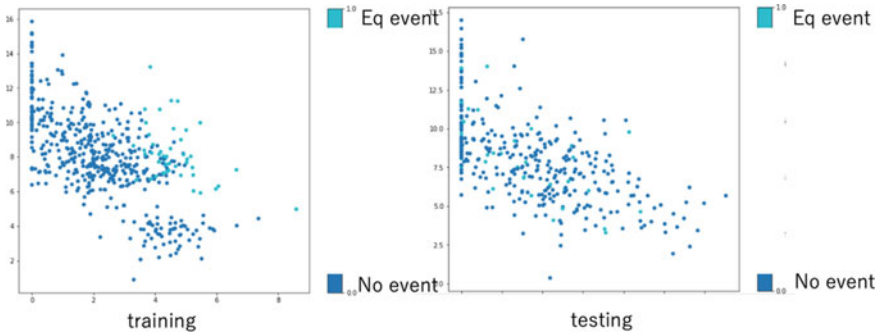

Fig. 7.37 Comparison of the latent space mapping of the VAE-CNN modeling of Okinawa region in the training (left) and testing (right) stages for earthquake (light blue) and nonearthquake (blue) labels, showing the identified cluster in the training but mixture in the testing

sample adding into training process of DCNN, RNN, and LSTM prediction modeling. Contrarily, judging from the fact that the DNNs modeling partly makes a possible prediction testing by the machine learning for the global and regional seismicity, and it may be clarified that the correlated seismicity signals contain something like preseismic precursors embedded in their time series. Therefore, it may conclude that there are still unknown signals of preseismic precursor involving the correlated seismicity time series such as their second moments and time derivatives.

7.10 Future Strategy of Earthquake Prediction Testing

In the previous chapters and sections, it has been discussed that the small subcritical cracks (types II and III) absorbing several amounts of H_2O molecule slowly grow by erosion of crack tips with advancing the time in the solid earth and they should propagate with very rapid speed emitting the elastic wave just after exceeding the critical size of the crack like Griffith crack. The critical size of the shear cracks depends on the content of absorbed H_2O molecule on the crack surface. In the cases of aqueous solution, there are many ionic species in the aqueous solution, and the crack surface in the natural rocks is constituted with radical state of the oxygen, and thus, it is easy to be reacted with dissolved cations such as H^+, Na^+, K^+, and Ca^{2+}, and Fe^{2+}, to decrease its surface energy. Then, the critical radius of the cracks should increase, and the shear cracks grow successively with absorbing aqueous water until cessation of water supply into the cracks. After crack radius is larger than the critical one, the shear cracks start to propagate and grow in the runaway mode emitting the elastic wave (seismic wave).

By the way, in the previous book, the author proposed the percolation model of the small shear crack clusters according to their elastic attractive interaction to make a rapid propagation from small to large shear crack. In the process of this coagulation

and propagation mode of crack cluster, micro- to small earthquakes clusters are very active before the present process and thus before the large earthquake as the pre-earthquake signals. In addition, the time scale of the duration of the signals may be strongly depending upon the inflow rate of aqueous water into the cracks of the cluster. Therefore, it is suggested that the supply of the aqueous solution and its ionic concentration are very sensitive for generation of the large earthquake and that the permeability change surrounding the large fault plane controls the onset of the rapid growth and propagation of the shear cracks that may coagulate with each other.

Furthermore, it is known that the percolation of the shear cracks is strongly enhanced with the crack density and crack size in the state of subcritical growth, and thus the statistical population density ratio of these various size of cracks that is called as *b*-value in GR law affects the onset of large earthquake. Therefore, it is suggested that the large volume ratio of aqueous fluid which occupies the open crack and related voids should control the frequency pattern of the size of the growing but not propagating cracks and then do the *b*-value: the rock mass of the small volume content of aqueous fluid may show the large *b*-value that implies the large ratio of small cracks by large cracks, but the rocks of large volume content do the small *b*-value.

As is well known, it is obvious that in the large volume content of water, the Vp and Vs are rather small and Vp/Vs is large, compared with the rocks in the small content of water. Therefore, it seems that the relatively low Vp/Vs and high Vp region appears surely the high *b*-value and low content of aqueous fluid. Contrarily, the high Vp/Vs and low Vp region may appear the low *b*-value and large content of fluid.

In the previous chapter, it seems that the aqueous fluid probably onsets the permeable convection along the damage zone of the plate boundary and intermittently it leaks away from the boundary. The two-dimensional convection is composed of the up-flow and down-flow regions along the plate boundary zone. It is probable that the porosity of the down-flow region becomes high with fluid–rock interaction but that of the up-flow region does low by precipitation of minerals from solution. Therefore, during the advance of the permeable convection of aqueous fluid, the coagulation rate of the shear cracks that grow in the geochemical effect mentioned previously seems to be high in the present down-flow region, but in the up-flow region the coagulation rate is probably low.

Above permeable convection may be unstable after enough precipitation of minerals in the pores of the up-flow region. It seems that the permeable convection migrates forward and backward in the narrow plate boundary zone along the trench axis. Therefore, the coagulation of the shear cracks in the slow speed mode may take place repeatedly in the plate boundary region, resulting in the repeating of slow slip event along the plate boundary damage zone. Observed time scales of the slow slip repeat range from several hundred days to several years (Schwartz and Rokosky 2006), suggesting the similar time scale of the porosity change in the plate boundary zone.

In the previous sections, it is concluded that the DNN machine learning of the global and regional correlated seismicity into the large earthquake event is available for the prediction testing rather than by the real seismicity rate of the gridded locality.

It is apparently strange that the fore-seismic signals before large earthquake appear in the correlated seismicity but not in the real seismicity. It may be possible that the large earthquake event is controlled by the wide region of the plate boundary by the elastic and plastic strain with cracks and voids filled with fluid and fluid flow, and the correlated seismicity of the global and regional system involving subduction zones is also affected by these parameters as discussed previously. It has been clarified that the global correlated seismicity time series manifest the systematic change in the seismic activity in the global subduction zones as shown in the previous chapters.

References

Bishop CM (2006) Pattern recognition and machine learning. Springer, New York
Chollet F (2017) Deep learning with Python. Manning Publishing, USA
Chollet F, Allaire JJ (2018) Deep learning with R. Manning Publishing, USA
Ekstrom G (2007) Global seismicity: results from systematic waveform analyses, 1976–2005. In: Kanamori H (ed) Treatise on geophysics 2007. Elsevier, pp 473–481
Fukao Y, Kubota T, Sugioka H, Ito A, Tonegawa T, Shiobara H, Yamashita M, Saito T (2021) Detection of "rapid" aseismic slip at the Izu-Bonin trench. J Geophys Res. Solid Earth 126:e2021JB022132. https://doi.org/10.1029/2021JB022132
Helske J (2018) KFAS: Exponential family state space models in R. https://cran.r-project.org/web/packages/KFAS/vignettes/KFAS.pdf
Ide S (2009) Scaling relations for earthquake source process. Jishin 61:S329–S338 in Japanese
Ogata Y (2015) Stochastic prediction of earthquakes—A strategy for the research. Proc Inst Stat Math 63(1):3–27
Okada A, Toriumi M, Kaneda T (2017) Spatial and temporal pattern of global seismicity extracted by dimensionality reduction. Int J Geology 11:26–34
Schwartz S, Rokosky JM (2006) Slow slip events and seismic tremor at circum—Pacific subduction zones. Rev Geophys 45:RG3004. https://doi.org/10.1029/2006rg000208
Thogersen K, Gilber A, Schuler TV, Sorenssen AM (2019) Rate- and -state friction explains glacier surge propagation. Sci Commun 10:2823. https://doi.org/10.1038/s41467-019-10506-4
Toriumi M (2021) Global seismicity dynamics and data driven science. Springer

Chapter 8
Conclusive Remarks

Abstract Geochemical mechanics is a new field of geosciences for the purpose of foundation of science that clarify the mechanical behavior of the solid earth involving the interaction of aqueous fluid and rock yielding with fracture. In this book, the author intends to introduce the various cracks sealed by minerals and related fracture processes, and the rapid processes of geological objects having various time and space scales. On the basis of the geochemical mechanics, the neural network modeling of the prediction testing of the large earthquakes from the global and regional geophysical monitoring data.

Keywords Geochemical mechanics · Rapid geophysical process · Neural network modeling of earthquake prediction testing

8.1 Conclusive Remarks

In this book, the author intends to propose a new aspect of the earth mechanics representing the fracture dynamics with geochemical interaction and of the prediction testing by means of the deep neural network modeling under the global correlated seismicity time series. In the mechanochemistry, the hydrogen embrittlement and hydrolysis of surface of minerals and metals have been already established, and on the other hand, in the geoengineering and tectonophysics, the weakening of rocks by aqueous solution and the rate and state law of friction (Dieterich and Ruina law) are also founded. Therefore, the geochemical mechanics concerning the geochemical and petrological reactions between rocks and aqueous solution related to the fracture mechanism and creep behavior of rocks in the solid earth is the important field for mechanical behavior of the plate boundary zone.

By the way, it is obvious that there are huge amounts of complicated parameters and rocks decoupled with surroundings by fault, shear zone, and the rock type contact which should be of different parameters of mechanics in the solid earth. Therefore, it is easy to be imaged that the geomechanical evolution of the deep-seated mass in the solid earth should be controlled by huge amounts of initial condition, boundary condition, and strain and stress, and volume fraction of fluid and mineral contents and sizes, and cracks of vast amounts of fractures rock units. Contrarily, there are

M. Toriumi, *Geochemical Mechanics and Deep Neural Network Modeling*,
Advances in Geological Science, https://doi.org/10.1007/978-981-19-3659-3_8

some macroscopic parameters observed by seismic observation and geochemical investigations in the plate boundary zones such as fluid flow, geothermal structure, seismic wave velocities, reflection structure, seismicity, and others. The vast amounts of basic units and parameters, as freedom of the system, may be treated by the dimension reduction method to be obtained actually important factors that are to be the robust and macroscopic invariant parameters in the huge amounts of observable parameters. The method available for the present object should be the deep neural network modeling including RNN, LSTM, CNN, and GVAE methods.

The correlated seismicity time series of the global subduction zone derived from machine learning PCA method (singular value decomposition of logarithmic seismicity in the gridded locality data matrix) manifest the characteristic pattern (feature pattern) of not only the global seismicity in the subduction and ridge zones but also the regional seismicity of the subduction zone and transform fault zone (Toriumi 2021). The characteristic features of the global correlated seismicity display the secular and periodic variations having various repeating time from several hundred days to several years. In addition, the sub-annual to tri-annual periodic variation can be found in the residual from the migration average of the time series of z_1–z_4, suggesting that there is near-annual variation of the global seismicity of the subduction zone.

On the other hand, as discussed in the previous chapter, the length of day (LOD) and satellite gravity time series especially of zonal component C20 also have clear seasonal variation in the residual subtracted by the secular trend. The time series of the VLBI distance between Tasmania and Tsukuba, and Hawaii and Tsukuba show the distinctive seasonal variation as like as the grace gravity and LOD data. It is very impressive that these time series display the similar periodic variations having some different phases in the residual from the secular trend. Therefore, it seems that the global seismic activity of the subduction zones is probably controlled by the mechanism like to those of the earth rotation, zonal component of satellite gravity, and short-term plate velocity (VLBI distance).

By the way, in the fluid earth dynamics, it has been discussed that the seasonal variation of the LOD and the zonal component of the gravity should be derived from the water redistribution among ocean, land and solid earth interior (e.g., Cheng and Ries 2017). The sea surface height (SSH) temporal variation includes semiannual variation and the secular variation. Until now, it seems that the ocean general circulation model (OGCM) can explain both of seasonal and semiannual variation and secular change of the SSH and resultant temporal variation of the LOD (earth rotation) and zonal component of satellite gravity C20 change (Chen and Wilson 2003). The mechanism of the earth rotation is the elliptical change of the ocean mass along the low latitudinal zone accompanied with total mass increase of ocean migrated from the land ice and water.

It is very important to be noted that the global correlated seismicity of the subduction zones has also the various temporal variations that show the semiannual to several annual variation and the secular trend, being likely to those of the SSH observed by satellite altimetry (Cheng et al. 2011). On the other hand, the correlated regional seismicity appears clearly the semiannual temporal variation in northern California

and Japanese islands region, and it looks like the seasonal variation of the precipitation rate as shown by Johnson et al. (2017) and Heki (2007). In addition, it is very noteworthy that the secular temporal variation of the global correlated seismicity and the regional one resembles of the secular variation of LOD and C20 as described previously. The variational ranges of them are likely to each other, thereby suggesting that the secular trend of the global correlated seismicity is mainly governed by the total mass change of ocean by gradual land and polar ice melting.

The reason of the increase in the correlated global seismicity z_1 from 2003 after 1990 is seemingly responsible for the global mass increase of ocean derived by global warming of the ocean and resultant ice melting in the high latitude and polar region. Furthermore, as suggested by Ekstrom (2007) and previous book (Toriumi 2021), the temporal change of the global seismic moment release rate manifests the rapid increase after 2003 as same as that of the correlated seismicity z_1. It seems that these similar temporal change may show the global earth mechanics changing after 2003 in the period of 1990–2021.

On the other hand, recent study by Blagoveshchenskaya et al. (2019) of the relation between the Chandler wobble that is derived from celestial mechanics among earth, moon, and sun, and the seismic activity of the global ridge zones strongly suggests the time series of the ridge seismicity synchronized with the temporal variation of the Chandler wobble during 1965–1990. This is consistent with the fact that the investigation of the earth rotation rate is synchronized with the global correlated seismicity change both of subduction zone and ridge zone in the period from 1990 to 2021, and they are governed by the nonlinear dynamics having the pitchfork bifurcation as indicated in Chapter 5.7.

In this book, the author will investigate the prediction testing of the large earthquakes during 1990–2021 in the global subduction zones. In this object, the monitoring data tried for the testing are the logarithmic seismicity of the gridded localities and the correlated seismicity obtained from the SVD (and PCA) decomposition of the above logarithmic seismicity together with their partial b-values. Otherwise, it is shown that the logarithmic seismicity is not available for the prediction testing of large earthquakes occurred in the relevant grids, but the correlated partial b-value and the correlated seismicity are both potential indicative to the testing after enough training on DNN. It is apparently strange that the near seismicity does not have any fore-seismic signal, but the correlated seismicity is yes. It is probable that the shear cracks generating the large earthquake may be related to the characteristic features of the density variation of rather small shear cracks in the wide region and the regional to global background stress change. This suggestion is partly supported by comparison of the change in Pearson's mapping of seismicity correlation between the logarithmic seismicity and the correlated seismicity as mentioned in the previous chapter: in Pearson's map, that displays the degree of correlation of the time series of parameters, of the correlated seismicity, the feature pattern changes at the earthquake events are clearer than those of the logarithmic seismicity.

Accordingly, it may be inferred that the long-term secular trends from 1990 to 2021 in the global earth and 1998–2021 in the regional case showing the high level in the correlated seismic activity after 2003 are the reason of disturbance for the

available prediction testing from the training data from 1990 to 2003. Therefore, it seems that the input data sets of the correlated seismicity containing the data of 2003–2021 in the global and regional system have a potential signature for better prediction testing on the large earthquakes after 2021 to near future, but it needs to be accumulated the seismic data in the present periods. It should be the future problem to be solved.

References

Blagoveshchenskaya E, Lyskova E, Sannikov K (2019) Variation of seismic activity caused by the Chandler wobble, E3S Web of Conferences. Solar-Terrestrial Relations and Physics of Earthquake Precursors 127:03007. https://doi.org/10.1051/es3conf/201912703007

Chen JL, Wilson CR (2003) Low degree gravitational changes from earth rotation and geophysical models. Geophys Res Lett 30(24):257. https://doi.org/10.1029/2003GL018688

Cheng M, Ries JC, Tapley BD (2011) Variations of the Earth's figure axis from satellite laser ranging and GRACE. J Geophys Res 116:B01409. https://doi.org/10.1029/2010JB000850

Cheng MK, Ries JC (2017) The unexpected signal in GRACE estimates of C20. J Geodesy. https://doi.org/10.1007/s00190-016-0995-5

Ekstrom G (2007) Global seismicity: results from systematic waveform analyses, 1976–2005. In: Kanamori H (ed) Treatise on geophysics 2007, Elsevier, pp 473–481

Heki K (2007) Secular, transient and seasonal crustal movements in Japan from a dense GPS array: implicate for plate dynamics in convergent boundaries. In: Dison T, Moore C (eds) Seismogenic zone of subduction thrust faults, pp 512–539

Johnson CW, Fu YN, Burgmann R (2017) Seasonal water storage, stress modulation, and California seismicity. Science 356(6343):1161–1164. https://doi.org/10.1126/science.aak9547

Toriumi M (2021) Global seismicity dynamics and data-driven science. Springer

Appendix

The python 3 codes written for processing in this book with KERAS—Tensorflow in Google Colaboratory and code of Gaussian base Bayesian regression model are listed.

```
#1, data sender to google colab.
from google.colab import files
uploaded=files.upload()
```

```
#2, data format in colab.
import pandas as pd
import io
xdf=pd.read_csv(io.StringIO(uploaded['filename.csv'].
decode('utf-8')), sep=',')
from numpy import array
from numpy import hstack
import numpy as np
xdf=np.arra

# output(356,11) matrix

y(xdf)
print (xdf.shape)
from sklearn import preprocessing
scaler=preprocessing.MinMaxScaler()
xdf=scaler.fit_transform(xdf)
print (xdf)
```

```
#3, data splitter

from numpy import array
def split_sequences(sequences, n_steps):
 X, y = list(), list()
 for i in range(len(sequences)):
   end_ix = i + n_steps
   if end_ix > len(sequences):
    break
```


M. Toriumi, *Geochemical Mechanics and Deep Neural Network Modeling*, Advances in Geological Science, https://doi.org/10.1007/978-981-19-3659-3

```
   seq_x, seq_y =
sequences[i:end_ix, :10 -1], sequences[end_ix-1,9:12 -1]
# (10, 9:12) to be changed in your model
   X.append(seq_x)
   y.append(seq_y)
 return array(X), array(y)
n_steps=9    #(arbitrary)
X, y = split_sequences(xdf, n_steps)
print (X.shape, y.shape)
print (X)
print (y)
x_1=X
y_1=y

# output matrixes (348,9,9)(348,2)

#3, output data save in Mac download
# from outdata from CNN intermediate layer, outdata
import pandas as pd
from google.colab import files
xpred_out=pd.DataFrame(outdata)
xpred_out.to_csv('outcnn8.csv')
from google.colab import files
files.download('outcnn8.csv')

#from output data of prediction;pred
import pandas as pd
from google.colab import files
xpred_out=pd.DataFrame(pred)
xpred_out.to_csv('oki1predlstm.csv')
from google.colab import files
files.download('oki1predlstm.csv')

#4,cnn modeling1
import numpy as np
import pandas as pd
import matplotlib.pyplot as plt
from numpy import array
from keras.models import Sequential
from keras.layers import Dense
from keras.layers import Flatten
from keras.layers.convolutional import Conv1D
from keras.layers.convolutional import MaxPooling1D

timesteps=7   #example
n_features=7  #example

model = Sequential()
model.add(Conv1D(filters=64, kernel_size=2, activation='relu',
input_shape=(timesteps, n_features)))
model.add(MaxPooling1D(pool_size=1))
model.add(Conv1D(filters=32, kernel_size=2, activation='relu'))
model.add(MaxPooling1D(pool_size=1))
model.add(Flatten())
model.add(Dense(64, activation='relu'))
```

```
model.add(Dense(8, activation='relu'))
model.add(Dense(2, activation='sigmoid'))
model.compile(optimizer='adam', loss='binary_crossentropy')
history = model.fit(x_1, y_1, epochs=250, verbose=0)
pred=model.predict(x_2)

fig, ax=plt.subplots()
ax.plot(y_2[:500, :].reshape(-1), linewidth=0, marker="o",
markersize=5)
ax.plot(pred[:500, :].reshape(-1), linewidth=0, marker="o",
markersize=5)
ax.set_xticks(np.arange(0,800,2))
ax.set_yticks([0, 1])
ax.legend(["label", "predcnn"])
ax.grid()
plt.show()

loss = history.history["loss"]
#acc=history.history["acc"]
fig, ax=plt.subplots()
ax.plot(loss)
#ax.plot(acc)
ax.legend(["loss", "acc"])
plt.show()

print(pred)
print(pred.shape)

model_2 = Sequential()
model_2.add(hidden_layer_model)
pred=model_2.predict(hidden_layer_model(X))

fig = plt.figure(figsize=(18, 30))
for i in range(5):
   ax = fig.add_subplot(6, 3, 3*i+1)
   ax.imshow(X[i][:, 0], cmap='gray_r')
   ax = fig.add_subplot(6, 3, 3*i+2)
   ax.imshow(model_2.X[i:i+1])[0][:, 0], cmap='gray_r')
   ax = fig.add_subplot(6, 3, 3*i+3)
   ax.imshow(model_2.predict(X[i:i+1])[0][:, 1], cmap='gray_r')
plt.show()

#5,cnn modeling2
import numpy as np
import pandas as pd
import matplotlib.pyplot as plt
from numpy import array
from keras.models import Sequential
from keras.layers import Dense
from keras.layers import Flatten
from keras.layers.convolutional import Conv1D
from keras.layers.convolutional import MaxPooling1D

timesteps=5
n_features=5
```

```
model = Sequential()
model.add(Conv1D(filters=64, kernel_size=2, activation='relu',
input_shape=(timesteps, n_features)))
model.add(MaxPooling1D(pool_size=1))
model.add(Flatten())
model.add(Dense(64, activation='relu'))
model.add(Dense(32, activation='relu'))
model.add(Dense(1, activation='sigmoid'))
model.compile(optimizer='adam', loss='binary_crossentropy')

history = model.fit(x_1, y_1, epochs=300, verbose=0)
pred=model.predict(x_2)

fig, ax=plt.subplots()
ax.plot(y_2[:800, :].reshape(-1), linewidth=0, marker="o",
markersize=8)
ax.plot(pred[:800, :].reshape(-1), linewidth=0, marker="o",
markersize=5)
ax.set_xticks(np.arange(0,800,2))
ax.set_yticks([0, 1])
ax.legend(["training", "pred"])
ax.grid()
plt.show()

loss = history.history["loss"]
#acc=history.history["acc"]
fig, ax=plt.subplots()
ax.plot(loss)
ax.plot(acc)
ax.legend(["loss", "acc"])
plt.show()

#6, RNN and LSTM modeling
import numpy as np
import pandas as pd
import matplotlib.pyplot as plt
from keras.models import Sequential
from keras.layers import Dense, SimpleRNN, GRU, LSTM

timesteps=7
features = 9
actfunc="sigmoid"
model =Sequential()
model.add(LSTM(64, activation =
'relu', batch_input_shape=(None, timesteps, features)))
#the case of LSTM
model.add(Dense(32, activation = 'relu', ))
model.add(Dense(2, activation='sigmoid'))
model.compile(optimizer='adam', loss='binary_crossentropy')
history = model.fit(x_1, y_1, batch_size=64, epochs=700, verbose=0)
pred=model.predict(x_2)
print(pred)

fig, ax=plt.subplots()
ax.plot(y_2[:400, :].reshape(-1), linewidth=0, marker="o",
```

```
markersize=8)
ax.plot(pred[:400, :].reshape(-1), linewidth=0, marker="o",
markersize=5)
ax.set_xticks(np.arange(0,800,2))
ax.set_yticks([0, 1])
ax.legend(["label", "prediction"])
ax.grid()
plt.show()

loss = history.history["loss"]
fig, ax=plt.subplots()
ax.plot(loss)
ax.legend(["LSTMts7okis9"])
plt.show()

#7, output data save in Mac download from outdata from CNN intermediate
layer; outdata import pandas as pd
from google.colab import files
xpred_out=pd.DataFrame(outdata)
xpred_out.to_csv('outcnn8.csv')
from google.colab import files
files.download('outcnn8.csv')

#8 from output data of prediction; pred
import pandas as pd
from google.colab import files
xpred_out=pd.DataFrame(pred)
xpred_out.to_csv('oki1predlstm.csv')
from google.colab import files
files.download('oki1predlstm.csv')

#9 vae modeling

#9-1 vae-dnn
from __future__ import absolute_import
from __future__ import division
from __future__ import print_function
from keras.layers import Lambda, Input, Dense
from keras.models import Model
from keras.losses import mse
from keras import backend as K
import numpy as np
import matplotlib.pyplot as plt

#reading datasets
#(x_1, y_1). (x_2, y_2) sets have been preprocessed
x_train=x_1.T
x_test=x_2.T
y_train=y_1[:,0]
y_test=y_2[:,0]
image_size = x_train.shape[1]
original_dim = image_size*image_size
x_train = np.reshape(x_train, [-1, original_dim])
x_test = np.reshape(x_test, [-1, original_dim])
x_train=x_train.astype('float32')
```

```
x_test=x_test.astype('float32')
y_train=8*np.ravel(y_train)
y_test=8*np.ravel(y_test)
print (y_train)
input_shape = (original_dim, )
latent_dim = 2
#reparameterization
def sampling(args):
    z_mean, z_logvar =args
    batch = K.shape(z_mean)[0]
    dim = K.int_shape(z_mean)[1]
    epsilon = K.random_normal(shape=(batch, dim), seed =5)
    return z_mean + K.exp(0.7*z_logvar)*epsilon
#vae structure
inputs = Input(shape=input_shape)
x1 = Dense(64, activation='relu')(inputs)
x2 = Dense(32, activation='relu')(x1)
z_mean = Dense(latent_dim)(x2)
z_logvar = Dense(latent_dim)(x2)
z =
Lambda(sampling, output_shape=(latent_dim,))([z_mean, z_logvar])
encoder=Model(inputs, [z_mean, z_logvar, z], name='encoder')
encoder.summary()

latent_inputs = Input(shape=(latent_dim, ))
x3 = Dense(32, activation='relu')(latent_inputs)
x4 = Dense(64, activation='relu')(x3)
outputs = Dense(original_dim, activation='tanh')(x4)
decoder=Model(latent_inputs, outputs, name='decoder')
decoder.summary()

z_output = encoder(inputs)[2]
outputs = decoder(z_output)
vae=Model(inputs, outputs, name='variational_autoencoder')

kl_loss = 1 + z_logvar - K.square(z_mean) - K.exp(z_logvar)
kl_loss = K.sum(kl_loss, axis=-1)
kl_loss *= -0.5

reconstruction_loss = mse(inputs, outputs)
reconstruction_loss *=original_dim

vae_loss =K.mean(reconstruction_loss +kl_loss)
vae.add_loss(vae_loss)
vae.compile(optimizer='adam')
vae.fit(x_train, epochs=300, batch_size=128, validation_data=
(x_test, None))

#test image decoding
decoded_imgs = vae.predict(x_train)
n=10
plt.figure(figsize=(10,2))
for i in range(n):
   #test image
    ax=plt.subplot(2, n, i+1)
```

```
    plt.imshow(x_train[i].reshape(7, 7))
    plt.gray()
    ax.get_xaxis().set_visible(False)
    ax.get_yaxis().set_visible(False)

#decoded image
    ax = plt.subplot(2, n, i+1+n)
    plt.imshow(decoded_imgs[i].reshape(7, 7))
    plt.gray()
    ax.get_xaxis().set_visible(False)
    ax.get_yaxis().set_visible(False)
plt.show()

import matplotlib.cm as cm
def plot_results(encoder, decoder, x_test, y_test, batch_size=128,
model_name="vae_data"):
    z_mean, _,_ = encoder.predict(x_test, batch_size=128)
    plt.figure(figsize=(12, 10))
    cmap=cm.tab10
    plt.scatter(z_mean[:, 0], z_mean[:,1], c=cmap(y_test))

    m=cm.ScalarMappable(cmap=cmap)
    m.set_array(y_test)
    plt.colorbar(m)
    plt.xlabel("z[0]")
    plt.xlabel("z[1]")
    plt.show()
   #(-4,4) ~ (4,4) 30x30 split
    n=30
    digit_size =7
    figure = np.zeros((digit_size*n, digit_size*n))
    grid_x = np.linspace(-4, 4, n)
    grid_y = np.linspace(-4, 4, n)[:: -1]
    for i, yi in enumerate(grid_y):
        for j, xi in enumerate(grid_x):
            z_sample = np.array([[xi, yi]])
            x_decoded = decoder.predict(z_sample)
            digit = x_decoded[0].reshape(digit_size, digit_size)
            figure[i*digit_size: (i+1)*digit_size,
                   j*digit_size: (j+1)*digit_size] = digit

    plt.figure (figsize = (10, 10))
    start_range = digit_size // 2
    end_range = n*digit_size + start_range +1
    pixel_range = np.arange(start_range, end_range, digit_size)
    sample_range_x = np.round(grid_x, 1)
    sample_range_y = np.round(grid_y, 1)
    plt.xticks(pixel_range, sample_range_x)
    plt.yticks(pixel_range, sample_range_y)
    plt.axis("off")
    plt.imshow(figure, cmap='Greys_r')
    plt.show()

plot_results(encoder, decoder, x_test, y_test, batch_size=128,
model_name="vae_mlp")
```

```
#9-2 VAE-CNN

import numpy as np
import matplotlib.pyplot as plt
import pandas as pd
import sklearn
import time
cmap='tab10' #color code
x_train=x_1
x_test=x_2
y_train=y_1[:,0]
y_test=y_2[:,0]
image_size = x_train.shape[1]
original_dim = image_size*image_size
x_train=x_train.astype('float32')
x_test=x_test.astype('float32')
y_train=10*np.ravel(y_train)
y_test=10*np.ravel(y_test)
print (y_train)
latent_dim = 2
n=int(x_train.shape[0])

import keras
from keras.layers import Lambda, Input, Dense, Dropout
from keras.models import Model
from keras.losses import mse, binary_crossentropy
from keras.models import Sequential
from keras.layers import MaxPooling2D
from keras import layers
from keras.layers import Conv2D, Flatten
from keras.layers import Reshape, Conv2DTranspose
from keras import backend as K
pixel_size=image_size

def vae_cnn(x_train, x_test, latent_dim = 2, epochs =
10, pixel_size=pixel_size):
   x_train =
x_train.reshape((x_train.shape[0], pixel_size, pixel_size, 1))
   x_test =
x_test.reshape((x_test.shape[0], pixel_size, pixel_size, 1))
#network parameters
   input_shape = (pixel_size, pixel_size, 1)
   batch_size = 64
   kernel_size = 3
   filters = 16
#VAE model = encoder + decoder
#build encoder
   inputs = Input(shape=input_shape, name='encoder_input')
   x= inputs
   x =
Conv2D(filters=8, kernel_size=kernel_size, activation='relu',
padding='same')(x)
   x =
Conv2D(filters=16, kernel_size=kernel_size, activation='relu',
padding='same')(x)
```

```
    shape = K.int_shape(x)
    x = Flatten()(x)
   # x=Dropout(0.5)
    x = Dense(16, activation='sigmoid')(x)
    z_mean = Dense(latent_dim, name='z_mean')(x)
    z_log_var = Dense(latent_dim, name='z_log_var')(x)

    z =
Lambda(sampling, output_shape=(latent_dim,), name='z')([z_mean,
z_log_var]) # instantiate encoder model
    encoder = Model(inputs, [z_mean, z_log_var, z], name='encoder')

    encoder.summary()

    latent_inputs = Input(shape=(latent_dim,), name='z_sampling')
    x = Dense(shape[1] * shape[2] * shape[3], activation='relu')
(latent_inputs)
    x = Reshape((shape[1], shape[2], shape[3]))(x)
    x = Conv2DTranspose(filters=16, kernel_size=kernel_size,
activation='relu', padding='same')(x)
    x = Conv2DTranspose(filters=8, kernel_size=kernel_size,
activation='relu', padding='same')(x)
    outputs = Conv2DTranspose(filters=1, kernel_size=kernel_size,
activation='sigmoid', padding='same', name='decoder_output')(x)

#instantiate decoder model

    decoder = Model(latent_inputs, outputs, name='decoder')
    decoder.summary()

    outputs = decoder(encoder(inputs)[2])
    vae = Model(inputs, outputs, name='vae')

    reconstruction_loss =
binary_crossentropy(K.flatten(inputs), K.flatten(outputs))
    reconstruction_loss *= pixel_size * pixel_size
    kl_loss = 1 + z_log_var - K.square(z_mean) - K.exp(z_log_var)
    kl_loss = K.sum(kl_loss, axis=-1)
    kl_loss *= -0.5
    vae_loss = K.mean(reconstruction_loss + kl_loss)
    vae.add_loss(vae_loss)
    vae.compile(optimizer='adam')
    vae.summary()

#training the autoencoder

    result = vae.fit(x_train, epochs=epochs, batch_size=batch_size,
validation_data=(x_test, None))
    return encoder, decoder, result

def sampling(args):
    z_mean, z_log_var = args
    batch = K.shape(z_mean)[0]
    dim = K.int_shape(z_mean)[1]
    epsilon = K.random_normal(shape=(batch, dim))
    return z_mean + K.exp(0.73 * z_log_var) * epsilon
```

```
#plotting

encoder, decoder, result= vae_cnn(x_train, x_test, latent_dim =
2, epochs = 100, pixel_size=pixel_size)
Model: "encoder"
plt.plot(result.history['loss'], label='loss',color='r')
plt.plot(result.history['val_loss'],label='val_loss',color='b')
plt.legend()
plt.xlabel('epoch')
plt.ylabel('loss')
plt.show()
z_mean, _, _ =
encoder.predict(x_train.reshape((x_train.shape[0],pixel_size,
pixel_size,1)))
plt.figure(figsize=(10, 8))
plt.scatter(z_mean[:, 0], z_mean[:, 1], s=25, c=y_train, cmap=cmap)
plt.colorbar()

#10 others

model.summary()

#Model."sequential_4"
_________________________________________________________________
Layer (type)           Output Shape          Param #
=================================================================
conv1d_4 (Conv1D)        (None, 6, 64)         1216
_________________________________________________________________
max_pooling1d_4 (MaxPooling1 (None, 6, 64)         0
_________________________________________________________________
conv1d_5 (Conv1D)        (None, 5, 32)         4128
_________________________________________________________________
max_pooling1d_5 (MaxPooling1 (None, 5, 32)         0
_________________________________________________________________
flatten_2 (Flatten)       (None, 160)           0
_________________________________________________________________
dense_10 (Dense)         (None, 64)           10304
_________________________________________________________________
dense_11 (Dense)         (None, 8)            520
_________________________________________________________________
dense_12 (Dense)         (None, 2)            18
=================================================================
Total params: 16,186
Trainable params: 16,186
Non-trainable params: 0

#10-1 output of intermediate layer of model
from keras.models import Model

layer_name = 'dense_11'
intermediate_layer_model =
Model(inputs=model.input, outputs=model.get_layer(layer_name).
output) intermediate_output =
intermediate_layer_model.predict(x_2)
outdata1=intermediate_output
```

```
#dense 22 layer 2dim  and next is the case of first cnn layer output
data1=outdata[45, 0,:,]+outdata[45, 1,:,]
data2=outdata[6, 0, :,]+outdata[6, 1, :,]
data3=outdata[34, 0, :,]+outdata[34, 1, :,]
data4=outdata[62, 0, :,]+outdata[62, 1, :,]
print(data4)
#print(X)
print(outdata[:,2,150])

import pandas as pd
from google.colab import files
xpred_out=pd.DataFrame(data1)
xpred_out.to_csv('modelparam206.csv')
from google.colab import files
files.download('modelparam206.csv')

#10-2 cnn intermediate data plotting
import numpy as np
import matplotlib.pyplot as plt
import pandas as pd
import sklearn
import time
import matplotlib.cm as cm
cmap=cm.tab10
plt.figure(figsize=(10, 8))
plt.scatter(outdata1[:, 0], outdata1[:, 3], s=25, c=y_2[:,0],
cmap=cmap) plt.colorbar()

#11 gaussian bayesian regression#anaconda codes
%matplotlib inline
import numpy as np
import matplotlib.pyplot as plt
import pandas as pd
SS= pd.read_csv('daytimes.csv')
#t=pd.read_csv('glxc2.csv')
XX=np.array(SS)
t=(XX[:,0]-110)/2100
X=(XX[:,1])/1200

print (X)
print(t)

def phi(x):
  s=0.04
  return np.append(1, np.exp(-(x-np.arange(0,1+s,s))**2/(2*s*s)))
PHI=np.array([phi(x) for x in t])
#w=np.linalg.solve(np.dot(PHI.T,PHI), np.dot(PHI.T,X))
alpha=0.1
beta=6.0
Sigma_N=np.linalg.inv(alpha*np.identity(PHI.shape[1])+beta*np.
dot(PHI.T, PHI))
mu_N=beta*np.dot(Sigma_N, np.dot(PHI.T,X))
xlist=np.arange(0,1,0.000868)
ss=[np.dot(mu_N, phi(x)) for x in xlist]
#plt.plot(list,[np.dot(w, phi(x)) for x in list])
```

```
plt.plot(xlist,[np.dot(mu_N, phi(x)) for x in xlist])
plt.plot(t,X,'o')
plt.show()
print (np.shape(mu_N))
print (ss)
ss=pd.DataFrame(ss)
ss.to_csv('daytimes2.csv')
```